

STUDY OF NEUTRON UNBOUND STATES USING  
THE MODULAR NEUTRON ARRAY (MONA)

By

William Alexander Peters

A DISSERTATION

Submitted to  
Michigan State University  
in partial fulfillment of the requirements  
for the degree of

DOCTOR OF PHILOSOPHY

Department of Physics and Astronomy

2007

## ABSTRACT

### STUDY OF NEUTRON UNBOUND STATES USING THE MODULAR NEUTRON ARRAY (MoNA)

By

William Alexander Peters

The Modular Neutron Array (MoNA) at MSU NSCL, was conceived and built by a collaboration of primarily undergraduate schools, to perform neutron coincident experiments studying nuclear structure. The purpose, goals, setup, and results of the commissioning of MoNA utilizing the Sweeper magnet and its detectors to identify the charged particle residues in coincidence with the neutrons in MoNA are introduced. Calibration techniques are detailed along with analysis procedures. The first test experiments are presented and analyzed.

A measurement of the system resolution is made by comparing data from the one-proton knockout of  $^8\text{Li}$  to the known unbound resonance of  $^7\text{He}$  to detailed simulation of the MoNA/Sweeper setup (using a new Monte Carlo code, `SIMPLE TRACK`). The accuracy of the resolutions determined by calibration tests are confirmed by the final agreement with a  $^7\text{He}$  resonance at  $0.425 \pm 0.02$  MeV and a width of  $0.18 \pm 0.04$  MeV.

The absolute efficiency of the MoNA detector setup is determined from a Coulomb breakup experiment of  $^{11}\text{Be}$ . This reaction is chosen because the decay energy and the cross section can be calculated through both the virtual photon method and the continuum discretized coupled channels method. The data agree very well with the calculated decay curves and the total system efficiency is determined. MoNA's absolute efficiency is deduced to be  $73 \pm 6\%$  for 90 MeV neutrons. This is above the original design goal and agrees with MoNA GEANT simulations.

The first two physics experiments for the MoNA/Sweeper system are presented.

The first is a measurement of the one-neutron knockout cross section from  $^{10}\text{Be}$  to the ground state of  $^9\text{Be}$ . Because  $^9\text{Be}$  has no bound excited states the observance of  $^9\text{Be}$  in the Sweeper focal plane detectors uniquely determines the reaction channel. The reduction factor the  $0p_{3/2}$  single particle spectroscopic factor in  $^{10}\text{Be}$  is determined to be  $0.66 \pm 0.07$ . The results are compared to other spectroscopic factors near the same  $\Delta S$  (neutron minus proton separation energies).

The second experiment concerns the population of different paired-neutron wave functions in the ground state of  $^{12}\text{Be}$  ( $(1s_{1/2})^2$ ,  $(0p_{1/2})^2$  and,  $(0d_{5/2})^2$ ). The relative cross section to the different single particle states in  $^{11}\text{Be}$  can be used to determine relative admixture abundance of the corresponding neutron-pair wave function in  $^{12}\text{Be}$  above a  $^{10}\text{Be}$  core. The relative cross section to the unbound  $5/2^+$  in  $^{11}\text{Be}$  is measured by a neutron knockout reaction using MoNA. The decay energy curve for the current study confirms the reported results of the previous measurements. Differences in the decay energy spectrum with previous measurements concerning the cross section to populate the  $^{10}\text{Be}$   $2^+$  state are noted and likely due to limited efficiencies at forward angles for the previous work.

Finally, a discussion of MoNA's capabilities is presented and experiments completed to date are summarized. Plans for the future of MoNA are also introduced. MoNA analysis and calibration guides are included in the appendices.

*My efforts are inspired by my friends, family, and my dear wife Nicole.*

## ACKNOWLEDGMENTS

I would like to specifically thank members of my advising committee Michael Thoennesen, B. Alex Brown, Carl Schmidt, Wayne Repko, Thomas Glasmacher, and Filomena Nunes. Their guidance and has been a source of focus and very much appreciated. I only hope to do as well as job as they did for me, to others someday. Their knowledge was ever-present and ever-giving. Michael Thoennesen, in particular, was nurturing and strict with wonderful equanimity.

I would also like to thank God for making the universe so complex and exponentially incomprehensible that after thousands of years of trying, there is still a lot a physics left to discover.

The environment at MSU has been wonderful, especially Debbie, and Laura; without whom I would have paid more money to MSU in fees. They have been guides in some ways on life and academics many times.

My appreciation also goes out to my friends, Pete, Anca, Ali, Mark, Josh, my brother Rob, and those of you who know who you are. I feel blest to have made it this far considering many of my friends, that are better than I in many ways, could not.

My grandparents have done a great job of building strong stable families for my parents, and in turn, for me. I draw a lot of strength and courage from this base, and feel supported constantly by its foundations.

My parents have always supported me, even when maybe I should have been set straight. Mom, and dad, you make me strive to live up to your investment in me. I try forever to make you as proud as you have made me loved.

My wife Nicole, who is currently working on our own real baby, has brought joy into my life that I did not think was possible for me. Honey, I cherish every day you love me and pray I can keep you happy and safe forever. You love me in ways that transcend my ability to describe. Thank you. Thank you all.

# TABLE OF CONTENTS

<b>List of Figures</b>	<b>xi</b>
<b>List of Tables</b>	<b>xiv</b>
<b>1 Introduction</b>	<b>1</b>
1.1 Magic Numbers and the Shell Model . . . . .	1
1.2 Neutron Rich Nuclei . . . . .	2
1.2.1 Neutron Unbound States . . . . .	3
1.3 Neutron Detection Tools . . . . .	3
1.4 Commissioning Experiments . . . . .	8
1.4.1 Unbound ${}^7\text{He}$ Ground State . . . . .	8
1.4.2 ${}^{11}\text{Be}$ Coulomb Breakup . . . . .	8
1.5 First Physics Results from MoNA/Sweeper . . . . .	9
1.5.1 One Neutron Knockout of ${}^{10}\text{Be}$ . . . . .	9
1.5.2 Ground State Wave Function of ${}^{12}\text{Be}$ . . . . .	10
<b>2 Modular Neutron Array (MoNA)</b>	<b>11</b>
2.1 Design . . . . .	11
2.1.1 Detection Method . . . . .	13
2.1.2 Light Propagation . . . . .	14
2.2 Electronics . . . . .	15
2.2.1 Light To Signal Processing . . . . .	15
2.2.2 Digital Signal Conversion . . . . .	17
2.2.3 Timing Signal Processing . . . . .	18
2.2.4 Light Amplitude Processing . . . . .	19
2.2.5 Level 1 Logic Modules . . . . .	20
2.2.6 Level 2 Logic Module . . . . .	21
2.3 Calibration . . . . .	21
2.3.1 Gain Matching the PMTs . . . . .	23
2.3.2 QDC Calibration . . . . .	26
2.3.3 QDC Thresholds . . . . .	27
2.3.4 TDC Calibration . . . . .	31
2.3.5 Position Calibration . . . . .	32
2.3.6 Time Offsets . . . . .	32
<b>3 MoNA/Sweeper Experimental Setup</b>	<b>36</b>
3.1 Layout . . . . .	36
3.2 MSU/FSU Sweeper Magnet . . . . .	38
3.3 Charged Particle Detectors . . . . .	38
3.3.1 Target Chamber . . . . .	40
3.3.2 CRCDs . . . . .	42

3.3.3	Ion Chamber . . . . .	42
3.3.4	Thin/Thick Plastic Scintillators . . . . .	43
3.4	Reaction Residue Identification . . . . .	43
3.4.1	Element Identification . . . . .	44
3.4.2	Isotope Identification . . . . .	44
3.5	Trigger Logic . . . . .	46
3.5.1	MoNA/Sweeper Coupling . . . . .	46
3.5.2	Coincidence Timing . . . . .	49
3.5.3	MoNA Level 1 Trigger Logic . . . . .	50
3.5.4	Level 2 Logic . . . . .	52
3.5.5	Level 2 Timer . . . . .	53
3.5.6	Auxiliary Inputs . . . . .	57
3.5.7	Level 2 Trigger Conditions . . . . .	58
3.6	Decay Energy Reconstruction . . . . .	59
3.6.1	Invariant Mass . . . . .	59
3.6.2	Charged Particle Reconstruction . . . . .	60
3.6.3	Energy and Angle of Neutrons . . . . .	62
<b>4</b>	<b>Performance</b>	<b>63</b>
4.1	Neutron Detector Simulation . . . . .	63
4.1.1	Reaction Cross Sections . . . . .	64
4.1.2	Light Response . . . . .	66
4.1.3	Simulated MoNA Intrinsic Efficiency . . . . .	68
4.1.4	MoNA/Sweeper Layout Simulation . . . . .	71
4.2	Resolution Measurements . . . . .	72
4.2.1	MoNA Time Resolution . . . . .	72
4.2.2	MoNA X Resolution . . . . .	73
4.2.3	MoNA Y,Z Resolution . . . . .	75
4.2.4	MoNA Energy Resolution . . . . .	77
4.2.5	Focal Plane Resolutions . . . . .	78
4.2.6	Simulated Resolution . . . . .	78
4.3	$^7\text{He}$ Resolution Test . . . . .	79
4.3.1	Experimental Setup . . . . .	80
4.3.2	Resolution Results . . . . .	81
4.4	Measured MoNA/Sweeper System Efficiency . . . . .	81
4.4.1	Experimental Setup . . . . .	82
4.4.2	Virtual Photon Calculations . . . . .	82
4.4.3	Experimental Comparison . . . . .	84
4.4.4	Second $^{11}\text{Be}$ Experiment for Efficiency Measurement . . . . .	85
4.4.5	Measured Incoming Rate . . . . .	87
4.4.6	Detector Acceptances . . . . .	89
4.4.7	Simulation Input Parameters . . . . .	91
4.4.8	System Efficiency . . . . .	92
4.4.9	CDCC Cross Section Calculations . . . . .	94

<b>5</b>	<b>One Neutron Knockout of <math>^{10}\text{Be}</math></b>	<b>96</b>
5.1	Introduction . . . . .	96
5.2	Experimental Details . . . . .	97
5.3	Analysis . . . . .	98
5.3.1	Cross Section Calculations . . . . .	98
5.3.2	Parallel Momentum Comparisons . . . . .	104
5.4	Conclusions . . . . .	107
<b>6</b>	<b>Ground State of <math>^{12}\text{Be}</math></b>	<b>108</b>
6.1	Introduction . . . . .	108
6.2	Experimental Details . . . . .	111
6.3	Analysis . . . . .	112
6.3.1	Comparisons to Previous Results . . . . .	114
6.3.2	Diffractive Breakup and Two-Neutron Decay . . . . .	119
6.4	Conclusions . . . . .	120
<b>7</b>	<b>Outlook</b>	<b>122</b>
7.1	Evaluation of Design . . . . .	122
7.2	Multiple-Neutron Capabilities . . . . .	122
7.3	Other Completed Experiments . . . . .	126
7.3.1	Oxygen Isotopes . . . . .	126
7.3.2	$^8\text{Li}$ Coulomb Breakup . . . . .	126
7.3.3	Fragmentation to Multiple Unbound States . . . . .	126
7.3.4	Double-Neutron Experiments . . . . .	127
7.3.5	Cosmic Ray Survey . . . . .	128
7.4	Scheduled Future Experiments . . . . .	128
<b>8</b>	<b>Conclusion</b>	<b>129</b>
8.1	MoNA Efficiency and Resolution . . . . .	129
8.2	$^{10}\text{Be}$ Neutron Knockout . . . . .	129
8.3	$^{12}\text{Be}$ Ground State Wave Function . . . . .	130
<b>A</b>	<b>Experimental Startup</b>	<b>131</b>
A.1	Introduction . . . . .	131
A.2	Experimental Account . . . . .	131
A.2.1	Password . . . . .	132
A.2.2	Group Members . . . . .	132
A.2.3	SSH . . . . .	133
A.2.4	Event Space . . . . .	133
A.2.5	Log Book . . . . .	134
A.3	Bash Profile . . . . .	134
A.4	Directory Structure . . . . .	134
A.4.1	Mona . . . . .	135
A.4.2	Tandem . . . . .	135
A.4.3	Experiment . . . . .	135
A.4.4	Desktop . . . . .	137



A.5	Running Experiment . . . . .	138
A.5.1	Edit Settings Files . . . . .	138
A.5.2	Orphaned Runs . . . . .	138
A.6	Post Experiment . . . . .	140
A.6.1	Calibration Runs . . . . .	140
A.6.2	Archive Tapes . . . . .	141
A.6.3	Analysis Space . . . . .	142
A.6.4	Executables . . . . .	143
<b>B</b>	<b>MoNA SpecTcl Analysis Guide</b>	<b>145</b>
B.1	Introduction . . . . .	145
B.1.1	MoNA Parameters . . . . .	145
B.2	Configuration files . . . . .	147
B.2.1	MoNA Config Directory . . . . .	148
B.3	Running SpecTcl . . . . .	150
B.3.1	Open SpecTcl . . . . .	150
B.3.2	Creating Spectra . . . . .	153
B.3.3	Configuring Xamine . . . . .	154
B.3.4	Attaching Data . . . . .	154
B.3.5	Setting up Gates . . . . .	154
B.3.6	Copying Spectra . . . . .	156
B.3.7	Displaying New Spectra . . . . .	156
B.3.8	Applying Gates . . . . .	157
B.4	Analyzing Data . . . . .	157
B.4.1	Exporting Data . . . . .	158
B.4.2	Importing into Excel . . . . .	158
B.5	Simplifying . . . . .	159
B.5.1	Settings Files . . . . .	159
B.5.2	Creating Custom Pseudos . . . . .	160
B.5.3	Filtered Data . . . . .	162
B.5.4	Useful Tips . . . . .	163
<b>C</b>	<b>MoNA Calibration Guide</b>	<b>164</b>
C.1	Introduction . . . . .	164
C.1.1	Proper Links . . . . .	165
C.2	High Voltage Gain Matching . . . . .	166
C.2.1	Getting Started . . . . .	167
C.2.2	Take Cosmic Data . . . . .	167
C.2.3	Voltage Matching Code . . . . .	169
C.2.4	Setting New Voltages . . . . .	170
C.3	QDC Calibration . . . . .	171
C.3.1	Calibration Steps . . . . .	171
C.4	TDC Calibration . . . . .	173
C.4.1	Record Time Calibration Run . . . . .	173
C.4.2	Running Calibration Code . . . . .	176
C.4.3	File Names . . . . .	179

C.5	X Position Calibration . . . . .	179
C.5.1	Record Cosmic Run . . . . .	180
C.6	Independent Tmean Offsets . . . . .	183
C.6.1	Finding Independent Offsets . . . . .	183
<b>D</b>	<b>Tandem SpecTcl Guide</b>	<b>187</b>
D.1	Getting Started . . . . .	187
D.1.1	Standard Variables . . . . .	187
D.1.2	Loading a Settings File . . . . .	188
D.2	Tree Structure . . . . .	189
D.2.1	Sweeper Tree . . . . .	189
D.2.2	User Tree . . . . .	190
D.2.3	Using the Tree Parameter GUI . . . . .	190
D.3	SpecTcl Code Procedures . . . . .	192
D.3.1	Raw Sweeper Parameters . . . . .	192
D.3.2	Tree Calibrations . . . . .	194
D.3.3	Third-Level Parameters . . . . .	196
D.3.4	MoNA Hits . . . . .	197
D.3.5	Valid Tandem Hit . . . . .	197
D.3.6	Tracked Parameters . . . . .	199
D.3.7	MoNA Tandem Parameters . . . . .	200
D.4	Analysis Suggestions . . . . .	203
D.4.1	Tandem Control Buttons . . . . .	203
D.4.2	Beamline Forward Tracking . . . . .	204
D.4.3	Sweeper Inverse Tracking . . . . .	205
D.4.4	MoNA Timing . . . . .	206
D.4.5	Isotopic Separation . . . . .	206
D.4.6	Decay Energy . . . . .	207
D.4.7	Multiple Neutrons . . . . .	207
D.4.8	Limitations . . . . .	208
	<i>Bibliography</i> . . . . .	209

## LIST OF FIGURES

1.1	Magic numbers from W-S potential and spin-orbit coupling. . . . .	4
1.2	Chart of the nuclides. . . . .	5
1.3	Methods of studying nuclei near the neutron drip line. . . . .	6
1.4	Computer image of original MoNA design. . . . .	7
2.1	Diagram of one MoNA module. . . . .	14
2.2	Diagram of MoNA DAQ system. . . . .	16
2.3	Left and right QDC response for cosmic-ray muons. . . . .	20
2.4	Sample routing map of Virtex FPGA. . . . .	22
2.5	Cosmic-ray muons flux through MoNA. . . . .	23
2.6	Side view of MoNA array with cosmic-ray muon tracks. . . . .	24
2.7	Raw QDC spectrum for background run used for calibration. . . . .	25
2.8	cosmic-ray muon peak fit for raw QDC spectrum. . . . .	26
2.9	Raw QDC pedestal peak for PMT B-00-L. . . . .	28
2.10	Raw QDC pedestal peak for PMT B-02-L. . . . .	29
2.11	CFD threshold calibration. . . . .	30
2.12	Raw TDC spectrum with peaks from time calibrator. . . . .	31
2.13	Calibrated time difference spectrum for $x$ position calibration. . . . .	33
2.14	Straight down gate on muon tracks for time offsets. . . . .	34
2.15	Time difference ( $\Delta t$ ) between two bars triggered by a muon track. . . . .	35
3.1	Drawing of Coupled Cyclotron Facility (CCF). . . . .	37
3.2	MoNA/Sweeper setup. . . . .	39
3.3	Drawing of Sweeper detector box. . . . .	40
3.4	Target ladder diagram. . . . .	41
3.5	Example of adjusted $\text{ToF}_{\text{rigid}}$ isotope separation. . . . .	45

3.6	Diagram of MoNA/Sweeper coupling and timing. . . . .	48
3.7	MoNA Level 1 logic diagram. . . . .	51
3.8	Diagnostic scaler display from Level 1 logic modules. . . . .	52
3.9	MoNA Level 2 logic diagram. . . . .	54
3.10	Signal times for typical coincident event. . . . .	55
4.1	Drawing of GEANT-3.2.1MoNA setup with neutrons. . . . .	64
4.2	Hydrogen and carbon neutron cross sections used in GEANT. . . . .	65
4.3	Neutron reaction cross sections for MoNA plastic used in GEANT. . . . .	65
4.4	Measured light response curve for 35-40 MeV neutrons. . . . .	66
4.5	Neutron kinetic energy spectrum for 80-100 MeV neutrons. . . . .	67
4.6	Measured light response curve for 80-100 MeV neutrons. . . . .	68
4.7	Simulated total intrinsic efficiency for MoNA. . . . .	69
4.8	Incoming neutron count calculated by efficiency simulation. . . . .	70
4.9	CFD hardware threshold analysis. . . . .	70
4.10	Resolution of $x$ position in MoNA calculated by GEANT. . . . .	73
4.11	Calibrated $x$ position of muons gated above and below. . . . .	75
4.12	Plot of $x$ versus $y$ in MoNA for sample data. . . . .	76
4.13	Sample plot of neutron angle relative to the beam axis. . . . .	76
4.14	Plot of $z$ position in MoNA by layer. . . . .	77
4.15	Sample decay energy spectra from ST-mona simulation. . . . .	79
4.16	Decay energy resolution from ST-mona simulation. . . . .	80
4.17	Decay energy of $^7\text{He}$ fit with experimental resolutions. . . . .	81
4.18	$^{11}\text{Be}$ calculated E1 cross section. . . . .	84
4.19	Isotope identification for $^{11}\text{Be}$ Coulomb breakup. . . . .	85
4.20	Focal plane data compared with ST-mona simulation for 03048. . . . .	86
4.21	Coulomb breakup decay energy compared to ST-mona simulation. . . . .	87
4.22	Isotope separation for $^{11}\text{Be}$ Coulomb breakup. . . . .	88

4.23	Second isotope gate on ToF for 07503. . . . .	88
4.24	Reaction residue gated and ungated neutron ToF. . . . .	89
4.25	Focal plane data compared with ST-mona simulation for 07503. . . . .	90
4.26	Simulated $y$ position at the thin focal plane scintillator. . . . .	91
4.27	MoNA position data compared with simulation for 07503. . . . .	92
4.28	Acceptance of MoNA as a function of $^{11}\text{Be}$ decay energy. . . . .	93
4.29	Fragment angle comparison for CDCC calculation. . . . .	94
4.30	Cross section for CDCC and virtual photon methods. . . . .	95
5.1	Reduction factor versus nucleon separation energies. . . . .	97
5.2	Isotope identification plot for one-neutron knockout of $^{10}\text{Be}$ . . . . .	99
5.3	Sweeper focal plane $x$ acceptance of $^9\text{Be}$ residue for run 2114. . . . .	100
5.4	Sweeper focal plane $x$ acceptance of $^9\text{Be}$ residue for run 2121. . . . .	101
5.5	Sweeper focal plane $y$ acceptance of $^9\text{Be}$ residue. . . . .	102
5.6	Reduction factor versus nucleon separation energies with $^{10}\text{Be}$ . . . . .	103
5.7	Reconstructed target angle acceptance of $^9\text{Be}$ residue. . . . .	104
5.8	Momentum distribution of $^{10}\text{Be}$ beam through the reaction target. . . . .	105
5.9	Parallel momentum distribution of $^9\text{Be}$ residue compared to p-wave fit. . . . .	106
6.1	Diagram of decay channels for $^{12}\text{Be}$ neutron knockout. . . . .	109
6.2	Isotope identification for the $^{12}\text{Be}$ ground state experiment. . . . .	112
6.3	$^{10}\text{Be}$ residue kinetic energy from the $^{12}\text{Be}$ ground state study. . . . .	113
6.4	Neutron kinetic energy from the $^{12}\text{Be}$ ground state study. . . . .	114
6.5	Relative velocity for the $^{12}\text{Be}$ ground state study. . . . .	115
6.6	Opening angle versus relative velocity for the $^{12}\text{Be}$ ground state study. . . . .	116
6.7	$^{12}\text{Be}$ experiment fit to data fixing cross sections to previous work. . . . .	117
6.8	$^{12}\text{Be}$ experiment fit to data allowing individual amplitudes to adjust. . . . .	118
7.1	Future vault configuration for MoNA/Sweeper setup. . . . .	123
7.2	Alternate setup for direct fragmentation experiment. . . . .	127

B.1	The MoNA SpecTcl control window. . . . .	151
B.2	The Xamine startup window. . . . .	151
B.3	The console shell. . . . .	152
B.4	The Tkcon window. . . . .	152
B.5	Gated $x$ position Xamine window. . . . .	158
C.1	Raw QDC Xamine spectra. . . . .	168
C.2	Calibrated TDC Xamine spectra. . . . .	176
C.3	X position Xamine spectra. . . . .	181
C.4	X position A0 spectrum. . . . .	182
C.5	Tmean difference spectra. . . . .	185
D.1	Tree parameters user window. . . . .	188
D.2	Tandem SpecTcl control window. . . . .	204

Images in this dissertation are presented in color.

## LIST OF TABLES

1.1	Comparison of existing major neutron detectors. . . . .	7
2.1	Founding institutions of the MoNA collaboration. . . . .	12
2.2	Dominant neutron reactions in plastic for 90 MeV neutrons. . . . .	13
3.1	Level 1 Majority bits . . . . .	50
3.2	Level 2 timer delay times. . . . .	56
3.3	Cosy or traditional transformation matrix parameters. . . . .	61
4.1	Light-response coefficients for GEANT. . . . .	68
4.2	Resolutions for MoNA at 8 m and 14 m positions. . . . .	78
4.3	Detector efficiencies and acceptances for 07503. . . . .	93
5.1	Cross section and spectroscopic factor for 1n knockout of $^{10}\text{Be}$ . . . . .	103
6.1	Summary of results from previous studies of $^{12}\text{Be}$ . . . . .	110
6.2	Relative intensities of $^{12}\text{Be}$ decay compared to previous work. . . . .	116

# Chapter 1

## Introduction

### 1.1 Magic Numbers and the Shell Model

Much effort is put toward studying the evolution of “magic” numbers in atomic nuclei, especially in the neutron-rich region. Characteristics of magic nuclei include a sharp decrease in the nucleon separation energy when one or two neutrons or protons are added to a magic number nucleus [1, 2]. These discontinuities in the separation energy are a consequence of gaps in the binding energy between shell levels at a magic number of protons or neutrons for the next nucleon. Magic nuclei with an even number of both protons and neutrons have a much higher first excited state ( $2^+$ ) than non-magic nuclei. The transition probability to this first excited state is much lower in neighboring even–even nuclei due to the lack of collectivity since strongly bound ground states are highly spherical and take a lot of energy to excite (to the  $2^+$  excited state).

Quantum mechanical approaches developed to account for these magic numbers reproduce the proper gaps in binding energy for these particular numbers of nucleons by using a Woods-Saxon potential

$$V_{WS}(r) = \frac{-V_o}{1 + e^{(r-R)/\alpha}} - V_{ls} \quad (1.1)$$



with an additional spin-orbit coupling term ( $V_{ls}$ ). The spin-orbit coupling lowers the potential energy of  $l + s$ , where  $l$  is the orbital angular momentum quantum number and  $s$  is the spin of the nucleon (always  $1/2$  for fermions). The effect is opposite for  $l - s$  states. Figure 1.1 displays the results of Equation 1.1 (from Reference [3]). The vertical scale represents relative binding energy. The quantum number  $l$  for the orbital angular momentum for a harmonic oscillator is coupled to the spin ( $1/2$ ) of the nucleon to create the nuclear shell levels. In some cases this effect is so large as to create a new magic number for one shell, like between 20 and 28 for the  $1f_{7/2}$  shell. These shell levels are populated by up to  $(2j+1)$  nucleons, where  $j$  is the total angular momentum quantum number ( $j = l \pm s$ ). The values on the right of Figure 1.1 are the maximum number of protons or neutrons each shell level can hold, and the total number, illustrating the magic numbers. This nuclear model is called the spherical shell model and reproduces the nuclear structure of nucleons near stability [3, 4].

## 1.2 Neutron Rich Nuclei

The shell model reproduces many of the observed qualities of nuclear structure (particularly shell level populations) but requires adaptation for nuclei not near the region of stability. Figure 1.2 is a chart of the nuclides and shows the full known and unknown landscape of nuclei (stable nuclei are displayed as black squares). The red dashed lines mark the magic numbers for protons and neutrons. Close to the drip lines (the limit of binding energy where no more protons or neutrons can be bound within a nucleus by the nuclear potential), some of these magic numbers no longer indicate stronger binding energies; shell gaps disappear and new ones appear. Sometimes a specific number of protons can bind many more neutrons than the neighboring element. Fluorine ( $Z = 9$ ), for example, is bound to at least  $N = 22$  while oxygen is only bound until  $N = 16$  [5]. Furthermore, phenomenon like neutron and proton halo nuclei are found to exhibit strange properties that cannot be modeled by nucleons in a simple potential

well. Studying the evolution of these shell levels constrains theoretical explanations and predictions. The level structure of neutron-rich nuclei can change dramatically from one nucleus to the next due to interactions that are not observed near the valley of stability because of the different proton and neutron configurations of rare nuclei. Discoveries like these drive current efforts of nuclear structure experimentation and shell model theory [6] and the undiscovered region of the chart of the nuclides in Figure 1.2 is mostly neutron rich where neutron detectors are likely to play an important role in their study.

### 1.2.1 Neutron Unbound States

Some of the most important nuclear structure quantities include the nuclear populations within shell levels and the level structure (binding order of shell level within the nucleus) for nuclei far from stability. Near the neutron drip line, methods for studying energy levels are limited to neutron-spectroscopy experiments. Figure 1.3 illustrates the extent of nuclei where other methods would not be sufficient to record the energy levels of these nuclei. Nuclei whose excited states are unbound cannot be studied by using  $\gamma$ -ray detectors. This covers a large number of nuclear states near the drip line that require neutron spectroscopy to study [7]. In addition, nuclei that are at the drip line cannot be populated by  $\beta$ -decay experiments that require a  $(N+1, Z-1)$  feeder nucleus.

Neutron spectroscopy involves detecting neutrons from an unbound resonance that are forward focused from fast beams, greater than 10 MeV per nucleon (MeV/u), about zero degrees in coincidence with the residual nucleus.

## 1.3 Neutron Detection Tools

Neutron detectors for energies between 10 and 100 MeV are generally made of an organic scintillating material. A volume of scintillating material is coupled to one or

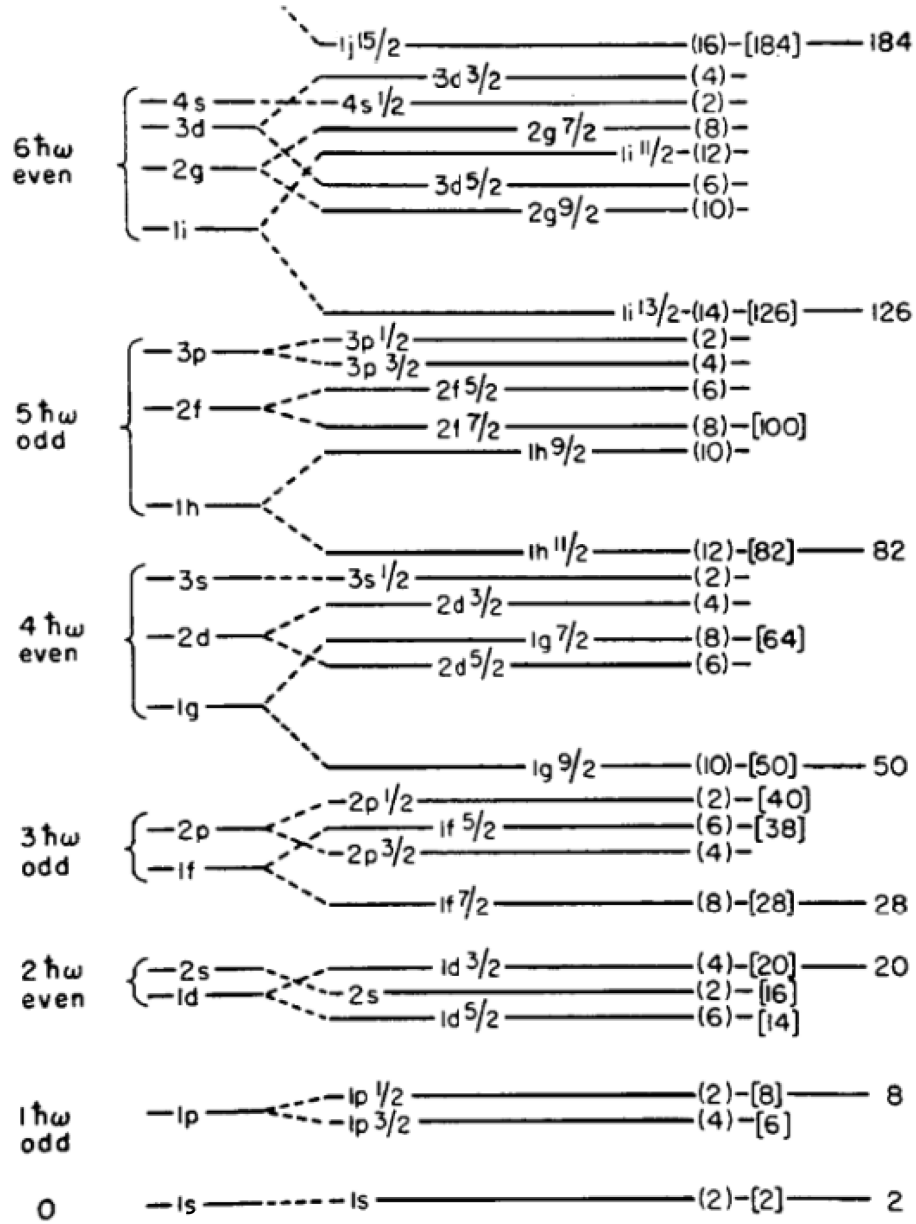


Figure 1.1: Level diagram using a Woods-Saxon potential for nuclei and coupling spin-orbit interactions leads to groupings and gaps corresponding to the experimentally known “magic numbers” (from Reference [3]). The numbers in brackets on the right side refer to the number to fill each shell level and the total number to that point. The notation for shell levels in this figure starts at  $1s_{1/2}$  while the prevailing current notation (and used within this thesis) starts at  $0s_{1/2}$ .

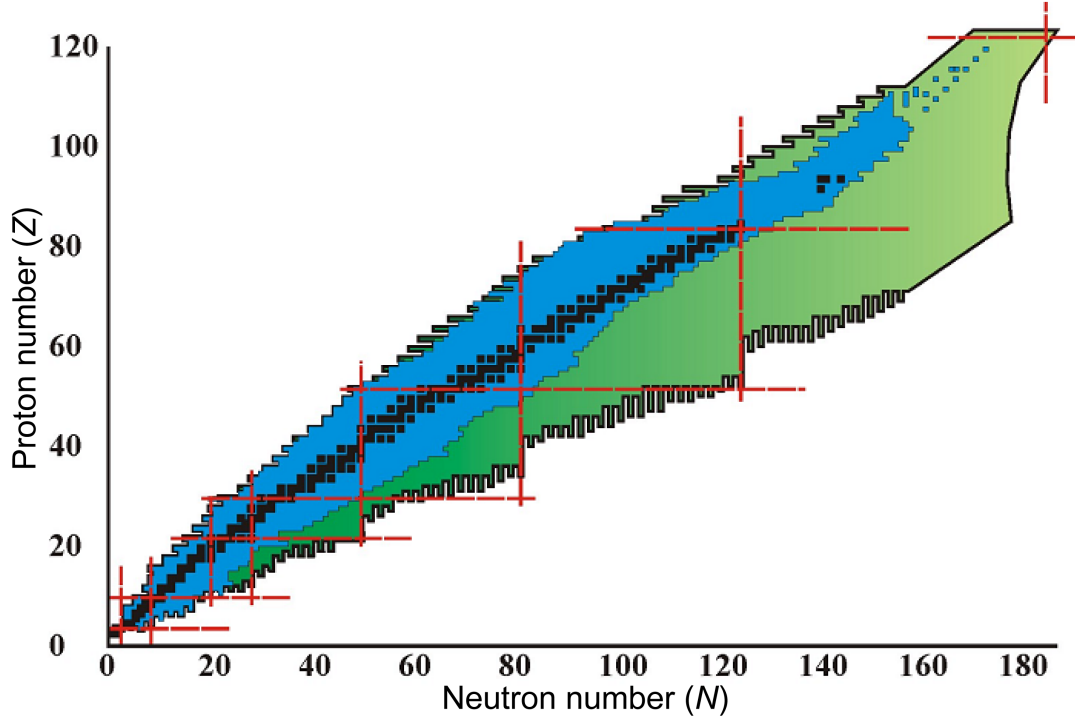


Figure 1.2: Chart of the nuclides, the full nuclear landscape as proton number ( $Z$ ) versus neutron number ( $N$ ). Regions that are yet undiscovered, but predicted to exist, are shown in green. The magic numbers are marked by dashed red lines.

more photo-multiplying tubes (PMT) to convert the light response from an interacted neutron to time and amplitude signals. The time-of-flight (ToF) of the reactions relative to a target timing detector are used to determine the neutron's velocity.

Table 1.1 lists neutron detectors at major fragmentation facilities. The DeMoN array in GANIL, France [8] is an array of liquid NE213 [9] detectors mounted on stands that can be easily rearranged and placed at large angles relative to the beam axis. The efficiency of this detector is only about 10%. The first large neutron detector at the National Superconducting Cyclotron Laboratory (NSCL), Michigan State University, USA consists of the neutron walls. They comprise two walls of liquid NE213-filled glass bars. The coverage area is 2 by 2 meters and it is primarily used for neutron energies less than 40 MeV [10]. The Large Area Neutron Detector (LAND) at GSI, Germany is a large array of 0.5 cm thin BC408 [11] plastic scintillator plates sandwiched between 0.5 cm thin passive iron plates. The sandwich is repeated 10 times for a 10 cm thick,

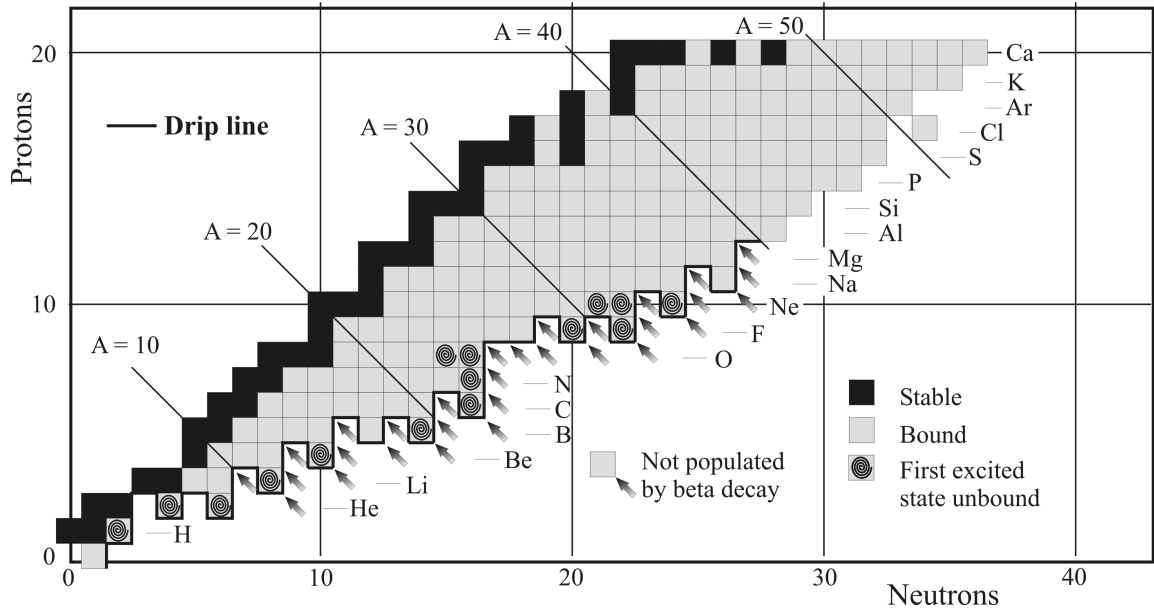


Figure 1.3: Many nuclei near the neutron drip line can not be adequately studied by methods other than neutron spectroscopy. Populating unbound resonances by  $\beta$  decay cannot be done for nuclei without a feeder nucleus (marked by arrows). Also, nuclei with no bound excited states (swirls) cannot be studied by  $\gamma$ -ray spectroscopy. Measuring the resonant energy of the ground state for any unbound nucleus beyond the drip line, also can only be done with neutron spectroscopy.

200 cm long bar and then all ten plastic scintillators are coupled to one PMT at each end. The full array has ten layers of criss-crossed bars with a total of 50 cm of both iron and plastic scintillator [12] and takes up a volume of 3 cubic meters. The NEUT detector at RIKEN, Japan [13] has only two layers of scintillating plastic, limiting its total efficiency. The total array has 30 bars (15 in each layer. Each bar is 6.1 cm thick ( $z$  axis) and tall ( $y$  axis) and 214 cm wide ( $x$  axis).

The Modular Neutron Array (MoNA) [14, 15] assembled at NSCL at Michigan State University in 2003 was designed to detect neutrons at energies consistent with experiments utilizing rare isotope beams from in-flight fragmentation as currently done at the NSCL (about 30-100 MeV/u). It is also capable of running with passive iron converters, similar to LAND, in between the last six layers to increase the efficiency for higher energy neutrons ( $> 100$  MeV). It has 90 cm of active plastic scintillator when arranged in its current configuration of 9 layers ( $z$  axis) of 16 rows

Table 1.1: Specifications of various neutron detectors including the original design goals for MoNA [18]. Efficiencies are listed for a representative energy within the normal range of neutron energies for each detector.

Detector	Lab	Material	Neutron energies	Efficiency
NEUT	RIKEN	Plastic	40–200 (MeV)	14 %
DeMoN	GANIL	NE213	5–50 (MeV)	10 %
Neutron Walls	NSCL	NE213	10–100 (MeV)	30 %
LAND	GSI	BC408	100–1000 (MeV)	90 %
MoNA	NSCL	BC408	30–200 (MeV)	70 %

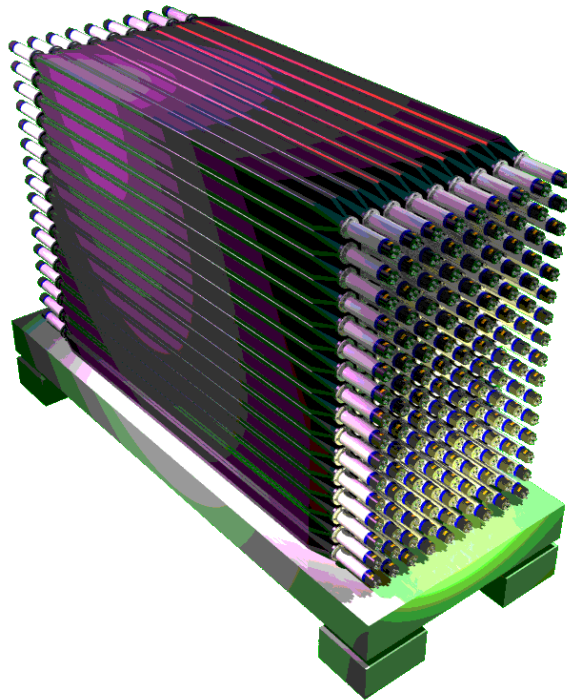


Figure 1.4: Computer-generated image of the original MoNA design, including 144 plastic modules ( $10 \times 10 \times 200 \text{ cm}^3$ ) arranged in an array of  $9 \times 16$  to cover a large area and accept forward-focused neutrons at energies greater than 30 MeV.

( $y$  axis). Figure 1.4 shows a computer drafted image of the design for MoNA. The charged-particle residues from a neutron-unbound state are deflected by a large-gap dipole magnet, called the Sweeper magnet [16, 17], allowing the neutrons to pass through at zero degrees (see Section 3.2 for details). The Sweeper Magnet was built at the National High Magnetic Field Laboratory at Florida State University.

## 1.4 Commissioning Experiments

The first experiments for MoNA were performed to test the design goals of the system and quantify properties like resolution and efficiency. To measure the resolution of MoNA, a known resonant energy with a known width must be replicated and compared to previous results. To measure the system's efficiency a reaction with a known cross section for the production of a neutron-fragment pair must be performed to calculate the ratio of the known number of neutrons produced to the number of neutrons recorded by MoNA.

### 1.4.1 Unbound ${}^7\text{He}$ Ground State

The ground state of  ${}^7\text{He}$  is unbound and an ideal choice to measure the energy resolution of the reconstructed decay energy for the MoNA/Sweeper system. This resonant state has been studied extensively and can be used for testing a neutron detector system. The width of the  ${}^7\text{He}$  ground state resonance is known to be  $160 \pm 30$  keV with a resonance energy of  $430 \pm 20$  keV [19,20]. By simulating the MoNA/Sweeper configuration, including a reaction model, target properties, and the beam properties, the simulated physics parameters like energy and angle can be compared to measured parameters. The individual detector resolutions, measured by various methods, can be programmed into the simulation to determine which parameters contribute the most to the experimental resolution of the reconstructed resonant energy.

### 1.4.2 ${}^{11}\text{Be}$ Coulomb Breakup

The Coulomb breakup of  ${}^{11}\text{Be}$  was used to measure the absolute efficiency of MoNA. Since the cross section for the release of a neutron is calculable, the recorded neutron events counted in MoNA directly relates to the efficiency of the MoNA detector, after effects due to acceptance are removed. The Coulomb excitation is induced by a high- $Z$  reaction target of gold, and the cross section is calculated using by the virtual photon

method [21–23] and the continuum discretized coupled channels (CDCC) method [24, 25]. By adjusting reaction parameters in a Monte Carlo simulation for both the  $^{10}\text{Be}$  residue and the accompanying neutron to match the recorded distributions in the focal plane and MoNA detectors, the system acceptance can be extracted. Once this is completed, a calculation reveals the efficiency of the MoNA detector to compare to design goals and GEANT simulations (see Section 4.4).

## 1.5 First Physics Results from MoNA/Sweeper

The disappearance of the  $N = 8$  magic number in neutron-rich nuclei is evident in the beryllium isotopes where  $^{11}\text{Be}$  has a ground state that is an intruder  $1/2^+$  state (due to a neutron in the  $1s_{1/2}$  shell). The normal shell level ordering for stable nuclei would populate the  $0p_{1/2}$  shell for the seventh neutron, and the  $1s_{1/2}$  shell would start to fill with the ninth neutron. In addition  $^{11}\text{Be}$  is a neutron halo nucleus, and ( $Z = 3$ ,  $N = 8$ )  $^{11}\text{Li}$  is a double neutron halo nucleus [26] further indicating a loosely-bound  $N = 8$  neutron.

### 1.5.1 One Neutron Knockout of $^{10}\text{Be}$

The first experiment studying the beryllium isotopes concerns the population of the  $0p_{3/2}$  shell of  $^{10}\text{Be}$  predicted by the shell model to contain a neutron single-particle strength of 2.45 neutrons [27]. By measuring the cross section of the one-neutron knockout reaction to the  $^9\text{Be}$  ground state and comparing it to a theoretical knockout cross section calculated for that system by the eikonal model of fast reactions [28], an empirical reduction factor can be determined. The reduction factor is a gauge of the shell model’s accuracy in describing the system as an inert core with the last valence shell partially filled. Since the shell model calculations do not include 3-body nucleon-nucleon-core short-range interactions, nuclei that experience such interactions have single-particle populations less than those predicted by the shell model,



and thus, a reduction factor less than 1. In the case of  $^{10}\text{Be}$ , the decay channel is uniquely identified as a  $0p_{3/2}$  neutron knockout by the  $^9\text{Be}$  residue, since  $^9\text{Be}$  has no bound excited states, and does not require the use of MoNA. Chapter 5 details the experiment using the Sweeper magnet and the focal plane detectors to measure the reduction factor for  $0p_{3/2}$  neutron knockout of  $^{10}\text{Be}$ .

### 1.5.2 Ground State Wave Function of $^{12}\text{Be}$

The second experiment continues the study of the evolution of the lower neutron shell levels in beryllium isotopes at the neutron drip line. The standard order of filling the nuclear shell levels for stable nuclei is already broken by the neutron halo nucleus  $^{11}\text{Be}$  so, the mixture of neutron pair correlations in the  $0^+$  ground state wave function for  $^{12}\text{Be}$  is predicted not to be just a simple combination of  $(1s_{1/2})^2$  or  $(0p_{1/2})^2$  paired neutrons built on a  $^{10}\text{Be}$  core. Indeed the first experiment to measure the populations of these configuration found about half of the total neutron single particle population missing [29], suggesting a strong admixture of  $(0d_{5/2})^2$  neutron pair wave function. More recently, a second experiment, including the ability to measure the neutron-unbound levels in  $^{11}\text{Be}$ , confirmed the hypothesis [30] by observing the  $5/2^+$  level in  $^{11}\text{Be}$  by stripping one of the  $(0d_{5/2})^2$  paired neutrons from  $^{12}\text{Be}$ . Using MoNA, a third experiment was performed with higher statistics (enabled by MoNA's high efficiency for fast neutrons) focusing on the neutron-unbound exit channels from one-neutron knockout of  $^{12}\text{Be}$  to compare to previous works. Chapter 6 details this experiment and the results.

# Chapter 2

## Modular Neutron Array (MoNA)

A collaboration of eight primarily undergraduate institutions along with Michigan State University and Florida State University, separately requested and received National Science Foundation grants to build and assemble the Modular Neutron Array (MoNA) [14]. Undergraduate students built and assembled 16 modules from bars of plastic scintillator and tested them [15]. Table 2.1 lists the founding institutions of the MoNA collaboration. The array of nine vertical layers (one layer from each school) with 16 modules each was assembled at the National Superconducting Cyclotron Laboratory (NSCL) at MSU.

### 2.1 Design

MoNA was designed for use with in-flight fragmentation rare isotope beams produced by the CCF at the NSCL [31]. Secondary beam energies are generally between 30-100 MeV/u. Neutrons from unbound states populated within the reaction target will have similar energies and are forward focused in the lab. Reconstruction of the decay energy of the unbound states requires both the energy and position (angle) of the neutron (see Section 3.6.1). With sufficient distance from the target, the time-of-flight (ToF) can be used to calculate the velocity and energy, while the position

Table 2.1: Founding institutions of the MoNA collaboration and their principle investigator for the NSF grants.

Institution	Principle Investigator	NSF grant
Ball State University, Indiana	R. Howes <sup>a</sup>	PHY-0132367
Central Michigan University, Michigan	J. Finck	PHY-0132532
Concordia College, Minnesota	B. Luther	PHY-0132725
Florida State University, Florida	K. Kemper & S. Tabor	PHY-0132434
Hope College, Michigan	P. DeYoung & G. Peaslee	PHY-0132405
Indiana University South Bend, Indiana	J. Hinnefeld	PHY-0132567
Michigan State University, Michigan	M. Thoennessen	PHY-0132434
Millikin University, Illinois	J. Brown <sup>b</sup>	PHY-0132507
Western Michigan University, Michigan	P. Pancella	PHY-0132438
Westmont College, California	W. Rogers	PHY-0132641

<sup>a</sup>Now with Marquette University, Wisconsin.

<sup>b</sup>Now with Wabash College, Indiana.

can be determined by the individual detector hit within a larger array. With these considerations in mind MoNA was designed with 144 detector modules and assembled in an array. Because each MoNA bar measures 10 cm by 10 cm by 200 cm, the full array takes up a volume of 2.88 cubic meters. The array can be moved by an overhead crane to center it 8 to 14 meters downstream of the reaction target leading to solid angles covering 0.574 to 0.205 steradian, respectively. By assembling MoNA nine layers in depth, the estimated efficiency of about 20% for one bar is compounded 9 times. Each layer has 16 modules labeled 0 through 15; the nine layers are labeled by letters A through I. For example, the tenth module of the sixth layer from the front is labeled F9. The array is assembled on a stand that is adjusted so that the beam axis is aligned to center of the ninth bar from the bottom (bar A8). Figure 1.4 shows the final design configuration for the 144 modules into one array.

Table 2.2: Dominant neutron reactions for hydrogen and carbon in plastic scintillators at 90 MeV [32]. The  $Q$ -value for the reaction is also listed for specific cases. The total cross section for 90 MeV neutrons with carbon is reported to be 500 mb [33] with about half from elastic scattering.

Reaction	$\sigma$ at 90 MeV (mb)	$Q$ -value (MeV)
${}^1\text{H}(n,n')\text{p}$	80	0.0
${}^{12}\text{C}(n,n'){}^{12}\text{C}'$	250	0.0
${}^{12}\text{C}(n,2n){}^{11}\text{C}$	22	18.72
${}^{12}\text{C}(n,n'){}^{12}\text{C} + \gamma$	14	4.43
${}^{12}\text{C}(n,p)\text{B} + \text{Xn}$	95	12.59
${}^{12}\text{C}(n,d)\text{B} + \text{Xn}$	24	15.96
${}^{12}\text{C}(n,n')3\alpha$	10	7.26
${}^{12}\text{C}(n,\alpha){}^9\text{Be}$	3	5.71
${}^{12}\text{C}(n,\text{X})2\alpha$	28	n/a
${}^{12}\text{C}(n,\text{X})\text{Li}$	40	n/a

### 2.1.1 Detection Method

As is the case for all plastic neutron detectors, the dominant interaction for detection is elastic scattering of the neutrons off the protons in hydrogen atoms. Since protons have a mass so close to the mass of the neutron, they are especially effective at absorbing energy when they scatter neutrons. For this reason, it is beneficial to use a plastic with a high hydrogen density. Bircon BC408 [11] (used for the MoNA bars) has a hydrogen to carbon mass ratio of 1.104 and a total density of 1.032 g/cm<sup>3</sup>. In addition, there is a significant contribution from inelastic reactions with carbon atoms producing a variety of possible charged particles or  $\gamma$  rays. Table 2.2 lists the major contributing reactions of an organic (hydrogen and carbon) plastic scintillator including their energy thresholds. Reactions emitting alpha particles have minimum required energies ( $Q$ -value) of at least 5.7 MeV and account for a noticeable increase in total cross section with plastic for neutron energies near 30 MeV. Since alpha particles do not induce as much scintillation light, due to their mass, reactions that produce alpha particles do not add significantly to the detection efficiency unless the detector threshold is relatively low, less than 3 MeV electron equivalent (MeVee).

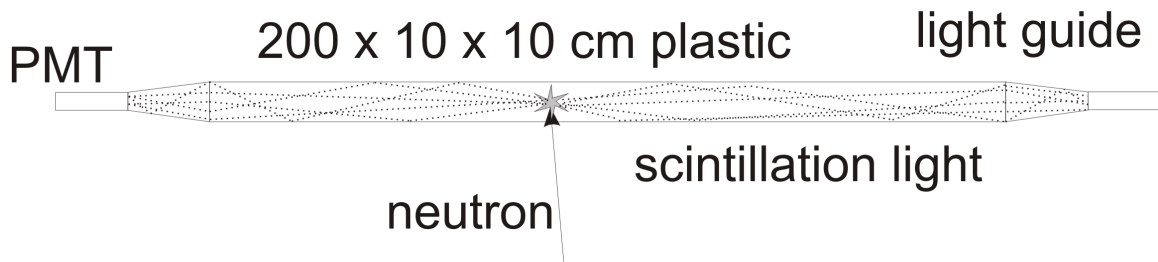


Figure 2.1: Diagram of one MoNA module and illustrates production of scintillation light (dotted lines) by charged particles released from neutron reactions (see Table 2.2). The light is captured by the two PMTs coupled to the bar with light guides.

### 2.1.2 Light Propagation

When a charged particle passes through the lattice of a plastic scintillator it excites the large organic molecules that subsequently de-excite via release of a photon in the visible range. The number of photons released by this scintillation process is proportional to the energy lost by the charged particle through Coulomb interactions with the lattice and depends on the charge, mass, and speed of the particle. BC408 is organic scintillating plastic that has an index of refraction equal to 1.58 and an attenuation length of about 2–3 meters for the scintillation light (as determined by MoNA student experiments and Reference [34]) with a maximum intensity at a wavelength of 425 nm. This attenuation length becomes important for light response calibration (see Section 2.2.4).

It is important to note that charged particles within the scintillating plastic are necessary to produce any light and register an event. Even  $\gamma$  rays produced in these interactions are only indirectly detected through Compton scattering with an electron. The cross section for photo peak absorption is related to the proton number,  $Z$ , of the material to the fifth power and therefore carbon ( $Z = 6$ ) has an extremely low probability to absorb the entire  $\gamma$ -ray energy compared with other elements.

Figure 2.1 is a diagram of a MoNA module, illustrating how a neutron reacts within the scintillating plastic and releases light that travels to the ends of the bars where a light guide passes it into a photo multiplying tube (PMT).

## 2.2 Electronics

Figure 2.2 shows the basic data acquisition (DAQ) configuration for MoNA. The MoNA setup utilizes a variety of digital electronic modules to process and record the light response from the plastic, including photo multiplying tubes (PMTs), constant fraction discriminators (CFDs), and time and charge digital convertors, (TDCs and QDCs). The digital electronic modules are all (IEEE 1014 standard) VME compatible modules and are manufactured by the same company, CAEN [35]. They are installed in three VME crates and are connected to a DAQ computer via fiber optic cables to control and read out all the VME modules needed for MoNA. Section 3.5 details the sequence of functions for the Level 1 and Level 2 logic.

### 2.2.1 Light To Signal Processing

A total of 288 Photonis XP2262B [36] 12-stage photo multiplying tubes (PMT) are coupled and bolted to the support flange. The PMT window is lime glass with an index of refraction equal to 1.54 and is coupled to the acrylic BC802 light guide by optical grease. The PMTs were selected to have a spectral response range that peaks at 420 nm and has a full range of 290–650 nm to closely match the scintillation light from the BC408 plastic, that has a maximum intensity near 425 nm. To counter the effect stray variable magnetic fields have on the electrons in the multiplying tube, a mu-metal shield [37] is also fixed to the flange surrounding the tube.

Each PMT is powered by a separate high voltage (HV) line that is set to yield a consistent light response to cosmic-ray muons. This gain matching process is discussed in detail in section 2.3. The HV power is supplied by two CAEN SY1527 supply controllers. They are modular, expandable, and can be remotely controlled. Eleven CAEN A1833BN 28-channel voltage banks are installed into the SY1527 controller that sets and monitors the negative voltages for the 288 PMTs. The operational voltage range for the XP2262B model is 1500–2400 Volts.

## MoNA DAQ Overview

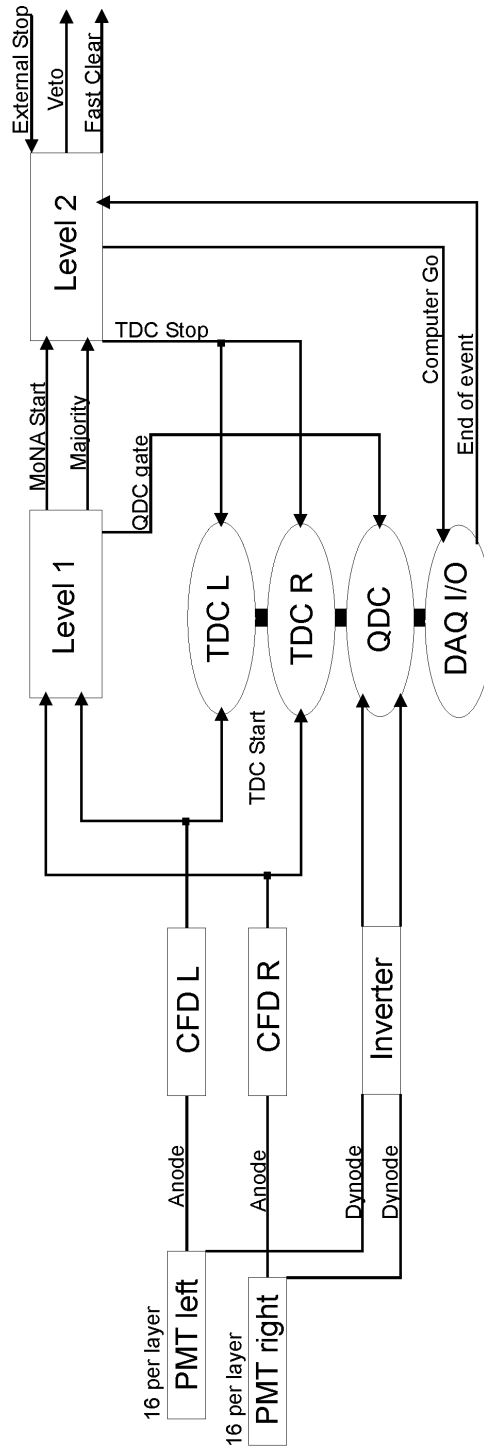


Figure 2.2: The basic MoNA DAQ system. The MoNA PMT anode signals are recorded by the TDCs while the dynode signals are recorded by QDCs. The Level 2 logic (Section 3.5.4) determines if the event is accepted (“computer go”) or rejected (“fast clear”).

There are two analog output signals for each PMT from the dynode and the anode. The PMT has a 12-stage dynode cascade following the photoelectron producing photocathode and the anode signal has a gain of about  $10^7$  with a transit time of 30 ns. Each anode signal is transmitted to a CFD with a 16 foot (25 ns) coaxial cable. The positive dynode signal is taken from the next to last step in the multiplicative chain and is connected to a passive inverter with a 60 foot (90 ns) coaxial 50  $\Omega$  BNC cable and routed into a QDC.

### 2.2.2 Digital Signal Conversion

The standard MoNA setup uses 18 constant fraction discriminators (CFDs) to convert the analog anode signal from each PMT to a digital pulse. The CAEN V812 CFDs have 16 negative polarity 50  $\Omega$  LEMO inputs. The internal timing delay chips are set to 3 ns which is about 80% the typical rise time for the raw anode signal from the PMTs. The outputs are a fan-out of two ECL 110  $\Omega$  impedance 17 pin ribbon cables, whose logic pulse width is controlled from 15 to 250 ns. One side of one MoNA layer is connected to each 16 channel CFD and then routed to half of a 32 channel TDC through the ECL inputs. The other ECL ribbon output is connected to the XLM72 logic module for Level 1 trigger logic control (see section 3.5.3). Each CFD channel has its own rejection threshold set in 1 mV steps from 0 to -255 mV. The standard operating CFD threshold is set to -10 mV.

Each CFD also has an “OR” output LEMO port that is activated for any valid CFD channel. This output is used as a diagnostic counter. When an additional CFD is used with auxiliary detectors, this “OR” output is used as an auxiliary trigger signal (see Section 3.5.6).



### 2.2.3 Timing Signal Processing

The time-to-digital converters (TDCs) are CAEN model V775 with 32 ECL input channels each. For consistent and symmetric cabling of the CFDs, each side of MoNA uses 5 TDCs for 288 total channels. The full scale of each TDC can be set from 140 to 1200 ns. For MoNA’s standard configuration the range is set to 350 ns representing about 0.085 ns for each bin in the 12 bit digitized spectrum. These TDCs can be run in common-start or common-stop mode. The standard configuration runs in common-stop mode where the neutron interaction within the MoNA bar acts as the individual “start” for the corresponding TDC channel. This mode is used since the random background rate does not overload our detectors compared to coincident events with a correlated external stop signal. It also allows for the use of less delay cables for the 288 TDC channels. In common-stop mode just one delay is used for the “stop” trigger from the thin target scintillator (see Section 3.3.1).

#### Fast clear capabilities

One desirable feature of the CAEN TDCs is their “fast clear” capabilities. This feature allows the user to send a logic signal to clear all digitized channels and buffers and prepare for the next start signal. These modules take only 600 ns to complete the full fast clear cycle and to be ready for the next event. If the trigger logic (discussed in Section 3.5.4) rejects the current event, the TDC can be fast cleared before the module is finished digitizing and even before a common stop signal has arrived. This saves many microseconds and dramatically increases the live time ratio of the system compared to not using the fast clear option. Without this fast clear capability the DAQ system would have to wait for the module to digitize and then issue a standard sequence of “end-of-event” and “clear” signals before the module clears its buffers for the next possible event. The MoNA trigger logic holds the “fast clear” signal level for 800 ns to ensure all TDCs and QDCs modules are cleared before releasing.

## 2.2.4 Light Amplitude Processing

MoNA uses 9 CAEN V792 charge-to-digital converters (QDCs) with 32 ECL input channels each for all 288 PMT dynode signals. In the standard MoNA configuration all 32 dynode signals of a 16-module layer are connected to one QDC. Channels 0–15 for the left side PMT dynodes and channels 16–31 for the right. The QDCs use negative current integrating ribbon cable inputs from the passive dynode inverter boxes. The module accepts a logic integrating gate that is set in compliance with the module’s maximum integrated charge of 400 pC. As with the CAEN TDCs, the QDCs also have “fast clear” capabilities.

The scintillation light from a charged particle reaction in a MoNA bar is attenuated as it passes to the ends of the bar to the light guides. The rate of attenuation for the light to the left and right PMTs are exponentials given by

$$l_l = l_o(e^{-(\frac{L}{2}-x_o)/\lambda}) \quad (2.1)$$

$$l_r = l_o(e^{-(\frac{L}{2}+x_o)/\lambda}) \quad (2.2)$$

with  $x_o$  corresponding to the  $x$  position measured within the MoNA bar (between negative 100 and positive 100 cm), and  $\lambda$  is the attenuation length (about 3 meters for BC408).

Because of this attenuation the final signal recorded by the QDC is less than the actual light produced as a function of the distance away from the end. To recover an even distribution for the light deposited within the bar independent of the position, the geometric mean is calculated

$$Q = \sqrt{l_l l_r} \quad (2.3)$$

Figure 2.3 illustrates the effectiveness of this equation, where the left and right individual QDC spectra are displayed versus the horizontal position of the reaction in

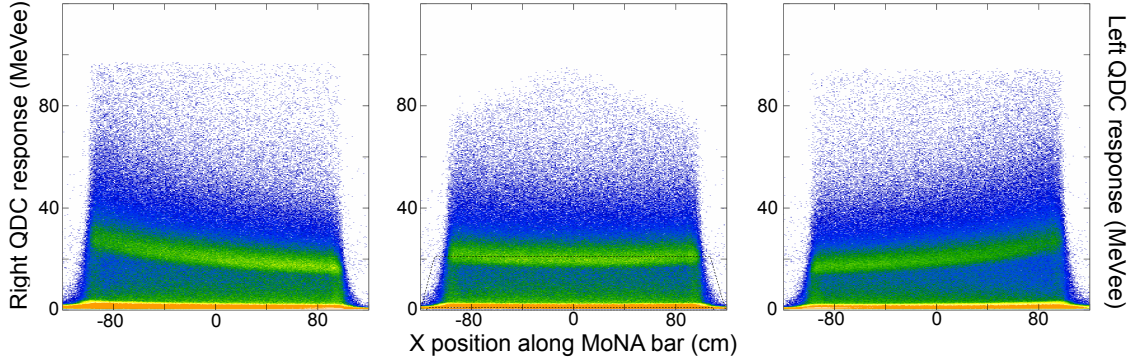


Figure 2.3: The center frame shows the geometric mean of the left and right QDC responses (in the neighboring frames) by Equation 2.3. The background due to low energy  $\gamma$  rays dominate the lower bins of the spectra, while the cosmic-ray muons are calibrated to 20.5 MeVee.

the bar. The center frame shows that the  $Q$  parameter is flat for the whole length of the bar. There is a second-order effect to the attenuated light not recovered through this treatment from the reflected light that travels a full bar length extra. Due to the geometric shape of the MoNA bars and the large attenuation length,  $\lambda$ , the effects from the reflected light for MoNA are not more than 1%, as seen by the position independence of the  $Q$  parameter in Figure 2.3. Furthermore, effects from the reflected light for less elongated scintillation volumes are generally less than 5% and mostly effect interactions at the ends of the bars for energies just above threshold [38].

## 2.2.5 Level 1 Logic Modules

The basic logic processes for each layer of 16 modules utilize JTEC model XLM72 universal logic modules [39]. These are versatile and programmable modules that interface with VME systems and use Xilinx XCS40XL Field Programmable Gate Arrays (FPGA) that run on a 80 MHz clock cycle for logic operations and a Texas Instruments digital signal processor TMS320C6711 running up to 900 Mflops for the numerical operations. The external interface has 72 ECL ports that are hardware configured as either inputs or outputs. The interface with the VME bus is made through 32-bit and 16-bit data transfer rates up to 40 Mbytes per second. The XLM72

also features two banks of asynchronous static random access memory (ASRAM) of 2 Mbytes each and enough flash memory to store up to four FPGA configuration files.

Each XLM72 is programmed to serve as a Level 1 logic unit for each of the nine layers of MoNA bars. Here each CFD outputs for all the PMT signals in that layer are cabled to the ECL input ports in the front of the XLM72. The Level 1 logic counts the number of coincident left–right signals accumulated and forwards it to the next level in the trigger logic. These processes are described in more detail in Sections 3.5.3 and 3.5.4. The raw CFD signal count is also read by the VME bus by a tcl/tk program to display the live rate of all the input channels (from 288 CFD channels) for diagnostic purposes.

## 2.2.6 Level 2 Logic Module

The Level 2 logic is contained in one JTEC model Virtex XLM module. The exterior design and ECL ports are the same as the XLM72 model. The Virtex XLM has increased memory and FPGA logic capabilities by using the high-performance high-capacity Xilinx Virtex model FPGA chips.

All trigger discrimination and Level 2 logic processing are done in the JTEC Virtex XLM, as described in Sections 3.5.4 and 3.5.7. A diagram of the internal routing architecture in the Virtex FPGA unit is shown in Figure 2.4.

## 2.3 Calibration

The detailed process of calibrating MoNA for an experiment is explicitly presented in Appendix C. The light response and position calibration for each MoNA module is performed with cosmic-ray muons. cosmic-ray muons are produced high in the atmosphere from very fast charged particles permeating deep space. Due to the thickness of the Earth’s atmosphere, the muon flux ( $I_\mu$ ) relative to the the zenith at any point on the surface is a function of the cosine of the zenith angle ( $\theta_z$ ) squared. Figure 2.5

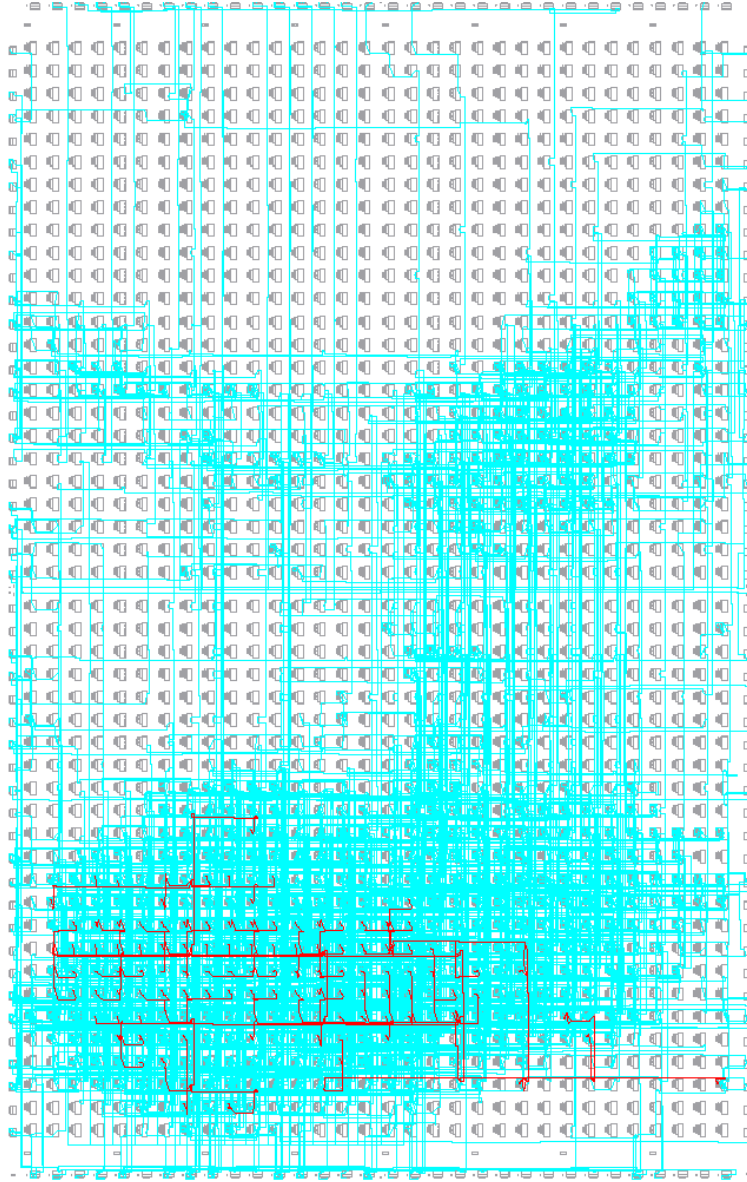


Figure 2.4: The internal routing map between logic gates for the Virtex FPGA is displayed for a sample Level 2 logic code. One input, and the pathways that signal takes, is highlighted in red.

shows actual muon flux data taken from MoNA over the course of a few weeks. The intensities of each  $\delta\theta$  in the N-S and E-W directions are adjusted for the angular coverage to account for the rectangular shape of the array.

The muons that reach the surface are traveling at 29.8 cm/ns (nearly the speed of light). The muons will lose energy through a material based on its density and thickness. For 10 cm BC408 this energy loss is an average of 20.5 MeV and they take

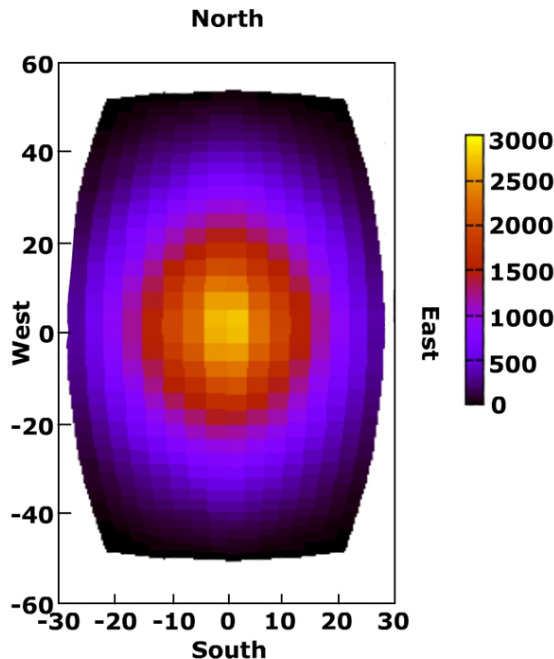


Figure 2.5: Cosmic-ray muon flux through MoNA in degrees from the zenith. The plot was completed by MoNA undergraduate students at Westmont College [40].

0.345 ns to traverse each detector bar. Since the flux per volume is constant, the full width of every bar will be illuminated. Figure 2.6 illustrates a couple of possible muon paths through MoNA. The beam axis is marked in front of bar A8 by a blue arrow. This procedure has been used for other plastic neutron detectors [41].

### 2.3.1 Gain Matching the PMTs

Since the timing and rise time of the PMTs can change depending on the voltage applied, to ensure comparable values for each detector bar, the voltages must be adjusted to gain match the PMTs to a standard light response.

The voltages for the PMT channels are chosen to place the peak associated with cosmic-ray muons at the same relative position for all the raw QDC spectra. This technique will ensure consistent dynode signal intensity because the QDC integration gates and pedestal currents are the same for all QDC channels. By recording a day-long run of background data, a strong cosmic-ray muon peak corresponding to

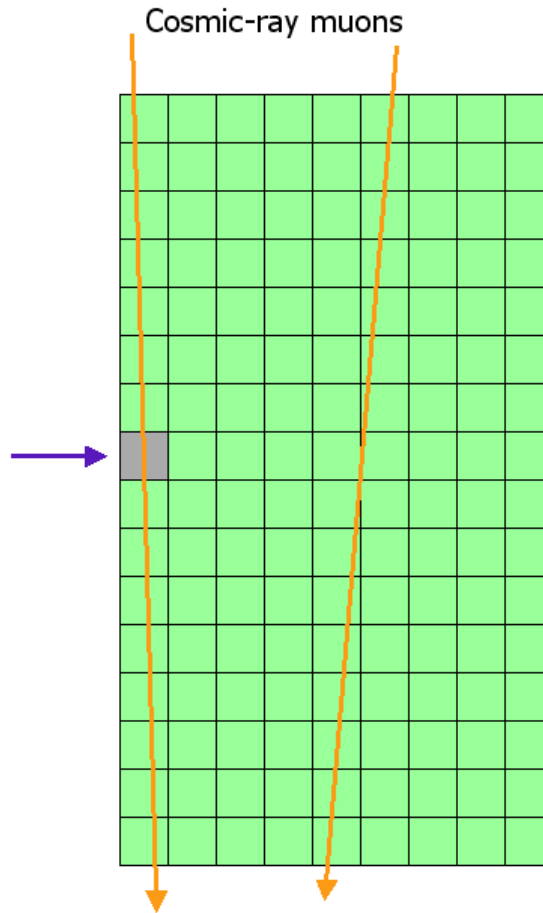


Figure 2.6: Side view of MoNA showing cosmic-ray muons that travel through MoNA and are used to calibrate many properties of MoNA. The time offsets for the whole array relative bar A8 (highlighted), are set from muons that go straight down one layer or cross to the neighboring layer as shown.

20.5 MeVee appears in the QDC spectra, as seen in Figure 2.7. The voltages of all channels are adjusted until the difference between the pedestal peak (null value) and the muon peak is about 800 bins out of a 12 bit (4096 bins) raw QDC spectrum. This not only ensures the PMT signals are matched, but also sets the QDC full range to about 100 MeVee. This procedure provides an approximate gain matching to set the thresholds consistently and to ensure similar PMT response times, but it does not substitute for proper calibration of the energy deposited within the bar (see Section 2.3.2).

Adjustments to the voltages are done by fitting the muon peak portion for the

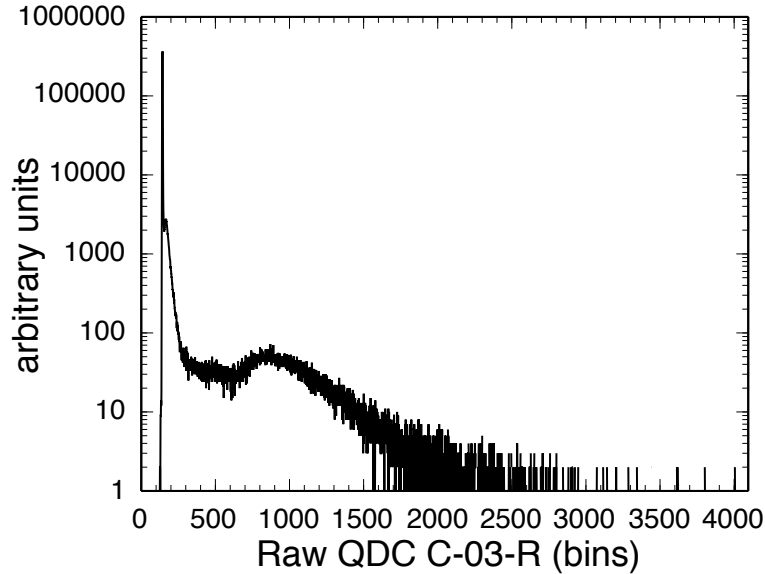


Figure 2.7: Raw QDC spectrum for PMT C-03-R (the right PMT dynode signal of the forth bar in the third layer). The dominance of the pedestal peak in the lowest channels is clearly seen, followed closely by the self-triggered CFD threshold that appears only as a shoulder a couple decades less intense right next to it. The cosmic ray muon peak is set 800 bins above the pedestal peak to gain match the PMT voltages.

spectra with a Gaussian and an exponential. Figure 2.8 is a close up view of the spectrum in Figure 2.7 for PMT C-03-R (right PMT of the fourth bar in the third layer) fitted by the exponential–Gaussian combination on a linear scale. The difference between the pedestal and the muon peak is calculated and compared to 800. The voltage is adjusted accordingly using an algorithm that takes into account the 12 multiplicative steps of the MoNA PMTs. Another day-long MoNA run is recorded and another iteration is performed, and so on, until a the pedestal–muon differences are consistent with 800 bins such that another iteration would not improve the result. This usually occurs after two or three iterations.

### **Pedestal peak**

Since all 32 channels of each QDC share a common integration gate, all events with less than 16 coincident left–right PMT hits will have some QDC channels with no signal. Most events in MoNA are 1-fold events, or a single left–right coincidence for



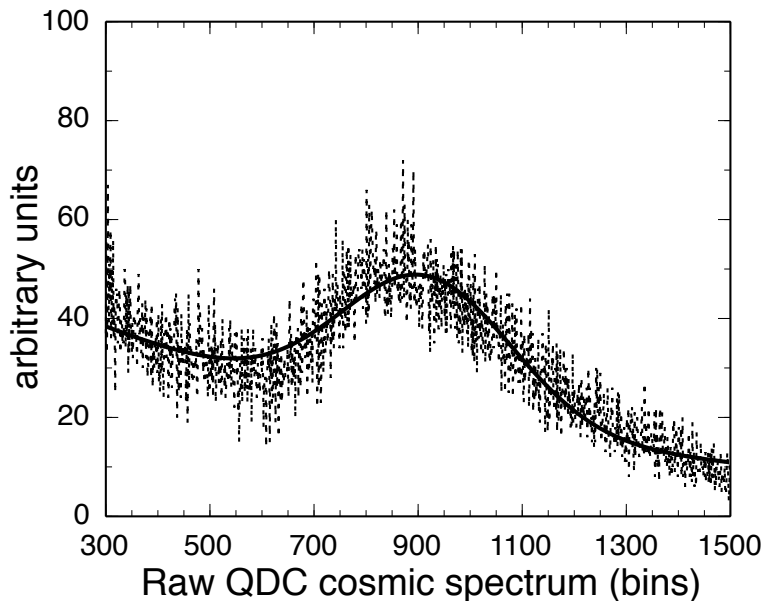


Figure 2.8: The region near the muon peak is fitted by the sum of an exponential decay and a Gaussian (solid line). The center of the Gaussian fit is used for both gain matching the PMTs and latter, to calibrate the QDCs.

one bar. The other 30 QDC channels will have a null result, and indeed the count rate of the pedestal peak for any given QDC channel is usually two or three orders of magnitude stronger than the rest of the raw spectrum (see Figure 2.7). The QDC collects charge from the internal pedestal current for the duration of the integration gate and compiles a non-zero value that depends on the pedestal current and the width of the integration gate. The pedestal current and integration gate is adjusted to place the pedestal peak near bin 100 in the 12-bit (4096 bins) raw QDC spectra (see Figure 2.9).

### 2.3.2 QDC Calibration

Once the PMTs are properly gain matched the QDCs are calibrated using the same light-response curve of cosmic-ray muons used to gain match the PMTs. The raw QDC spectra are fitted with a Gaussian plus an exponential background to the muon peak as shown in Figure 2.8. The pedestal peak is used as the zero-point for each QDC calibration. The average energy loss for cosmic-ray muons per centimeter of BC408

plastic is 2.0 MeV for MoNA plastic [42]. As determined by GEANT simulations [43] using the angular flux of cosmic-ray muons and the geometry of MoNA, the Gaussian-fitted muon peak is set to 20.5 MeVee. This linear calibration has been checked with  $\gamma$ -ray sources (energies near 1 MeV) for a few bars on the outer layers and found to be correct within  $\pm 0.075$  MeVee.

### 2.3.3 QDC Thresholds

As mentioned in section 2.3.1 the count rate of the pedestal peak is usually over a hundred times stronger than the count rate into the rest of the bins in the raw QDC spectrum. Since these counts in the pedestal peak come from null-value events and have no corresponding TDC data, including them in the data stream can unnecessarily slow the readout process. A hardware threshold can be set for each QDC channel such that channels with a digitized value less than the threshold will be ignored during readout.

The threshold bit of the CAEN V792 QDC modules can be set in multiples of 16 bins (i.e. 0, 16, 32, 64, 80, 96, 112, 128, 144, ...). This can cause insufficient pedestal subtraction when the pedestal peak for a given QDC channel is near any of these values. Figure 2.9 shows the QDC response for background events when all 32 PMTs for a whole layer are turned on, the width of the pedestal peak is about five bins. Two possible threshold values are drawn as dotted lines at multiples of 16. If the pedestal peak value is just below one of the possible threshold values, like PMT B-00-L (left PMT for the first bar in the second layer) shown in Figure 2.9. Setting the threshold to the nearest threshold value at bin 128 will still allow nearly half of the pedestal peak to be readout. The relative magnitude between the allowed half of the pedestal peak to the rest of the raw spectrum will still be too great for efficient data recording of these channels.

Another situation is shown in Figure 2.10 for PMT B-02-L, where the pedestal

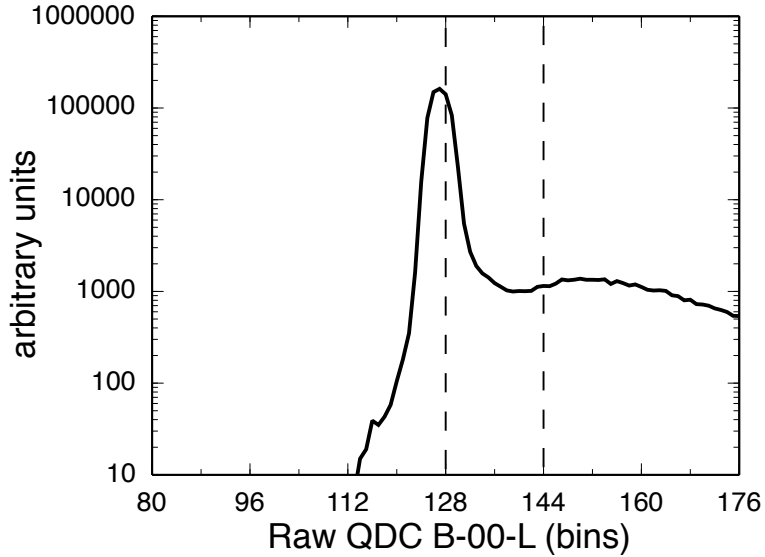


Figure 2.9: The raw QDC pedestal peak for PMT B-00-L is too close to threshold value bin 128 to effectively reduce the null result count rate. Both the simple and improved methods for setting the threshold value sets it to 144 for this QDC channel.

peak is a few bins below a possible threshold value. Here setting the threshold at the next nearest possible value at bin 128 would be ideal to cut most of the pedestal peak intensity and cut a minimum of the overall spectrum, but a consistent automated method for determining the best threshold value to use and a case by case basis is not simple.

### Simple threshold cuts

For the  $^{12}\text{Be}$  experiment the thresholds were set to the second nearest threshold value above the pedestal peak. This cuts a minimum of 17 bins above the pedestal peak from the QDC response (as is the case for PMT B-00-L) and a maximum of 32 bins for channels where the peak is equal to a possible threshold value. Using the same automated process to set the QDC threshold for channel B-02-L will unnecessarily cut into the portion of the non-pedestal spectrum at bin 144. As discussed above, the nominal calibration for the QDC response is 800 bins per 20.5 MeVee (0.025 MeVee per bin). Therefore, this method for setting the QDC thresholds results in minimum energy thresholds of 0.42 to 0.82 MeVee depending on the location of the original

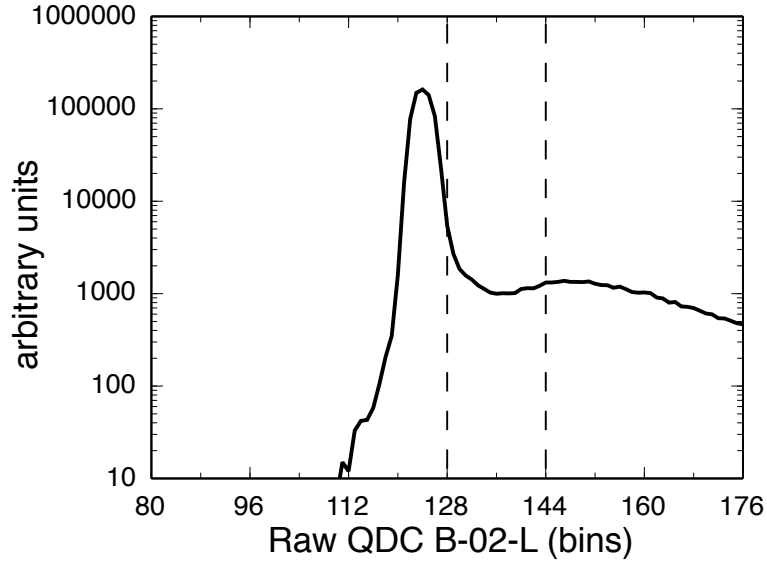


Figure 2.10: The raw QDC pedestal peak for PMT B-02-L is a few bins below a possible threshold value 128. The simple method for setting the threshold value places it at bin 144 for this QDC channel, while the improved method sets it to 128.

pedestal peak in the raw spectra.

The CFD adjustable threshold for the anode signal that triggers the QDC gate was set to -10 mV, which was calibrated at 0.65 MeVee as shown in Figure 2.11. The CFD calibration was performed with a known  $\gamma$ -ray source by recording the value in a calibrated QDC spectrum that the intensity drops by half while adjusting the CFD threshold. Having as low a threshold as reasonably possible is important for increased efficiency of detecting neutron scattering interactions, because events that deposit less than 4 MeVee outnumber high-energy events where the neutron transfers almost all of its kinetic energy to a recoil proton. Using this simple QDC threshold procedure, the QDC threshold may be above the CFD/TDC threshold and many events may be recored with no associated QDC information.

### Improved threshold cuts

Following the commissioning experiments, a new automated method was found for setting the QDC threshold that corresponds to a minimum energy cut of less than 0.5 MeVee for all channels. By first adding three bins to the pedestal peak value

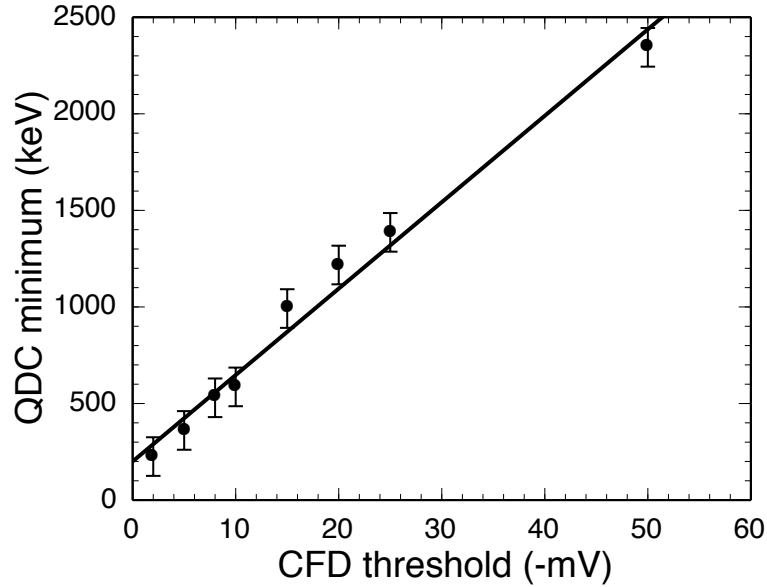


Figure 2.11: The threshold for the CFDs were calibrated by recording the calibrated QDC spectrum edge (one half amplitude) for a range of different CFD thresholds in mV. The linear fit crosses -10 mV at 0.65 MeVee.

and then setting the threshold to the nearest possible value above this bin, the newer technique only cuts a maximum of 19 bins and a minimum of 3 bins above the pedestal peak. This minimum of 3 bins is sufficient to cut most of the pedestal peak and reduce the over abundance of pedestal values by a few orders of magnitude compared to the uncut peak. This new method would apply the QDC threshold at bin 144 for both PMT B-00-L and at bin 128 for B-02-L (since the peak is four bins below 128). By applying the proper calibration the improved threshold cut to B-02-L (Figure 2.10) the minimum energy recorded is 0.1 MeVee compared to 0.51 MeVee with the simple method. This difference is even more pronounced for QDC channels where the pedestal is right at a possible QDC threshold value (0.41 MeVee with the improved method compared to 0.82 MeVee before). The full range of possible QDC thresholds for this improved method corresponds to minimum energy cuts of 0.08-0.475 MeVee. Since these cuts are at or below the CFD threshold of -10 mV (about 0.65 MeVee), in this mode there are nearly the same number of valid TDC and QDC events in the recorded data. This method was not used for the commissioning experiments, but has

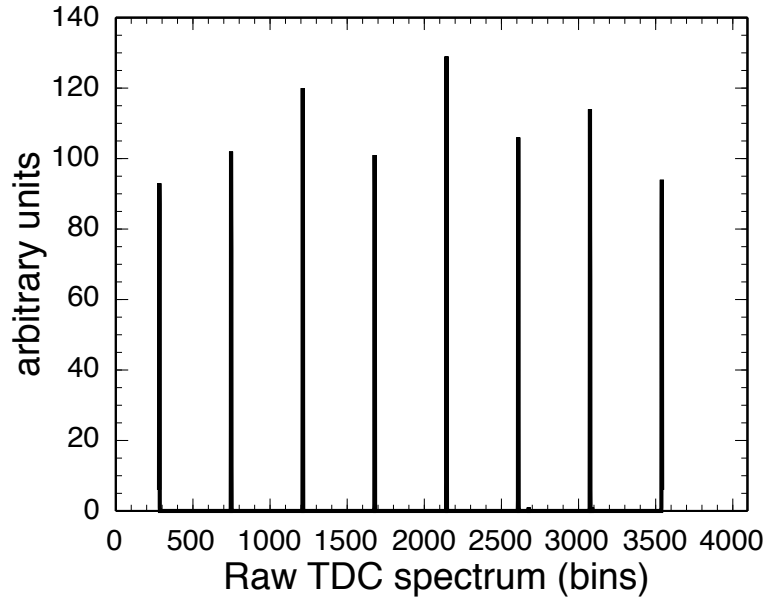


Figure 2.12: The distinctive “picket fence” spectrum from a time calibrator connected to the TDC with a period 40 ns is used to calibrate this TDC channel.

been implemented since.

### 2.3.4 TDC Calibration

The only calibration that does not utilize cosmic ray muons is the TDC calibration. As is standard for timing calibration, a time calibrator module is used in conjunction with a CFD to create logic pulses at set time intervals. The calibrator changes the start–stop interval by a multiple of a selected time interval so that multiple time difference peaks appear in a raw spectrum. The time calibration setting used for the MoNA TDC calibrations was set to a range of 320 ns with 40 ns intervals. The full range of the 12-bit TDC was set to 350 ns. The distinctive “picket fence” spectrum shown in Figure 2.12 is recorded and fitted by a fortran code that finds the peak positions above a set count for each spectrum and fits the location of these bins with a linear function. The slope is then used to convert the raw bins to nanoseconds.

### 2.3.5 Position Calibration

Once the TDC is calibrated, the time difference between left and right TDC channels can be used to determine the interaction position within the bar. Again, using cosmic-ray muons and their uniform flux with respect to the MoNA bar axis, the width of each bar can be calculated in nanoseconds. Figure 2.13 shows the time-difference spectrum used to calibrate the horizontal position of MoNA bar B11. A cut is made in the respective QDC channels above 8 MeVee to ensure there is no  $\gamma$ -ray background and the gated time difference spectrum is calibrated to 200 cm and the center is offset to zero. While the distribution of muons through the bar is uniform, the recorded distribution is not. Some muons that strike the corners of a MoNA module may not pass through enough plastic to deposit enough light, such that both left and right CFDs fire. This effect is modeled by a Monte Carlo simulation and determines the width of the time-difference distribution at 1/3 the maximum plateau corresponds to the actual 200 cm width of the MoNA bar. The nominal calibrated conversion from time-difference in nanoseconds to centimeters for the MoNA bars is approximately 8 cm/ns.

### 2.3.6 Time Offsets

Even after the TDC response is calibrated to nanoseconds, the time relative to a common stop signal cannot be determined without knowing the individual time offsets for each channel. In yet another way of using the cosmic-ray muon flux through MoNA, the small differences in the amplification time for the individual PMTs and the differences in the cable lengths for the TDC common stop signal (that is daisy-chained to all MoNA TDCs) can be measured by the known muon speed through each MoNA layer. Since cosmic-ray muons travel nearly the speed of light (actually 29.80 cm/ns) the time signature of vertically-traveling muons in successive MoNA bars can be calculated from the nominal distance between them (10.27 cm).

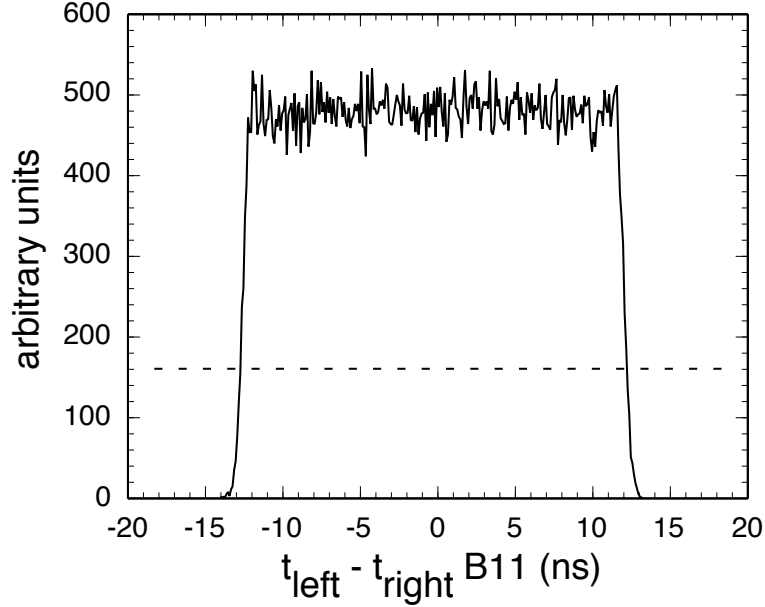


Figure 2.13: The calibrated times for each end are subtracted in this time-difference spectrum for bar B11. The width at one third the average amplitude of the center region is calibrated to the full 200 cm of MoNA plastic (illustrated by the dashed line).

A coincidence gate is applied to the transverse position for the top and bottom bars in one layer to make certain the muons travel straight down through the layer. In addition, a gate that only accepts events that strike all 16 bars in that layer have to be fulfilled. The mean time ( $t_{\text{bar}}$ ) of the two calibrated TDC parameters for the left and right end of each bar is calculated and is independent of the position of the interaction.

$$t_{\text{bar}} = \text{ToF}_n = (t_{\text{left}} + t_{\text{right}})/2 \quad (2.4)$$

This mean time is also the time-of-flight ( $\text{ToF}_n$ ) parameter for a neutron hit in MoNA when the TDC common stop signal comes from a thin scintillator at the target position during an experiment.

The mean time for the top bar (number 15) is subtracted from each successive



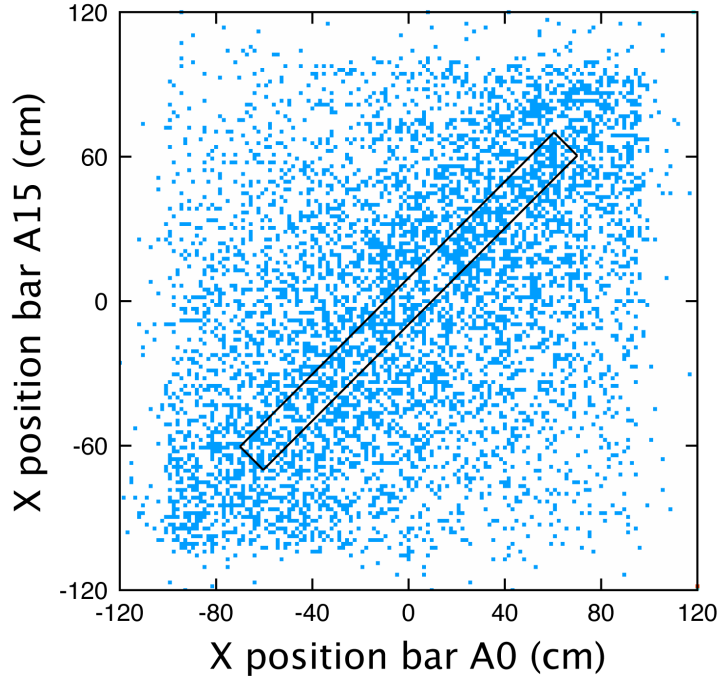


Figure 2.14: Muon tracks that travel straight down through bar A0 and A15 depicted in Figure 2.6 will pass this two dimensional gate, ensuring a minimum amount of spread in the time difference plots between neighboring MoNA modules used to calibrate their relative time offsets.

bar ( $i$  runs from 0 to 14) creating 15 bar time-difference spectra.

$$\Delta t_i = t_{15} - t_i \quad (2.5)$$

Since the time offsets for each bar are determined relative to bar A8,  $t_8$  is used as the reference instead of  $t_{15}$  for all of layer A, as seen in the example for A7-A8 ToF parameters in Figure 2.15.

These time-difference spectra should correspond to the travel time between the two bars,  $\delta t = 0.345$  ns per bar. The offsets for each calibrated mean time is set to ensure the difference spectra meet this condition. Figure 2.15 shows the time difference between bars A7 and A8. The distribution shown will be fitted and offset to the proper  $-0.345$  ns by the fitting program. The offsets for the next layers are determined by first applying gates that include the diagonal track from the top of one row to the

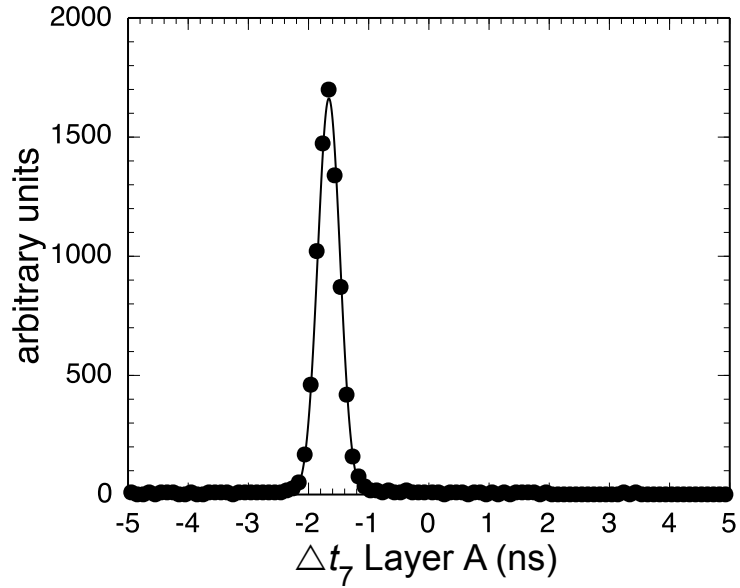


Figure 2.15: The time difference ( $\Delta t$ ) between A7 and A8 triggered by a fast muon in a downward track calculated per Equation 2.5.

bottom of the next (for example A15 to B0). A slightly different  $\delta t$  (0.346 ns) is used to account for the diagonal distance. Then the offsets within the next layer can be calculated as before from this one corrected mean time. The whole MoNA array of 144 bars are calibrated relative to bar A8, which is centered on the beam axis. Bar A8's offset is set during each experiment using the  $\gamma$  rays produced by stopping the beam in a thick target and the measured distance from the target to the center of bar A8.

# Chapter 3

## MoNA/Sweeper Experimental Setup

Combining MoNA and the Sweeper magnet along with the focal plane charged-particle detectors to a single detector system completes an arrangement suitable for measuring the neutron-unbound states of exotic nuclei near the neutron drip line with neutron kinetic energies above 30 MeV/u. The setup allows the neutrons from an unbound state created at the reaction target to be detected at zero degrees by MoNA, while the Sweeper magnet bends the charged particles into the focal plane detector box.

### 3.1 Layout

Figure 3.1 shows the Coupled Cyclotron Facility (CCF) [31] and the A1900 fragment separator [45] leading to the experimental vaults and the current position of MoNA. The CCF accelerates the stable primary beam. After impinging on a primary target, the fragmented beam then travels through the A1900 to select the rare isotope of interest. This secondary beam is then delivered to the experimental vault. MoNA is currently placed behind the Sweeper magnet located inside the N4 vault of the NSCL

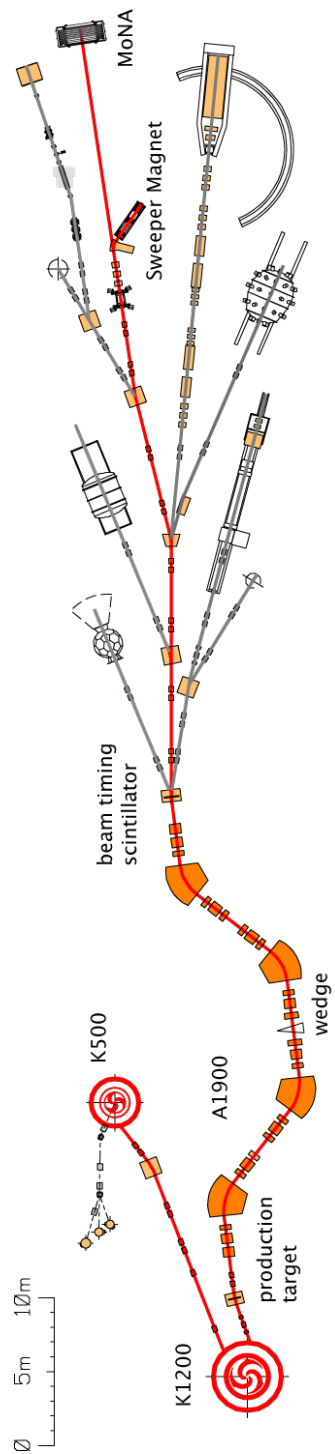


Figure 3.1: The Coupled Cyclotron Facility (CCF) provides the beam for the MoNA/Sweeper setup. The A1900 fragment separator selects the nucleus of interest from the resulting cocktail of fragments created at the production target behind the K1200 cyclotron at velocities of nearly half light speed. Image from Reference [44].

at MSU. The distance between the target and MoNA must be optimized for each experiment to balance velocity resolution and angular acceptance.

## 3.2 MSU/FSU Sweeper Magnet

The Sweeper magnet was built by the National High Magnetic Field Laboratory at Florida State University [16, 17]. Its superconducting coils are made of niobium–titanium for a maximum magnetic field of 4 Tm, requiring a large 10 foot iron return yoke. The magnetic field is controlled to deflect the charged particles into a focal plane detector box at  $43^\circ$  in the horizontal dispersive plane ( $x$ ). In order to allow neutrons to pass through, the Sweeper magnet has a large 14 cm gap sealed with a thin (0.25 inch) steel plate at zero degrees. This thin steel “neutron window” scatters 4% of the high-energy neutrons from the target and seals the vacuum of the beam line and focal plane. Two copper resistive trim coils are attached to the yoke to reduce the Sweeper magnet’s significant fringe field which effect the magnetically sensitive detectors nearby.

## 3.3 Charged Particle Detectors

Figures 3.2 and 3.3 show schematic diagrams of the charged particle detectors in the MoNA/Sweeper setup. The target chamber contains a thin target scintillator used for the both the fragment and neutron timing. The Sweeper magnet detector box contains two position sensitive detectors, two energy-loss detectors (one gas one plastic), a thin timing detector and a total-energy detector. Details of the Sweeper focal plane electronics and DAQ modules can be found in Nathan Frank’s Ph.D. Dissertation [47].

The Sweeper focal plane detectors are designed to accurately identify the charge and mass of the reaction residues and their position and angle relative to the Sweeper

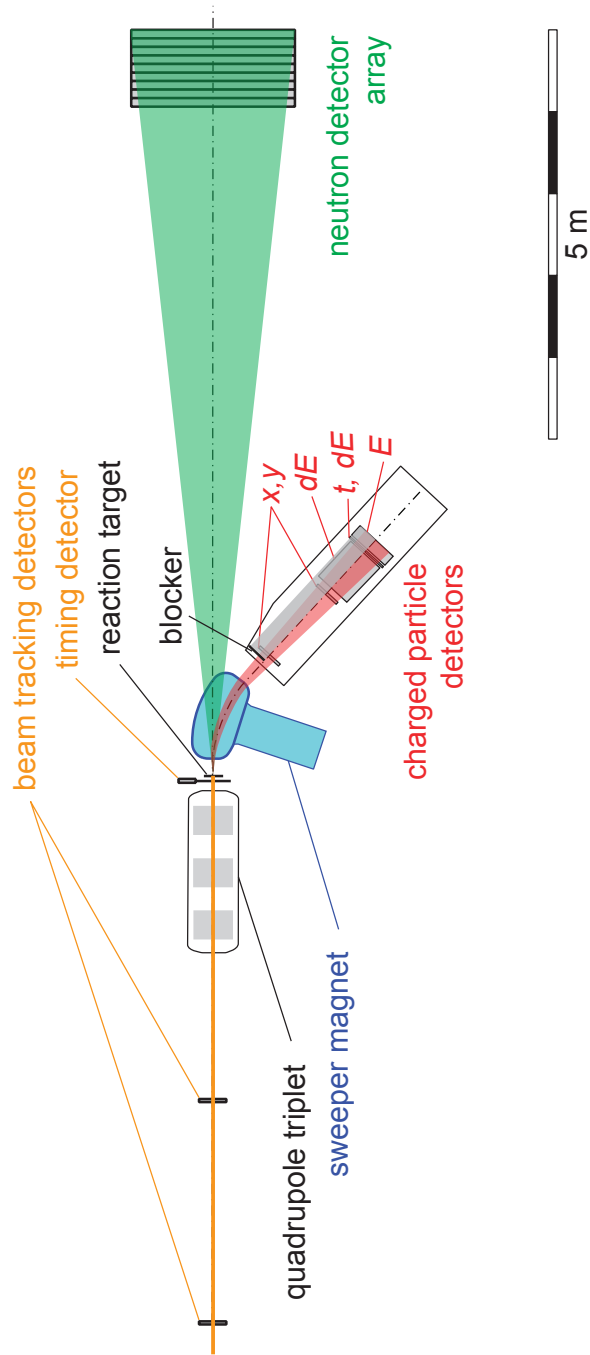


Figure 3.2: The MoNA/Sweeper setup includes charged particle detectors in the Sweeper focal plane detector box. The target timing detector is used for the time-of-flight measurements for both the neutrons to MoNA and the charged particles to the focal plane thin scintillator ( $dE$ ). An optional blocker is installed to limit the count rate to the rate-sensitive CRDC detectors ( $x, y$ ). Original image from Reference [46].

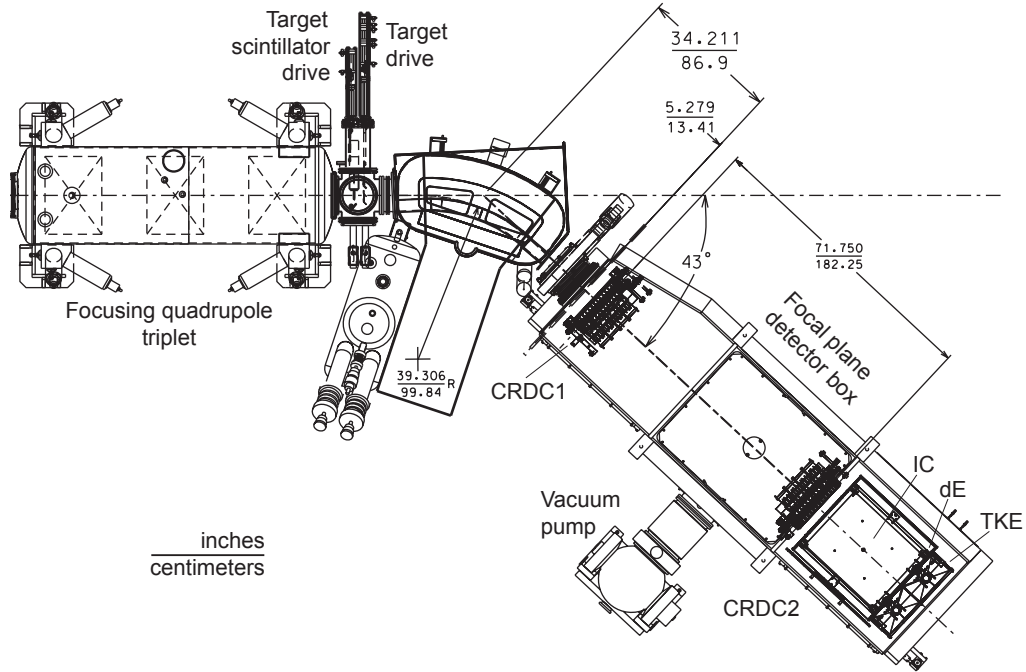


Figure 3.3: Top view of the Sweeper detector box. The Sweeper’s deflection angle of  $43^\circ$  and the target chamber, with its two drives, in front of the magnet are shown. The CRDCs slide on rails and can be a maximum of 182 cm apart. Image from Reference [44].

magnet. The angle and position of each particle is used to reconstruct the energy and angle of the nucleus at the reaction target. Each detector is mounted on a rail parallel to the Sweeper magnet exit axis,  $43^\circ$  from the beam line, so they also can be positioned at distances that balance acceptance with velocity resolution for the specific experiment.

### 3.3.1 Target Chamber

As shown in Figure 3.2 the target position for the standard MoNA/Sweeper configuration is downstream of the final focusing quadrupole triplet magnet. Installed into the beam line here is a large-bore six-sided connection cross. There are two remotely operated drive mechanisms attached to the cross, each with multiple positions.

The first drive assembly has two positions to put a thin timing scintillator in or out

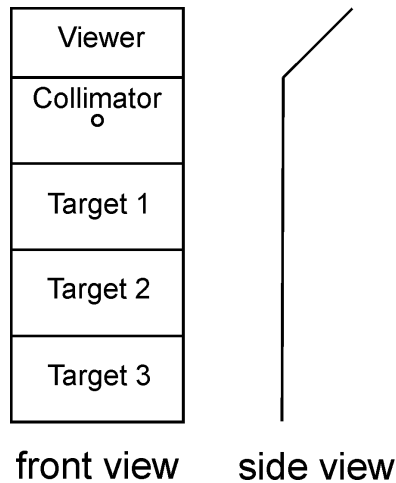


Figure 3.4: The target chamber drive ladder contains 3 target positions along with a 7 mm steel collimator and a fluorescent aluminum viewer plate.

of the beam. This target scintillator is used for ToF measurements and is 0.254 mm thick BC404 organic scintillating plastic. It is connected to a PMT whose output is processed by a CFD within the Sweeper electronics rack before being used as the “common stop” for all MoNA TDC channels (see Figure 3.6 for a diagram of the timing cables).

The second drive assembly has six positions and drives a target ladder that holds the primary reaction target and three other alternate 1 by 2 inch targets, shown in Figure 3.4. The six drive positions are for the fluorescence viewer plate, four target slots, and a retracted position. The side view of the target ladder in Figure 3.4 shows how the viewer plate is angled so the glow created by the beam impacting the fluorescence can be seen through a window by a camera above the target chamber. Installed in the top alternate target position is usually a thick (7 mm) steel block with a 1 mm bore through the center position. This block is used both as a collimator for the beam and, since it stops a majority of the beam, to create a flash of prompt  $\gamma$  rays to calibrate MoNA’s time offset.



### 3.3.2 CRCDs

There are two Cathode Readout Drift Chambers (CRDC) inside the Sweeper focal plane detector box to record the angle and position of the fragments after being deflected by the Sweeper magnet. They each have 128 cathode pads spaced 2.54 mm apart in the dispersive plane. The vertical position is measured from the drift time to the anode wire of the ionized electrons released by the charged particles through the gas. The anode wire uses a nominal voltage of 750 V. Both CRDCs share the same gas handling system and use 20% iso-butane and 80% CF<sub>4</sub> with an operating pressure of 50–150 Torr.

CRDC1 and CRDC2 are calibrated with a mask that is driven up in front of each CRDC. After proper calibration the positions recorded by the CRDCs are accurate to within a millimeter. The angular resolution depends on the separation between the CRDCs within the detector box, and is 0.06° when one meter apart. CRDC1 is fixed inside the front edge of the detector box, and its position information is used when calculating the transformation matrix for fragment energy reconstruction.

### 3.3.3 Ion Chamber

The Sweeper ion chamber (IC) is a gaseous detector with 16 collection plates that get recorded by 16 peak-sensing ADC channels. Their sum is used as an energy loss ( $dE$ ) measurement. The chamber is filled with 100–200 Torr of P10 gas (90% argon and 10% methane). The negative drift voltage is tuned for the charge range of particles being detected and is typically between 600–1200 V. The 16 collection plates are generally held at a positive potential of 100 V to attract the free electrons “pushed” by the negative drift voltage.

### 3.3.4 Thin/Thick Plastic Scintillators

Both thin and thick BC404 organic plastic scintillators [11] have four PMTs mounted close to the corners that are connected to a TDC through a fast CFD with a delay time set to 3 ns. The linear average of the four calibrated timing spectra from the thin scintillator is used for the ToF parameter for the fragments. If less than four PMTs fire for one detector, the correct time can be recovered by calculating the position of interaction from the CRDC data and then taking a weighted average of the remaining TDC parameters.

The 5 mm thin scintillator is used primarily as a timing detector and a second  $dE$  measurement. The thick plastic scintillator is 15 cm thick, which is enough to stop all the fragments and yield a total remaining kinetic energy ( $TKE$ ) signal. These parameters are determined by routing each PMT signal to a peak-sensing ADC and taking a position-corrected average of the four signals for the thin or thick scintillators for the  $dE$  and  $TKE$  measurements, respectively. To gain-match the light response of the raw ADC channels the Sweeper magnet is tuned to direct a small spot of the secondary beam, collimated by a thick steel collimator, to the center of the focal plane. The eight thin/thick voltages are tuned to match their raw spectra. Typical voltages are 1500–2100 V. The beam is then swept across the active region of the detectors to ensure the ADC spectra are not saturated when the fragment nears the corners and to position-correct the average of the four raw signals. An absolute energy calibration is often not necessary to separate or identify the reaction fragments.

## 3.4 Reaction Residue Identification

The detectors mounted in the Sweeper focal plane detector box are designed to aid in the identifying and analyzing the charged particle residue in coincident with a neutron in MoNA. The residual fragment from the neutron-unbound state must be positively

identified to reconstruct the corresponding decay energy. The Sweeper magnet separates these residues from beam contaminants and other reaction products not related to the nucleus of interest.

### 3.4.1 Element Identification

The element number of the charged fragments is identified from the  $dE$  signal recorded by the thin scintillator detector or the IC. Energy loss is proportional to the  $Z$  of a charged particle, and the  $dE$  parameter is calibrated by the known secondary beam (often one or two elements higher than the nucleus of interest). This process is described in more detail in Reference [47].

### 3.4.2 Isotope Identification

Although the  $TKE$  signal in the thick focal plane scintillator is related to the mass of the charged particle residue, sometimes the resolution is not sufficient to accurately separate the isotopes, and a more powerful method must be utilized. Given the design of the beam optics with a focusing quadrupole triplet in front of the target and the dipole Sweeper magnet after, the charged fragments traveling through the Sweeper magnet will be separated by their magnet rigidities. A particles magnetic rigidity ( $B\rho$  measured in Tesla meters) is related to its charge ( $q$ ), mass ( $m$ ), speed ( $v$ ), as described by:

$$B\rho \propto mv/q \tag{3.1}$$

For nuclei with the same magnet rigidity, heavier ones will have a slower velocity and thus, longer ToF. Since the Sweeper focal plane accepts a range of nearly 18% in momentum, other parameters must be used to correctly identify the magnetic rigidity of each particle. After passing through a dispersive beam element like the dipole Sweeper magnet, the rigidity of a particle depends on the dispersive position

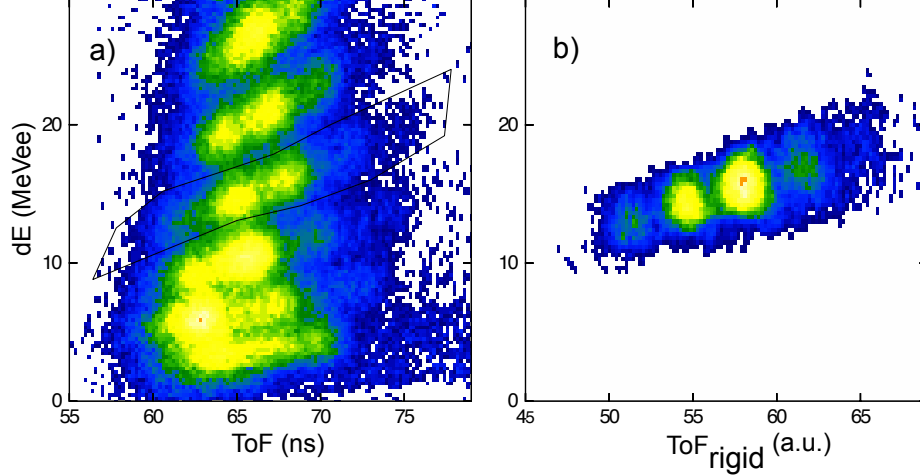


Figure 3.5: Separation of carbon isotopes by their magnetic rigidities using the adjusted  $\text{ToF}_{\text{rigid}}$  parameter. a)  $dE$  versus calibrated  $\text{ToF}$  for many fragments and the gate used to select carbon. b) The gated carbon events after Equation 3.2 is applied with appropriate values, separating the isotopes for identification.

and angle ( $x$  and  $\theta_x$ ). By adjusting the fragment's  $\text{ToF}_f$  parameter, we can further separate the particles by their rigidity. The adjustment is made using two correction factors,  $C_x$  and  $C_\theta$  to the dispersive positions and angles in the focal plane:

$$\text{ToF}_{\text{rigid}} = \text{ToF}_f + (C_x x) + (C_\theta \theta_x) \quad (3.2)$$

$\text{ToF}_{\text{rigid}}$  is a  $\text{ToF}$  parameter of arbitrary units calculated by adding the two  $x$  and  $\theta_x$  correction terms to the original fragment time between the target scintillator and the focal plane thin scintillator,  $\text{ToF}_f$ .

When optimal values are chosen for  $C_x$  and  $C_\theta$ , this first-order adjustment will effectively separate particles with the same magnetic rigidity in time-of-flight as if the Sweeper focal plane momentum acceptance was very small. After gating on a specific element, the adjusted  $\text{ToF}_{\text{rigid}}$  spectra can be used to identify the isotopes. Figures 3.5 a and b are examples of separating various carbon isotopes by their magnetic rigidities. The gate shown in part a is applied to part b after  $C_x$  and  $C_\theta$  are set to optimize the separation.

For most experiments a combination of  $x$  or  $\theta_x$  versus  $\text{ToF}_{\text{rigid}}$  and the  $TKE$  signal

will effectively separate the mass number for a selected element.

## 3.5 Trigger Logic

When MoNA and the Sweeper magnet are used in coincidence mode all the data acquisition (DAQ) modules are routed through one VME I/O (CAEN V262) module connected to the MoNA computer. All the DAQ modules of the two setups are connected by five cables and the MoNA Level 2 logic discriminates between events to readout and those to clear. An accepted event results in reading the DAQ modules and an “end of event” signal produced by the MoNA computer and routed to all modules through the VME bus. A rejected event is “fast cleared” to reset the DAQ modules. An overview of the MoNA DAQ electronics is shown in Section 2.2.

### 3.5.1 MoNA/Sweeper Coupling

The Sweeper DAQ system is interconnected to the MoNA DAQ system by five 120 ns (76 ft) co-axial cables, labeled A, B, C, D, and E in Figure 3.6. These cables take a valid Sweeper event trigger through Cable A, and a “common stop” target timing signal through Cable E. The MoNA trigger logic sends back three signals to the Sweeper DAQ modules.

Cable A is the CFD logic signal from the upper-left PMT channel of the thin scintillator in the back of the Sweeper focal plane. This signal is passed to MoNA’s logic as the “sweeper” signal input. Cable B is the latched “veto” signal that prevents any incoming signals to all MoNA and Sweeper modules while the latch is activated. This latch is opened by the Level 2 logic when a trigger is received and is released by either an “end-of-event” signal or with the end of a “clear” signal. The “veto” latch remains on while the MoNA computer is busy reading out the DAQ modules. Cable C is the “fast clear” signal from the MoNA Level 2 logic and is used to clear the Sweeper DAQ system. The “fast clear” is also copied locally to the MoNA DAQ modules

(Section 2.2.3 discusses this feature). This signal is sent instead of the “computer go” for rejected events. The “fast clear” and “computer go” signals are mutually exclusive. Cable D is the master trigger or “computer go” output from the Level 2 logic to the V262 I/O module to start the readout of all the modules connected to the VME bus. It is also used by the Sweeper electronics as a common start for the TDCs, since it is precisely timed from the incoming Cable A signal (thin scintillator upper-left). The Level 2 logic takes 337.4 ns to process the event and issue this master trigger. The total transit time for the thin scintillator’s signal is illustrated in Figure 3.6 and all Sweeper timing signals into the Sweeper TDC are delayed to wait for it.

Cable E carries the CFD output of the target timing scintillator. The thin target scintillator is positioned just in front of the reaction target and is used as the “common stop” for all MoNA TDCs, after appropriate delay is manually added. This time along with the measured distance to each bar in MoNA is used to calculate the velocity and thus the energy of each neutron detected in MoNA. While these five signals are shared by the MoNA and Sweeper systems, those internal to the Sweeper’s digital logic are described in more detail in Reference [47].

### **QDC gating**

The positive dynode signal from each MoNA PMT is delayed by a 95 ns (60 ft) cable and then inverted by a passive inverter chip before going into the QDC modules. Each CAEN V792 QDC processes all 32 channels from one layer in MoNA. The delay is chosen such that by the time the raw dynode signal arrives at the QDC an integration gate has already been opened by the Level 1 logic for every layer with a valid anode signal above the CFD threshold also creating a “mona start” logic pulse.

### **TDC timing**

When an event occurs in a MoNA module, the anode signal from each PMT is processed by a CFD whose logic output signal is copied to two modules. The first goes

## MoNA/Sweeper Coupling

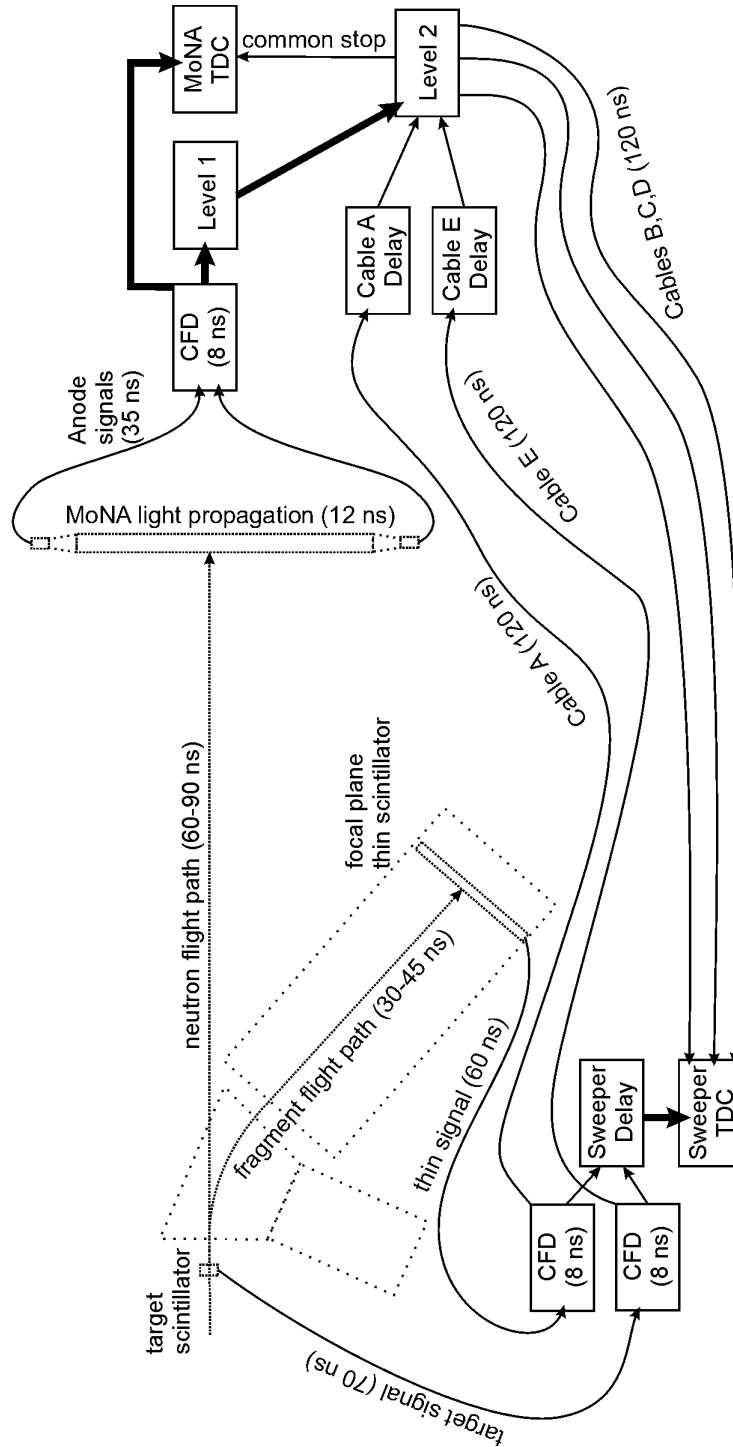


Figure 3.6: The timing channels important for coincident events are shown along with the five cables (described in the text) used to couple the data acquisition electronics between the MoNA and the Sweeper systems. Signal transit times are given for flight paths and signal cables. Transit times for signals passed within the same rack mount (straight arrows) are less than 5 ns. Double-wide lines represent multiple signals passed through one ribbon cable.

to a TDC as the start signal, while the second goes to Level 1, to open the QDC integration window, to be counted for the “majority” bit, and copied to Level 2 as the “mona start”. The TDCs are run in common-stop mode and are stopped by the delayed target timing scintillator signal in cable E. Therefore, the raw TDC channels have a negative time slope which is taken into account when the left and right channels are calibrated and then averaged to get the time-of-flight from the target to each bar.

### 3.5.2 Coincidence Timing

The delays shown in Figure 3.6 are chosen to ensure all timing signals are within the TDC’s range. The delay times depend on the speed of the secondary beam, the distance from the target to MoNA, and the TDC full range. For most MoNA experiments the TDCs are set to 350 ns full range to accept the prompt  $\gamma$  rays from the target, the full neutron time distribution, and a significant window for background events.

The delay for Cable E (target scintillator) used as the “common stop” is set to place the neutron peak near the middle of the raw TDC spectrum. The  $\gamma$  rays appear about 30 ns in the calibrated spectrum (depending on the distance) and the neutron peak is between 60-90 ns (depending on the beam energy). This leaves sufficient time in front of the  $\gamma$ -ray peaks for recording random background events and sufficient time for slower neutrons to arrive within the TDC range. To accomplish this, the delay time for Cable E is generally near 100 ns.

The delay for Cable A is generally around 80 ns. Here the “sweeper” signal must arrive within the coincident window defined by one of the set times for Level 2 as described in Section 3.5.4.



Table 3.1: The “majority” bits are set based on the number of coincident left-right pairs of CFD channels in one layer.

coincident pairs	“majority” bits
zero	00
one	01
two	10
three or more	11

### 3.5.3 MoNA Level 1 Trigger Logic

Each MoNA layer contains 16 detector modules with 2 PMTs each, leading to 32 CFD, TDC, and QDC channels. The MoNA Level 1 trigger logic counts the number of coincident (left–right) signals from the CFDs from each layer and the number of individual PMT channels fired. Each CFD has two outputs, one starts the corresponding TDC channel and the other triggers the Level 1 logic. A schematic diagram of the Level 1 logic is shown in Figure 3.7. The JTEC XLM72 logic modules (described in Section 2.2.5) whose FPGAs are programmed as Level 1, perform a variety of primary functions. There are nine Level 1 logic modules, one for each layer A through I. When a “calculate” signal is received from the MoNA Level 2 logic (that will be discussed in the Section 3.5.4) Level 1 adds all the coincident left–right pairs of MoNA PMTs and a binary 2-bit “majority” channel is set according to the Table 3.1. The “majority” bits are read by the Level 2 Virtex XLM (2.2.6) logic module and used in determining whether to accept or reject the event.

In addition to setting a “majority” bit the Level 1 logic also sends out the integration gate to the 32-channel QDC for that layer as soon as the first MoNA signal arrives from a CFD. This gate is made sufficiently long (120 ns) to ensure the whole dynode signal from every PMT in that layer is integrated. The first MoNA CFD trigger is transmitted to the Level 2 logic module as “mona start” to open the coincidence window.

The Level 1 logic modules have also been programmed to count the total number

# Level 1 Logic Diagram

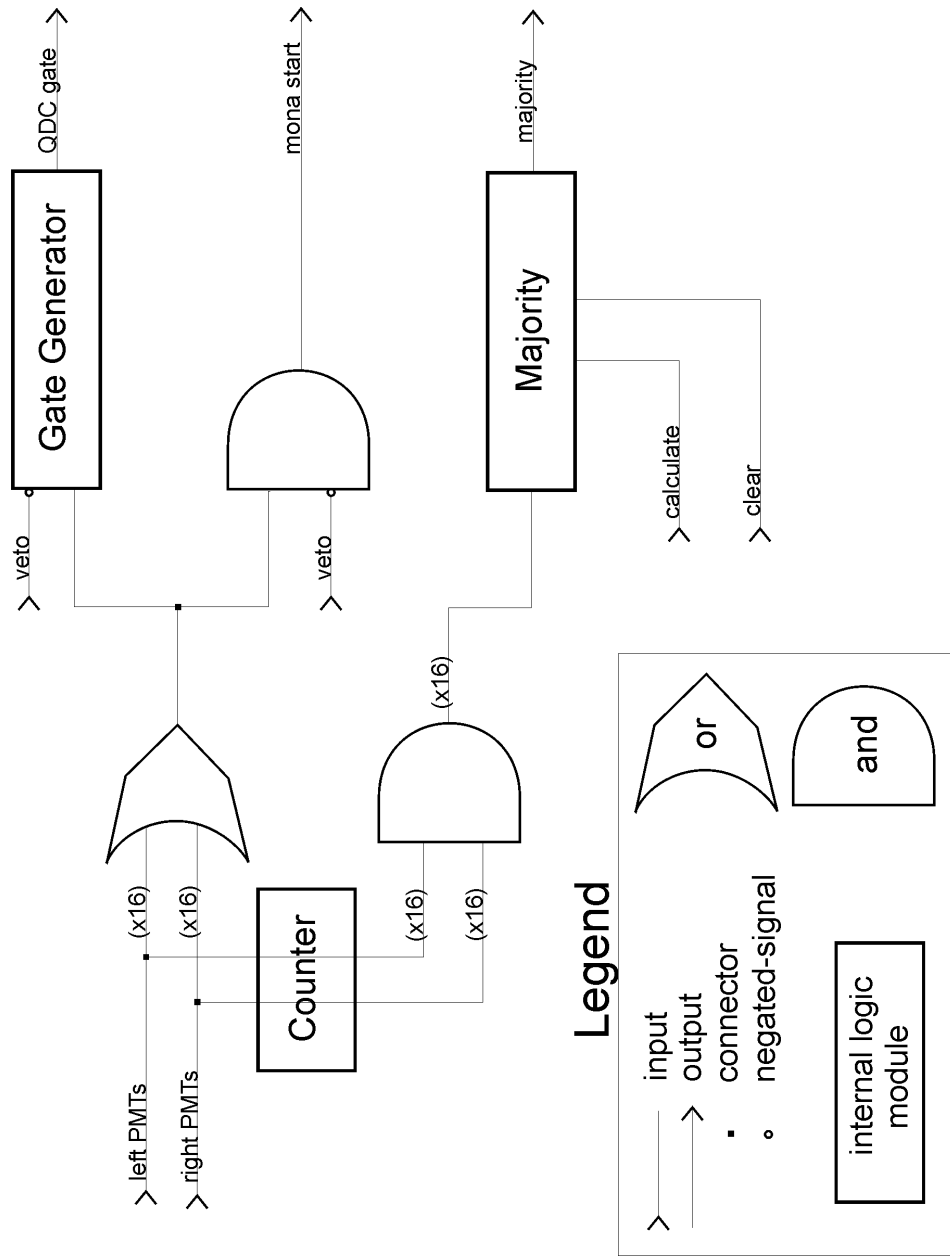


Figure 3.7: The Level 1 logic code is programmed into nine XLM72 modules, one for each layer. The QDC gate outputs are used directly by the QDC modules for that layer as the integration window, while the other output signals are used by the Level 2 logic.

		Reset	Hold	Run	Exit				
left	A	B	C	D	E	F	G	H	I
15	561.0	445.0	350.5	338.0	301.5	402.0	427.0	343.0	608.5
14	559.5	300.0	306.5	303.5	245.5	240.5	303.5	341.5	272.0
13	469.0	311.0	218.0	179.0	209.0	207.5	250.0	238.5	443.5
12	334.5	206.5	166.0	175.5	155.0	160.5	185.0	240.5	458.5
11	362.0	230.0	183.5	170.5	156.0	153.5	213.5	263.0	347.5
10	371.5	224.5	184.5	181.5	133.5	169.5	170.0	251.5	412.0
9	437.5	196.5	207.0	151.5	161.0	160.0	172.5	248.5	411.0
8	306.5	237.5	170.0	162.0	158.0	173.5	176.5	264.0	371.5
7	390.5	282.0	176.5	136.0	148.0	159.0	176.5	218.0	446.0
6	329.0	256.0	159.0	163.0	159.5	160.5	180.0	238.0	304.0
5	370.5	255.5	287.5	154.5	143.5	160.5	170.5	245.5	348.0
4	332.0	230.5	159.0	122.5	144.5	174.5	221.5	217.0	329.5
3	339.0	210.0	146.0	174.0	169.5	194.0	175.5	233.0	243.0
2	415.0	302.5	201.0	187.0	177.0	200.0	217.5	286.5	395.5
1	411.5	264.5	266.0	199.0	235.5	261.0	258.0	385.0	350.5
0	387.5	416.5	314.5	290.5	328.5	310.5	308.5	387.5	155.5
right	A	B	C	D	E	F	G	H	I
15	486.5	398.5	389.5	404.5	329.5	354.5	431.5	465.5	479.5
14	438.5	320.0	241.0	256.0	226.0	180.5	262.5	325.0	401.0
13	358.0	252.5	238.5	187.5	210.0	177.0	258.5	290.0	440.5
12	410.0	233.5	212.5	145.5	163.0	136.0	219.5	224.0	343.5
11	385.0	225.0	173.0	138.0	151.0	137.0	165.0	256.5	303.0
10	366.5	239.5	165.5	186.5	296.0	137.0	180.0	220.5	379.5
9	386.5	355.5	169.5	156.0	126.0	131.5	160.0	199.0	343.5
8	420.0	218.5	164.5	148.0	148.5	133.5	179.0	234.0	293.5
7	407.0	249.0	204.0	205.0	141.5	173.5	209.0	254.0	398.5
6	508.5	263.5	254.5	144.5	155.5	168.0	240.5	286.5	512.5
5	397.5	268.5	191.5	137.5	171.0	194.5	190.0	311.5	399.0
4	391.0	257.0	212.5	196.5	156.0	189.5	249.5	268.5	376.0
3	266.0	267.0	217.5	185.0	180.0	178.0	206.0	290.5	441.0
2	535.0	298.0	229.5	217.5	234.0	236.0	300.0	306.0	348.0
1	379.0	315.5	237.0	270.5	228.5	206.5	290.0	267.0	450.0
0	524.5	490.5	444.5	353.5	402.5	349.5	438.5	422.0	539.5

Figure 3.8: Each cell is the average rate per second of raw CFD triggers for that MoNA module PMT counted by the Level 1 logic module. The lighter color indicates a higher count rate.

of hits every two seconds for each PMT and hold this value in a readable VME bus (labeled “Counter” in Figure 3.7). A separate Tcl/Tk program interfaces with the VME buffer and reads these channels and displays a diagnostic array of all the PMT rates for viewing during the run to ensure the voltages are still set properly and the PMTs are functioning normally. This diagnostic display is shown in Figure 3.8.

### 3.5.4 Level 2 Logic

The Level 2 logic unit consists of a JTEC Virtex XLM logic module containing a larger Virtex FPGA. This unit processes the “majority” bits and the “mona start” for all nine Level 1 logic modules along with the “primary start” to accept or reject an event and send the corresponding signals to the Sweeper electronics through cables B,C and D. Figure 3.9 is a schematic drawing of the Level 2 logic programmed into

the Virtex XLM.

### 3.5.5 Level 2 Timer

The XLM72 internal clock runs at a frequency of 80 MHz. All outputs and logic conditions are set by the end of a clock cycle and are, therefore, discretized by 12.5 ns. Because of this, all the delays used for “and” gates with coincident logic signals must have at least 13 ns overlap to ensure proper logic conditions. These internal delays are set through a Tcl/Tk program to interface with the XLM unit before each recorded run. There are three values to set in units of clock cycles:  $\text{Set}_1$ ,  $\text{Set}_2$ , and  $\text{Set}_3$ . These values, along with the trigger conditions, are used to set the process times for each of the five output channels of the Level 2 logic Timer:  $t_a$ ,  $t_b$ ,  $t_c$ ,  $t_d$ , and  $t_e$ . The delay times are as indicated by Table 3.2. The delay time for  $t_c$  is equal to  $\text{Set}_2$  if the “primary” signal starts the Timer and equal to the sum of  $\text{Set}_1$  and  $\text{Set}_2$  if the “secondary” signal comes first. This is to allow more time for a coincidence between MoNA and the “primary” trigger condition when MoNA is used in tandem mode along with the Sweeper detectors.

Typical values for  $\text{Set}_1$ ,  $\text{Set}_2$ , and  $\text{Set}_3$  are 18, 6, and 60, respectively. This corresponds to a coincidence window of 225 ns after the timer starts, and a delay of 75 ns before the “TDC veto” asserts. The final set time is the duration of the “clear” window to ensure any fast cleared modules are ready for the next event. Figure 3.10 details the sequence signals from the target reaction to the “computer go” or “fast clear” signals.

The delays for the external cables A through E are adjusted for the specific experimental setup. Such factors as distance between the target to MoNA and the speed of the charged particle residues are taken into account to make certain the timing signals come within the valid window set by the TDC range and the timing overlaps of the Level 2 timer.

# Level 2 Logic Diagram

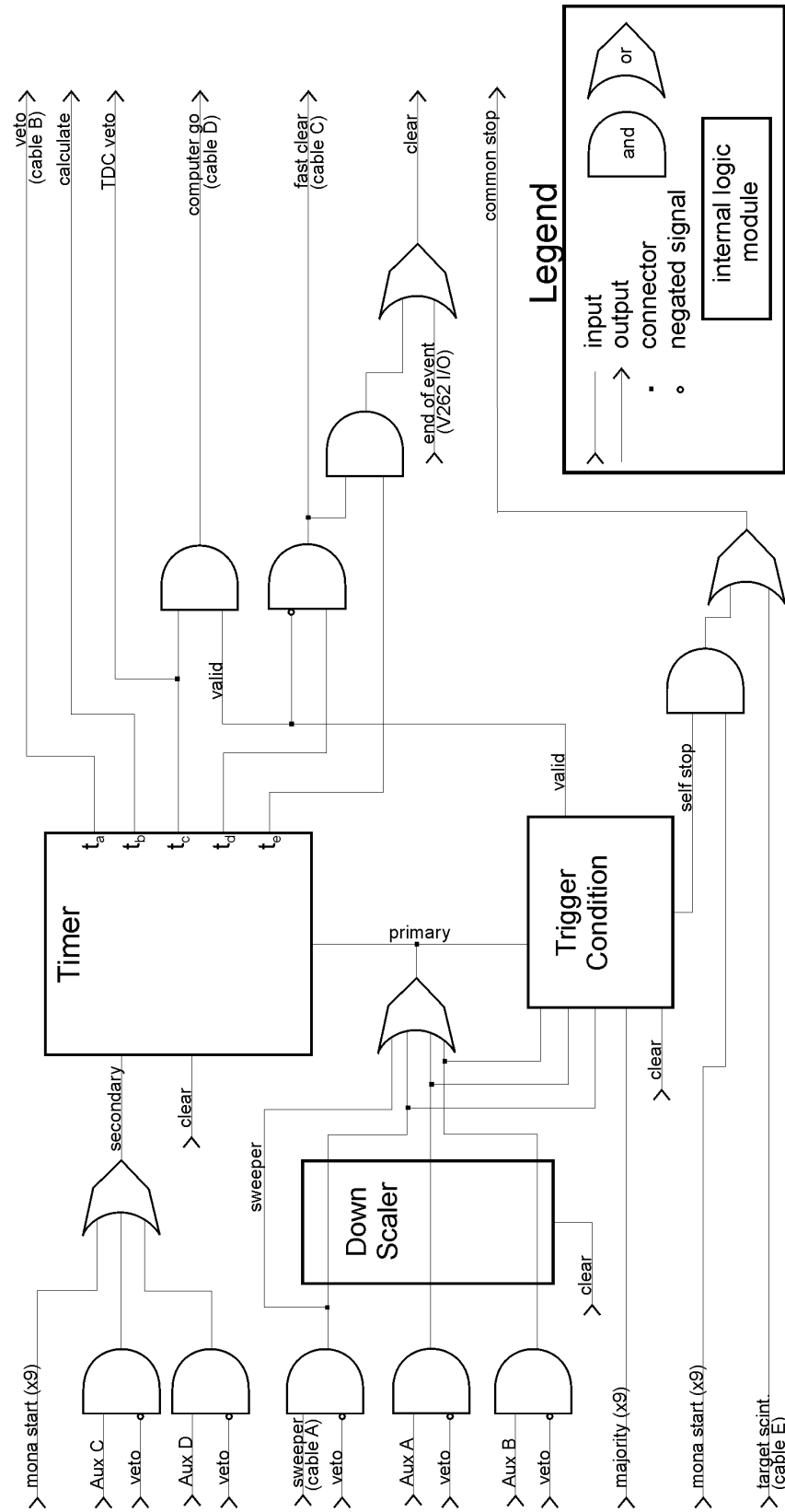


Figure 3.9: The Level 2 logic programmed into the Virtex XLM controls the acceptance or rejection of an event.

## Standard timing sequence

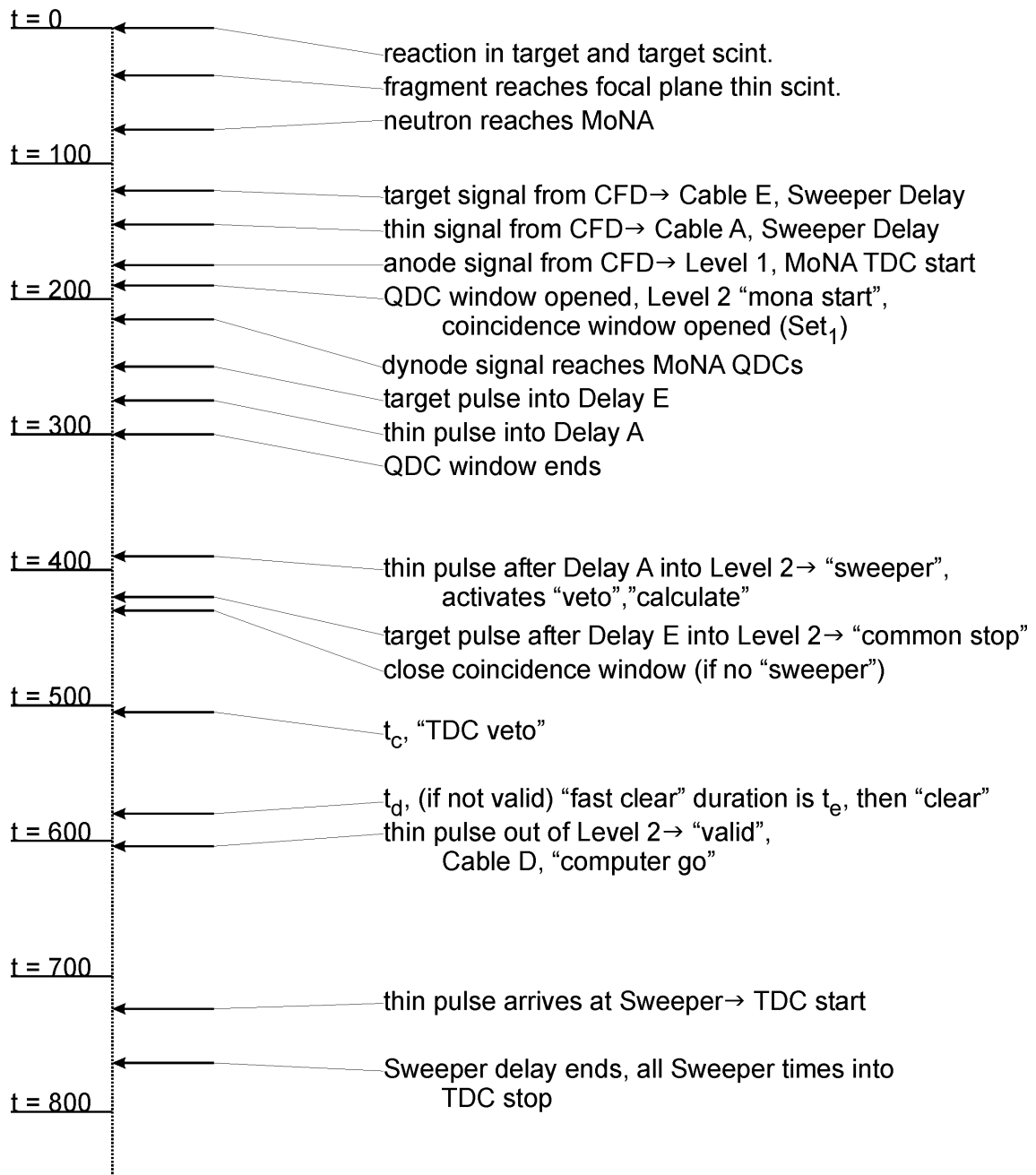


Figure 3.10: The timing sequence is shown for a typical coincident event. The scale on the left side is in nanoseconds, so the entire sequence takes less than  $1 \mu\text{s}$  to accept or reject an event. The readout of all MoNA and Sweeper modules may take a few ms, and a rejected event is cleared by the "fast clear" signal ( $t_d$ ) in less than 800 ns. Signal dependences and set times are described in Sections 3.5.1 to 3.5.5.

Table 3.2: The five output signals from the Level 2 timer are determined by the three set values.

Output time	Corresponding set values (clock cycles)
$t_a$	Set <sub>1</sub>
$t_b$	Set <sub>1</sub>
$t_c$	Set <sub>2</sub> or Set <sub>1</sub> + Set <sub>2</sub>
$t_d$	$t_c + 6$ cycles
$t_e$	Set <sub>1</sub> + Set <sub>2</sub> + Set <sub>3</sub> + 6 cycles

For a normal coincident event during a production run, the entire logic system has been cleared from the previous event and awaits a “start”. Usually, a “mona start” signal comes from Level 1 to start the timer. Then a “primary” signal enters the timer before the end of the coincidence window, and the “veto” latch is activated and copied to cable B for the Sweeper electronics. A “computer go” signal is then asserted that is anded with the “valid” signal from the Level 2 trigger condition logic. Along with this “computer go” signal, the Timer also sends out the “TDC veto” to close the TDC inputs near the end of the TDC range.

If no “valid” signal is received from the Trigger Condition logic then, a “fast clear” signal is issued to clear all QDC and TDC modules and is copied to cable C for the Sweeper electronics. This is followed by a “clear” signal that resets the logic modules and closes the “veto” latch to accept the next “start”.

If a “valid” signal is sent before the coincidence window closes, the “computer go” signal activates the readout of the QDCs then the TDCs modules. This signal is also sent back to the Sweeper modules as a “common start” through cable D for the delayed Sweeper timing channels. The MoNA QDC modules are done digitizing before the TDCs, since the QDC integration window is shorter than the TDC range, and readout first. The rest of the MoNA/Sweeper DAQ modules have time to digitize and await their turn at being read out by the data acquisition (DAQ) system. When the DAQ computer is done reading the event an “end of event” signal is issued that enables the “clear” signal and closes the “veto” to ready all the electronics for the

next event.

### 3.5.6 Auxiliary Inputs

Additional detectors can be incorporated into the logic system through the auxiliary inputs. The auxiliary A and B inputs can be substituted for the Sweeper focal plane's thin upper-left PMT channel and used to enable the "primary trigger". Both A and B inputs have a down-scaled option that allows one to automatically switch to these alternate triggers. The down scaled factors are set through the user interface in powers of two. The auxiliary C and D inputs can be substituted for the "mona start" from Level 1 as an alternate way of enabling the "secondary" trigger.

These auxiliary inputs have been tested and used successfully. The target timing scintillator has been routed to the Aux-A input and down-scaled to record events where no particle travels to the thin scintillator in the back of the detector box. Together with a beam-line timing detector further upstream, these events are used to determine the beam purity. This is possible because nuclei with different mass to charge ratio will have a different speed through the beam optics. The secondary auxiliary inputs have also been used with  $\gamma$  ray detectors and a separate neutron detector connected as Aux-C input. By enabling both the MoNA and Aux-C secondary triggers one can record coincident events with the primary trigger for either of them.

#### Down scaler

The down scaler logic unit is set to accept a fraction of the inputs connected to it. The down scaled factors are set through the user interface in powers of two. Any primary inputs that are enabled, including the auxiliary inputs A or B, that pass through the down scaler will be accepted as the "primary" trigger.

Down-scaled data of an auxiliary input can be used to determine if there are any beam contaminants that do not strike all the focal plane detectors. By connecting



the beam line scintillator to the Aux-A input of the down scaler, one can record a small fraction of the beam timing events relative to the target scintillator. Since most secondary beam contaminants will have a different ToF through the beam line, contaminants can be identified even if they do not reach the focal plane detectors.

### 3.5.7 Level 2 Trigger Conditions

The determination of whether to accept or reject an event is made within the Level 2 Trigger Condition logic and is controlled by a Tcl/Tk user interface. The first condition determines whether to require coincident events between a “primary” trigger and the “majority” output from Level 1. If this condition is active then the logic will not issue a “valid” without receiving both signals, otherwise every “primary” trigger enables a “valid” signal. The second condition determines the minimum acceptable “majority” bit value. A “valid” signal is not sent unless the “majority” value is larger than a user-programmed set value. If the first condition requires a coincidence the minimum “majority” bit must also be met before a “valid” signal is issued. The “valid” signal, once sent, is anded with the “TDC veto” signal from the Timer to make the “computer go” signal that starts the V262 I/O module and DAQ process as described in Section 3.2.

#### **Self stop, self trigger**

An alternate trigger condition setup overrides the requirement of the “primary” trigger allowing the MoNA system to run in “self stop” and “self trigger” mode. This override is usually only used during the MoNA calibration runs involving cosmic-ray muons, without an external time-of-flight detector or trigger. In this mode the “mona start” from Level 1 is copied to the TDC “common stop” signal. The absolute time is meaningless in this mode but the time difference between the two ends of a bar is still valid for calibrating the  $x$  position along the bar and the independent timing

offsets for each bar (see Appendix C for its use).

## 3.6 Decay Energy Reconstruction

The energy of the unbound system is converted to kinetic energy of the reaction residues. Both the fragment and the neutron get equal momentum kicks, and since the neutron is often 10 times lighter or more, it gets a much larger velocity kick compared to the fragment. By measuring the velocities and angles of both reaction residues in the center of mass reference frame, the relative energy between the two can be calculated by determining the Lorentz four-vector  $P^\mu$  (with the unit-less convention  $c = 1$ ):

$$P^\mu = (-E, p_x, p_y, p_z) = (-E, \vec{p}) \quad (3.3)$$

for both the fragment and the neutron.  $E$  is the total energy of the particle, equal to the mass if at rest. The decay energy of the unbound system can be calculated by the invariant mass method independent of the reference frame.

### 3.6.1 Invariant Mass

Because the square of any Lorentz four-vector is equal to the square of mass of the particle ( $P^\mu P_\mu = (P^\mu)^2 = m^2$ ), the kinematic equation of the unbound system before and after the decay reduces to quantities that can be measured in the lab frame:

$$(P_i^\mu)^2 = (P_f^\mu + P_n^\mu)^2 \quad (3.4)$$

where  $i$  denotes the pre-fragment unbound system. The subscripts f and n refer to the reaction residue (fragment) and the released neutron in the lab frame. Since the left side of Equation 3.4 is just the total initial mass of the system (including decay energy),

$$(P_i^\mu)^2 = m_i^2 \quad (3.5)$$

Equation 3.4 expands to:

$$(E_{\text{decay}} + m_f + m_n)^2 = m_f^2 + m_n^2 + 2(E_f + E_n - p_f p_n \cos \theta) \quad (3.6)$$

including the masses of the fragment ( $m_f$ ), the neutron ( $m_n$ ), and the energy by which the system is unbound ( $E_{\text{decay}}$ ). The opening angle between the fragment and neutron in the lab,  $\theta$ , is calculated from the  $x, y, z$  coordinates of neutron and the reconstructed angle of the fragment.

The decay energy is then solved for as:

$$E_{\text{decay}} = \sqrt{m_f^2 + m_n^2 + 2(E_f + E_n - p_f p_n \cos \theta)} - m_f - m_n \quad (3.7)$$

The final decay energy depends more strongly on the neutron parameters than those of fragment due to its lighter mass. Indeed, using the neutron angle instead of the opening angle will not change the peak energy by more than 20%.

### 3.6.2 Charged Particle Reconstruction

Since the invariant mass equation requires the momentum vector of the fragment where the decay reaction occurs at the reaction target, the angles and positions recorded by the CRDCs after the Sweeper magnet must be transformed back to the target position using a measured magnet field map of the Sweeper magnet. An inverse matrix is calculated that is specific for the magnet setting and the charged reaction residue.

Table 3.3: The positions and angles at CRDC 1 are transformed to the  $y$  (non-dispersive) position, both angles, and the relative energy at the reaction target.

Input Parameters at CRDC 1	Output Parameters at Target
$x$	$\theta_x$
$\theta_x$	$\theta_y$
$y$	$y$
$\theta_y$	$\delta_e$

### Inverse matrix

A series of measurements were made for eight different Sweeper magnet currents using an array of seven Hall probes at over forty positions along 35 arcs within the Sweeper magnet’s 14 cm curved gap [47]. These measurements cover the whole operational range of the magnet and a permanent reference Hall probe was used to extrapolate to the field strength used during an experiment. Once a reference Hall probe value is recorded for an experiment, a magnet field map is generated by IGOR PRO [48] using the archived series of measurements. The field is calculated for the mid-plane of the 14 cm gap and then imported to COSY INFINITY [49] along with the desired particle’s mass and charge to yield a transformation matrix from the target position in front of the Sweeper magnet to the position of CRDC 1 inside the focal plane detector box.

The matrix relates the particle’s horizontal and vertical angles and positions at CRDC 1 to the angles and energy at the target. Table 3.3 shows the parameters related by the transformation matrix. This matrix is inverted to output the parameters in the right column using the left column as the input. The relative energy  $\delta_e$  is the ratio of the charged particle energy to the nominal energy of the central track calculated by *COSY INFINITY*.

### Incoming tracking

One drawback of this inverse matrix is that in order to calculate the relative energy  $\delta_e$  it must assume the dispersive  $x$  position at the target is zero. As shown in the figure of the experimental layout (3.1), there are two position-sensitive detectors upstream from the target. These were not used in the  $^{12}\text{Be}$  or  $^{10}\text{Be}$  experiments, but have been used in other MoNA/Sweeper experiments to assist in the reaction residue reconstruction. A separate COSY INFINITY transformation matrix can be used to calculate the positions and angles of the incoming beam through the focusing quadrupole triplet in front of the target using the measured positions and angles of the beam line tracking detectors. The dispersive position at the target can be used as an additional input to better reconstruct the energy of the charged particle [50].

### 3.6.3 Energy and Angle of Neutrons

After MoNA has been calibrated for time, light response (QDCs), and position (see Section 2.3), the momentum vector used to reconstruct the decay energy can be determined from the TDC-related parameters. The horizontal distance along any bar ( $x$  axis) is given by the calibrated time-difference between the left and right time signals. The distance from the target along the beam axis ( $z$  axis) and the vertical position ( $y$  axis) is determined by the layer and row. These three dimensions are used to calculate the 3d position and angle relative to the target for the reacted neutron. The neutron's velocity, and consequently its energy, is calculated from the position and the mean time  $\text{ToF}_n$  (Equation 2.4).

# Chapter 4

## Performance

MoNA's performance in terms of efficiency, acceptance and resolution was tested with cosmic-ray data and in-beam neutron experiments and the results were compared to simulations. The MoNA collaboration has written two separate Monte Carlo programs to simulate the efficiency, acceptance, and resolution for MoNA experiments. The first is based on GEANT-3.2.1 [43] and is used to determine the efficiency of a single MoNA detector module and compounded for the whole 16 by 9 array. The second program is SIMPLE TRACK and simulates the layout and acceptances and resolutions of the full MoNA/Sweeper Magnet setup [51]. When SIMPLE TRACK is configured for a MoNA/Sweeper experiment it is referred to as ST-mona.

Control experiments were performed to test the validity of these simulations. With the efficiency, acceptance and resolutions determined, the simulations can be used to analyze experiments and optimize the design of future experiments.

### 4.1 Neutron Detector Simulation

The GEANT-3.2.1 based simulation was designed to determine MoNA's efficiency as a function of neutron energy and detection threshold. The two most important components of an efficiency simulation are the reaction cross sections of the detector

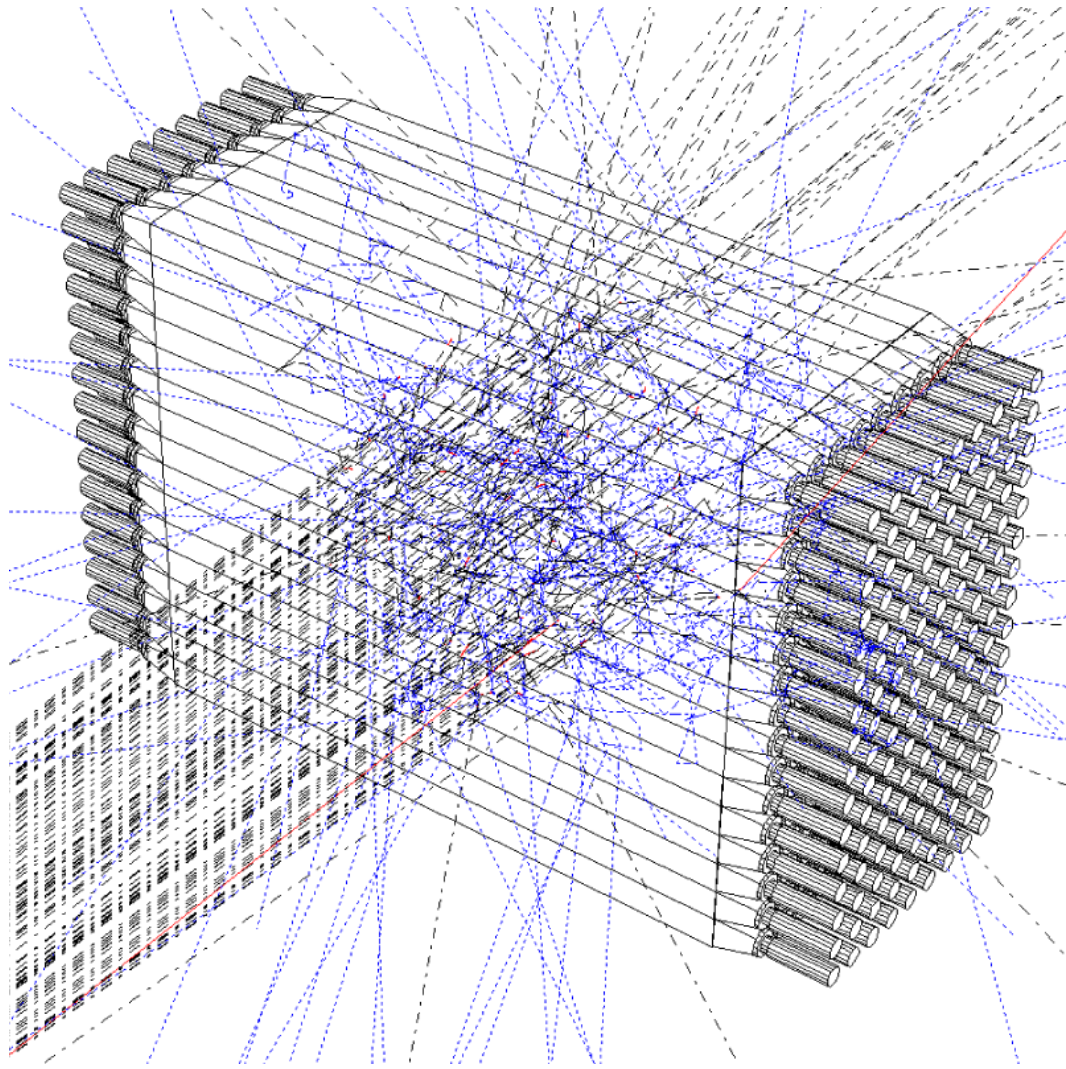


Figure 4.1: Neutrons (black dot-dash lines) approach MoNA from 8 meters in this GEANT-3.2.1 simulation. Reactions products include proton scatter (solid red lines) and  $\gamma$  rays (blue dotted lines).

material as a function of the neutron energy, and the light response curve for each reaction residue as a function of the released energy.

#### 4.1.1 Reaction Cross Sections

GEANT uses an extensive library of neutron reaction cross sections on a variety of elements. These are used, along with the relative density of hydrogen and carbon in BC408, to determine the neutron reaction cross section for one MoNA bar. By using the FLUKA-MICAP method within GEANT the neutron cross sections are determined

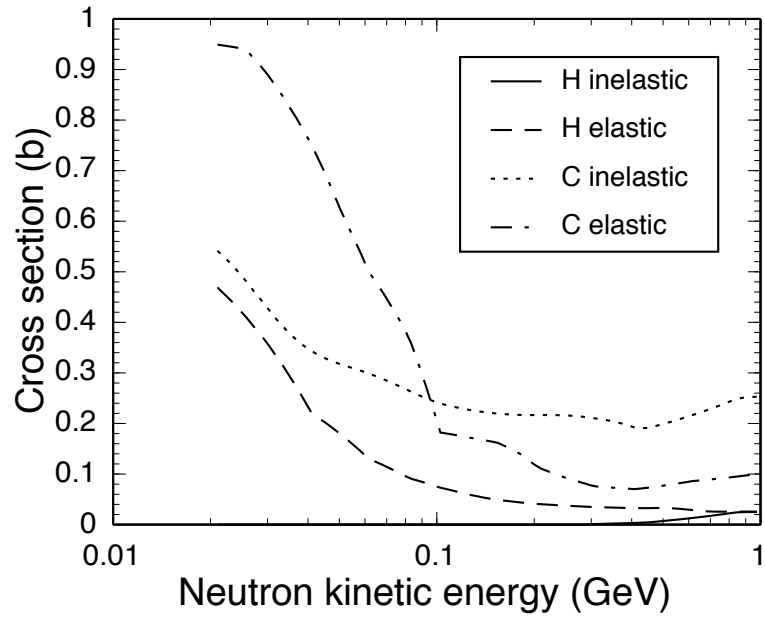


Figure 4.2: Inelastic and elastic reaction cross sections of neutrons on carbon and hydrogen used by the GEANT simulation. The FLUKA package cross sections are used above 20 MeV. Cross sections taken from the evaluated nuclear data files (ENDF) [52] are used below 20 MeV.

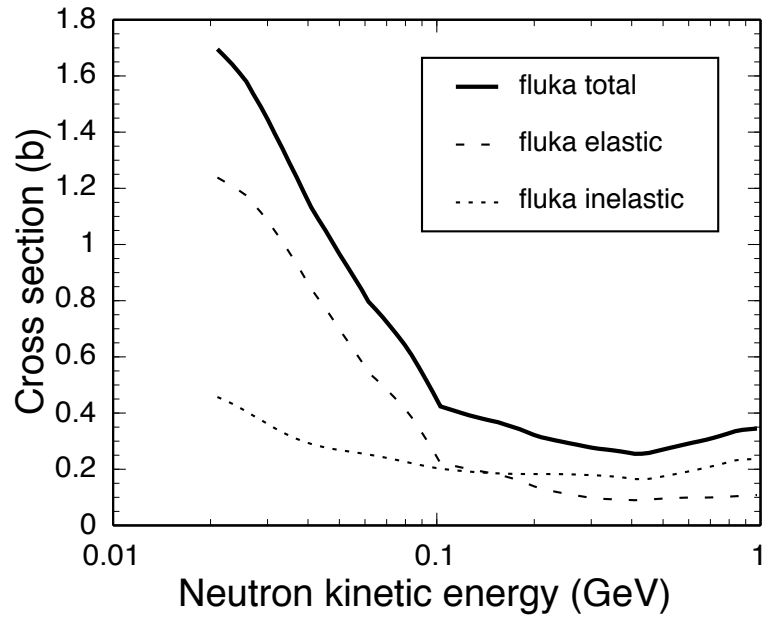


Figure 4.3: Inelastic and elastic reaction cross sections of neutrons on BC408 (MoNA plastic) used by the GEANT simulation.



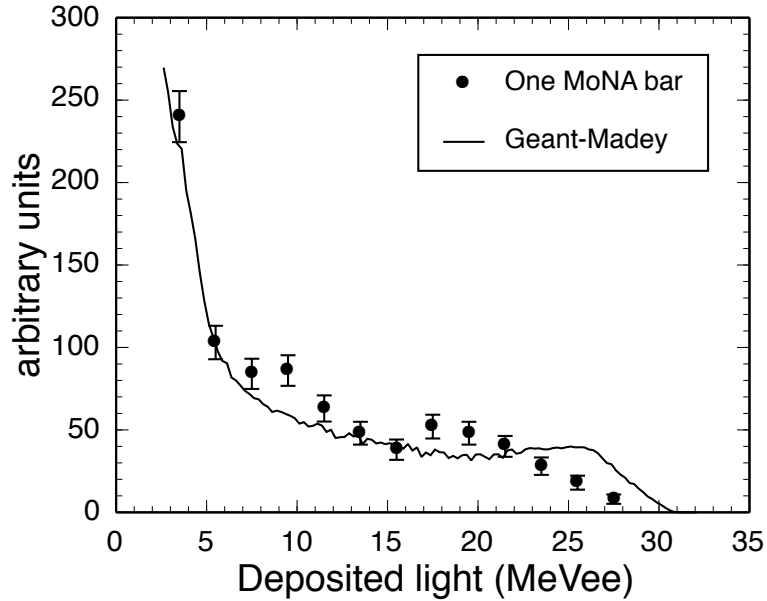


Figure 4.4: Measured light response curve for 35-40 MeV neutrons compared to GEANT simulation using the Madey light response equation 4.1.

by the FLUKA package of cross sections down to 20 MeV [53,54], below which, neutron cross section tables from the evaluated nuclear data files (ENDF) [52] are used that incorporate various resonant reactions with carbon. The inelastic and elastic neutron cross sections for carbon and hydrogen used by the FLUKA package are displayed in Figure 4.2. These are combined in appropriate proportions for BC408 plastic in Figure 4.3.

### 4.1.2 Light Response

The light produced by a charged particle passing through BC408 plastic [11] is different for different charged particles. This light response must be accurately simulated in order to determine the number of reactions that deposit enough energy to meet the threshold requirements of the detector. Protons and alpha particles from the interaction of the neutron in the plastic yield less light than an electron of equivalent kinetic energy due to their increased mass. The GEANT simulation determines the number and energies of protons, alpha particles, and electrons produced by the interactions

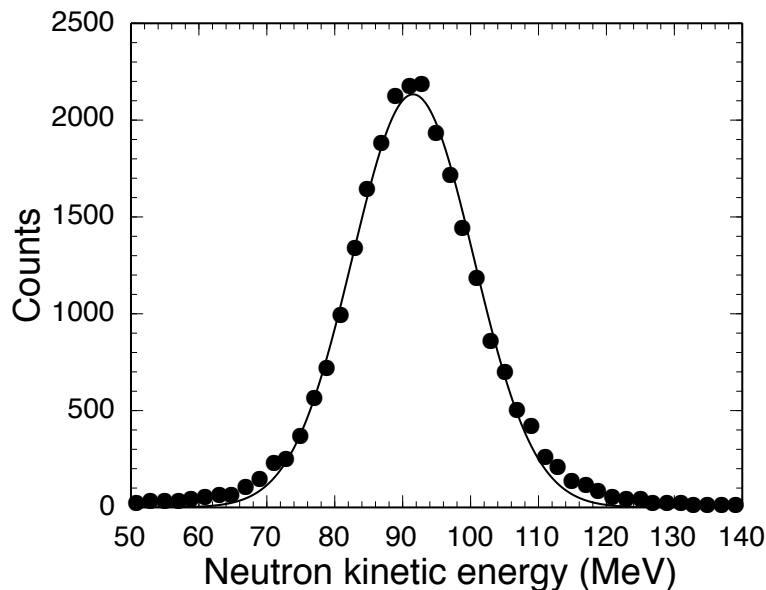


Figure 4.5: The Gaussian fit to the neutron kinetic energy data is used as an input for GEANT to compare the light response, shown in Figure 4.6.

of neutrons within the BC408 plastic.

Two separate experiments were performed to test the simulation’s light response for MoNA at two different energy ranges and two different situations. The first produced a wide range of neutron energies by stopping most of a 40 MeV/u argon beam in the thick steel collimator, at the target position. The resulting neutron distribution covered energies between 25–60 MeV. 35–40 MeV Neutrons were gated by their time-of-flight ( $ToF_n$ ) and a 12.5 cm wide area near the center of one bar to compare with GEANT.

For the second experiment, neutrons were produced by the Coulomb breakup of  $^{11}\text{Be}$  on a gold target at 90 MeV/u.  $^{10}\text{Be}$ -coincident neutron data from the whole array were used to compare to simulation. The Gaussian fit of the distribution of neutron energies shown in Figure 4.5 was used as the input distribution in GEANT for the comparison plotted in Figure 4.6.

The light response curve is calculated as per Reference [55] by:

$$l = a_1 E - a_2 [1 - \exp(-a_3 E^{a_4})] \quad (4.1)$$

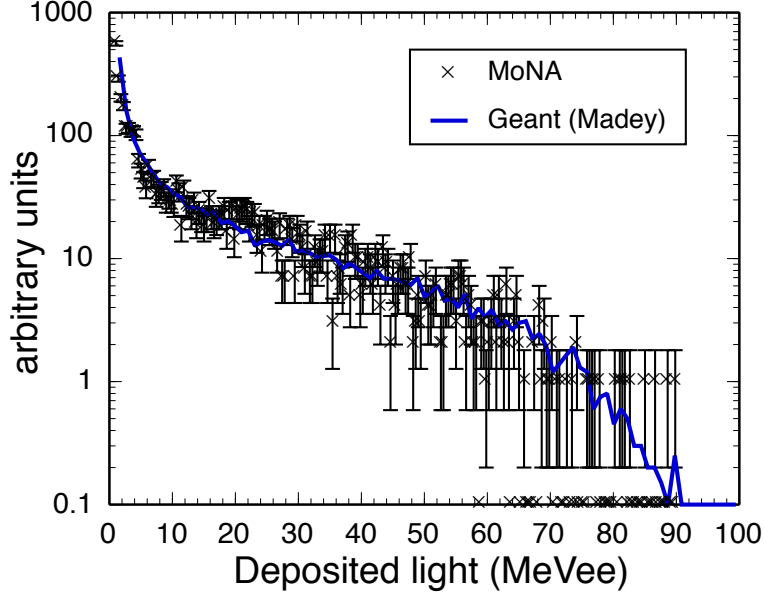


Figure 4.6: Measured light response curve for the neutron data from Figure 4.5 into the full MoNA array compared to GEANT simulation using the Madey light response equation 4.1.

with coefficients ( $a_{1-4}$ ) set according to Table 4.1, and  $E$  is the energy-loss for the charged particle, calculated in small steps of path-length through the plastic. The curves closely reproduce the MoNA data from both experiments (Figures 4.4 and 4.6).

### 4.1.3 Simulated MoNA Intrinsic Efficiency

Figure 4.7 shows the intrinsic efficiency for MoNA, as calculated by GEANT, for a wide range in neutron energies and several light-response threshold values (in MeVee).

A software gate, applied to the calibrated  $Q$  parameter (defined in Section 2.2.4) is needed to accurately identify a position-independent threshold for comparison with

Table 4.1: Light-response coefficients used by GEANT in Equation 4.1. The values are taken from Reference [55].

charged particles	$a_1$	$a_2$	$a_3$	$a_4$
protons	0.95	8.0	0.1	0.9
alphas	0.41	5.9	0.065	1.01

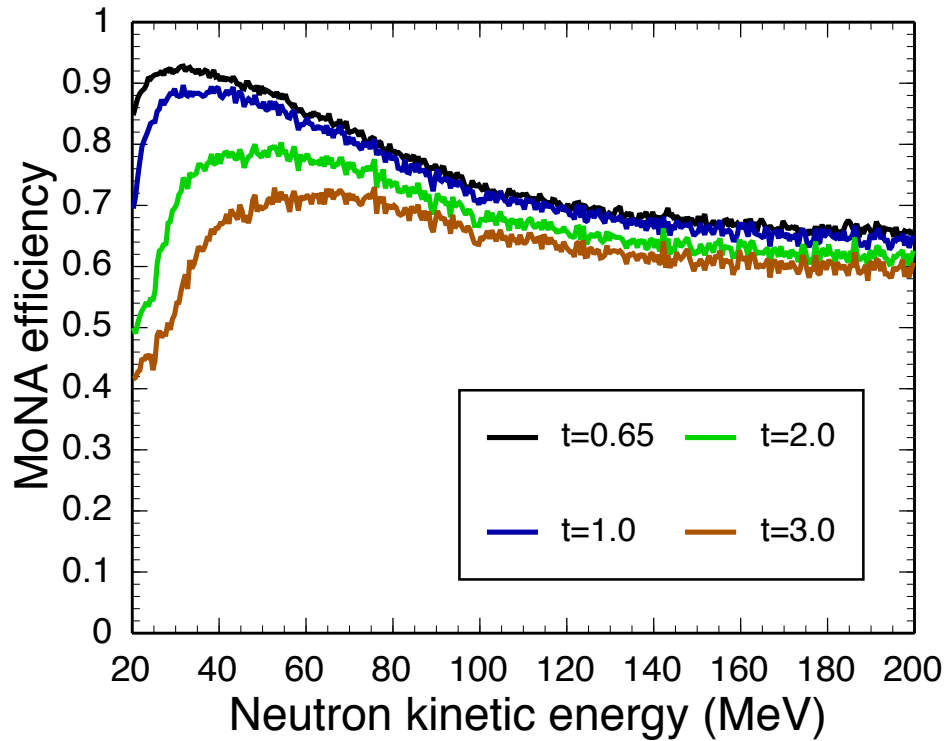


Figure 4.7: Simulated total calculated intrinsic neutron efficiency for MoNA with threshold values of 0.65, 1.0, 2.0, and 3.0 MeVee.

simulations. Due to the difficulty of producing a calibrated beam of neutrons at the NSCL, an alternate method was used to compare with simulation. Neutrons produced by stopping an argon beam on a thick collimator at the target position provided a broad range of neutron energies at MoNA. By gating on a small range of neutron energies and subtracting a background, the number of detected neutrons was determined for each energy range. The number of detected neutron events above a software threshold for each energy range was divided by the GEANT simulation's efficiency for the corresponding threshold to yield the calculated count of incoming neutrons. Figure 4.8 shows the calculated number of neutrons striking one MoNA module during this test run for four energy ranges and three threshold values. Since the energy distribution of the neutrons was not flat, the count for each 5 MeV bin does not need to be the same as the others, but the three points for each bin should be consistent if the light response calculations in GEANT are correct. The efficiencies used for each

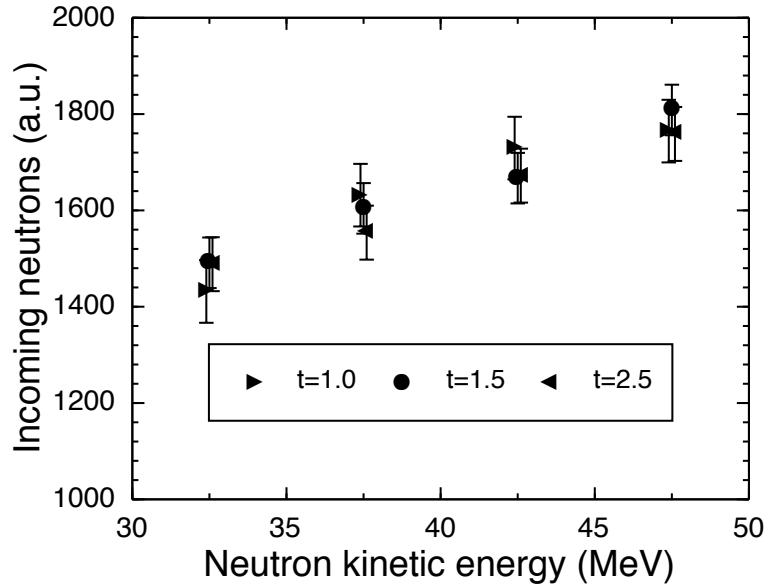


Figure 4.8: The incoming neutrons per 5 MeV-energy bin is calculated from the simulated efficiency for each threshold value (plotted in Figure 4.9).

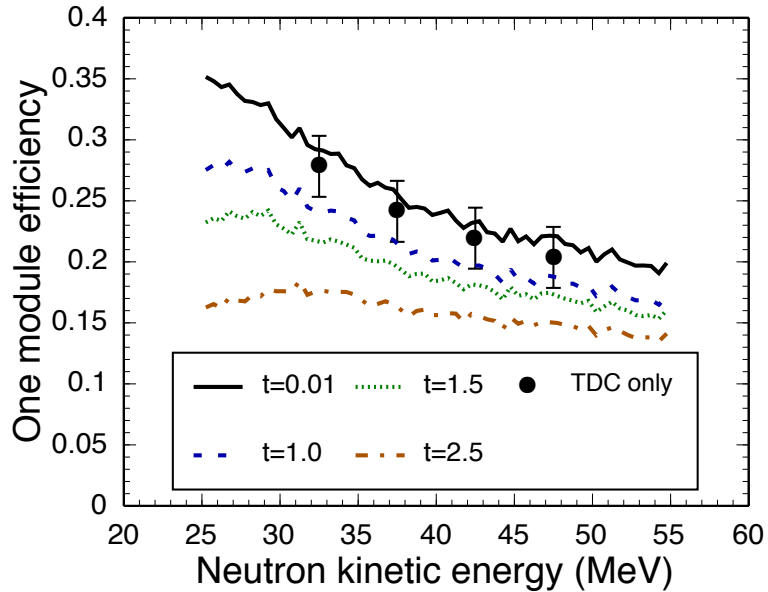


Figure 4.9: Efficiency curves as a function of neutron energies for one MoNA module. The various simulated thresholds are labeled and the data points correspond to the relative efficiency for valid TDC events in MoNA using the incoming rate from Figure 4.8 (described in the text).

energy range for the three threshold values is displayed in Figure 4.9.

As a check, the reverse process was used to confirm the relative threshold for the CFD/TDC hardware without a software gate on  $Q$ . By dividing the ungated counts in the MoNA bar for each energy bin by the mean value of the number of incoming neutrons from Figure 4.8, the efficiency for just the valid TDCs events in each energy bin can be calculated. The results, displayed in Figure 4.9, are consistent with the calibrated 0.65 MeVee CFD threshold determined in Section 2.3.3.

#### 4.1.4 MoNA/Sweeper Layout Simulation

The SIMPLE TRACK simulation, ST-mona [51], was designed to reconstruct the full kinematics of the decay of an unbound nucleus to a neutron and a residue. It includes acceptance cuts and individual detector resolutions to resemble the recorded distributions. It uses a forward transformation matrix from COSY INFINITY [49] to track charged particle through the Sweeper magnet into the focal plane detectors.

The simulation starts with a user defined distribution of beam particles at a target set to match the parameters recorded by the experiment. A choice of reactions is then simulated within the target. For knockout reactions populating a neutron-unbound state a Glauber-model kick is applied [56]. The decay energy distribution itself can be entered as a flat distribution, a constant (single) value, a Gaussian distribution, or a Breit-Wigner distribution given by:

$$d\sigma/dE \propto \frac{\Gamma}{(E - E_d)^2 + (\Gamma^2/4)} \quad (4.2)$$

or a thermal (Maxwell) distribution:

$$d\sigma/dE \propto \sqrt{E_d} e^{-E_d/T} \quad (4.3)$$

where  $E_d$  and  $\Gamma$  are the resonant energy and width of the unbound state, respectively,

and  $T$  is the “temperature” of the Maxwell distribution (all units MeV). A custom distribution for the decay can also be implemented.

The acceptances and detector resolutions of a particular experimental setup are determined either by the information from the beam-line tracking detectors, or by matching the focal plane detector distributions. After configuring the input parameters for ST-mona, the positions and angles of the fragments at the point of the reaction are reconstructed through the inverse matrix. This information is then combined with the neutron parameters as per Equation 3.7, to yield a simulated decay energy curve to compare directly with experimental data.

## 4.2 Resolution Measurements

### 4.2.1 MoNA Time Resolution

The intrinsic resolution of each TDC channel corresponds to the TDC range divided by the number digitization bins (4096 for a 12-bit TDC). For a TDC range of 350 ns this is 0.085 ns per bin. The resolution of the CFD logic output from the raw anode signal of the PMTs is estimated to be about 0.1 ns [35]. The neutron time-of-flight parameter,  $\text{ToF}_n$  is calculated by the average of the left and right TDC channels for a given MoNA module, Equation 2.4. The resolution for this parameter is about 0.18 ns.

Evidence of the measured time resolution where the time difference between neighboring bars is plotted for cosmic-ray muons traveling straight down through them is plotted in Figure 2.15. The Gaussian fit shown has a standard deviation of 0.18 ns. Since this data is self-triggered and self-stopped, the time resolution of any external timing detector must be added in quadrature to this value for an accurate resolution of the neutron  $\text{ToF}_n$ .

The  $\text{ToF}_n$  parameter is also effected by CFD “walk” for events that do not deposit

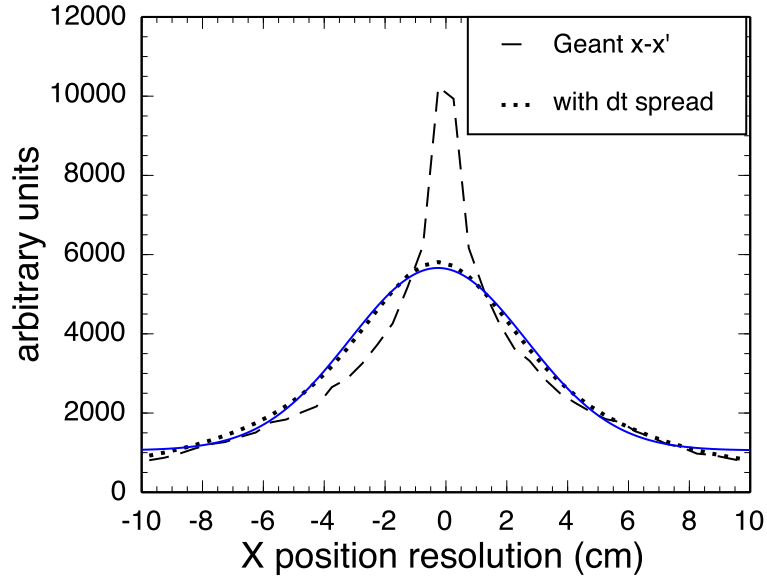


Figure 4.10: The neutron interaction point ( $x$ ) minus the center of deposited energy ( $x'$ ) is the intrinsic resolution of the MoNA plastic. Calculated by GEANT, it shows two trends. The wider component of the dashed line that dominates the edges of the spectrum is from interactions off carbon that, at first, do not deposit enough energy to trigger the CFDs. The central region shows the intrinsic position resolution for a scattered proton. The dotted line includes effects from timing resolutions (0.18 ns) of the signal and is fitted by a Gaussian distribution (blue line) with a standard deviation of 3 cm.

enough light in both PMTs to ensure proper CFD timing. For events where the signal amplitude is close to the CFD threshold, the CFD timing acts more like a leading edge discriminator and the output logic pulse timing is dependent on the signal amplitude. This effect is mostly canceled for the time-difference parameter used for the  $x$  position calibration, but is magnified by two for the  $\text{ToF}_n$  parameter and is in addition to the intrinsic CFD resolution. The CFD walk was measured to be less than 0.1 ns for signals less than 2 MeVee, and is nearly non-existent above.

## 4.2.2 MoNA X Resolution

For the  $x$  axis, the position is determined by the difference between the two timing parameters from each end of the module. As mentioned before (2.3.5), the conversion from the time-difference parameter to centimeters along the bar is nearly 8 cm/ns.



Using this slope, and the intrinsic time resolution detailed in the previous section, the intrinsic  $x$  axis resolution becomes  $\sigma = 1.5$  cm. This does not account for effects from neutrons interacting in the plastic. The GEANT simulation code calculates that the point of interaction of a neutron within the plastic is not always equal to the position of the deposited energy. This is true for reactions that release  $\gamma$  rays, since they can scatter significantly while exciting electrons that then create the scintillation light. For carbon-scattering interactions, the neutron's path can change dramatically before depositing energy by a second interaction.

Figure 4.10 shows the intrinsic resolution from the GEANT simulation (dashed line). The wider component of the dashed line that dominates the edges of the spectrum is from interactions that scatter before depositing enough energy to trigger the CFDs. The central region of the dashed line shows the intrinsic position resolution for a scattered proton. The dotted line includes effects from timing resolutions (1.5 cm) and is fitted by a Gaussian distribution (blue line) with a standard deviation of 3 cm.

Figure 4.11 shows the recorded distribution of cosmic-ray muons through MoNA bar B1 (second from the bottom), gated by 0–5 cm gates on the bars above and below it. The Gaussian fit in Figure 4.11 has a standard deviation of 2.2 cm. This resolution should be slightly less than the resolution for neutrons since muons have a negative charge and interact directly with the scintillating material.

These  $x$  resolution studies only apply for the first MoNA hit. Subsequent hits in MoNA could be highly scattered events from the first hit.

When MoNA was being assembled by undergraduate students, some of them performed a neutron shadow bar test to check the position resolution of an individual MoNA module. The data analysis was presented in a poster they made about their work on MoNA, and clearly identifies a  $x$  resolution of less than 3 cm.<sup>1</sup>

---

<sup>1</sup>Available through the MoNA Collaboration website <http://www.cord.edu/dept/physics/mona/>.

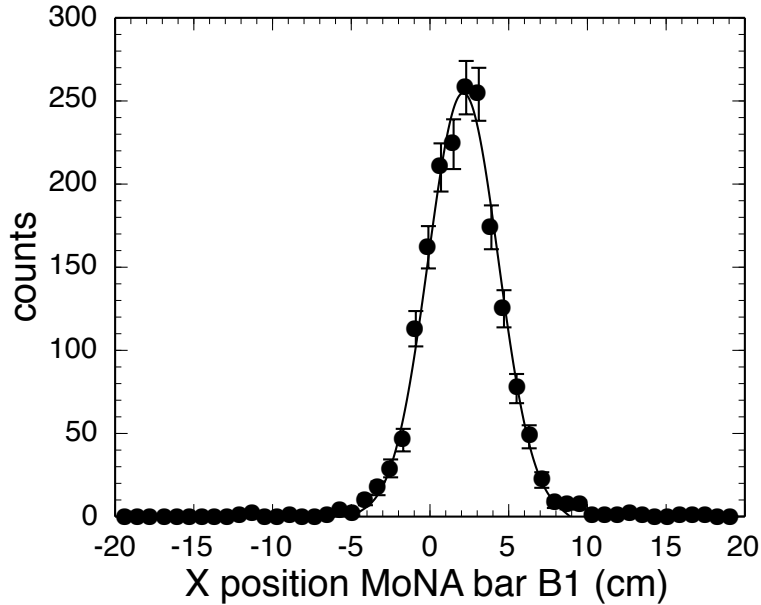


Figure 4.11: Calibrated  $x$  position spectrum of cosmic-ray muons paths in MoNA bar B1 gated above and below between 0 to 5 cm. The Gaussian fit has a standard deviation of 2.2 cm.

### 4.2.3 MoNA Y,Z Resolution

In both the longitudinal and vertical directions ( $z$  and  $y$ ) the interaction position of a neutron event can only be known to a precision of the depth and height of each MoNA bar; 10 cm. The  $y$  and  $z$  resolutions are simply  $\pm 5$  cm. Figure 4.12 shows the  $x,y$  distribution of neutrons in MoNA from the Coulomb excitation of  $^{11}\text{Be}$  on a gold target at 90 MeV/u. The effect of the quantized  $y$  position can be seen in lab angle ( $\theta$ ) of the neutrons displayed in Figure 4.13. Each subsequent spike in the  $\theta$  spectrum is due to neutrons striking the next row above or below. Figure 4.14 shows the same neutron data from the side of MoNA, through the nine layers. The increase in counts for the second layer is due to the fact that some highly-scattered protons can travel a couple centimeters and react in both the first and next layer.

The ST-mona simulation randomizes the actual position of the neutron hit within the bar while the reconstruction always uses the center of each bar and therefore, is quantized in 10 cm steps. The  $z$  axis uncertainty adds to the velocity uncertainty along with the time resolution.

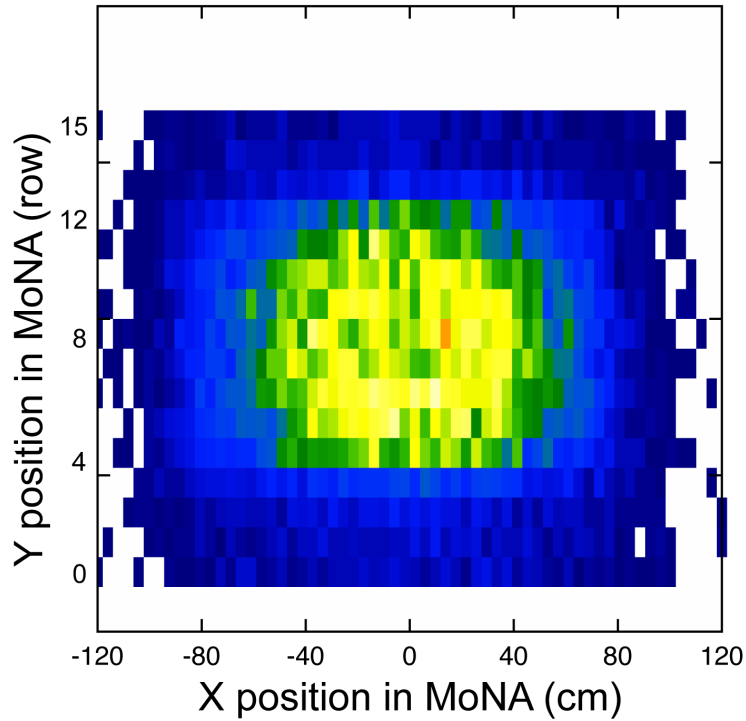


Figure 4.12: Plot of  $x$  versus  $y$  MoNA positions. The  $x$  direction is plotted in 4 cm bins, while the  $y$  position is quantized to the 10 cm bar height. A decrease in intensity can be seen for the lowest and highest rows caused by the finite opening (14 cm) of the Sweeper magnet's gap. The data is taken from experiment 03048; Coulomb excitation of  $^{11}\text{Be}$  on a gold target at 90 MeV/u.

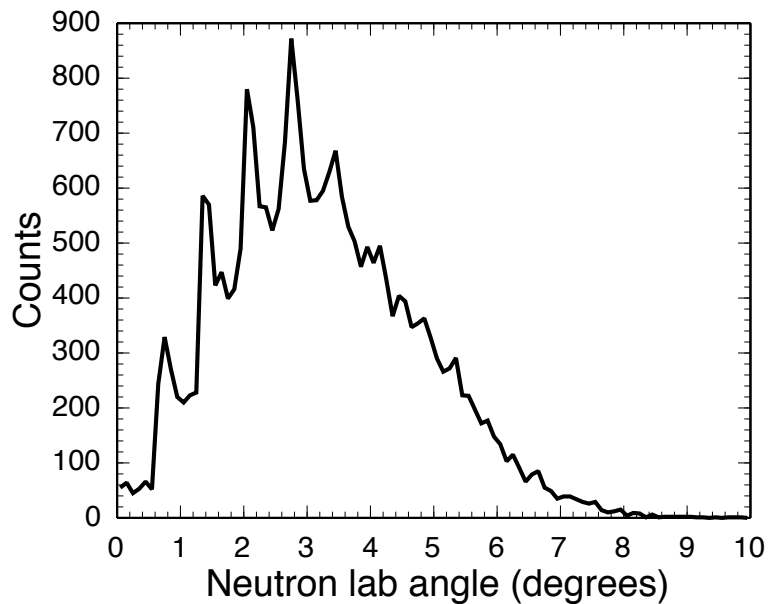


Figure 4.13: The neutron angle relative to the beam axis has spikes due to the quantized  $y$  parameter.

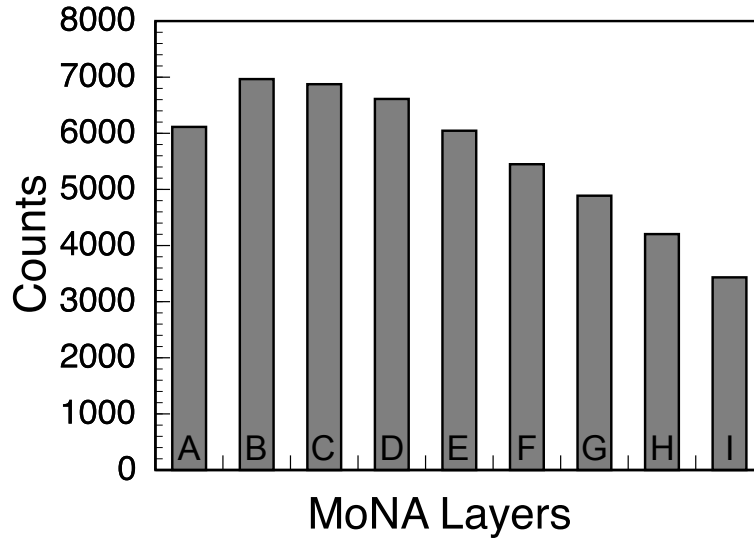


Figure 4.14: Plot of total hits in each MoNA layer for neutrons from experiment 03048.

The effective depth of each bar may be slightly less than the actual depth due to the “dead layer” effect. This effect is caused by the charged recoil particle from the neutron collision not having a long enough path within the bar to deposit sufficient light to trigger the CFD (with 10 mV threshold). For a 2 MeV proton recoil this “dead layer” is less than 3 mm. This effect is taken into account in the GEANT simulation and has little effect on the resolution of  $\pm 5$  cm for both the  $y$  and  $z$  directions. A neutron that reacts within the small dead layer of a MoNA bar and the recoil proton travels into the next layer, will record a wrong  $z$  position by no more than about 5.3 cm.

#### 4.2.4 MoNA Energy Resolution

The velocity ( $v_n$ ) and kinetic energy ( $K_n$ ) of the neutron are determined from the calculated reaction point within MoNA relative to the target and the neutron ToF<sub>n</sub>.

$$v_n = \sqrt{x^2 + y^2 + z^2} / \text{ToF}_n \quad (4.4)$$

$$K_n = \gamma m_n - m_n \quad (4.5)$$

Where  $\gamma$  is the relativistic Lorentz scaling factor  $1/(\sqrt{1 - (v_n^2/c^2)})$  such that the total energy  $E$  is equal to  $\gamma m_n$ .

The farther MoNA is stationed away from the target along the  $z$  axis, the better the velocity (and also energy) resolution becomes, because the  $\pm 5$  cm resolution for each bar in the  $z$  direction becomes a smaller percentage of the total distance. Resolution for various parameters for  $K_n = 70$  MeV (or 11 cm/ns) neutrons are listed in Table 4.2.

#### 4.2.5 Focal Plane Resolutions

The energy and angle of the charged particle fragments are reconstructed from the position and angle measured by the CRDCs in the Sweeper focal plane detector box. The position resolutions for these are measured using a steel mask with 0.5 mm holes. The recorded distributions are analyzed to determine the resolution in both the  $x$  and  $y$  directions. This is covered in more detail in Reference [47]. The CRDC resolutions are determined to be 1.6 mm. This corresponds to an angular resolution of 1.7 mrad when the CRDCs are separated by their maximum distance of 1.82 m.

#### 4.2.6 Simulated Resolution

By including all the individual detector resolutions and running ST-mona for different decay energies, the overall decay energy resolution for the system can be simulated.

Table 4.2: Resolutions, given as the standard deviations, for various MoNA parameters for  $K_n = 70$  MeV neutrons with MoNA positioned 8 m or 14 m from the target.

MoNA position	$\delta t$ (ns)	$\delta v$ (cm/ns)	$\delta\theta_y$ (mrad)	$\delta\theta_x$ (mrad)	$\delta K_n$ (MeV)
8 m	0.18	0.10	6.2	3.7	1.44
14 m	0.18	0.05	3.6	2.1	0.72

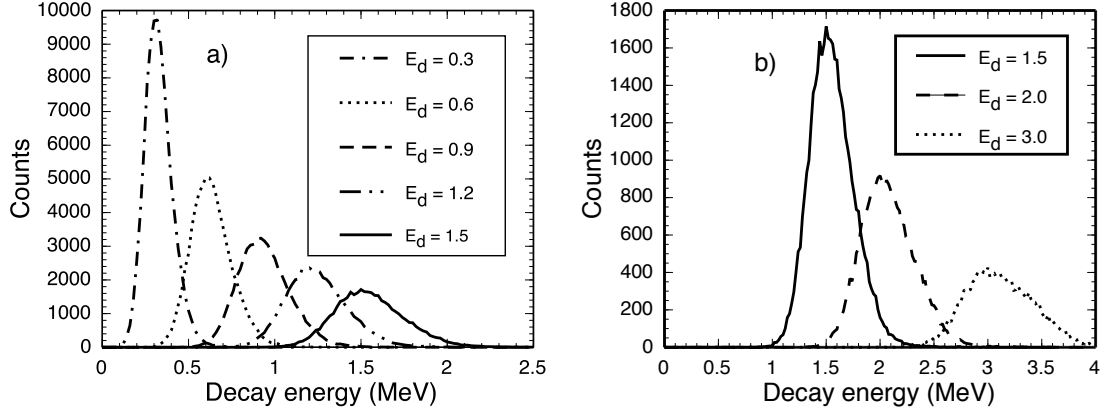


Figure 4.15: Each curve corresponds to a calculated decay energy using MoNA/Sweeper detector resolution and simulated data by ST-mona. Part a shows the lower energy curves and Part b shows the higher energies. For comparison, the curve from a decay energy of 1.5 MeV is a solid black line in both parts. The mass ratio for these simulations was 10:1 (as is the case for  $^{11}\text{Be}$  Coulomb breakup).

Figure 4.15 shows the decay energy resolution for neutrons from the Coulomb excitation of  $^{11}\text{Be}$  on a gold target and 90 MeV/u. Each curve was run with 100,000 fragment-neutron coincident events. The loss or total counts as the decay energy increases are due to acceptance losses (see Figure 4.28). The full width for a 900 keV decay energy is 400 keV. The distributions in Figure 4.15 were each fit by a Gaussian and the standard deviation of these fit are plotted in Figure 4.16. The final decay energy resolution depends on the distance to MoNA, the mass of the unbound nucleus, and the thickness of the reaction target. Other factors, including the TDC range used for the MoNA and the sweeper TDCs and the separation between the CRDCs in the Sweeper focal plane detector box also play a role, but are not as important. All these factors are simulated by ST-mona and can be adjusted on a case by case basis.

### 4.3 $^7\text{He}$ Resolution Test

To directly compare the simulated MoNA/Sweeper system using GEANT and ST-mona, a study of the known unbound resonance of the ground state of  $^7\text{He}$  was performed. A secondary  $^8\text{Li}$  beam was stripped of a proton by a  $^9\text{Be}$  reaction target

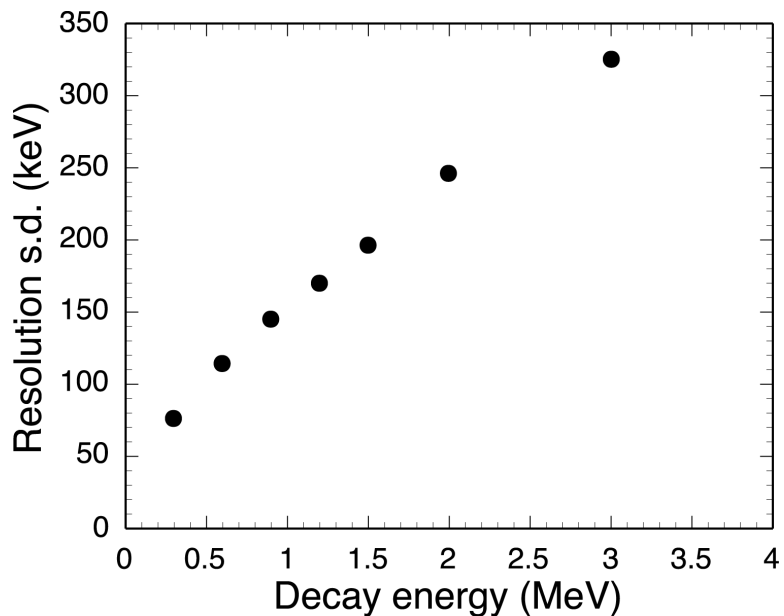


Figure 4.16: Standard deviations of the resolution curves shown in Figure 4.15 plotted versus the decay energy.

and  ${}^6\text{He} + n$  coincident events were recorded by MoNA and the Sweeper focal plane detectors. Inputting the experimentally determined resolutions into SIMPLE TRACK and adjusting the energy and width of the  ${}^7\text{He}$  resonance to match the data, the result is then compared with previous works.

### 4.3.1 Experimental Setup

A primary beam of  ${}^{18}\text{O}$  was accelerated through the Coupled Cyclotron Facility [31] at the NSCL to 120 MeV/u and impinged onto a production target of  ${}^9\text{Be}$  with a thickness of 3526 mg/cm<sup>2</sup>. The secondary beam of 99% pure  ${}^8\text{Li}$  with  $\pm 0.5\%$  momentum spread was selected from the resulting cocktail by the A1900 fragment separator [45] utilizing a 825 mg/cm<sup>2</sup> Al wedge installed at the dispersive plane, see Figure 3.1.

The secondary beam was directed into the N4 vault and onto a reaction target of  ${}^9\text{Be}$  with a thickness of 102 mg/cm<sup>2</sup> at the target position in front of the Sweeper magnet. The Sweeper magnet focal plane detectors were used to identify and count the

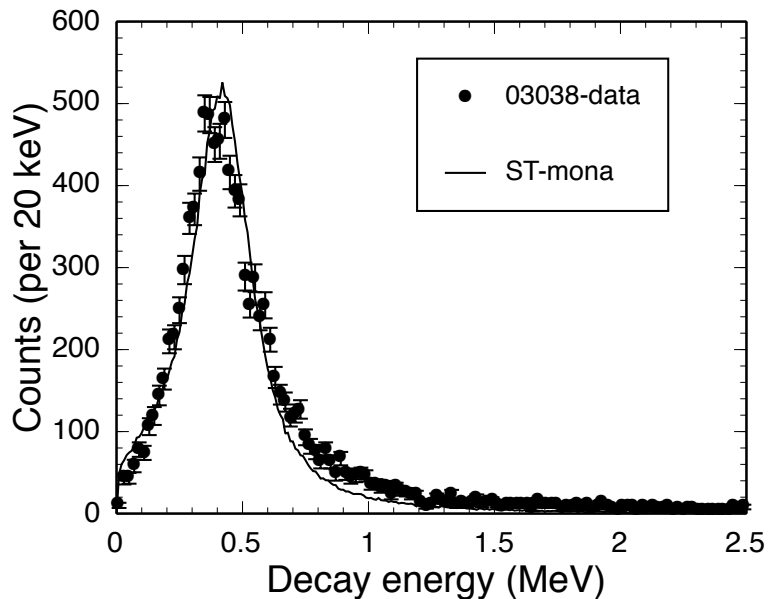


Figure 4.17: The  ${}^7\text{He}$  decay energy is fitted with a Breit-Wigner curve run through ST-mona with peak energy at 0.425 MeV and  $\Gamma$  width equal to 0.18 MeV.

charged-particle reaction products (see Figure 3.2). MoNA was positioned 8.2 meters from the reaction target.

### 4.3.2 Resolution Results

Figure 4.17 shows the best reduced- $\chi^2$  fit Breit-Wigner decay curve on top of the data (experiment 03038). The resonant energy is  $0.425 \pm 0.020$  MeV and the  $\Gamma$  width is  $0.18 \pm 0.04$  MeV. The uncertainties are calculated by the values needed to increase the reduced- $\chi^2$  fit by 1.0. The current results agree well with previous measurements from References [20, 57] that report the ground state resonance at  $0.43 \pm 0.02$  MeV and a width of  $0.16 \pm 0.03$  MeV. This confirms the individual resolutions used as an input for ST-mona and the ability of the simulation to reproduce data.

## 4.4 Measured MoNA/Sweeper System Efficiency

The Coulomb excitation of a nucleus from passing near another nucleus by exchanging a virtual photon [22] is well understood and calculable [23] and therefore, is an ideal



case to calibrate the efficiency of the MoNA/Sweeper setup. By Coulomb exciting  $^{11}\text{Be}$  above its neutron separation energy of 0.504 MeV with a gold target, the  $^{10}\text{Be}$  residue is deflected by the Sweeper Magnet into the focal plane detector box, and the released neutron travels straight into MoNA. The energy spectrum of virtual photons for a specific nucleus-target combination can be calculated for a given beam velocity. This spectrum, along with the incoming rate of  $^{11}\text{Be}$  can be used to calculate the number of neutrons produced. With the aid of the simulations, the acceptance of the system can be divided by the number of recorded neutron events to reveal the intrinsic efficiency of the MoNA detector.

#### 4.4.1 Experimental Setup

MoNA and the Sweeper Magnet were setup in the standard configuration with the reaction target just in front the Sweeper Magnet, and MoNA 8.2 meters down stream. The A1900 fragment separator with a 795 mg aluminum wedge at the dispersive image was used to purify the secondary beam of 90 MeV/u  $^{11}\text{Be}$  from a  $^{18}\text{O}$  primary beam at 120 MeV/u impinging on a 1692 mg/cm<sup>2</sup>  $^9\text{Be}$  production target. The Coulomb excitation occurs inside the 258 mg/cm<sup>2</sup> gold target, positioned in front of the Sweeper Magnet. Gold was chosen for its high proton number (79). A thick steel plate was installed inside the focal plane detector box to block the unreacted  $^{11}\text{Be}$ .

#### 4.4.2 Virtual Photon Calculations

As the positively charged projectile passes near the positively charged target nucleus they repel each other through the Coulomb force and exchange a virtual photon [21]. This photon excites the projectile through an E1 transition. Both the cross section for an E1 transition and the energy spectrum of the virtual photons can be calculated by the virtual photon method.

The virtual photon method uses the charge of the target nuclei ( $Z$ ) and speed

of the projectile ( $v$ ) to determine the number of virtual photons for a given target nucleus, shown is Figure 4.18. The formal calculation of the total breakup cross section is given by:

$$\frac{d\sigma_{\text{E1}}}{dE_\gamma} = \frac{1}{E_\gamma} n(\omega)_{\text{E1}} \sigma_\gamma^{\text{E1}} \quad (4.6)$$

The density ( $n(\omega)_{\text{E1}}$ ) of E1 photons is calculated by for relativistic speeds ( $\gamma \gg 1$ ) [23] with  $\alpha$  the fine structure constant and modified Bessel functions of order zero ( $K_0$ ), and one ( $K_1$ ):

$$n_{\text{E1}}(\omega) = \frac{2}{\pi} Z^2 \alpha \frac{c^2}{v^2} (\xi K_0 K_1 - \frac{v^2 \xi^2}{2c^2} (K_1^2 - K_0^2)) \quad (4.7)$$

as a function of the virtual photon's frequency,  $\omega$ , where ( $E_\gamma = \hbar\omega$ ); and:

$$\xi \cong \frac{\omega R}{\gamma v} \quad (4.8)$$

where  $R$  is the sum of the radii for the projectile ( $^{11}\text{Be}$ ) and the target ( $^{197}\text{Au}$ ) calculated by  $A^{1/3} \times 1.2$  fm and is set to 8 fm.

The cross section for the E1 photons:

$$\sigma_\gamma^{\text{E1}} = E_x \frac{dB(\text{E1})}{dE} \frac{9\hbar c}{16\pi^3} \quad (4.9)$$

is calculated with the transition probability  $dB(\text{E1})/dE$ :

$$\frac{dB(\text{E1})}{dE} = S \frac{e^{(2\kappa r_o)}}{1 + \kappa r_o} \frac{3\hbar^2 e^2 Z^2 \sqrt{E_s} (E_x - E_s)^{3/2}}{\pi^2 \mu A^2 E_x^4} \quad (4.10)$$

Here,  $\kappa = \sqrt{2\mu E_s}/\hbar$  where  $\mu$  is the reduced mass of residue and the neutron,  $E_s$  is the separation energy of  $^{11}\text{Be}$  (0.504 MeV). The radius of an appropriate square-well potential  $r_o$  [58] is set according to Reference [59] to 4.0 fm.  $S$  is the spectroscopic factor

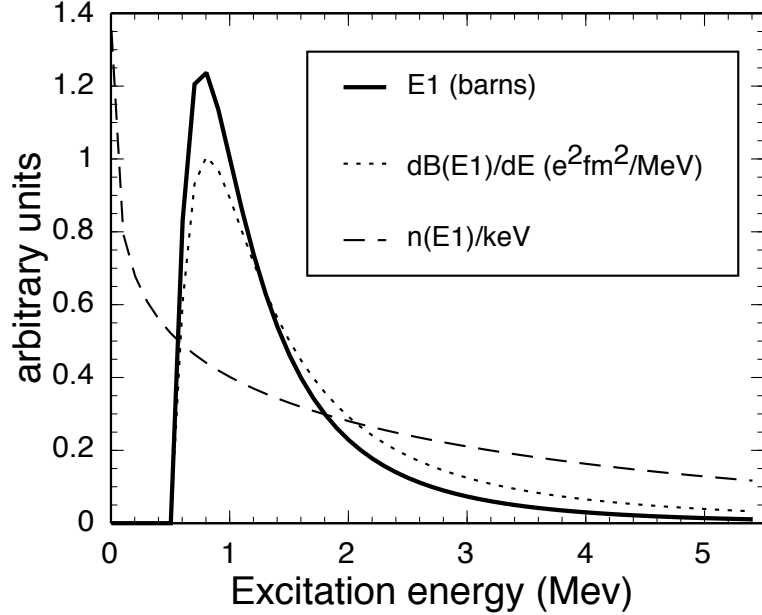


Figure 4.18: The calculated cross section for E1 excitation of  $^{11}\text{Be}$  from  $^{197}\text{Au}$  at 90 MeV/u, calculated from Equation 4.6, is shown by the solid curve. The dashed line is the number of virtual photons per keV as calculated by Equation 4.7. The dotted curve is the E1 transition probability as calculated from Equation 4.10.

Figure 4.18 shows the energy spectrum for the number ( $n_{\text{E1}}(\omega)$ ) of virtual photons (dashed line) from 90 MeV/u  $^{11}\text{Be}$  passing  $^{179}\text{Au}$  along with the transition probability (dotted) and the total cross section (solid). This calculation is nearly identical to Reference [60] for  $^{11}\text{Be}$  on a lead target at 40 MeV/u instead of a gold target at 90 MeV/u.

### 4.4.3 Experimental Comparison

The energy-dependent E1 cross section (solid line of Figure 4.18) can be included in ST-mona and the simulation and then compared to the data from experiment 03048. The isotopic identification of the  $^{10}\text{Be}$  residue is shown in Figure 4.19. The tail of the unreacted  $^{11}\text{Be}$  distribution tracks a large positive angle through the focal plane due to its high magnetic rigidity compared to the  $^{10}\text{Be}$  residues. Figure 4.20 shows various focal plane parameters used to restrict the input of the simulation and to ensure proper reconstruction. The comparison of the decay curve from ST-mona

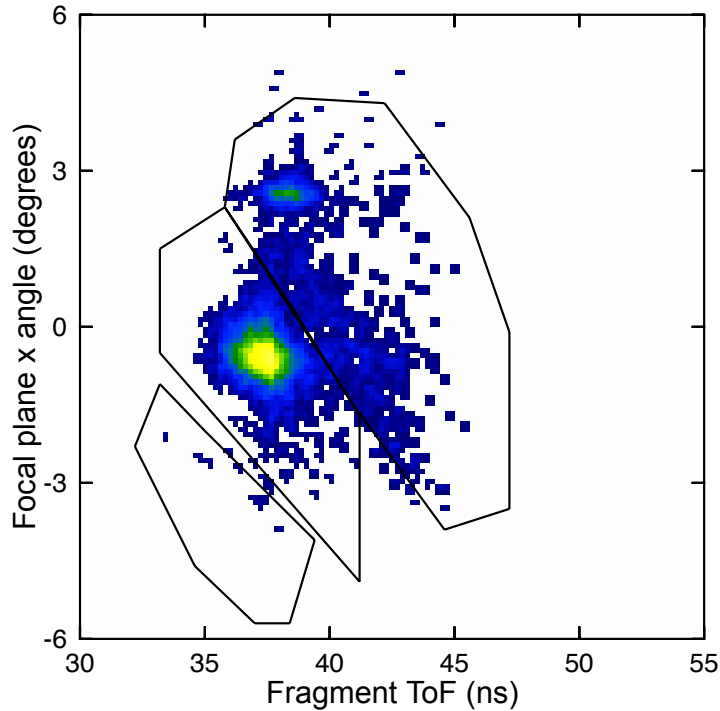


Figure 4.19: Isotopic identification by the method discussed in Section 3.4.2 using the dispersive angle in the focal plane ( $\theta_x$ ) and the fragment ToF. The gates select (from left to right)  ${}^9\text{Be}$ ,  ${}^{10}\text{Be}$ , and  ${}^{11}\text{Be}$ . For this experiment the separation did not require calculating  $\text{ToF}_{\text{rigid}}$ .

using the E1 cross section calculated through Equation 4.6 to the experimental data is shown in Figure 4.21. The close match between the experimental and simulated curves again confirms the correct simulation of the MoNA/Sweeper system.

#### 4.4.4 Second ${}^{11}\text{Be}$ Experiment for Efficiency Measurement

Unfortunately, the beam blocker installed for the 03048 experiment prevented an accurate measurement of the incoming rate, and therefore a second  ${}^{11}\text{Be}$  Coulomb breakup experiment was performed. The setup for 07503 was nearly identical except that the blocker was moved to accept a large portion of the distribution. In addition, the Sweeper magnet had since been tested to a higher magnetic setting, sufficient to deflect the unreacted beam into the focal plane detectors for a beam rate calibration. A disadvantage of 07503 was the limited acceptance of CRDC2. The drift voltage was

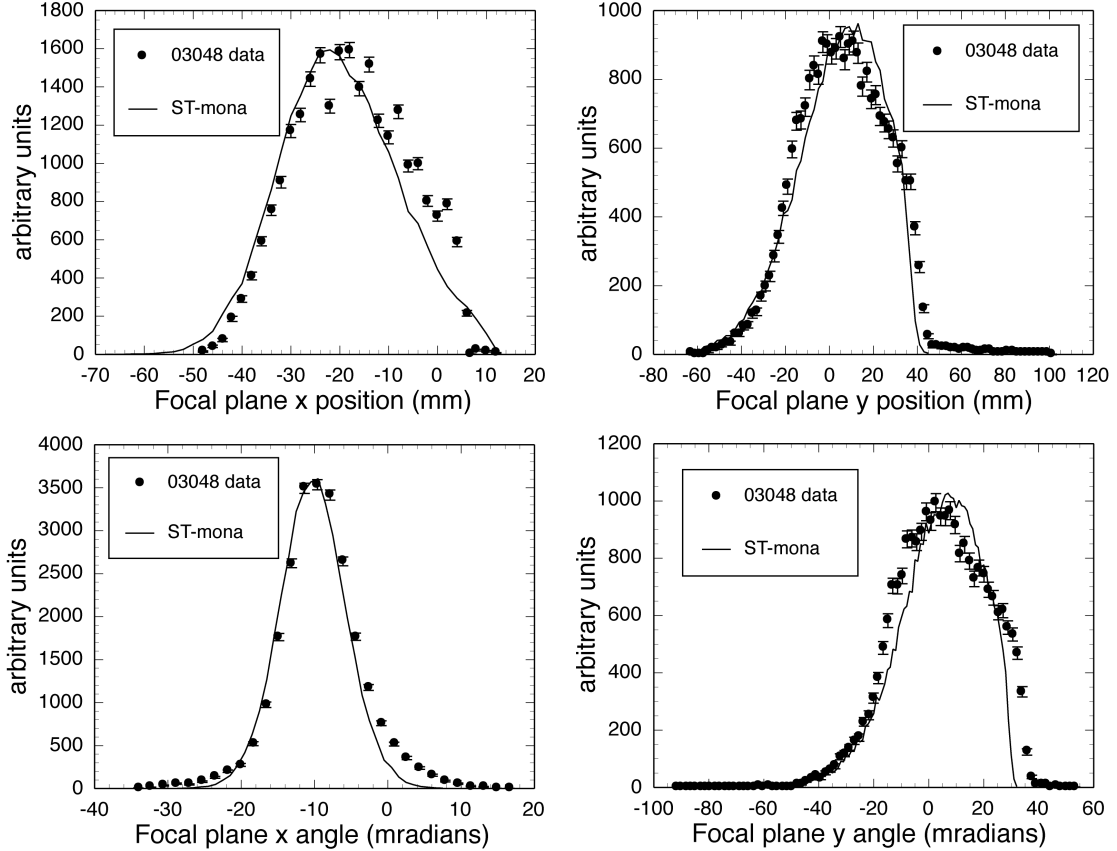


Figure 4.20: The relevant focal plane parameters for the  $^{11}\text{Be}$  Coulomb experiment, 03048, are fit by the ST-mona simulation code.

not large enough to collect all the electrons and this caused it to miss more than 50% of the events, and seriously cut into the distribution. Thus the analysis of the data was performed without CRDC2.

To identify the isotopes in this experiment, the ratio of light deposited into the four PMTs on the focal plane thin scintillator substituted for a second dispersive position measurement along with CRDC1. The identification plot is shown in Figure 4.22. The horizontal axis is the log of the ratio of light deposited in the two left PMTs to the two right PMTs. Here also, some of the unreacted  $^{11}\text{Be}$  reaches the focal plane and tracks a large positive angle through the detectors. Figure 4.23 shows the second gate on the dispersive light ratio from the thin scintillator and the fragment ToF parameter necessary to gate out the remaining  $^{11}\text{Be}$ .

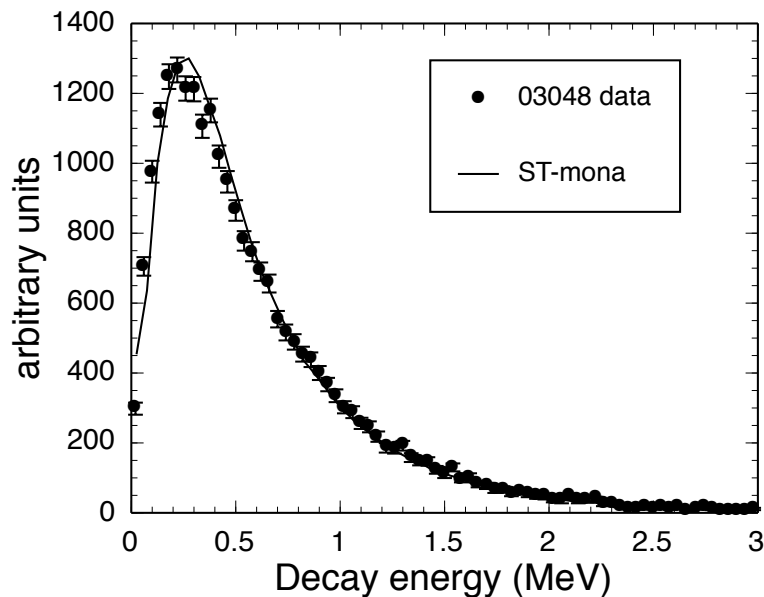


Figure 4.21: The decay energy data from 03048 is overlaid with the simulated decay energy curve after acceptance and resolution effects are added by ST-mona. The acceptance of the thin scintillator rejects almost all events where the  $^{10}\text{Be}$  exits the target at angles above 2.5 degrees. This has the effect of selecting almost purely Coulomb excitation reactions, as evident by the good agreement to just the E1 cross section of Equation 4.6.

The neutron time-of-flight ( $\text{ToF}_n$ ) is shown ungated and gated on  $^{10}\text{Be}$  in Figure 4.24. The gated spectrum (dotted line) is scaled up by a factor of two, to demonstrate the lack of background events in the coincident spectrum.

#### 4.4.5 Measured Incoming Rate

In order to calculate the system efficiency, the incoming rate of  $^{11}\text{Be}$  onto the target must be measured. This was done by calibrating the beam timing scintillator raw scaler rate to the Sweeper focal plane thin scintillator with the  $^{11}\text{Be}$  unreacted beam, tuned to travel straight to the middle of the focal plane thin scintillator. By taking into account the live-time of the production runs, the total number of incoming nuclei can be calculated and compared to raw rate of the beam line scintillator. The raw scaler rates between the focal plane thin scintillator and the beam line scintillator indicate they are over 99% coincident.

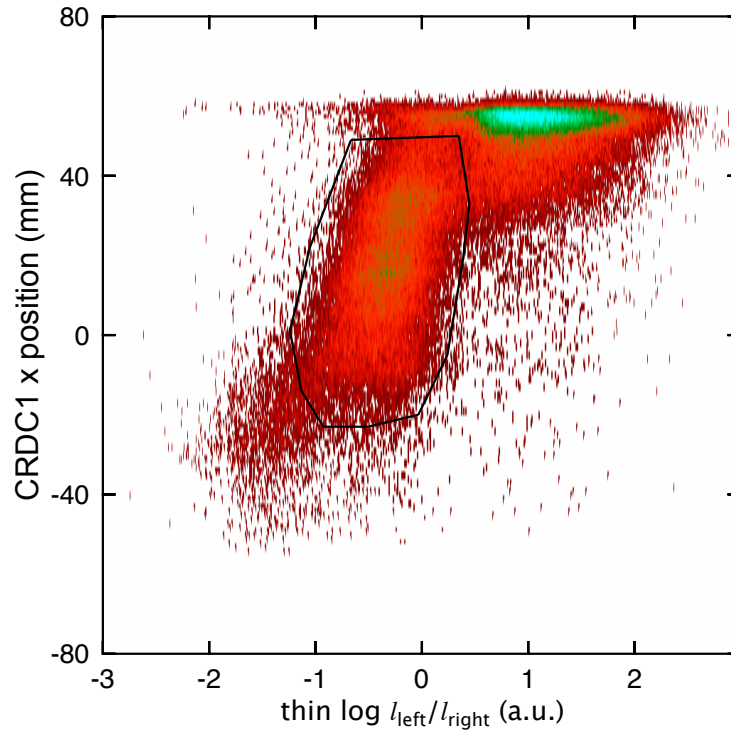


Figure 4.22: The ratio of light between the left and right sides of the thin scintillator is plotted against the dispersive position in CRDC1 to gate  $^{10}\text{Be}$  residues for the Coulomb breakup experiment 07503.

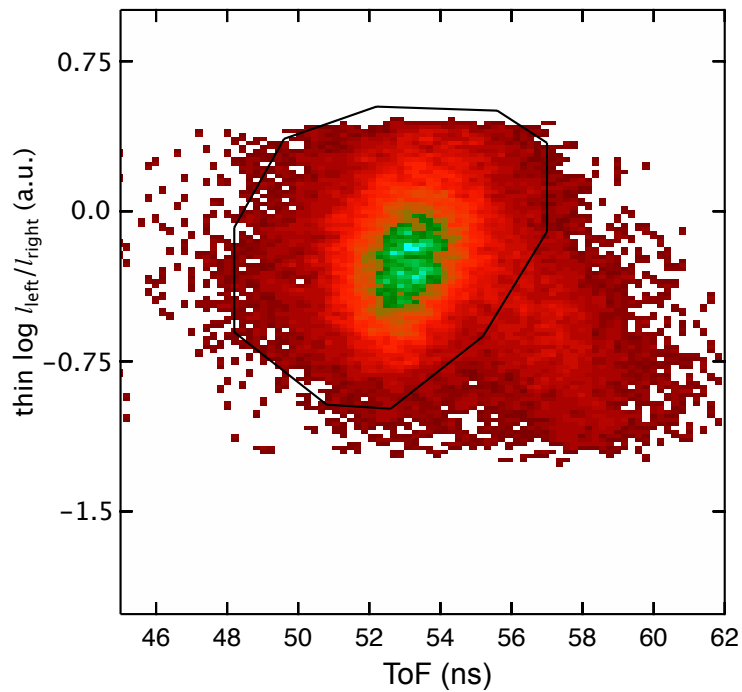


Figure 4.23: A second gate on ToF versus light ratio is used to reject a small contamination of unreacted  $^{11}\text{Be}$  that passes the first gate.

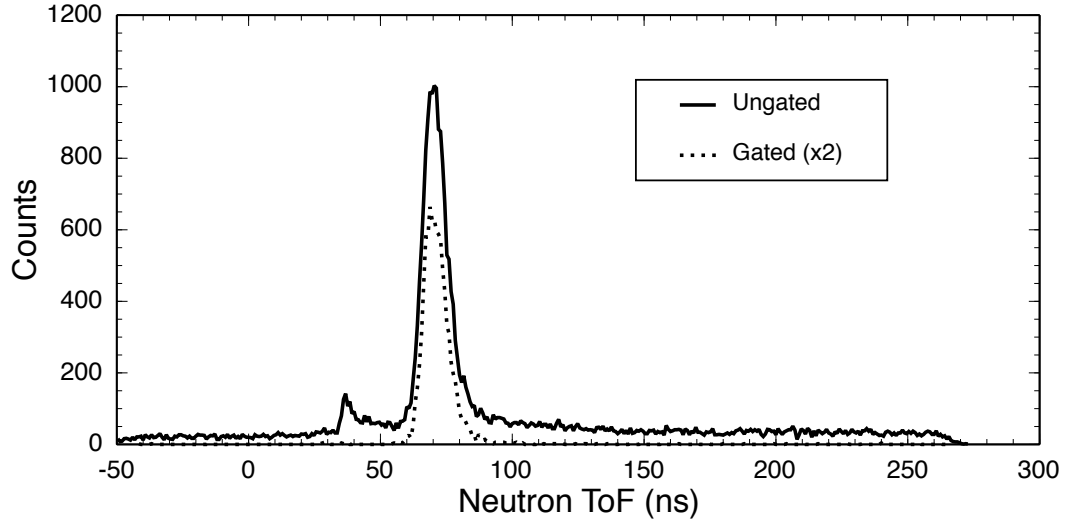


Figure 4.24: The background seen in the ungated  $\text{ToF}_n$  parameters nearly completely disappears when gated on a coincident  $^{10}\text{Be}$  residue. A smaller peak near 30 ns in the ungated spectrum is due to prompt  $\gamma$  rays induced by the beam on the reaction target.

#### 4.4.6 Detector Acceptances

Again ST-mona is used to simulate the focal plane acceptances and match to the focal plane parameters. Figure 4.25 shows the simulated curve with the focal plane data for experiment 07503. Data from CRDC2 is also shown to ensure the  $y$  angles and positions match the real distributions. It was not used in the calculation of the efficiency or isotopic identification, since fitting such a restrictive distribution leads to large uncertainties. The large angular spread needed to match the focal plane detectors causes some of the acceptance to be cut by the limit of the thin focal plane scintillator, which is  $\pm 200$  cm in both the  $x$  and  $y$  directions. This acceptance cut is illustrated in Figure 4.26 with simulated data and the  $\pm 200$  cm cuts are shown. This cut reduces the acceptance by 23%. Including the geometric acceptance of CRDC1 and the blocker, an additional 13% misses the focal plane detectors.

In addition to the acceptance cuts of the  $^{10}\text{Be}$  residue, the neutrons are collimated by the edge of the 0.25 inch steel neutron “window” at the back wall of the Sweeper Magnet vacuum cavity. This opening is 14 cm in the vertical ( $y$  axis) direction and



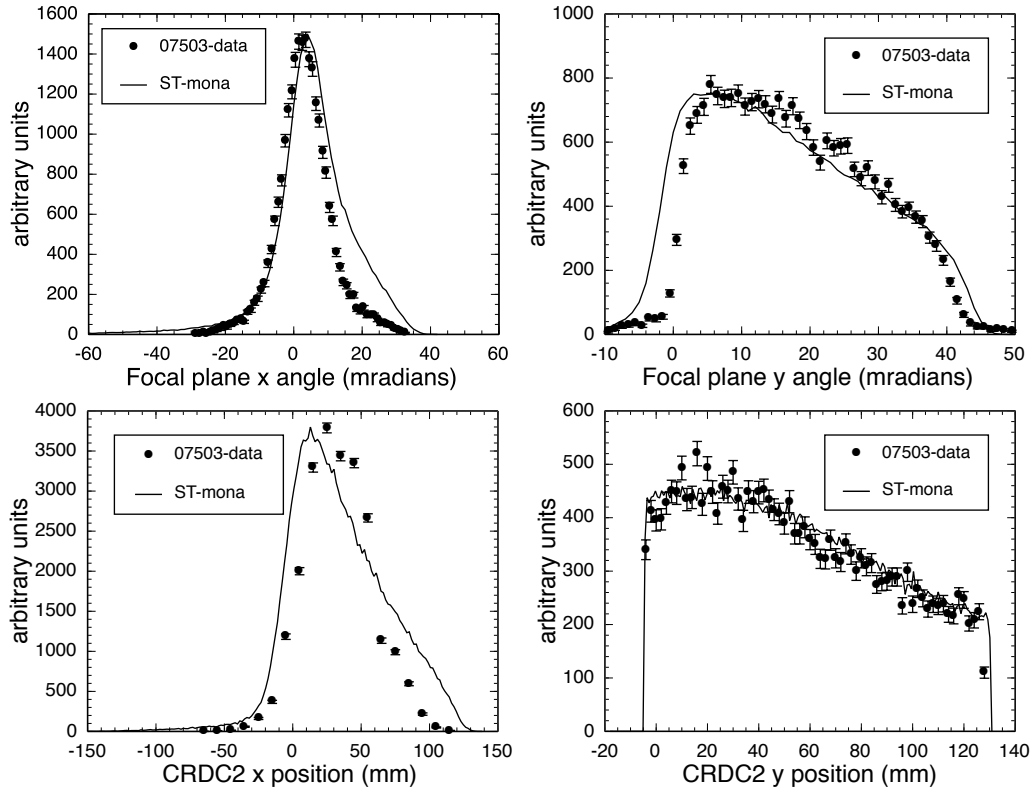


Figure 4.25: The important focal plane parameters are compared to ST-mona simulated events for experiment 07503. Due to the small acceptance of CRDC2 in the  $y$  direction, it was not used to gate  $^{10}\text{Be}$ .

cuts some of the neutrons that receive a strong vertical kick in the center of mass from the decay of excited  $^{11}\text{Be}$ . The thickness of the iron also reduces the overall neutron flux at MoNA by 4% due to scattering off iron nuclei at angles that miss MoNA. This 4% loss in acceptance must be taken into account when determining MoNA's intrinsic efficiency.

All these acceptances were programmed and accurately into the ST-mona simulation code and used to adjust the detected count for the system efficiency calculation. The MoNA acceptance as a function of decay energy is reflected in Figure 4.28. For higher decay energies the neutron acceptance dominates the losses, while for lower energies the acceptance is cut uniformly by the steel blocker and the broad  $y$  distribution and are not dependent on decay energy.

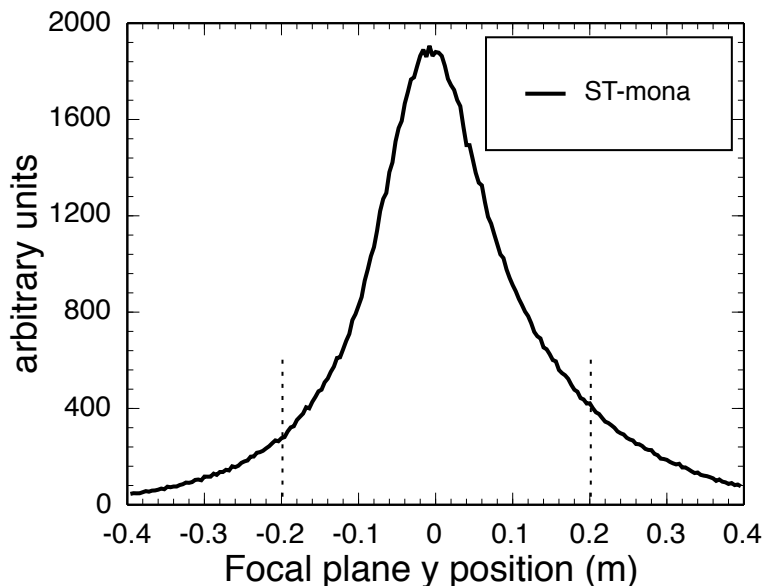


Figure 4.26: The  $y$  position at the focal plane thin scintillator is simulated by ST-mona. The acceptance in the vertical direction of the thin scintillator is  $\pm 0.2$  m (within the dotted lines).

#### 4.4.7 Simulation Input Parameters

Since ST-mona does not have a setting specifically for a Coulomb breakup reaction, the input parameters must be set to reproduce the measured detector distributions as accurately as possible. Figures 4.25 and 4.27 display the results of this effort. In order to properly fit the dispersive parameters in the focal plane, the incoming beam angle centroid was set off zero. This setting is confirmed by the  $x$  distribution in MoNA (Figure 4.27). The wide distribution in the  $y$  direction accounts for the largest acceptance cut in the focal plane detectors. By not using CRDC2, the precise values for the input parameters have less an effect on the final acceptance of the thin scintillator, as illustrated by Figure 4.26. The distributions for the  $x$  position and angle in the focal plane still did match exactly to the data as seen in the left panels of Figure 4.25, but they do not significantly effect the acceptance of the system.

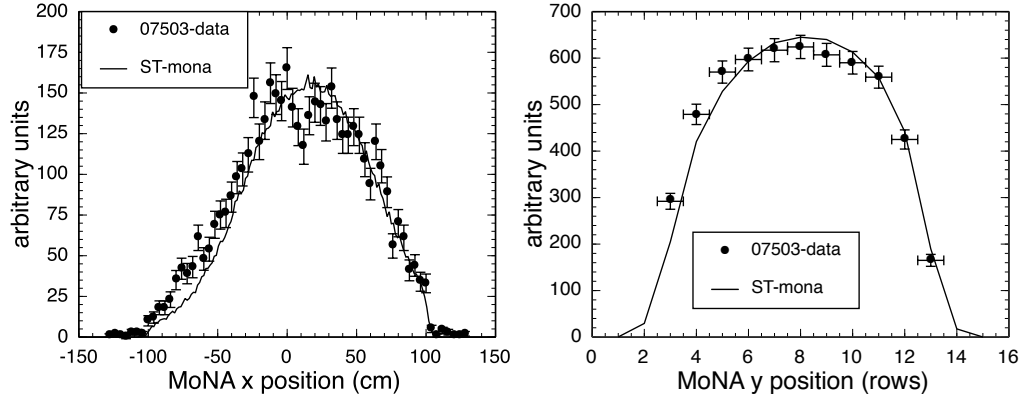


Figure 4.27: The  $x$  and  $y$  positions are simulated by ST-mona and agree well with the data from experiment 07503. The center of the  $x$  distribution at MoNA is not at zero and this agrees with the input angle required to simulate the focal plane data. The  $y$  distribution in MoNA is cut by the Sweeper gap of 14 cm, and agrees well with the angles used by the simulation.

#### 4.4.8 System Efficiency

Integrating the total E1 cross section ( $\sigma_{E1}$ ) curve from the virtual photon method (Equation 4.6) between 0 to 4.0 MeV, returns a cross section of 1.21 barns for a  $^{197}\text{Au}$  target. This number is used along with the target thickness ( $d$  in mass per area) to determine the reaction rate for the  $^{11}\text{Be}$  beam and thus, the number of neutrons ( $N_n$ ) available for the system to detect:

$$N_n = \sigma_{E1} N_{beam} (d/m) N_A \tau_{live} \epsilon_{\text{MoNA}} \epsilon_{\text{fp}} \eta_{\text{MoNA}} \eta_{\text{fp}} \quad (4.11)$$

where  $m$  is the molar mass of the target and  $N_A$  is Avagadro's number;  $\tau_{live}$  is the live-time ratio of the DAQ system.  $\epsilon_{\text{MoNA}}$ ,  $\epsilon_{\text{fp}}$ ,  $\eta_{\text{MoNA}}$ , and  $\eta_{\text{fp}}$  are the intrinsic efficiencies and geometric acceptances of MoNA and charged particle detectors that make up the total system efficiency.

During the production run,  $85.8 \times 10^6$   $^{11}\text{Be}$  nuclei passed through the gold target resulting in 71633  $^{10}\text{Be}$ -neutron pairs. A total of 9900, or 13.8%, were detected with the necessary detector combination to identify the  $^{10}\text{Be}$  residue and reconstruct the decay energy spectrum. When the live time ( $\tau_{live} = 47.45\%$ ) is accounted for, the total

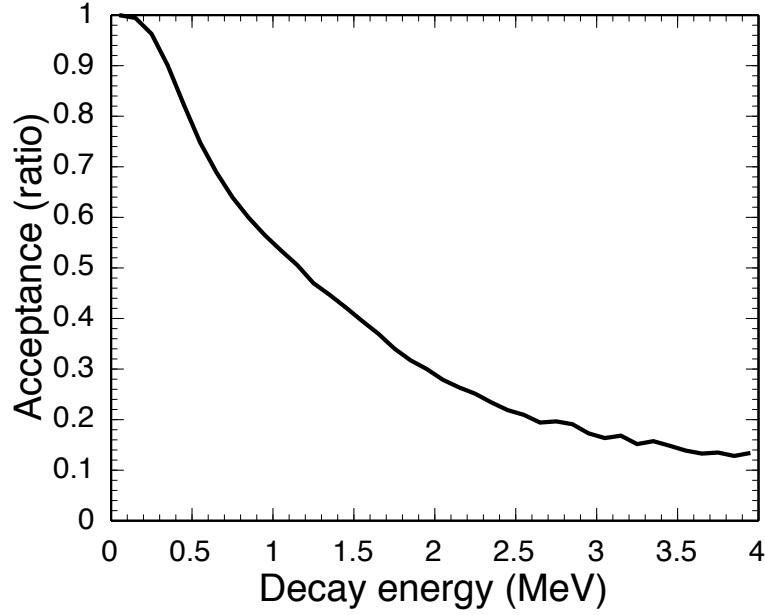


Figure 4.28: The acceptance of MoNA for the E1 excitation of  $^{11}\text{Be}$  to  $^{10}\text{Be} + n$  as a function of decay energy.

system efficiency is 29%. When acceptance cuts are taken into account the intrinsic efficiency of all the detectors ( $\epsilon_{\text{MoNA}}\epsilon_{\text{fp}}$ ) is calculated to be 68%. This includes the target and thin scintillators, focal plane CRDC1, and MoNA. Table 4.3 lists the intrinsic efficiencies and geometric acceptances for the focal plane detectors (as a whole) and MoNA. The uncertainties quoted for the are based on the simulation fit uncertainties, and the range of fits that still match the data from Figure 4.25.

This calculated intrinsic neutron efficiency of MoNA is  $73 \pm 6 \%$  is determined by measuring (or simulating) all other variables from Equation 4.11. The result is in range of the design goal of 70 % and consistent with the Geant simulations in Figure 4.7.

Table 4.3: Detection intrinsic efficiencies and geometric acceptances for the Sweeper focal plane detectors and MoNA for 07503.

$\tau_{\text{live}}$	$\epsilon_{\text{MoNA}}$	$\epsilon_{\text{fp}}$	$\eta_{\text{MoNA}}$	$\eta_{\text{fp}}$
47.45 %	$73.0 \pm 6\%$	$79.9 \pm 1\%$	$62.8 \pm 3\%$	$67.3 \pm 5\%$

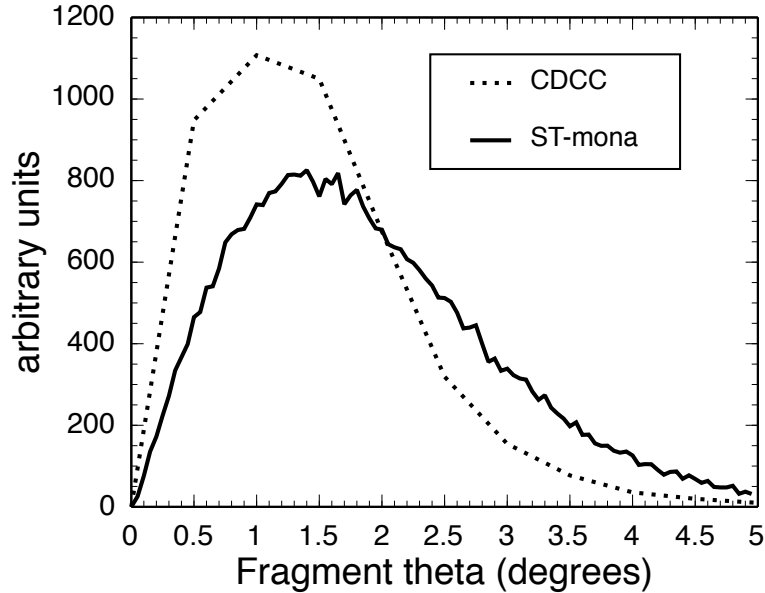


Figure 4.29: The fragment angle calculated through the CDCC method is compared to the angle simulated by ST-mona to match the focal plane data.

#### 4.4.9 CDCC Cross Section Calculations

An alternative to calculating the cross section with the virtual photon method is the continuum discretized coupled channels (CDCC) method [24, 25]. This method includes contributions and interferences between the many possible excitation levels, and the small nuclear (diffractive) decay channel is accounted for. The results of the calculation [61] are compared to the virtual photon decay curve and plotted in Figure 4.30. The total integrated cross section for the CDCC calculation is 1.26 barns (a little higher than the 1.21 barns calculated using the virtual photon method).

This method also yields a three dimensional differential cross section, that includes the angles and relative energies of the neutron and the  $^{10}\text{Be}$  residue in the lab frame. Figure 4.29 plots the CDCC calculated differential cross section as a function of  $^{10}\text{Be}$  angle, folded by the spread of the incoming beam used by ST-mona to fit the target-out focal plane data. The angle used by ST-mona to fit the 07503 data is also plotted. When this CDCC cross section curve from Figure 4.30 is put into ST-mona, the lower geometric acceptance of the higher decay energy events (above 2.0 MeV)

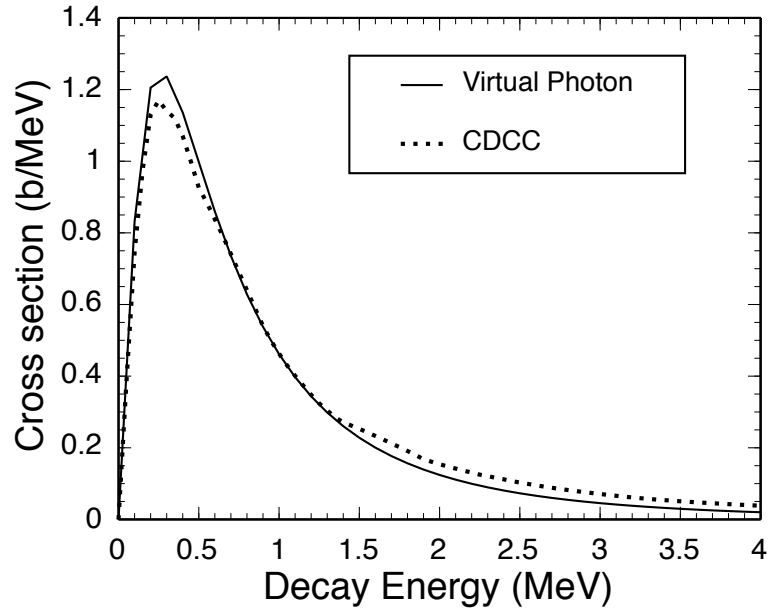


Figure 4.30: The calculated cross sections using the CDCC and virtual photon methods (described in the text). The distribution is slightly different, and the integrated cross section for the CDCC curve is 1.26 barns and 1.21 barns for the virtual photon cross section.

reduces the number of events (as per Figure 4.28) by more than the increase due to the total cross section. The resulting MoNA efficiency is higher than the virtual photon method results (78% compared to 73 %).

# Chapter 5

## One Neutron Knockout of $^{10}\text{Be}$

### 5.1 Introduction

A secondary beam of 99% pure  $^{10}\text{Be}$  (used for detector calibration of the  $^{12}\text{Be}$  experiment where the reaction residue is  $^{10}\text{Be}$ ) was utilized further to perform a measurement of the inclusive single-neutron knockout cross section to  $^9\text{Be}$  to compare with theory.

Using the shell model, the shell-level configuration and the spectroscopic factor for the valence nucleons can be calculated. These single-particle calculations, along with the eikonal reaction model [24], can calculate the cross section for the single-neutron knockout reaction of  $^{10}\text{Be}$  to  $^9\text{Be}$ . The eikonal approach assumes a sudden, straight-line trajectory for the nucleon's constituents and has been shown to be valid at the intermediate energies of radioactive beam production at NSCL [62]. These calculations do not include repulsive short-range 3-body nucleon-nucleon hard core interactions [63] and experimental cross sections rarely match the theoretical calculations for many systems where the short-range effects cannot be ignored. The ratio between the corresponding spectroscopic factors  $C^2S$  is known as the reduction factor ( $R_s$ ). The reduction factor represents a physically meaningful property when the shell model calculations remain a consistent reference for comparing a variety of

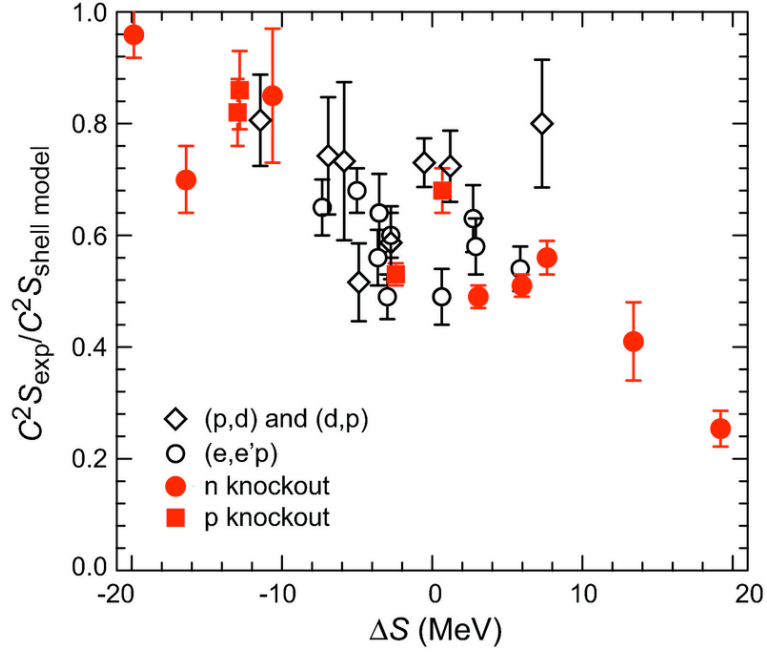


Figure 5.1: The reduction factor for a variety of different reactions is plotted versus the difference of nucleon separation energies ( $\Delta S$  equals  $S_n - S_p$  for neutron spectroscopic factors and  $S_p - S_n$  for protons). Figure reprinted from Reference [72], data originally compiled by Lee *et. al* [71] (see text for list of References).

different systems.  $R_s$  has been shown to follow a trend as a function of the difference between the neutron and proton separation energies  $\Delta S$  for proton and neutron knockout [64–68], (e,e'p) [69], and calcium transfer reactions [70], for energies ranging from 50-2000 MeV/u [71], see Figure 5.1.

This is the first measurement of the  $0p_{3/2}$  neutron knockout ( ${}^9\text{Be}({}^{10}\text{Be}, {}^9\text{Be})\text{X}$ ) in a neutron-rich nucleus and is the mirror process to the  $0p_{3/2}$  proton-knockout in neutron-deficient  ${}^9\text{C}$  [68]. This measurement will allow a comparison of single-particle abundances for the same  $0p_{3/2}$  shell at two extremes of bound nuclei.

## 5.2 Experimental Details

A primary beam of  ${}^{18}\text{O}$  was accelerated through the Coupled Cyclotron Facility at the NSCL [31] to 120 MeV/u and impinged onto a production target of  ${}^9\text{Be}$  with a thickness of 1222 mg/cm<sup>2</sup>. The secondary beam of 99% pure  ${}^{10}\text{Be}$  with  $\pm 0.5\%$



momentum spread was separated from the resulting production target cocktail by the A1900 fragment separator utilizing a 750 mg/cm<sup>2</sup> acrylic wedge installed at the dispersive plane, see Figure 3.1.

The <sup>10</sup>Be beam was directed into the N4 vault and onto a reaction target of <sup>9</sup>Be with a thickness of 102 mg/cm<sup>2</sup> at the target position in front of the Sweeper magnet. The Sweeper Magnet focal plane detectors were used to identify and count the reaction products.

The basic setup is shown in Figure 3.2, with the only change being that the blocker was moved out of the active range of the CRDCs. The focal plane acceptance was measured at nearly 18% momentum spread. Since the inclusive cross section was being measured, the electronics were run in Sweeper singles mode, thereby recording all events that reach the Sweeper focal plane.

## 5.3 Analysis

### 5.3.1 Cross Section Calculations

The reaction cross section was calculated with:

$$\sigma_{exp} = \frac{N_9}{(N_{beam}(d/m)N_A)} \quad (5.1)$$

where  $d/m$  is the target thickness in mass per area divided by its molar mass. With a 102 mg/cm<sup>2</sup> <sup>9</sup>Be target and  $N_A$  (Avogadro's number), the target nuclei per millibarn for this experiment was  $6.8 \times 10^{-6}$ . The number of <sup>9</sup>Be nuclei measured ( $N_9$ ) in the focal plane was adjusted for the efficiency and the incoming beam count ( $N_{beam}$ ) was adjusted for live time.

$n_{beam}$  was determined by using of a barium-fluoride (BaF) detector installed next to the production target in front of the A1900 (Figure 3.1). It is not inserted into the beam path but measures the radiation produced at the <sup>9</sup>Be production target. The

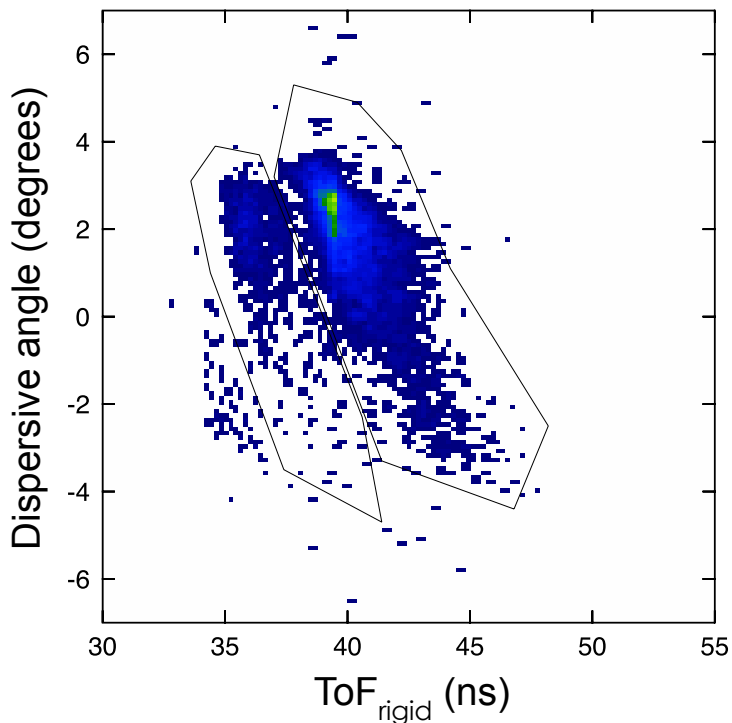


Figure 5.2: Dispersive ( $x$ ) angle versus fragment ToF. The two gates select  $^9\text{Be}$  (left) and  $^{10}\text{Be}$  (right).

count rate of the BaF is proportional to the primary oxygen beam intensity which, in turn, is proportional to the secondary beam rate of  $^{10}\text{Be}$ . The BaF scaler count, calibrated by deflecting the  $^{10}\text{Be}$  beam directly into the Sweeper focal plane thin scintillator, was used to determine the cross section for the production runs.

Even though the Sweeper magnet was set to accept the  $^9\text{Be}$ , some  $^{10}\text{Be}$  from a low momentum tail of the initial secondary beam distribution reaches the Sweeper focal plane. These two isotopes must be separated and identified as described in Section 3.4.2. Figure 5.2 shows the adjusted  $\text{ToF}_{\text{rigid}}$  versus the dispersive angle in the Sweeper focal plane detectors, clearly separating  $^{10}\text{Be}$  and  $^9\text{Be}$ .

While trying to optimize the Sweeper magnet, two different settings were recorded. The first setting at 3.1 Tm clearly accepts nearly the whole distribution of the  $^9\text{Be}$  residue as shown in Figure 5.3 but also accepted much more  $^{10}\text{Be}$  beam, requiring stricter limits on the incoming beam rate to avoid quenching the CRDCs (that should

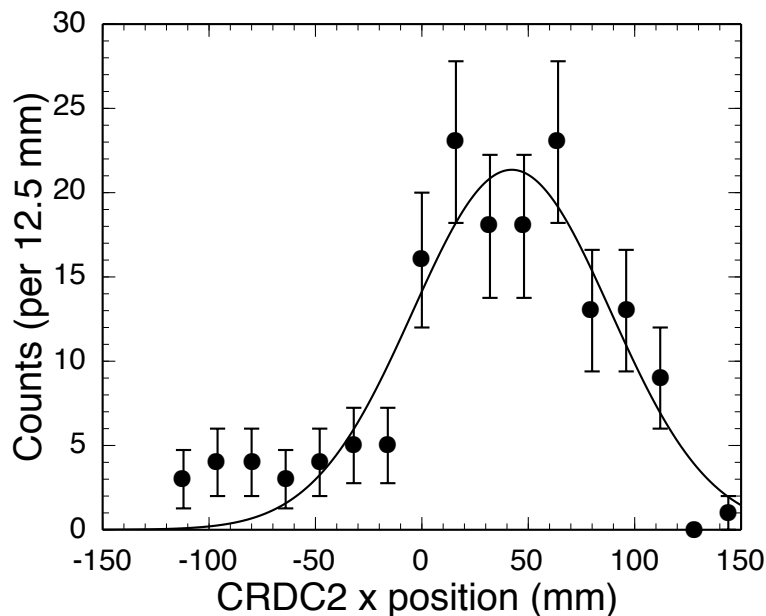


Figure 5.3: Sweeper focal plane acceptance of the  $^9\text{Be}$  residue from the  $1n$  knockout of  $^{10}\text{Be}$  for run 2114. Transmission for this run is nearly 100%, but the total count is much less than in run 2121.

not be run with more than  $10^4$  particles per second). The second setting at 2.9 Tm included less  $^{10}\text{Be}$  as shown in Figure 5.4, but cut 19% of the  $^9\text{Be}$  reactions.

The cross section measurement depends on determining the efficiency and geometric acceptance of the residue to properly scale the recorded counts. A tight beam focus in the dispersive direction ( $x$ ) caused a large spread in the  $y$  direction extending beyond the acceptance of CRDC2. A timing limit on the drift time for CRDC2 caused a cut at about 100 mm as shown in Figure 5.5. The total CRDC acceptance was  $67 \pm 6\%$  of the reacted  $^9\text{Be}$ , and was taken into account when calculating the cross section. The efficiency of all the focal plane detectors were measured by a calibration run of the unreacted  $^{10}\text{Be}$  deflected into the focal plane through both CRDCs. The measured charged particle efficiency of  $36 \pm 1\%$  was also factored into the cross section determination.

Because  $^9\text{Be}$  has no bound excited states, the inclusive cross section directly measured the total knockout cross section to the ground state including stripping and diffraction and a negligible Coulomb component. The cross sections for the single

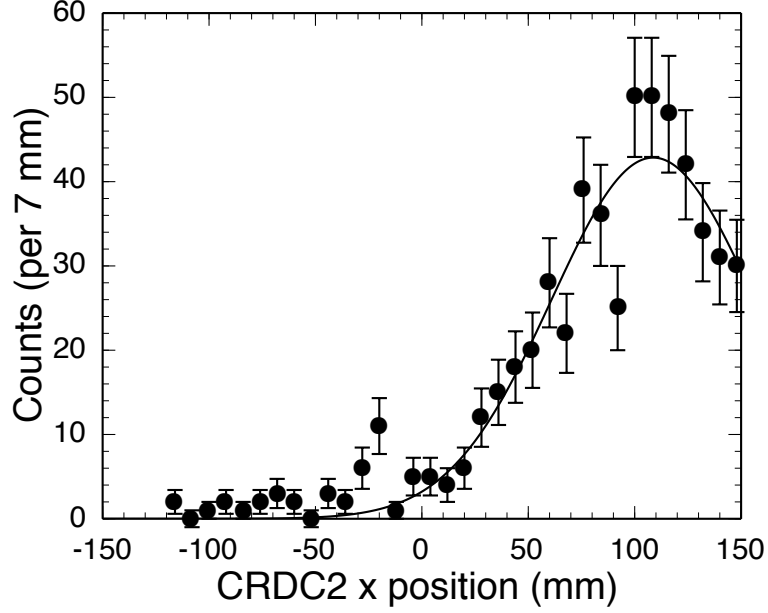


Figure 5.4: Sweeper focal plane acceptance of the  ${}^9\text{Be}$  residue from the 1n knockout of  ${}^{10}\text{Be}$  for the production run 2121 is cut by the horizontal edge of CRDC2 at 150 mm. Transmission is determined by integrating the Gaussian fit and is  $81\pm 4\%$ .

particle, stripping, and diffraction channels were calculated using the eikonal approach [73]. With the spectroscopic factor,  $C^2S$ , calculated using the WBP interaction in the p-shell [6], the total cross section can be determined by:

$$\sigma_{th} = (A/A - 1)C^2S(\sigma_{str} + \sigma_{dif} + \sigma_C) \quad (5.2)$$

where  $A$  is the nuclear mass of  ${}^{10}\text{Be}$ . Contributions from the wave function overlap or mismatch factor and the Coulomb cross section  $\sigma_C$ , were determined to be less than 1% and ignored in the present calculation [74]. The WBP shell-model interaction is specifically constructed for the  $0p1s0d$  shell including perturbative effects from the neighboring  $0s$  and  $0f1p$  shells.

The experimental cross section was calculated with the theoretical cross sections listed in Table 5.1 along with the calibrated BaF yield of incoming  ${}^{10}\text{Be}$  of  $5.5 \times 10^6$  and 569 recorded  ${}^9\text{Be}$  residues. Dividing out the charged particle detectors efficiencies ( $36\pm 1\%$ ) and geometric acceptances ( $67\pm 6\%$ ), and dividing by the  $102 \text{ mg/cm}^2$  Be

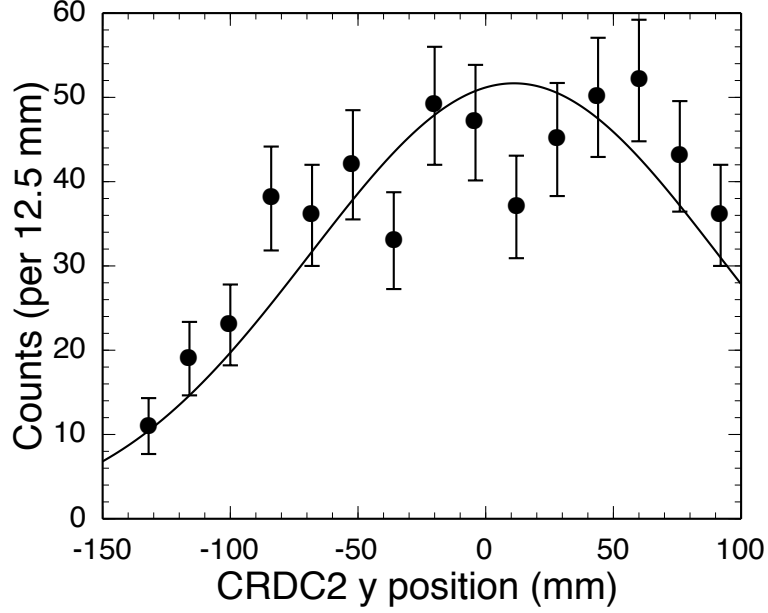


Figure 5.5: Sweeper focal plane acceptance of the  ${}^9\text{Be}$  residue from the  $1n$  knockout of  ${}^{10}\text{Be}$  for the production runs is cut by the vertical limit from the drift time of CRDC2 at 100 mm. Transmission is determined by integrating the Gaussian fit and is  $83\pm 4\%$ .

target thickness, yields  $68 \pm 7$  mb. The largest uncertainties are from the fits to the acceptance regions of CRDC2 and the low total count of  ${}^9\text{Be}$ . As displayed in Table 5.1 and plotted in Figure 5.6, this results in a reduction factor ( $R_s$ ) of  $0.66 \pm 0.07$ . This factor expresses the reduction of the single-particle occupancy due to short-range correlation effects.

Since the  $0p_{3/2}$  neutron knockout ( ${}^9\text{Be}({}^{10}\text{Be}, {}^9\text{Be})X$ ) is the mirror process to the proton-knockout in neutron-deficient  ${}^9\text{C}$  [68], this measurement allows a comparison of single-particle abundances for the same  $0p_{3/2}$  shell at two extremes of the chart of the nuclides. Not surprisingly, due to their near mirror relationship, there are several similarities shared by the  $({}^{10}\text{Be}, {}^9\text{Be})$  and  $({}^9\text{C}, {}^8\text{B})$  systems. Both reaction residues have no bound states, and their  $\Delta S$  values are both near -13 MeV,  $({}^9\text{C}, {}^8\text{B}) S_p - S_n$  equal to -12.96 MeV and  $({}^{10}\text{Be}, {}^9\text{Be}) S_n - S_p$  equal to -12.8 MeV. Comparing this new result with the  $0p_{3/2}$  proton-knockout of  ${}^9\text{C}$  near the proton drip line, reveals a decrease in the reduction factor from  $0.82 \pm 0.06$  to  $0.66 \pm 0.07$ . Some differences

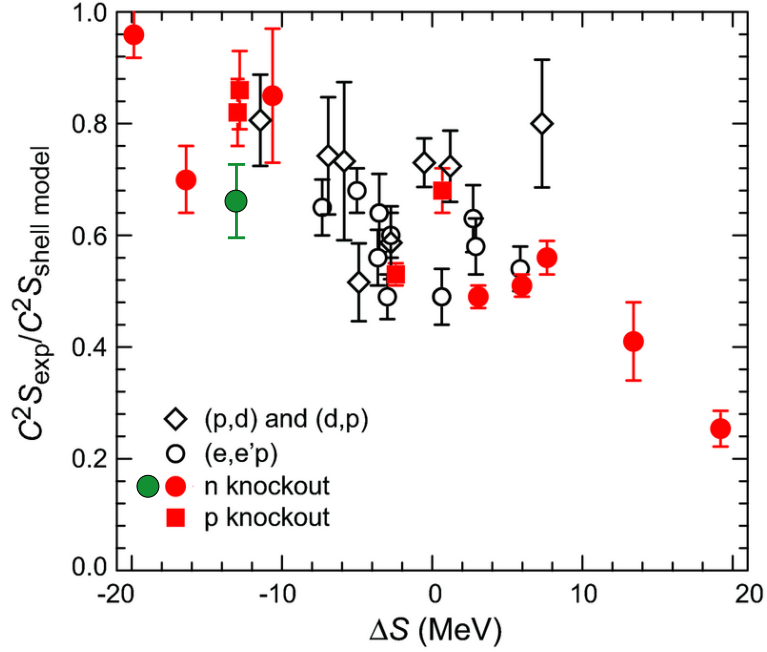


Figure 5.6: The reduction factor for a variety of different reactions is plotted versus the difference of nucleon separation energies ( $\Delta S$ ). The green point is added for the current measurement of the 1n knockout of  $^{10}\text{Be}$  at  $\Delta S = -12.8$  MeV.

between the two systems include the magnitude of the WBP shell-model spectroscopic factors, 0.94 protons for  $^9\text{C}$  compared to 2.45 neutrons for  $^{10}\text{Be}$ , where the extreme single-particle shell model would place 1 proton and 3 neutrons in the  $0p_{3/2}$  shell, respectively. Another difference is that  $^{10}\text{Be}$  is one neutron from removed a neutron halo state while the  $^8\text{B}$  residue is considered a proton halo [68]. The large effective radius of a halo nucleus could lead to less short-range correlations expressed by the reduction factor.

Table 5.1: Theoretical calculations for the 1n knockout and diffraction (nuclear) breakup channels of  $^{10}\text{Be}$  to the ground state of  $^9\text{Be}$ . The total theoretical cross section calculated per Equation 5.2 is compared to the current measurement to determine the reduction factor,  $R_s$ .

$\sigma_{str}$	$\sigma_{dif}$	$C^2 S$	$\sigma_{th}$	$\sigma_{exp}$	$R_s$
30.3 (mb)	8.0 (mb)	2.45	104 (mb)	$68 \pm 7$ (mb)	$0.66 \pm 0.07$

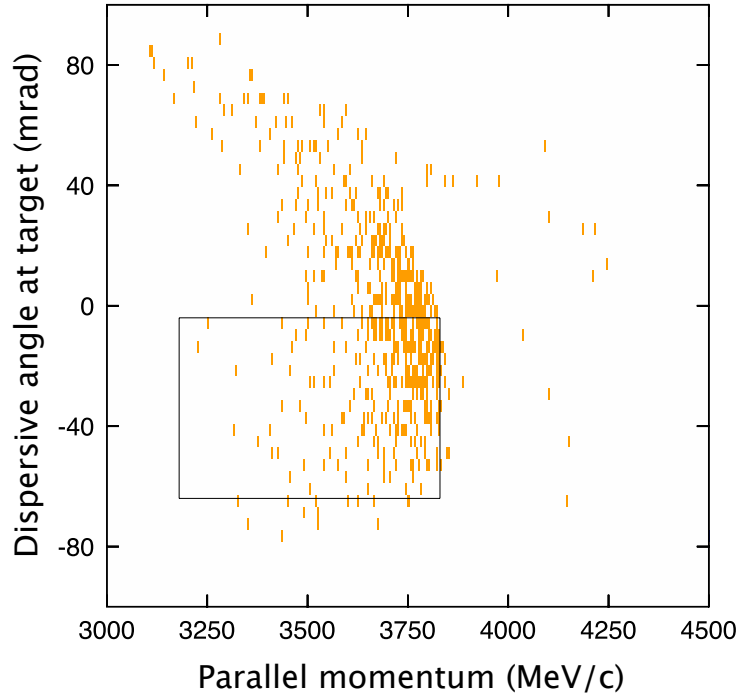


Figure 5.7: The reconstructed dispersive ( $x$ ) angle of the  ${}^9\text{Be}$  residue plotted versus the parallel momentum. The distribution is cut by the geometric acceptance of the Sweeper. The contour illustrates the gate used to recover a portion of the true distribution.

### 5.3.2 Parallel Momentum Comparisons

An additional check of the knockout process in the parallel momentum distribution. The angular momentum quantum number  $l$  of the stripped nucleon will determine the relative spread of residue's momentum distribution. A value of  $l$  equal to 1, corresponding to the stripping of a  $p$  shell nucleon, will result in a parallel momentum distribution that is wider than that for  $l = 0$ , but narrower than  $l = 2$ . This is due to an effect of the uncertainty principle where the larger spacial distribution of the lower angular momentum states will result in a smaller energy distribution. Since the ground state of  ${}^{10}\text{Be}$  is  $0^+$  and the state of  ${}^9\text{Be}$  is the  $3/2^-$  ground state, the momentum distribution of the residue should match well with a  $0p_{3/2}$  shell neutron.

Fragments that exit the target at large angles will strike the frame of the Sweeper magnet detector box, or miss the active region of the charged particle detectors, and

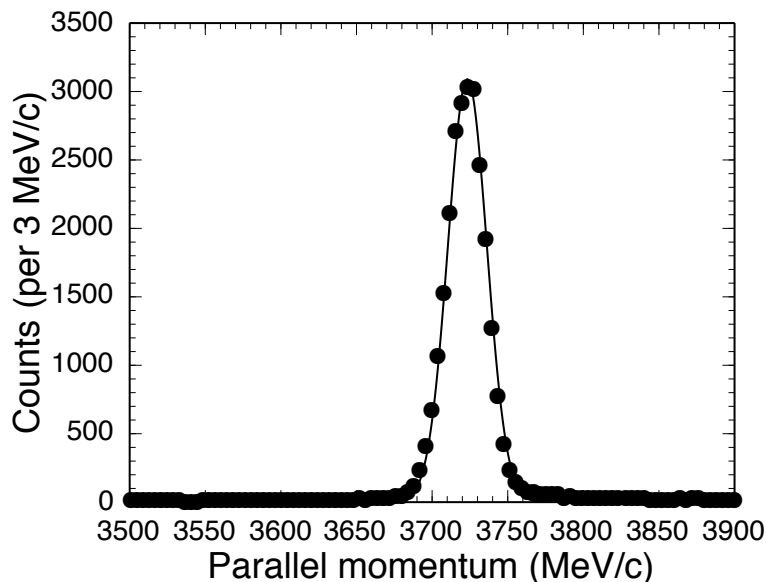


Figure 5.8: Parallel momentum distribution of the unreacted  $^{10}\text{Be}$  beam through the target. The Gaussian distribution, with a standard deviation of  $13.1 \pm 0.8$  MeV/c, was folded into the eikonal model momentum calculations used to fit the data in Figure 5.9.

fail to reach the thin scintillator trigger at the back of focal plane detector box. If this acceptance cut is correlated to the parallel momentum (which is true for the dispersive  $x$  plane), the resulting distribution will not accurately represent the actual distribution of the  $^9\text{Be}$  fragments exiting the target. Gating on a region within the angle-versus-momentum phase space that is not cut by the acceptance produces a distribution that accurately represents the true parallel momentum. Figure 5.4 shows how the dispersive position distribution is cut by the edge of CRDC2 for run 2121 with a Sweeper setting corresponding to a central  $B\rho$  of 2.9 Tm. Figure 5.7 shows the gate on reconstructed dispersive angle ( $\theta_x$ ) versus the reconstructed parallel momentum used to recover a portion of the true distribution of  $^9\text{Be}$ . Run 2114 taken with the Sweeper magnet rigidity set to 3.1 Tm did not cut the distribution of the  $^9\text{Be}$  residue as shown by Figure 5.3.

To increase the statistics the parallel momentum data from the higher rigidity setting (run 2114) was scaled and grouped with the gated lower rigidity data from run 2121. In order to compare theoretical distributions with the data, the theoretical



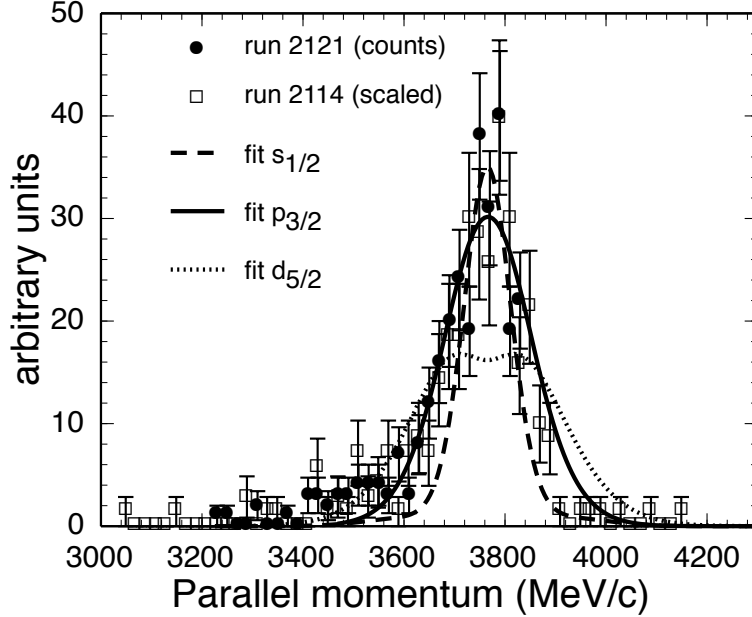


Figure 5.9: Parallel momentum distribution fitted with three theoretical curves. The data and error bars from run 2114 are scaled to match run 2121. The  $s$ ,  $p$ , and  $d$  wave knockout fits are individually scaled.

curve must be folded by with the parallel momentum of the incoming beam and boosted to the lab frame by multiplying the center-of-mass theoretical distribution by the Lorentz scaling factor (1.08) of the beam. The resulting distribution is then offset to match the centroid of the data. The unreacted beam's momentum distribution is plotted in Figure 5.8 and the Gaussian fit to this data has a standard deviation of  $13.1 \pm 0.8$  MeV/c.

Figure 5.9 shows the overlay with three parallel momentum calculations corresponding to the knockout from three different spin states used for the ground state of  $^{10}\text{Be}$ ,  $l = 0, 1$ , and 2 calculated by the eikonal approach [74]. The calculations for the  $l = 0$  and 2 curves were calculated as if the ground state of  $^{10}\text{Be}$  was from a  $s_{1/2}$  and  $d_{5/2}$  shell level, respectively, even though the  $^{10}\text{Be}$  ground state is known to be  $p_{3/2}$ . The parallel momentum of the  $^9\text{Be}$  residue is calculated from the reconstructed energy using the inverse transformation matrix described in Section 3.6.2. Since the magnitude is also a free parameter, the three curves were then each scaled independently to illustrate that the  $p_{3/2}$  curve is indeed the best match to the data. The

discrepancies at low momenta is common for these types of fits, and reported to be caused mostly by diffractive breakup [24].

## 5.4 Conclusions

The parallel momentum calculated by the eikonal reaction model successfully reproduces the expected  $0p_{3/2}$  neutron knockout distribution for the  ${}^9\text{Be}({}^{10}\text{Be}, {}^9\text{Be})\text{X}$  reaction. The calculated reduction factor of  $0.66 \pm 0.07$  is slightly less than other  $1n$  knockout systems near  $\Delta S = -13$  MeV. It is also slightly less than the mirror system of  $0p_{3/2}$  proton knockout in a neutron-deficient  ${}^9\text{C}$  nucleus with the  ${}^{12}\text{C}({}^9\text{C}, {}^8\text{B})\text{X}$  reaction [68], with  $R_s$  equal to  $0.82 \pm 0.06$ . To the extent that this difference is significant, the proton-halo property of  ${}^8\text{B}$  might lead to less short-range correlations. Some comparisons between  ${}^9\text{C}$ 's true mirror nucleus,  ${}^9\text{Li}$ , made in references [68, 75, 76] suggest other unexpected properties exist for  ${}^9\text{C}$ , which might account for the differences.

# Chapter 6

## Ground State of $^{12}\text{Be}$

### 6.1 Introduction

As discussed in the previous chapter, spectroscopic factors from knockout reactions are used as a diagnostic tool to study the single-particle occupancy of nuclear shells. The experiment described in the previous chapter focused on the  $0p_{3/2}$  shell level population of  $^{10}\text{Be}$ . The experiment detailed in this chapter is more complex and explores the relative single-particle occupancies of a few different shell levels comprising the ground state of  $^{12}\text{Be}$ .

$^{12}\text{Be}$  is at the neutron drip line and the supposedly magic number  $N = 8$ . This shell gap is known to break down away from the valley of stability at the neutron halo nucleus  $^{11}\text{Be}$  that has a  $1/2^+$  ( $1s_{1/2}$ ) ground state [19], while the order for filling shell levels for stable nuclei would place the seventh neutron in the  $0p_{1/2}$  shell level. For  $^{11}\text{Be}$ , this  $1/2^-$  state is at an excitation energy of 320 keV. The ground state of  $^{12}\text{Be}$  is mostly comprised of an admixture of different two-neutron wave functions above a  $^{10}\text{Be}$  core. Previous experiments have quantified the wave function as containing about 25%  $(1s_{1/2})^2$  and about 25%  $(0p_{1/2})^2$  paired-neutron configurations [29, 30], while the remaining 50% is thought to be mostly in the  $(0d_{5/2})^2$  configuration [77, 78]. The strong component of the  $(0d_{5/2})^2$  wave function is thought to indicate correlations

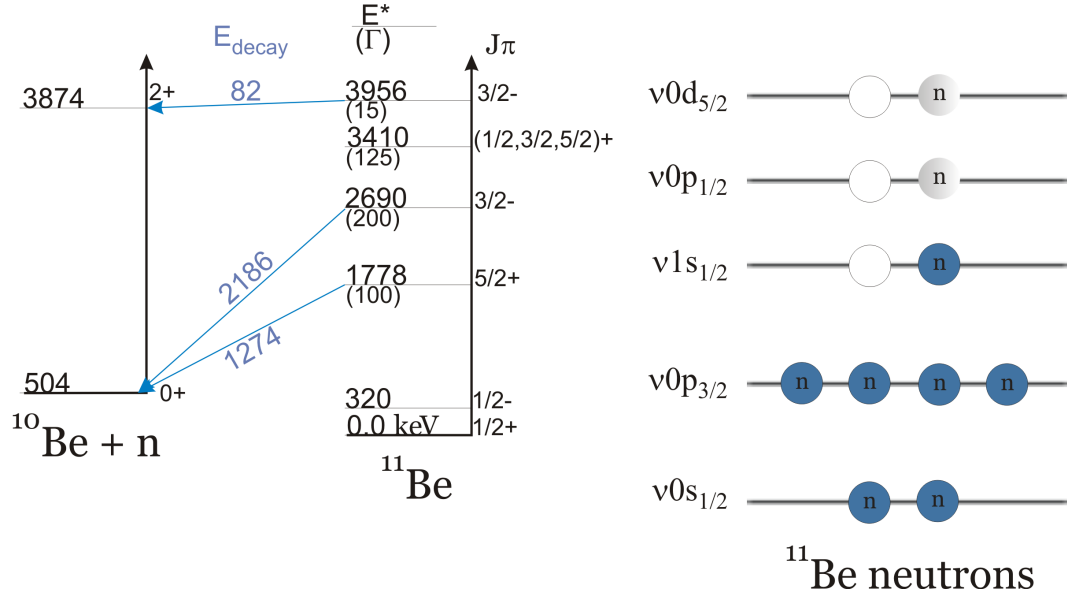


Figure 6.1: The diagram shows the simple shell level layout for  $^{11}\text{Be}$  after stripping of one valence neutron (open circles) from  $^{12}\text{Be}$ . The first three levels in  $^{11}\text{Be}$  correspond to these single-particle states [19, 80]. The resonant neutron-decay channels to  $^{10}\text{Be}$  seen in the current study are highlighted.

from nucleon pairing as discussed in [79] and coupling to vibrational modes [77].

The study is further complicated by the nature of the possible  $^{11}\text{Be}$  states after the 1n knockout of  $^{12}\text{Be}$ . If a  $1s_{1/2}$  neutron is stripped from the  $(1s_{1/2})^2$  configuration, the residue is in the ground state of  $^{11}\text{Be}$ . Stripping from the  $(0p_{1/2})^2$  configuration leads to a decay via  $\gamma$ -ray emission of 320 keV. Stripping from the  $(0d_{5/2})^2$  configuration leads to a  $5/2^+$  unbound state in  $^{11}\text{Be}$  at 1.78 MeV. Figure 6.1 illustrates the various single-particle wave function components and their decay paths for the stripping of one neutron.

There is also the possibility to knockout one of the non-valence neutrons of  $^{12}\text{Be}$  leading to an excited hole-state in  $^{11}\text{Be}$ . The  $0p_{3/2}$  shell level, with four neutrons, is a good candidate for just such a reaction. The possibilities for exciting states not coupled strongly to a single-particle state above  $^{10}\text{Be}$  or a hole from the  $^{12}\text{Be}$  ground state wave function are limited and not expected to contribute greatly to the  $^{10}\text{Be} + n$  coincident data. Although, there may be core-excited configurations that lead to the observed states in  $^{11}\text{Be}$  through 1n stripping that do not involve the paired-neutron

Table 6.1: Summary of results from previous studies of the ground state wave function of  $^{12}\text{Be}$ . The first experiment [29] could not measure neutron unbound states, while results from the second experiment [30] agree well with the first for the bound states.

Ref.	$E_{\text{beam}}$	$^{11}\text{Be } j^\pi$	E (MeV)	$S_{\text{exp}}$
[29]	78 MeV/u	$1/2^+$	0.0	$0.53 \pm 0.13$
[29]	78 MeV/u	$1/2^-$	0.32	$0.45 \pm 0.12$
[30]	39.3 MeV/u	$1/2^+$	0.0	$0.56 \pm 0.18$
[30]	39.3 MeV/u	$1/2^-$	0.32	$0.44 \pm 0.08$
[30]	39.3 MeV/u	$5/2^+$	1.78	$0.48 \pm 0.06$

configurations in the unperturbed single-particle shell model description of an inert core of  $^{10}\text{Be}$  in  $^{12}\text{Be}$ .

Yet another decay mode is through diffractive breakup of the  $^{12}\text{Be}$  nucleus [28,56] as it passes through the wave function of the  $^9\text{Be}$  target leading to  $^{10}\text{Be}$  and two neutrons in the decay channel, since  $^{11}\text{Be}$  is only bound by 0.5 MeV and the energy imparted to the nucleus can be well above that. This mode of decay has a non-resonant structure and forms a broad background below the resonant peaks in the  $^{10}\text{Be} + n$  decay energy spectrum.

Table 6.1 displays the single-particle spectroscopic factors from the previous two experiments (References [29] and [30]) studying the admixture of three paired-neutron shell levels in  $^{12}\text{Be}$  by neutron knockout to  $^{11}\text{Be}$ . The values for  $S_{\text{exp}}$  quoted in the table are the spectroscopic factors from  $^{12}\text{Be}$  1n knockout to the corresponding  $^{11}\text{Be}$  states (third column) and not necessarily only from the paired-neutron states in the  $^{12}\text{Be}$  wave function. These  $^{11}\text{Be}$  states can be populated by 1n knockout reactions that may include configurations that are not simply paired neutrons above an inert  $^{10}\text{Be}$  core, but can contribute to the cross section to these states [78].

While the first experiment [29] could only measure cross sections to the two bound states, both experiments agree that roughly 50% of the total occupancy of the assumed two valence neutrons above a  $^{10}\text{Be}$  core are in configurations other than the  $(1s_{1/2})^2$  or  $(0p_{1/2})^2$  for the ground state  $^{12}\text{Be}$ . The second experiment [30] did not find all of

the remaining missing single-particle strength in the  $5/2^+$  spectroscopic factor with roughly 25% still missing. The result suggests equal parts for all three paired-neutron configurations. The current experiment attempts to confirm the results of the second experiment at over twice the beam energy and with the superior neutron efficiency of MoNA, compared to the DeMoN array used in [30].

## 6.2 Experimental Details

A primary beam of  $^{18}\text{O}$  was accelerated through the Coupled Cyclotron Facility at the NSCL to 120 MeV/u and impinged onto a production target of  $^9\text{Be}$  with a thickness of 1081 mg/cm<sup>2</sup>. The secondary beam of 99% pure  $^{12}\text{Be}$  with  $\pm 0.5\%$  momentum spread was separated from the resulting cocktail by the A1900 fragment separator utilizing a 750 mg/cm<sup>2</sup> arcylic wedge installed at the dispersive plane, see Figure 3.1.

The secondary beam was directed into the N4 vault and onto a reaction target of  $^9\text{Be}$  with a thickness of 102 mg/cm<sup>2</sup> at the target position in front of the Sweeper magnet. The Sweeper magnet focal plane detectors were used to identify and count the charged-particle reaction products. A thick steel plate was installed in front of the first CRDC to protect the CRDCs from the high rate of the secondary beam (see Figure 3.2). The rigidity of the  $^{12}\text{Be}$  was too high to deflect it into the focal plane directly for a rate calibration and thus, all measurements for the cross section to different decay channels are taken relative to each other and calculated by comparison to previous measurements of Ref. [30].

Since the “common stop” signal used in the  $^{12}\text{Be}$  experiment was the focal plane thin plastic  $dE$  detector for all MoNA TDCs and Sweeper channels, instead of the target scintillator, the ToF measurement of the neutron was calculated by subtracting the target scintillator time from the average left and right MoNA times. This additional step adds to the uncertainty of the ToF measurement. Using the resolution of the thin plastic  $dE$  scintillator ( $\sigma = 0.2$  ns), yields a total of standard deviation = 0.4 ns

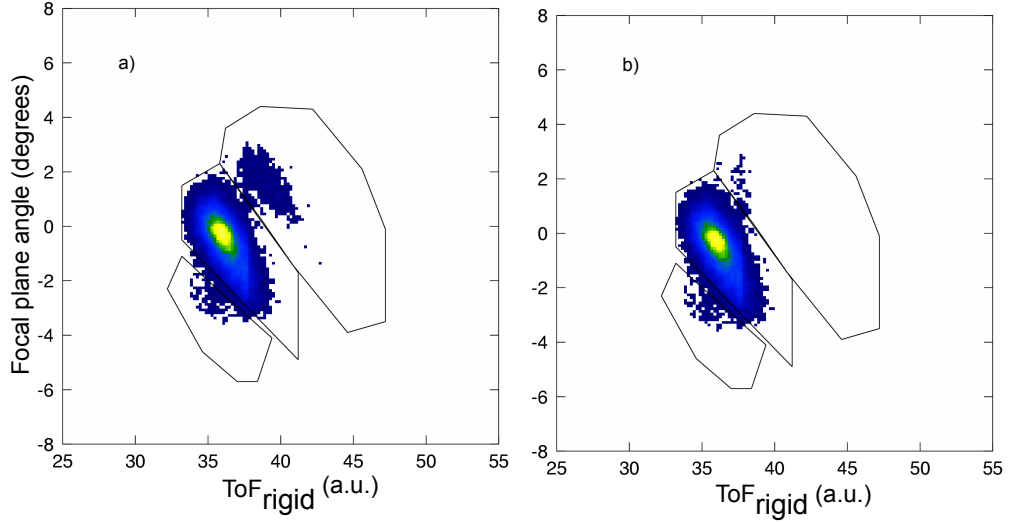


Figure 6.2: Isotope identification with a two dimensional gate. a) Gates are applied to select (from left to right)  $^9\text{Be}$ ,  $^{10}\text{Be}$ , and  $^{11}\text{Be}$ . b) The same plot in coincident with a neutron event in MoNA.

for the neutron time-of-flight  $\text{ToF}_n$ .

### 6.3 Analysis

Beryllium residues were gated by energy loss ( $dE$ ) through the focal plane thin plastic scintillator. Since the beam was also beryllium, a nearly all inclusive gate is made to the  $dE$ - $TKE$  spectrum and applied to the angle-ToF plot for isotope identification. This is completed by using the  $\text{ToF}_{\text{rigid}}$  method as discussed in Section 3.4.2. Figure 6.2 shows the gates used to select difference reaction residues. Part b of the figure confirms the identification of  $^{10}\text{Be}$ , not only by its angle through the focal plane detectors but also its relative rate of coincident neutrons compared with other beryllium isotopes.

Reconstruction of the target angles and position for the charged particles in the focal plane is then completed using the process described in Section 3.6.2 without the use of the beam-line tracking detectors (due to their inefficiencies for low  $Z$  beams). The reconstructed energy and angles of the residues at the target are combined with

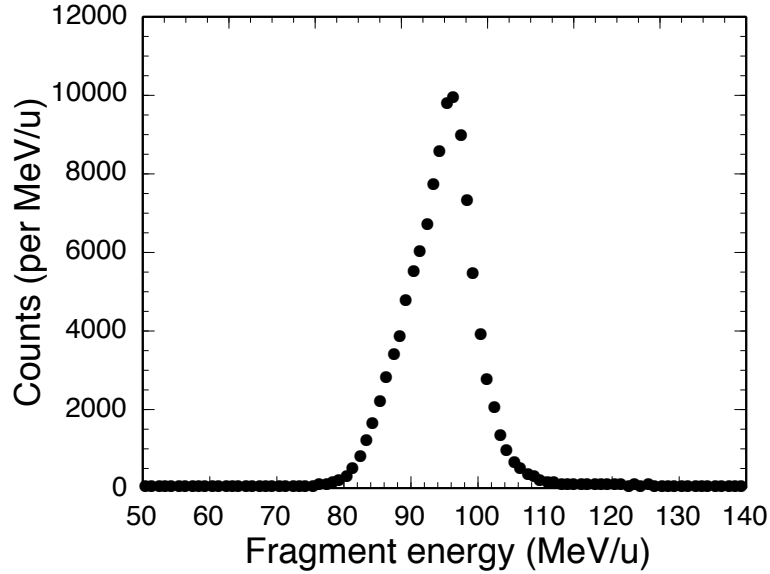


Figure 6.3: Reconstructed energy spread of the  $^{10}\text{Be}$  residue in coincidence with a neutron in MoNA.

the corresponding parameters for the neutrons in MoNA to determine the relative energy and opening angle between them. Figures 6.3 and 6.4 plot the measured kinetic energies for the coincident  $^{10}\text{Be}$  residue and neutrons, respectively. Subtracting the neutron velocity from the reconstructed fragment velocity yields the relative velocity spectrum shown in Figure 6.5. The similarity in spectrum shapes for the neutron kinetic energy and the relative velocity illustrate that most of the kinematic “response” of the reaction is carried by the neutron (due to it being 1/10 the mass of the fragment).

Data shown in Figure 6.6 illustrates the relationship between relative velocity and opening angle for the  $^{10}\text{Be} + n$  coincident data. The strong peak near 0,0 is from the highly excited 3.96 MeV state in  $^{11}\text{Be}$  decaying to the  $2^+$  state of  $^{10}\text{Be}$  ( $E = 3.87$  MeV) with the surrounding rainbow shape produced mostly by decay of the  $5/2^+$  (1.274 MeV) state. This spectrum is an alternate way of displaying the pertinent kinematic parameters used for the calculating the decay energy with Equation 3.7.

To account for acceptance cuts that may affect the resonant shape of the final decay energy spectrum, the MoNA/Sweeper Monte Carlo simulation (SIMPLE TRACK)



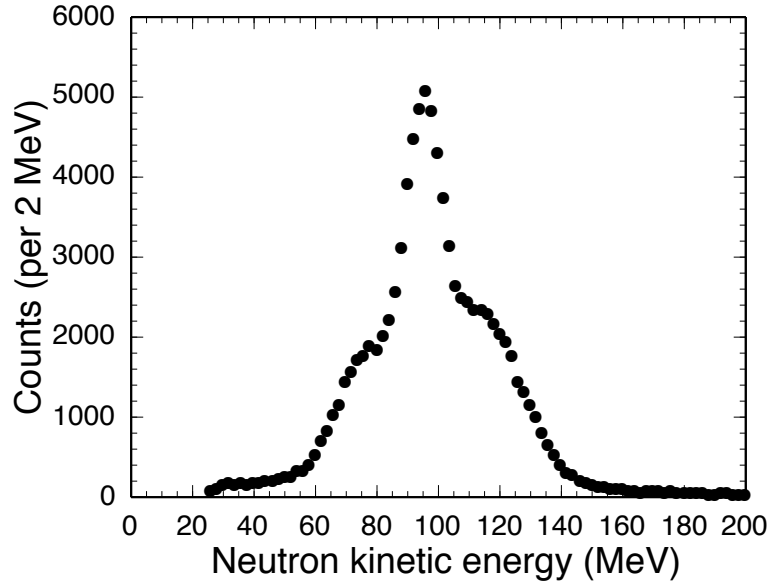


Figure 6.4: The neutron kinetic energy has a much larger range due to its small mass.

is again utilized configured as ST-mona (with MoNA/Sweeper detectors). It is run with the known widths and energies of the three resonant peaks populated with sufficient intensity with this setup, plus one thermal background curve simulating both the non-resonant neutrons and the diffractive breakup channel with two-neutrons. The input beam properties were adjusted to reproduce the angles and positions of the residues in the focal plane. Although the beam line tracking detectors were not used, they have little effect on the final decay energy spectrum since most of the kinematic properties are carried by the lighter neutron. After the simulation folds in the various detector resolutions for MoNA and the focal plane detectors (which in turn translate to target angle and energy resolutions), the final decay energy simulation is calculated and plotted on top of the data in Figure 6.7.

### 6.3.1 Comparisons to Previous Results

Due to the high energy of the  $^{12}\text{Be}$  beam (91 MeV/u) and the position of the steel blocker in front of the Sweeper focal plane, the unreacted beam could not be deflected into the focal plane detectors for a beam rate calibration as was done for the one-

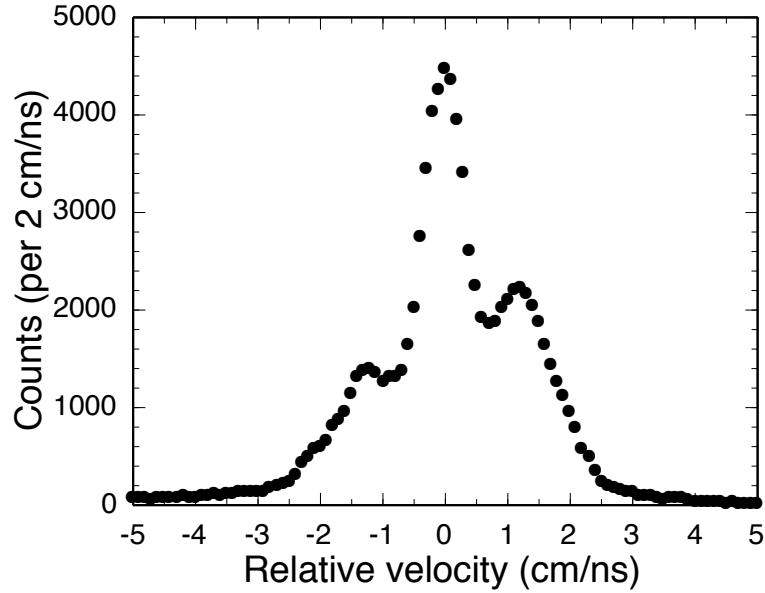


Figure 6.5: The relative velocity (neutron minus fragment) looks very similar in shape to Figure 6.4 and is slightly asymmetric due to the greater acceptance of forward-emitted neutrons.

neutron knockout of  $^{10}\text{Be}$  in Chapter 5. By simulating the reaction through the ST-mona code a relative comparison of the intensities, and by extension the cross sections, of the four curves can be made and compared to previous work.

Using the relative cross sections of the four decay channels in Table 6.2 reported by Reference [81] a fit to the current data taken is shown in Figure 6.7. The individual resonances are drawn and listed with their corresponding relative intensity (i.e. 0.069 is 6.9% of the integrated cross section less than 3.5 MeV is accounted for by the 1.274 MeV  $5/2^+$  state). The fit is a least- $\chi^2$  fit between energies 0.2 and 3.5 MeV for the scaling factor. The data from the current experiment are shown with statistical error bars and matches very well for the whole fitting region. In Figure 6.8 the relative intensity of each curve is treated as a free parameter but the absolute scale for the data was fixed at 1.09.

The only resonance not consistent with the previous measurement is the highly excited  $^{11}\text{Be}$  decay to the  $2^+$  state in  $^{10}\text{Be}$ . This apparent discrepancy of 40% can be accounted for by considering the efficiency and acceptance issues of low relative-

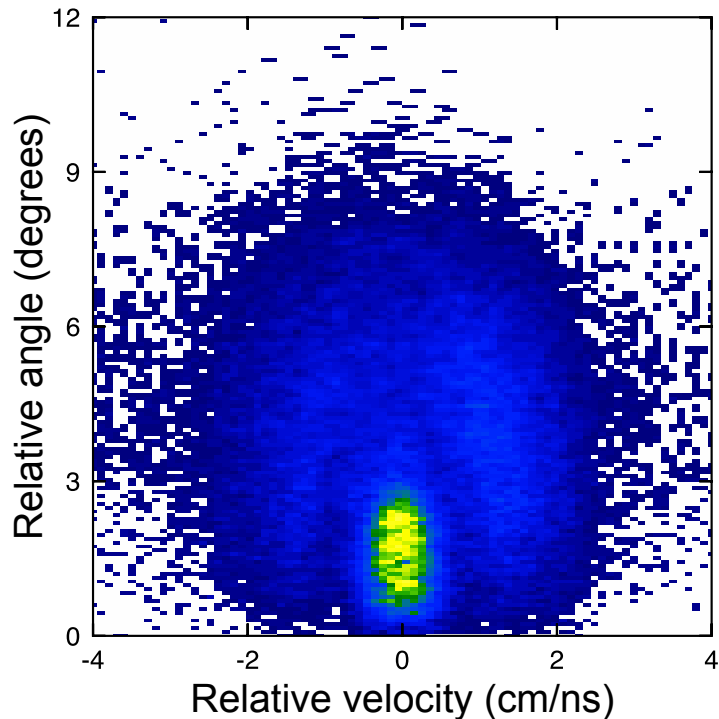


Figure 6.6: The relative angle and the relative velocity (neutron minus fragment) contains all the kinematic “information” used to calculate the decay energy.

energy zero lab-angle neutrons for the experimental setup of Ref. [30]. The efficiency for the lowest decay energies is less than the rest of the spectrum due to the lack of a large-gap dipole to deflect the charged particles off beam axis in the DeMoN setup.

This low energy decay channel is likely caused by knockout of a non-valence neutron in  $^{12}\text{Be}$  leading to a highly excited state in  $^{11}\text{Be}$  where the spin and parity of this excited single-particle state decays predominantly to the  $2^+$  state in  $^{10}\text{Be}$ . This core neutron is thought to be in the  $0p_{3/2}$  shell as calculated by B. A. Brown [27] using

Table 6.2: Decay energies and widths used by SIMPLE TRACK for  $^{12}\text{Be}$  decay simulation and relative comparisons ( $f_{exp}$ ) (taken from Figure 6.8) to the measured cross sections reported in Steve Pain’s Ph.D. thesis [81].

$E_{\text{decay}}$ (MeV)	Width (keV)	decay residue	$\sigma_{\text{pain}}$	$f_{\text{exp}}$
1.274	$\Gamma=100$	$^{10}\text{Be}$ g.s.	$22.4 \pm 4.4$	$1.04 \pm 0.2$
2.186	$\Gamma=150$	$^{10}\text{Be}$ g.s.	$18.3 \pm 3.7$	$1.04 \pm 0.4$
0.082	$\Gamma=15$	$^{10}\text{Be}$ $2^+$	$13.7 \pm 2.7$	$1.41 \pm 0.05$
3.50	thermal	$^{10}\text{Be}$ g.s.	$271 \pm 54$	$0.96 \pm 0.09$

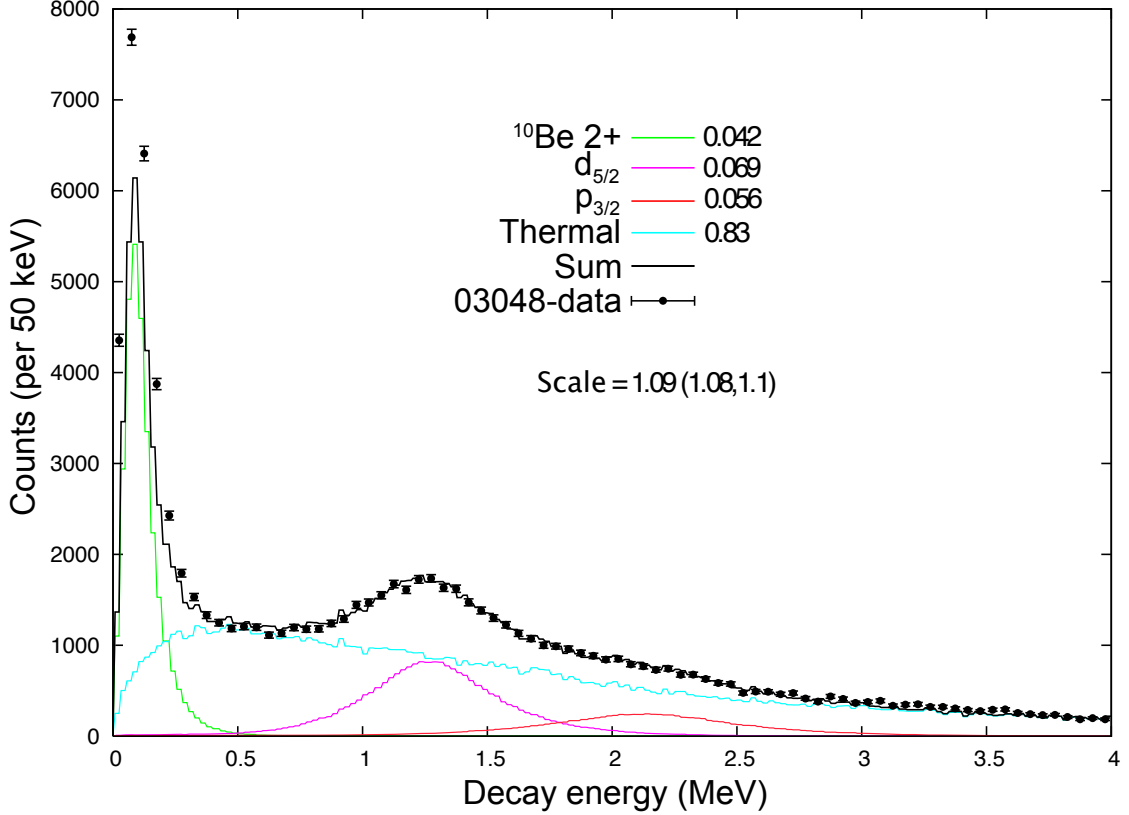


Figure 6.7: Fit to resonances listed in Table 6.2 simulated by ST-mona with cross section ratios as reported by [81]. The solid black line is the sum of the four decay curves:  $0d_{5/2}$  = violet,  $1p_{3/2}$  = red, decay to  $^{10}\text{Be } 2^+$  = green, diffractive channel = light blue. The fit is optimized for energies between 0.2 and 3.5 MeV. The only fit parameter returns  $1.09 \pm 0.01$  for the scale between the simulation counts and the data (used in Figure 6.8).

the WBP shell model calculations described in [6] that would decay roughly 90% to the  $2^+$  state in  $^{10}\text{Be}$ . Reference [30] attributes this decay channel to a  $5/2^-$  state that decays 50% to the  $^{10}\text{Be}$  ground state (a decay energy of 3.46 MeV) and 50% to the  $2^+$  state in  $^{10}\text{Be}$ . They cite Reference [82] that identifies the 3.96 MeV as a  $5/2^-$  state and the state at 3.4 MeV as  $3/2^-$ . A resonance with 3.46 MeV decay energy is outside of the acceptance range for an accurate analysis in the current study. But, Reference [80] describes a nearby  $5/2^-$  state at 3.90 MeV separate from the  $3/2^-$  state at 3.96 MeV, that could account for this discrepancy. Considering the other  $3/2^-$  state at 2.69 MeV could also come from stripping a neutron out of the  $0p_{3/2}$

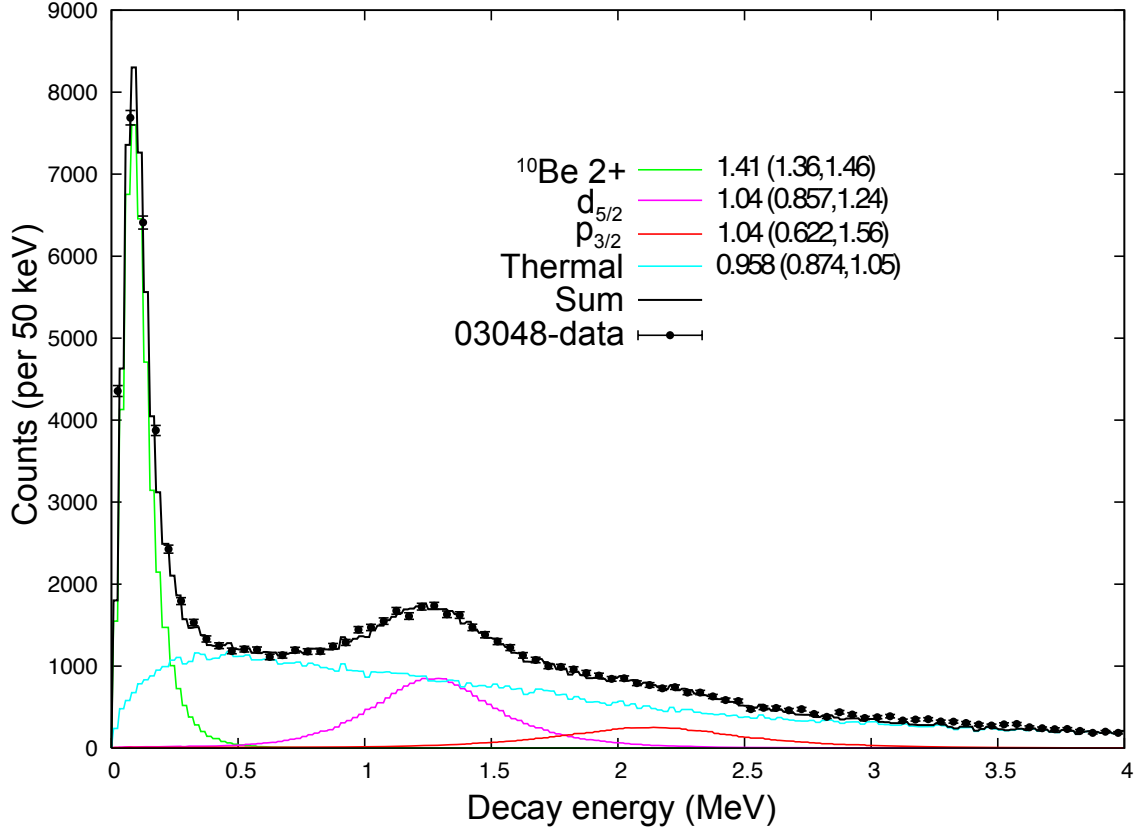


Figure 6.8: Same as Figure 6.7 with overall scale fixed at 1.09 while all four individual decay curves are adjusted relative to the reported cross section measurements [81] used for Figure 6.7, to find the best fit to the data. The fit range for this plot is 0.0 to 3.5 MeV. The fit values represent the ratio of our data to the cross sections reported by [81]. The only resonance that is not consistent with the previous measurement is the highly excited 3.96 MeV  $3/2^-$  state in  $^{11}\text{Be}$  decaying to the  $2^+$  state of  $^{10}\text{Be}$ .

shell, further shell-model analysis is needed to determine the coupling to the various states and their coupling to the  $2^+$  state in  $^{10}\text{Be}$  and the role core excitation plays in the initial  $^{12}\text{Be}$ .

The other three decay curves fit very well with the previous measurement and confirm the spectroscopic factors to the  $5/2^+$  state in  $^{11}\text{Be}$  reported in reference [30] that is produced mostly by stripping of one of the  $(0d_{5/2})^2$  neutrons in the ground state wave function of  $^{12}\text{Be}$ .

### 6.3.2 Diffractive Breakup and Two-Neutron Decay

The relative intensities of the fitted resonances depend on the shape and intensity of the non-resonant background curve. The diffractive breakup of  $^{12}\text{Be}$  to  $(^{11}\text{Be}^* + n)$  leading to  $(^{10}\text{Be} + 2n)$  or directly to  $(^{10}\text{Be} + 2n)$  is accepted by the gate used in Figure 6.2 and is a large contribution to the non-resonant background in both Figure 6.7 and 6.8. The precise shape of the cross section spectrum for this decay channel is not known, but was modeled by the diffractive channel leading to bound  $(^{11}\text{Be} + n)$  in Ref. [30]. The acceptance for  $^{11}\text{Be}$  reaction residue in the current study was severely cut and would not lead to a reliable estimate of the shape of the diffractive decay spectrum. The current analysis was made using a thermal (Maxwell) distribution with a temperature of 3.5 MeV per Equation 4.3 and closely matches the diffractive curve used by Ref. [30]. One piece of evidence supporting the choice of modeling the non-resonant breakup decay is that the two regions of the spectrum that are dominated by only this channel (near 0.5 and 2.7–3.5 MeV) are fit very well by the 3.5 MeV thermal distribution. Although, it is clear that the large uncertainty in the relative intensity of the  $3/2^-$  state at 2.1 MeV in Table 6.2 is largely due to the uncertainty in the non-resonant curve, and the lower acceptance as decay energy increases.

Analyzing the decay energy curve for events with two neutrons in the decay channel is different than for those with one neutron. Since the two neutrons in this case may not be correlated with each other, and the decay energy is calculated from the energy and angle of the first valid hit in MoNA, the resulting decay energy spectrum would have a wider spread of energies than the actual reaction energy of the decay. For example, given an uncorrelated two-neutron decay from a state 500 keV above the two-neutron separation energy, the sum of two decay energy calculations using the same energy and angle of the charged particle residue would equal 500 keV, but for just the first neutron, the calculated decay energy spectrum would be a curve between 0.0 and 500 keV (not including resolution effects). Furthermore, the first

neutron is not necessarily the neutron with the most decay energy (in the center of mass reference frame), since the initial reaction plane could project a fast neutron backwards in the lab frame, while the slower one reaches MoNA first and is used for the decay energy calculation. In the current experiment, the actual reaction energy for the diffractive breakup to two neutrons is not a distinct state, but instead a broad distribution caused by the overlap of the target nucleus onto the neutron wave function of  $^{12}\text{Be}$  [56]. The calculated decay energy for the first of two released neutrons, would be less than the total reaction energy. It is this calculated decay energy of the first neutron that is simulated by the thermal distribution (Equation 4.3) at 3.5 MeV with a peak energy near 0.5 MeV. The MoNA/Sweeper system acceptance for this distribution is simulated by ST-mona and the resulting broad curve is illustrated in Figures 6.7 and 6.8 by the light blue line.

An improved feature of the current experimental setup over the previous experiment, is that by utilizing MoNA, multiple neutrons can be recorded for one event. The absolute efficiency of MoNA is near 75% and thus, the efficiency to record two separate neutrons is about 50%. In contrast, the DeMoN array used in [30] has an absolute efficiency near 10% and thus the coincident two-neutron probability is closer to 1%. An effort is being made to positively identify two neutron events that can only come from the diffractive breakup of  $^{12}\text{Be}$  to get a more precise measurement of the shape and intensity for this decay channel, thereby improving the fit to the remaining resonances. This effort is discussed in more detail in Section 7.2.

## 6.4 Conclusions

The relative cross sections measured in the current experiment agree well with the previous measurements including the relative intensity for  $0d_{5/2}$  knockout, and confirms the spectroscopic factor for the 1n knockout to the  $5/2^+$  state in  $^{11}\text{Be}$  predominantly from the  $(0d_{5/2})^2$  configuration in the ground-state wave function of  $^{12}\text{Be}$ . This spec-

troscopic factor for the unbound decay channel does not increase the summed spectroscopic factor of the three paired neutron states (dominated by the stripping of one paired neutron) to the two neutrons in these states predicted by the unperturbed single-particle shell model description of an inert core of  $^{10}\text{Be}$  in  $^{12}\text{Be}$ . There may be higher shell configurations adding to the ground state wave-function not yet explored, or the simple assumption of two neutrons above an inert  $^{10}\text{Be}$  core might be inaccurate, and the contributions from core excitations cannot be ignored. The reliability of the current results rest on the relative intensities of the 2.69 MeV  $3/2^-$  resonance state in  $^{11}\text{Be}$  and the total non-resonant background. Close analysis suggests the previous experiment did not have consistent efficiency for the low relative energy zero lab-angle neutrons from the decay to the  $2^+$  excited state in  $^{10}\text{Be}$ , and undercounted this decay channel. The current measurement finds 40% higher relative cross section for the decay to the  $2^+$  excited state in  $^{10}\text{Be}$  from Reference [81] leading to a cross section of  $19 \pm 4$  mb. Further theoretical study is needed to determine the configuration of this 3.96 MeV  $3/2^-$  state in  $^{11}\text{Be}$ , including its overlap to the  $2^+$  state in  $^{10}\text{Be}$  and the likely mechanism from the  $^{12}\text{Be}$  ground state to populate this second  $3/2^-$  state in  $^{11}\text{Be}$ .



# Chapter 7

## Outlook

### 7.1 Evaluation of Design

The design goals for MoNA have been achieved by the performance shown through the analysis of the test experiments and other studies (see Chapter 4). Two simulation codes are shown to accurately reproduce nearly all aspects of the MoNA/Sweeper detector system.

MoNA is well suited for moderate to high energy (30-200 MeV/u) radioactive beam reaction experiments because of the forward focusing of the decaying neutrons at such speeds. But, it can also be arranged off-axis, in the new vault configuration shown in Figure 7.1 to gain acceptance for higher decay-energy resonances that emit neutrons at higher angles in the laboratory reference frame. In addition, the modular design capabilities of MoNA will be utilized in the future to increase the resolution for distinguishing multiple-hit neutron events and two-neutron events.

### 7.2 Multiple-Neutron Capabilities

Given MoNA's high efficiency, it has the capability to record multiple neutrons within one fragment-coincident event. However, these events have to be identified and sepa-

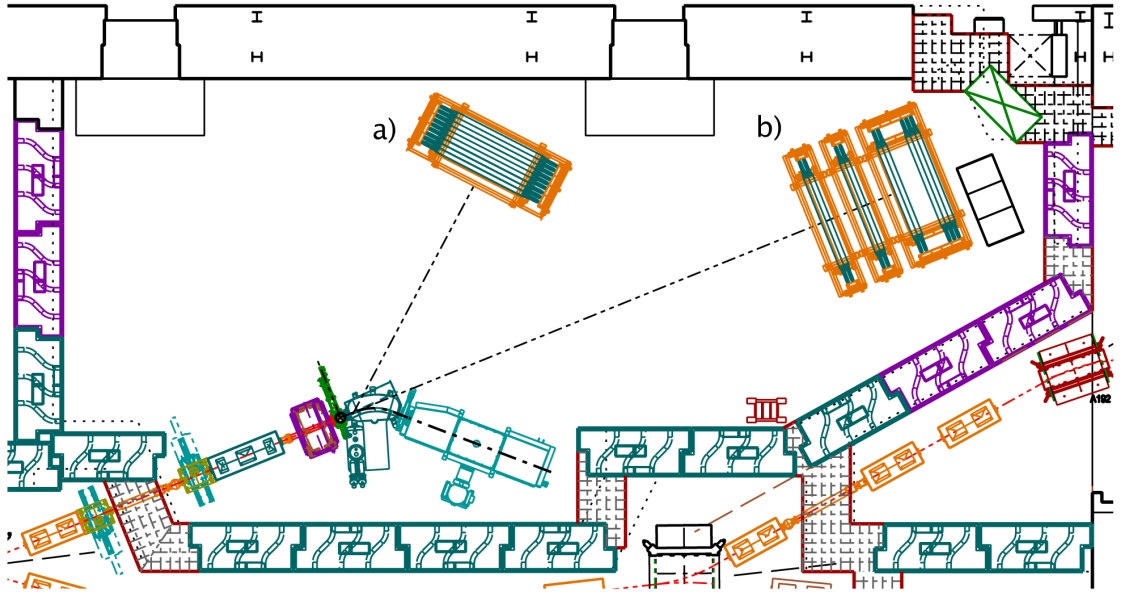


Figure 7.1: New vault configuration for the MoNA/Sweeper system, to be completed in the Summer of 2007 is a. a) Maximum angle position that will allow MoNA to accept neutrons at an angle up to 55 degrees relative to the beam axis. This will greatly increase acceptance for higher decay-energy resonances. b) Beam line position for MoNA showing the optional multiple-wall configuration of the array.

rated from the multiple hits recorded from a single-neutron events.

This is done by plotting the incoming velocity of the first hit in MoNA versus the velocity between the first and second hit and gating on the causality cone in distance and time from each first hit event. Only a separate neutron (or random background events) triggers a hit outside of this causality cone. The biggest challenge for implementing this analysis technique is the quantization of the MoNA position parameters. A neutron that triggers two neighboring MoNA bars in either the  $y-z$  directions will be recorded with a 10 cm distance between the two hits. For events where the first hit was near the back edge, 10 cm is an overestimation and vice versa for an event where the first hit was near the front face of the bar. For these cases the velocity between the first and second hit has a large uncertainty. To reduce this problem, the data set should be limited (if a sufficient number of counts are available) to events where the distance between the two hits is at least 50 cm. Indeed future

experiments using MoNA looking for two-neutron coincident events are changing the configuration of MoNA to include a large gap between layer D and E, creating two walls, for better resolution of the velocity for events where the first hit is in the front four layers (A–D) and the second hit is in the second group of layers (E–I).

An additional way of analyzing two-neutron events is by the relative intensity of total neutron events compared with events that determined to be one-neutron scattering events. Events where the second hit is from the same neutron as the first hit are difficult to determine conclusively. The energy deposited by scattering off a proton may be a simple relation,

$$Q_1 \propto \cos^2(\theta_{1,2}) \quad (7.1)$$

where  $\theta_{1,2}$  is the scattering angle between the first and second hit in MoNA, and  $Q_1$  is the recorded deposited energy of the first hit. But, there is a high cross section for elastic and inelastic scattering off of carbon that does not follow this relation. Nonetheless, if the signature of proton-scattered neutron events can be determined for reactions that only have one extra neutron in the system (like the Coulomb excitation of  $^{11}\text{Be}$  to  $^{10}\text{Be} + n$ ), the ratio of these proton-scattered events to the total scattering events should be constant (for a specific energy) since the ratio of carbon to hydrogen in MoNA remains constant. If the ratio of proton-scattered event to the total is significantly different for a particular experiment, the relative contribution from more than one neutron could be calculated. Current efforts to create a robust gate for identifying proton-scattered events include gating the inside of the causality cone mentioned above, and looking at the energy versus scattering angle spectrum for events that correspond to Equation 7.1.

One difficulty with calculating scattering angle is again the quantization of MoNA positions in the  $y$  and  $z$  directions. A large scattering length gate is applied here as well, that increases resolution but reduces the total count. Another problem that

involves using the  $Q$  parameter as calculated by Equation 7.1 to restrict the possible scattering angles off a proton, is the path length an energetic proton has in MoNA. Energy-loss calculations yield a path length of about 3 cm for 90 MeV protons in BC408 plastic. That means that nearly 30% of the highly-scattered neutrons off a proton will not deposit all their energy in the first bar, and punch through to deposit their remaining energy in the neighboring bar. This will lead to a calculated scattering angle that is less than the actual one.

In an attempt to compensate for these “punch through” hits, the  $Q$  parameters for the second hit, if it is the neighboring bar, is added to the first hit  $Q$  for a value that is much closer to the actual energy deposited. The third hit is then analyzed as the second hit for the purpose of determining the scattering angle. This analysis is complicated by the non-zero probability that the neutron actually scatters three times, twice in two neighboring bars and again in a third bar. Since the first two proton collisions are independent of each other, the twice-scattered neutron could end up at zero degrees again with reference to the beam angle. But, by using the analysis procedure as described above, the energy of the first two hits would be added and the result from Equation 7.1 will be a scattering angle too large to accept the event, even though it is a true proton-scattered neutron. Considering the efficiency of each vertical MoNA layer is about 25%, this could occur about 5% of the time.

Despite these challenges, progress is being made on both positively identifying two-neutron events and generating a standard ratio of single-neutron proton-scattered events to total single-neutron events. The ratio will be used to calculate the relative two-neutron component in a particular data set (for relative cross section measurements), while positively identifying the two-neutron subset of data will be used for calculating di-neutron decay energies.

## 7.3 Other Completed Experiments

### 7.3.1 Oxygen Isotopes

In two separate experiments the MoNA collaboration studied neutron unbound states for three Oxygen isotopes  $^{25,24,23}\text{O}$ . The first experiment used a  $^{26}\text{Ne}$  secondary beam and produced the first excited states (neutron unbound) in both  $^{24}\text{O}$  and  $^{23}\text{O}$  through  $2p$  and  $2p + n$  knockout reactions, respectively [83]. The second experiment used a  $^{26}\text{F}$  secondary beam and was designed to study the unbound ground state of  $^{25}\text{O}$  through the  $1p$  knockout [84]. It also produced significant amounts of highly excited  $^{24}\text{O}$  decaying to unbound  $^{23}\text{O}$  with a final residue of  $^{22}\text{O}$ . Some of the two-neutron identification techniques are being applied to these data.

### 7.3.2 $^8\text{Li}$ Coulomb Breakup

This experiment was performed to study the validity of nuclear-astrophysical models by comparing relative intensities of the Coulomb excitation of  $^8\text{Li}$  at different energies. The decay products were also measured as a function of the scattering angle (related to the impact parameter). Since the astrophysical inverse reaction  $(n,\gamma)$  has been measured and studied, a detailed study of the Coulomb dissociation, or  $(\gamma,n)$  reaction, can serve as a check to the assumptions used to determine the astrophysical properties of a reaction that cannot be studied directly. Preliminary analysis of this experiment were reported in Reference [85].

### 7.3.3 Fragmentation to Multiple Unbound States

By taking  $^{48}\text{Ca}$  directly to our reaction target this experiment populated neutron-unbound states directly from the fragmentation of the primary beam. Even though the cross-section to produce nuclei near the drip line is much smaller than from single or double nucleon knockout reactions, the beam flux increase of many orders of

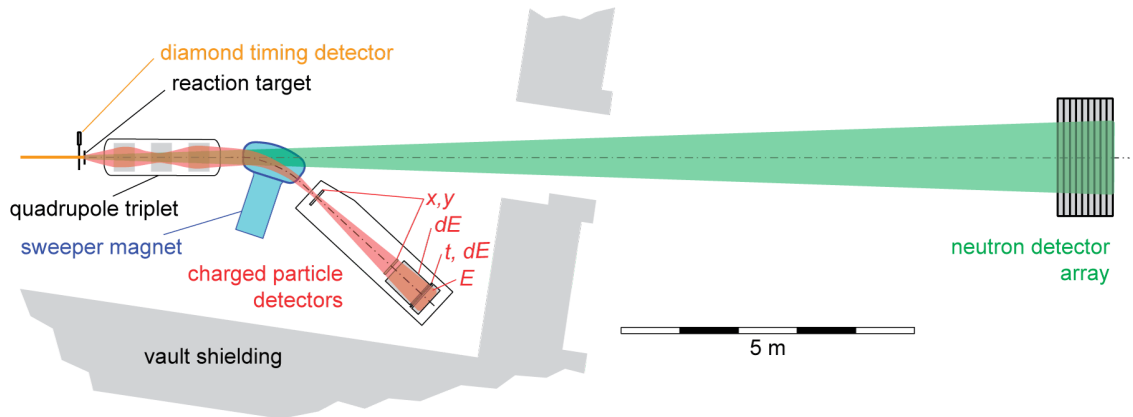


Figure 7.2: Alternate configuration of the reaction target placed in front of the focusing quadrupole triplet magnet to increase isotope separation by ToF. A high-rate diamond detector was used for the target timing signal. The total distance to MoNA is extended to 16.5 meters because the neutron acceptance is so small after passing through the bore of the triplet that they do not fill the full breadth of MoNA.

magnitude is more than enough to compensate the production rate. This experiment had a slightly different layout than the standard MoNA/Sweeper configuration and is shown in Figure 7.2. By placing the reaction target in front of the quadrupole triplet focusing magnet we were able to focus the fragments by their charge to mass ratio (or  $B\rho$ ) and more easily separate mass and proton number for a large range of reaction residues. Acceptance losses due to the bore radius of the triplet magnet in between the target and MoNA was not too restrictive to reduce the rates for many nuclei of interest. The analysis is still being completed, but there are over 500 neutron-fragment coincidences for at least a dozen identified nuclei [86].

### 7.3.4 Double-Neutron Experiments

In an effort to further test the capabilities to separate and analyze experiments with more than one neutron, an experiment to reconstruct the unbound ground state resonances for  $^{12}\text{Li}$  and  $^{13}\text{Li}$  was completed. They were produced by knockout from secondary beams of  $^{14}\text{B}$  (2 protons) and  $^{14}\text{Be}$  (1 proton), respectively, using the standard MoNA/Sweeper configuration.  $^{12}\text{Li}$  is unbound by more than 1 MeV while

$^{13}\text{Li}$  is unbound via two-neutron decay by about 3 MeV and likely decays through a  $^{12}\text{Li}$  resonance on the way to a  $^{11}\text{Li} + 2\text{n}$ .

### 7.3.5 Cosmic Ray Survey

MoNA collaborators at Westmont College in Santa Barbara, California have built the Cosmic Muon Detector Array [87] using smaller versions of MoNA detector modules. They record muon flux per solid angle of the sky over long periods of time. Recently, in an effort to utilize MoNA in between experiments, the FPGA logic modules were modified to record high multiplicity self-triggered events in MoNA to compare the cosmic ray muon flux from two opposite sides of the continent. Both detectors are synchronized to sidereal time (time relative to the stars in the cosmos, not the sun). A unique analysis code is used to account for MoNA's rectangular shape to get the angular flux.

## 7.4 Scheduled Future Experiments

Scheduled to run in the fall of 2007 is the di-neutron decay of  $^{16}\text{Be}$ . Unlike the two-neutron decay of  $^{13}\text{Li}$ , the ground state resonance of  $^{16}\text{Be}$  is predicted to have a two-neutron separation energy of about 1.5 MeV compared to about 1.8 MeV for the one-neutron separation energy for  $^{15}\text{Be}$ . This experiment will be the first to run in the new vault configuration and MoNA will also be separated into four walls, two layers in each of the first three walls, and layers G–I in the last wall. Each wall will be separated by 0.5 m. This setup should increase the resolution for identifying two-neutron events.

A study of the unbound ground state of  $^{21}\text{C}$  has also been approved. This experiment will utilize  $\gamma$  ray detectors near the target chamber as an auxiliary trigger to distinguish the ground state from excited states of the  $^{20}\text{C}$  residue.

# Chapter 8

## Conclusion

### 8.1 MoNA Efficiency and Resolution

The absolute efficiency of MoNA was measured for 90 MeV neutrons from the Coulomb breakup of  $^{11}\text{Be}$  on a gold target to be  $73 \pm 6 \%$ . This confirms the GEANT Monte-Carlo simulation's ability to reproduce the reaction cross section and light response for MoNA. The Coulomb breakup cross section was calculated via the virtual photon method [21, 23]. The results of a Briet-Wigner fit to the  $^7\text{He}$  data yields a peak at  $0.425 \pm 0.02$  MeV with a width ( $\Gamma$ ) of  $0.18 \pm 0.04$  MeV; consistent with previous measurements [20, 57]. The good agreement between Coulomb breakup data and reproducing the unbound resonance of  $^7\text{He}$  confirms the ability to accurately model the MoNA/Sweeper experimental setup with the SIMPLE TRACK and GEANT Monte-Carlo simulations.

### 8.2 $^{10}\text{Be}$ Neutron Knockout

The first experiment involving just the Sweeper focal plane detectors measured the reduction factor ( $R_s$ ) for the one-neutron knockout reaction of  $^{10}\text{Be}$  to the ground state of  $^9\text{Be}$ .  $^9\text{Be}$  has no bound excited states, so the observance of  $^9\text{Be}$  in the Sweeper



focal plane detectors uniquely determined the reaction channel. The reduction factor the  $0p_{3/2}$  single particle spectroscopic factor in  $^{10}\text{Be}$  is determined to be  $0.66 \pm 0.07$  from a cross section of  $68 \pm 7$  mb. This value follows the trend of the reduction factor versus  $\Delta S$  (the difference between neutron and proton separation energies of  $^{10}\text{Be}$ ) for values of  $\Delta S$  near  $-13$  MeV/u. This result is slightly less than the reduction factor for the mirror nucleus  $^9\text{C}$  (proton knockout from the  $0p_{3/2}$  shell) [68].

### 8.3 $^{12}\text{Be}$ Ground State Wave Function

The relative cross sections measured in the current experiment confirms the spectroscopic factor for the  $1n$  knockout to the  $5/2^+$  state in  $^{11}\text{Be}$  predominantly from the  $(0d_{5/2})^2$  configuration in the ground-state wave function of  $^{12}\text{Be}$  of 0.48 from Reference [30]. This spectroscopic factor for the unbound decay channel does not increase the summed spectroscopic factor of the three paired neutron states  $(0s_{1/2})^2$ ,  $(0p_{1/2})^2$  and  $(0d_{5/2})^2$ , dominated by the stripping of one paired neutron, to the total two neutrons predicted by the unperturbed single-particle shell model description of an inert core of  $^{10}\text{Be}$  within  $^{12}\text{Be}$ . There may be higher shell configurations adding to the ground state wave-function not yet explored, or the simple assumption of two neutrons above an inert  $^{10}\text{Be}$  core might be inaccurate and contributions from core excitations may be important.

There is evidence for a significant increase in the reported cross section for the knockout reaction to  $3.87$  MeV  $3/2^-$  state in  $^{11}\text{Be}$  [80] that decays predominantly to the  $3.96$  MeV  $2^+$  excited state in  $^{10}\text{Be}$ . Close analysis suggests the previous experiment did not have consistent efficiency for the low relative energy zero lab-angle neutrons from this decay energy, which is only  $82$  keV, and undercounted this decay channel. The current measurement finds  $40\%$  higher relative cross section for this cross section from [81], leading to a cross section of  $19 \pm 4$  mb.

# Appendix A

## Experimental Startup

### A.1 Introduction

The follow chapters describe how to manage a new MoNA-Sweeper experimental account.

Many experimental codes run programs that reside in the `/user/mona` account, like Readout and SpecTcl, but are called with setup and hardware files from within the new experimental account.

Most of the following procedures can be done from a `spice` machine by logging in with the experiment user account.

### A.2 Experimental Account

A couple weeks before the experiment is scheduled to run a user account should be created by the computer group. The user account name is set to the experiment number (#####) issued by the PAC (like 03038 or 05124). When the account is made a standard password will be assigned.

### A.2.1 Password

There are two passwords for every user. The first is the Linux (or DAQ) password and must be changed to a custom one when you login the first time by using the `> yppasswd` command. It will ask you to enter the original password and then your new one twice.

The second password is for the Windows machines. Go to the Data U. and login into a Windows machine and it will notify you that the standard password has expired and you must enter a new one. The password manager allows only ones that include capitals, lower case, and numbers. All three groups must be represented in the password. The Linux machines do not have this restriction, but it is advised to choose one that can be used for both.

### A.2.2 Group Members

Contact a member of the computer group or send a e-mail to add the users `mona` and `sweeper` to the experiments user group. Also ask that the new account be added to the `mona` and `sweeper` groups. This is to ensure that when we login as the new account we can copy over the necessary files from the `/user/mona` directories. You must also ask to add your personal account to the experiments user group along with other collaborators of your research team. You can view the members of a group by the following command:

```
> ypmatch monag group
```

Substitute "monag" with "#####g" or any group name you wish to query. You can also find the list of groups a user account is a member of. The following is an example for the user "mona".

```
> groups mona
```

### A.2.3 SSH

Many DAQ codes are called from the Data U. machine but actually run on another machine (usually spdaq16). Since the codes are trying to communicate with the spdaq machine, it will ask for the password before continuing. This pause in the action will usually cause the desired program call to fail. By setting up a proper `.ssh` directory you can then call these programs without providing a password.

There are directions in the Data U. for setting up the `.ssh` directory to ssh without passwords, but I will cover them here as well. From a Linux Data U. machine login in with the experiment account and follow these commands.

```
> cd ~/
> chmod 0750 .
> rm -rf .ssh
> mkdir .ssh
> cd .ssh
> chmod 0700 .
> ssh-keygen -t dsa -P "" -f id_dsa
> mv id_dsa.pub authorized_keys
> mv id_dsa identity
> chmod 0600 identity
> chmod 0640 authorized_keys
> cd ~/
```

### A.2.4 Event Space

When the account was created the computer group should have also issued space on an event disk for recording event files. Create a link called "stagearea" to this issued directory address.

```
> cd ~/
> ln -s /user/event3/05124 stagearea
```

Replace `event3` and `05124` with the proper assigned values issued by the computer group.

### A.2.5 Log Book

Log books are provided by the NSCL and one should be taken from the main-level copy room. Put the date and the experiment number on the cover.

#### Inside Cover

I like to use the inside cover to record the list of collaborators and the password.

## A.3 Bash Profile

Similar to the `.ssh` directory, some of the programs refer to the standard directory structure (outlined in the next chapter) and are given environment variables within the `.bashrc` file. The standard bash files can be copied from the `/user/mona/Bash_files` directory. After logging in with the experiment account, follow these commands.

```
> cd ~/
> cp -rp /user/mona/Dot\_files/ .
> cp -p ~/Dot\_files/.bash* .
```

## A.4 Directory Structure

As mentioned above many standard programs used in the DAQ system rely on strict directory structures and files.

### A.4.1 Mona

Copy the `/user/mona/mona` directory structure to the experimental account:

```
> cd ~/
> cp -rp /user/mona/mona/ .
```

#### Xamine Files

There are two Xamine files that get used to control the color and layout of Xamine.

To use the standard files, simply copy them from the `/user/mona` directory:

```
> cd ~/
> cp -p /user/mona/Xamine* .
```

### A.4.2 Tandem

Copy the `/user/mona/shared/exp_tandem` directory structure to a local `tandem` directory:

```
> cd ~/
> cp -rp /user/mona/shared/exp_tandem/ tandem
```

### A.4.3 Experiment

Readout needs an `/experiment` account to run properly. Create this by:

```
> cd ~/
> mkdir experiment
```

When Readout is first tested it will automatically make the subdirectories `current`, `orphans`, and `staged`. Also a folder is made after each run is completed called `run####`.

## Current

The contents of the `experiment/current` directory is copied into each `run####` folder. It can be made by hand before starting Readout. All important setting files for the experiment should be linked to from the `experiment/current` directory. Since there are also sweeper settings files to be linked, I make two folders:

```
> cd ~/experiment
> mkdir current
> cd current
> mkdir mona_settings
> mkdir sweeper_settings
```

Then I fill the `mona_settings` folder with important MoNA files (and the folder that contains all the cfd settings) that might change during the experiment.

```
> cd mona_settings
> ln -s /user/####/mona/config/MoNA_scaler_setup.tcl
> ln -s /user/####/mona/config/MoNA_setup_run.tcl
> ln -s /user/####/mona/config/MoNA_dynamic_var_run.tcl
> ln -s /user/####/mona/config/MoNA_readout_run.tcl
> ln -s /user/####/mona/config/MoNA_spectcl_run.tcl
> ln -s /user/####/mona/config/MoNA_hardware_run.tcl
> ln -s /user/####/mona/config/QDCfittedTHRE.tcl
> ln -s /user/####/mona/config/QDCfittedSLOOFF.tcl
> ln -s /user/####/mona/config/MoNA_Param_run.tcl
> ln -s /user/####/mona/config/Xpos_cal.tcl
> ln -s /user/####/mona/fpga/xlm_values.dat
> ln -s /user/####/mona/hv_control/hv_files/Vout_current.tcl
> ln -s /user/####/mona/cfd/
```

Daniel Bazin should fill the `current/sweeper_settings` folder with the proper Sweeper related files, or one could try to copy them from a previous experimental account and then he can edit them as needed. Daniel does not use links but instead sources the settings files from this folder directly when configuring the Sweeper DAQ.

## Complete

The scaler files are saved each time Readout is ended in a subdirectory of `experiment`. This makes it easier to transfer all the relevant data to tape after the experiment is finished. A new subdirectory called `experiment/complete` must be made.

```
> cd ~/experiment
> mkdir complete
```

### A.4.4 Desktop

The Desktop directory is used by the Data U. machines to create the desktop environment and the function call buttons. There is a standard set of buttons in the `/user/mona/shared/exp_desk` directory.

```
> cd ~/
> rm -rf Desktop
> mkdir Desktop
> cd Desktop
> cp -p /user/mona/shared/exp_desk/* .
```

Login to a Data U. machine with the experimental account and from the KDE environment right-click on a command button and check that the command path points to your current account, or through an environment variable, or to the correct `/user/mona` destination.



## A.5 Running Experiment

While running the experiment be sure to always save the settings like “xlm\_values” and cfd control files so they are up to date when copied by Readout from the links in the `experiment/current/mona_settings` folder.

### A.5.1 Edit Settings Files

Please read the MoNA report on MoNA calibration [88] to understand which files do what within the Readout and SpecTcl programs. Of particular importance are the different data packets created in the `mona/config/MoNA_hardware_run.tcl` file. Some of the commonly used packets are `mona`, `bitpattern`, and `ncans`. These are then added to the DAQ by the `MoNA_readout_run.tcl` file and added to the SpecTcl unpacker by the `MoNA_spectcl_run.tcl` file. Edit these as needed within the `mona/config` directory to add or subtract packets from the DAQ.

### A.5.2 Orphaned Runs

If Readout or the spdaq16 machine crashes during a run, the automatic copying and transferring of settings and event files will not happen properly. A properly recorded run creates a run folder, `/experiment/run####`, that contains the two settings folders and a link to the actual .evt file in `~/user/event#/#####/complete`.

To get the links and the Readout program back to working order after a crash first check to see if spdaq16 needs to be rebooted.

```
> ping spdaq16
```

Type `[CONTROL]C` to quit pinging. If there is no response you must go into the N6 area and reboot spdaq16 (directions for rebooting are on orange tape on the machine). If the pinging worked or after rebooting spdaq16 make sure there are no Readout codes running. The following command lists the current programs containing “eadout”.

```
> ps axuww|grep eadout
```

Then kill any programs still running by using the procedure number listed:

```
> kill #####
```

Rebooting spdaq16 will also kill stray procedures, but requires the user to restart many control programs after.

Follow this check list before continuing with the next run.

1. Restart Readout and manually increase the run number.
2. Start and then stop a run without recording.
3. Use the `>ls -la` command in the `~/experiment` directory to look for a run folder (`run####`) made for the interrupted run.
4. Look for copied `mona_settings` and `sweeper_settings` folders within the the run folder.
5. If needed, copy the settings folders into the interrupted run folder:

```
> cd ~/experiment
> cp -rp /current/mona_settings/ run####/
> cp -rp /current/sweeper_settings run####/
```

6. Now look for a linked `.evt` file.

Within the run folder, look for a linked `.evt` file pointing to the actual `.evt` file in one of the stagearea subdirectories.

Look for a linked `.evt` file in the `experiment/orphans` or `/current` directories.

7. Find the actual `.evt` file in `stagearea/complete` or `/current` or `/orphan` directories.

8. Move the actual .evt file for the interrupted run into `stagearea/complete`.
9. Fix links to the .evt file for the interrupted run within the `experiment/run####` folder to link to the actual file now located in the `stagearea/complete` directory.

```
> cd ~/experiment/run####  
> ln -s ~/stagearea/complete/run####-4096.evt .
```

10. If needed, delete old links from the `experiment/orphans` or `/current` directories.

If all goes well, the next run can now be recorded. Be sure to make a note in the log book during which run the Readout program halted.

## A.6 Post Experiment

As the experiment time is completed there a few prudent procedures to perform to ensure the data is capable of being analyzed properly.

### A.6.1 Calibration Runs

Before turning MoNA HV off, take a couple cosmic background runs for future calibration checks. One long run ( 6 hours) with MoNA self triggered/stopped and multiplicity set to “1-fold” and then another long run, again self triggered and stopped, with multiplicity set to “cosmics” (3-fold). The first one can be used to double check the QDC and Xpos calibration [88]. The second run is used to set the Tmean independent offsets for each bar [88].

## A.6.2 Archive Tapes

When all the experiment runs and the additional calibration runs are completed, the event files must be copied to tape and then read off the tape into the `evtdata` disk space. The NSCL provides a nice manual for copying data onto tapes called ‘Perparing to Close your Experimental Account’. I will not cover all the directions contained in that manual, so it should be read as well. I will go through the most common steps and address common problems that have arisen in the past.

1. Acquire a DTL or similar digital tape from the Computer help room.
2. Double check that all run folders within the `experiment` directory contain proper links to actual `.evt` files in the `stagearea/complete` directory.
3. Login to the “tapehost” machine (currently in the Data U. 2 cubicle) with the experimental account.
4. Change directories to the `experiment` directory. `> cd ~/experiment`
5. Identify the tape drive you are using. Maybe `/dev/st2` or `/dev/st0`. It is used as the third argument in steps 6 and 9.
6. Record entire `experiment` directory onto tape. `> tar -cvhf /dev/st2 .`
7. Wait for entire directory to be recorded onto the tape (it may take a couple hours). The terminal window should display all items written.
8. Change directories to the `evtdata/#####` space provided by the computer group. `> cd /evtdata/#####`
9. Read the files from the tape. `> tar -xvf /dev/st2 .`
10. When the reading is completed, check that the entire `experiment` directory was copied, including actual `.evt` files (not links).

11. Eject tape and label it with the date, experiment number, and runs included.

If all the `~/experiment` run folders were repaired properly if Readout crashed the actual `.evt` files should have been copied correctly. If they were not copied correctly, find the run folders for the missing `.evt` files and rewrite the link to the actual `.evt` file. Then delete the files you just wrote to the `evtdata/#####` space and start over from step 4.

Since this process copies each `.evt` file inside their respective `experiment/run####` folders, it is not possible to `attach multiple files` when analyzing the data with SpecTcl [89]. A useful trick is to make a new folder within the `/evtdata/#####` space that contains links to all the `.evt` files.

1. `> cd /evtdata/#####`
2. `> mkdir evt_links`
3. `> cd evt_links`
4. `> for i in ../experiment/run*/*.evt ; do ln -s $i . ; done`
5. Check that all `.evt` files have a link in this folder.

### A.6.3 Analysis Space

Along with an `/evtdata` space the computer group also should have provided a `/projects` space to copy the analysis files. The `/projects` area can be accessed from the high-speed spice machines, and should be used for all off-line analysis.

1. Login as the experiment onto “tapehost”.
2. `> cd /projects/proj#/#####`
3. `> cp -rp /user/#####/* .`
4. Check that all subdirectories got transferred properly.

## A.6.4 Executables

The executable files, specifically those that end in “.scr” use environment variables, that are defined inside the user’s `.bashrc` file, to navigate to the proper configuration files. Once the experimental user account is deleted the user becomes you and not the experimental account. This means that unless you only want to analyze one experiment, you can’t define these environment variables inside your `.bashrc` file. To overcome this limitation we must define the environment variables used for a specific executable directly in the file that sources it.

1. Start by opening the `tandem_spectcl.scr` for editing from the `/projects` directory it was copied into.
2. Comment out, or delete the first couple lines that source `etc/profile` and `~/.bashrc`.
3. Open the experimental account’s `.bashrc` file.
4. Copy list of exported variables and paste them at the beginning of the `.scr` file. They include:

```
export SHARED_READOUT=/user/mona/shared/readout
export SHARED_SCALER=/user/mona/shared/scaler
export SHARED_SPECTCL=/user/mona/shared/spectcl_shared

export MONA_DAQ=${HOME}/mona/daq
export MONA_READOUT=${MONA_DAQ}/readout
export MONA_SCALER=${MONA_DAQ}/scaler
export MONA_SPECTCL=${MONA_DAQ}/spectcl
export MONA_CONFIGDIR=${HOME}/mona/config
export MONASETUP=${HOME}/mona/config/MoNA_setup_run.tcl
```

```
export TREADOUT=${HOME}/tandem/readout
export TCONFIG=${HOME}/tandem/spectcl
export TSPECTCL=${HOME}/tandem/spectcl
```

```
export READOUT_SWEEPER=${HOME}/sweeper/scriptedReadout
export SPECTCL_SWEEPER=${HOME}/sweeper/spectcl
```

5. Add `export EXP_HOME=/projects/proj#/#####` to the very top of the `.scr` file. Be sure to fill in the appropriate directory address and note that one can't begin an exported environment variable with a number, but be creative with the `EXP_HOME` name to ensure it is not reused.
6. Edit all the following environment variables to begin with the name you choose for `$EXP_HOME` instead of `$HOME`.
7. This maybe the only executable you need to edit, but follow a similar procedure for any others that may need it.

# Appendix B

## MoNA SpecTcl Analysis Guide

### B.1 Introduction

This guide is intended to give you an idea of how to use SpecTcl to analyze data that MoNA has collected <sup>1</sup>. This guide is written for the analysis of data taken from cosmic rays, thus this may not be useful to you. However, it should give you an idea of what's involved in a fairly simple application of SpecTcl, which is all it's intended to do. Please read the NSCL documentation and general user guide [90] to familiarize yourself with the basic commands; especially the `spectrum` and `gate` commands.

#### B.1.1 MoNA Parameters

MoNA has 144 bars and 288 TDC, 288 QDC channels.

##### Raw and Cal Parameters

There are 576 raw and 576 calibrated parameters. The names of the raw parameters are a little confusing, but not needed that often. The raw QDC parameters and spectra are named:

---

<sup>1</sup>Portions of this guide were originally written by MoNA Collaboration undergraduate student A. Ratkiewicz.



(A\_QDC)00\_L or (A\_QDC)00\_R

The raw TDC parameters and spectra are named differently:

(TDC\_0L)00\_A or (TDC\_1R)00\_A

The calibrated parameters and spectra are named with `_CAL` appended to the raw name. The raw and calibrated TDC parameters are backwards in time, since the TDC's are stopped in common-stop mode by the `potscint` signal that comes before the CFD fires at MoNA.

### Bar parameters

These are then used to calculate a few parameters for each of the 144 bars:

`Xpos`, `Tmean`, `KE`, `Qmean`

The `Tmean` bar parameters (in ns) are calculated by the average of the two calibrated TDC parameters. A negative slope is used to put the time in the correct direction.

$$\text{Tmean} = ( (\text{TDC\_0L})00\_A\_CAL + (\text{TDC\_1R})00\_A\_CAL ) * -0.5$$

The `Qmean` bar parameters (in MeVee) are calculated by the geometric average of the two calibrated QDC parameters.

$$\text{Qmean} = \text{sqrt}( (\text{A\_QDC})00\_L\_CAL * (\text{A\_QDC})00\_R\_CAL )$$

The `Xpos` bar parameters (in cm) are calculated by the difference of the two calibrated TDC parameters. And, the `KE` bar parameters (in MeV) are calculated from the `Tmean` parameters, the `MoNA_Z_pos` variable, and the mass of a neutron. These bar parameters are, in turn, used to calculate the *Hit* parameters.

## Hit Parameters

These parameters are not as useful as one would like since the code is written to scan the whole MoNA array (starting with A0 to I15) and labels the first event with two valid TDC channels as hit 1, and so on. The `Multi_hit` parameter is the count of these valid hits for each MoNA event. The list of hit parameters is:

```
X_hit, Y_hit, Z_hit,  
TOF_hit, KE_hit, Q_hit,  
Theta_hit, Phi_hit,  
Multi_hit
```

Some pseudo parameters have been made to calculate the time-ordered hits [91] and should be used for more advanced analysis.

## B.2 Configuration files

There are plenty of files sourced by the `SpecTcl` code when it begins. Many are not to be adjusted in any way because they contain long lists of MoNA variable names and special `tcl` operations that are used by the underlying `cpp` code. In general, those files will get copied to your work space and never need to be adjusted or edited. There are a few files that contain calibrated variables that get set once for each experiment and then a few that contain adjustable variables to set as you see fit to best analyze the data for a particular run number.

### `SpecTclRC.tcl`

Make sure that the directory that contains the `spectcl.scr` file to launch `SpecTcl` also contains a `SpecTclRC.tcl` file and is edited to source the `SpecTcl` housed in a `/user/mona/mona/spectcl_shared` directory. You may also set your `WorkDirectory` and `EventDirectory` at the end of this file. The `SpecTcl_Driver.tcl` file is sourced

from this file. The `Driver` runs the Tk graphical user interface that displays the buttons and such we call the `SpecTcl Control Window`.

### B.2.1 MoNA Config Directory

The `/mona/config` directory contains many of the files that control the configuration settings for `SpecTcl`. The most important ones are:

#### `MoNA_setup_run.tcl`

This file contains many permanent lists and a few fitting flags and variables. The most important parts are the TDC and QDC setup lists that get read into the scriptable `SpecTcl` code to configure the Readout and `SpecTcl` codes. It also has the CFD lists of addresses and configuration file names for all 18 CFD's.

The top of the file has variables that can be edited for each experiment. Here we have a series of fitting flags:

```
QDC_thres_flag
QDCfitted
TDCfitted
Xposfitted
Tmean_indie_offset
```

These are set to "true" after the appropriate calibration or fitting code is completed [88].

The `tmean_offset` variable is a global time offset for all `Tmean` parameters of all bars and should be set from a MoNA gamma timing run or to some reasonable value to start (like 333.0 ns).

The `MoNA_Z_pos` variable should be set to the distance from the center of the reaction target position to the center of MoNA bar A8 (in centimeters).

The `MoNA_hits` variable is read in to create that many hit parameters and spectra. The default is 20 because the time-sorting scripts [91] use 20 hit parameters as inputs into the pseudos.

### **MoNA\_hardware\_run.tcl**

This file sources the `MoNA_setup_run.tcl` file and creates the scriptable data packets and commands to configure the VME modules (TDC's, QDC's and, Scaler's). Different QDC threshold lists are sourced if the `QDC_thre_flag` is set to "true". This file should not need adjusting unless the MoNA hardware changes (like adding neutron cans).

### **MoNA\_dynamic\_var\_run.tcl**

This file sources all the default variable settings and then the calibrated or fitted ones if the appropriate flags are set in `MoNA_setup_run.tcl`. This file also creates all the non-raw MoNA parameters from large lists that are defined in `MoNA_Param_run.tcl`. It does not need editing.

### **MoNA\_spectcl\_run.tcl**

This file is directly sourced by the `.scr` script file that launches `SpecTcl`. Its main function is to define the data packets to unpack in `SpecTcl` that are defined in the hardware file, for example:

```
unpack add mona
unpack add bitpattern
```

It does this by first sourcing the `MoNA_hardware_run.tcl` file and the `MoNA_dynamic_variables` files. It also sources the `MoNA_Param_run.tcl` file to create all the raw parameters from its lists. This file is replaced by `Tandem_spectcl.tcl` for the Tandem version of `SpecTcl` [89].

## MoNA\_readout\_run.tcl

This file is similar to `MoNA_spectcl_run.tcl` but tells the Readout code which packets to fill, for example:

```
readout add mona
readout add bitpattern
```

## B.3 Running SpecTcl

There must be a SpecTcl executable created that can be run from your user account or an experimental account. These executables have been traditionally housed in the `/user/mona/spectcl_shared` directory and accessed through the local `/mona/daq/spectcl` script files that source the local `/mona/config` directory filled with relevant settings and calibration factors.

### B.3.1 Open SpecTcl

Open SpecTcl by either clicking the button on a DAQ machine display of a current experimental account, or executing the script by typing:

```
> ./run_spectcl.scr
```

or the equivalent script file in the `/mona/daq/spectcl` directory. You will see four windows pop up B.1, B.2, B.3, and B.4.

The TkCon window should have listed many configuration settings including which fittings flags are set and whether or not you are using calibrated slope/offset values for QDC, TDC, Tmean, and Xpos parameters. This listing of settings finishes with `Done,Done`. The code also lists the data packets it recognizes like maybe `Level2` (when the `bitpattern` data packet is used).

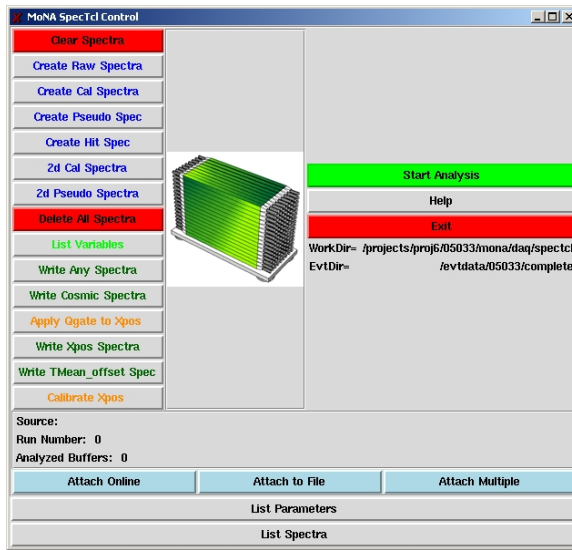


Figure B.1: The MoNA SpecTcl Control window.

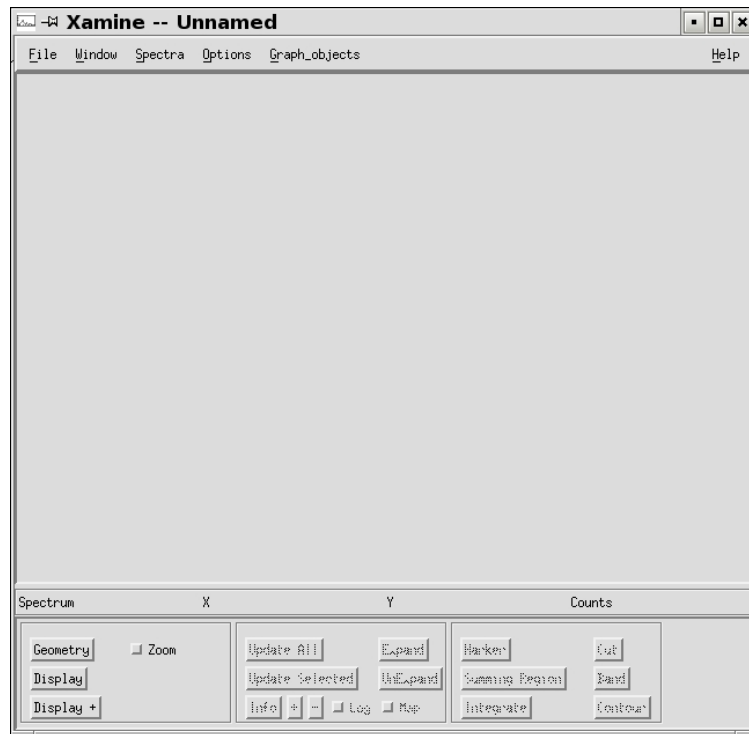


Figure B.2: The Xamine startup window.

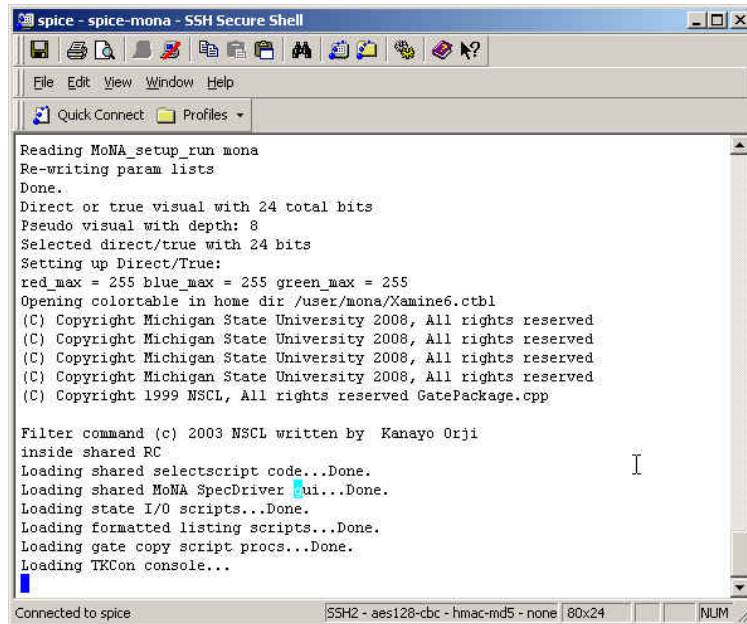


Figure B.3: The console shell.

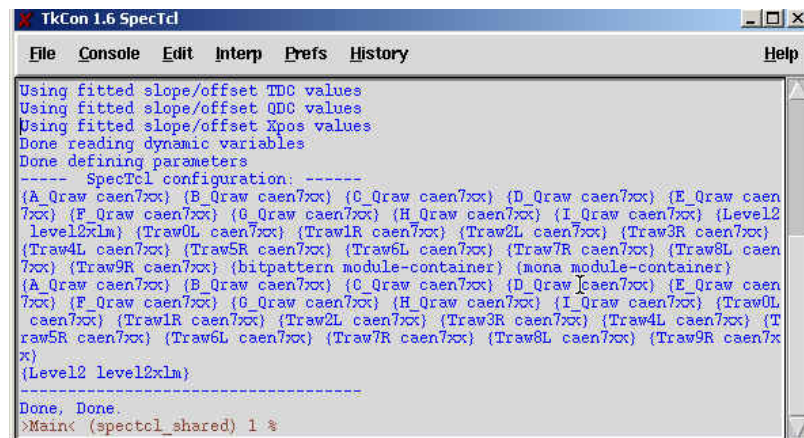


Figure B.4: The Tkcon command window.

Look at the right side of the SpecTcl Control window and find the `WorkDir` and `EvtDir`. The first should be set to the current working/spectcl directory, usually `/mona/daq/spectcl`. The second should be set to the directory containing the event files you wish to analyze (maybe `/stagearea/complete`). If they are not set, or set incorrectly, set them using the TkCon window:

```
% set WorkDirectory ~/mona/daq/spectcl
% set EventDirectory ~/stagearea/complete
```

### B.3.2 Creating Spectra

Use the `spectrum` in-line command in the TkCon window to create spectrum from any parameters. To view a list of the parameters type:

```
% parameter -list
```

Or press the *List Parameters* button on the bottom of the SpecTcl control window. If you forget the syntax just type:

```
% spectrum
```

and the error message will display the syntax it's looking for.

When you've made a spectrum of a parameter, it must be bound to SpecTcl to view on Xamine, so type the command:

```
% sbind -all
```

There are a few pre-set buttons to create and bind many of the commonly used spectra types. These buttons are on the left side of the SpecTcl control window. For viewing the X position of each bar, you need to create position spectra; do this by clicking the *Create Pseudo Spec* button on the SpecTcl Control window. After you've done this, you can press the *List Spectra* button to list all the current spectra loaded into SpecTcl and verify that spectra with the group name `Xpos` exist.



### B.3.3 Configuring Xamine

In the Xamine window, click on the *Geometry* button in the lower left hand corner of the screen. Change the configuration of the resulting pop-up dialogue to 4x4. Then click the *Display +* button and use the *Apply* command in the pop-up window to add desired spectra to the Xamine cells. Using the *Okay* command will close the pop-up window after inserting the selected spectra.

You can save any Xamine configurations by selecting **Write Configuration** from the **Window** menu on top. be sure to save it as a `.win` file in the `/win` directory. You may also read in previously saved configurations, but you must be sure the included spectra have been bound to SpecTcl first. For this example, select the configuration file `pseudo_win/Xpos_A.win` to display all the Xpos spectra for layer A.

### B.3.4 Attaching Data

In the SpecTcl Control window, click on *Attach to File* and select a run to read in. Once this is done, SpecTcl will begin analyzing the data. Let it run for a short while so that you have an idea where the peaks and valleys in your data will be. For the example procedures that follow, you need to source a cosmic background run (preferably one with the MoNA trigger set for 3-fold cosmic coincidence).

If you do not need to read in the whole event file, and when you've got an idea where the peaks and valleys in your data are, click on the *Stop Analysis* button.

### B.3.5 Setting up Gates

Back in Xamine, double click on first cell (the cell in the upper left-hand corner of the window) to zoom in on it. This should be Xpos\_A0. Now click the *Cut* button in the lower right hand corner. Here, we are going to tell SpecTcl that we want gate on events that hit in a certain part of the tube. For this example choose (for this bar) the region between -80.0 cm and -60.0 cm. Move the cursor to -80 cm on the

spectrum in Xamine and click once, then move to -60 cm and click again. This will fill the coordinates into the appropriate box in the *Cut* pop-up window. Select the *name* box and label the gate, `gate1` and then select *Ok* to accept. Cuts can also be declared with the `gate` in-line command in the Tk Con window (see Ref [90] for details).

MoNA is set into a right-handed coordinate system with positive *z* in the direction of the moving beam and positive *y* as the up direction (toward ceiling). This means positive *x* is to the left when looking at the front of MoNA (layer A). Xamine displays spectra from lower value to higher value, so the range -150 150 301 will have the correct coordinates, but left and right will be reversed on the screen. Just image you are viewing the Xpos of a bar from behind MoNA (where spdaq16 sits). This way positive *x* is to the right of the viewer since you are looking in the negative *z* direction.

In the TkCon shell, type:

```
% gate -list
```

to verify that the gate has been created. Note that if you've made a mistake in gate definitions, you can use the `gate -delete gatename` command to zero out the gate. This command does not remove the gate from SpecTcl, it just gets rid of all its arguments. This is handy; it allows you to change gates at the last minute without changing much else.

Now do the same thing for the last cell (Xpos\_A15) in Xamine as you did for the first, but use different points for the cut (use the positive value for the second, since you're trying to get a feel for how the ray travels through MoNA). We will gate the middle bars to see the cosmic rays travel from top left to bottom right through layer A.

Finally, you need to set up an `and` gate. If you called the first gate for Xpos\_A0 `gate1` and the one for Xpos\_A15 `gate2`, then to create an `and` gate going to the TkCon shell and typing:

```
% gate -new andgate * {gate1 gate2}
```

Here, `gate -new andgate` tells SpecTcl that you are making a new gate called `andgate`, the `*` tells it that the gate is a logical `and`, with `gate1 gate2` as the arguments, so that the gate is only true if both `gate1` and `gate2` are true. This is the only way to apply more than one condition on a spectrum. An `and` gate using `*` can depend on many other gates; just list all the ones you want to include inside the brackets.

### B.3.6 Copying Spectra

Now that you've got your gates set up, you want to make a copy of all the spectra you'll be applying them to. This is mainly for safety reasons; you don't want to change your source data by gating it. Go to the TkCon shell and type:

```
% spectrum -new xpos_a0_gate1 1 {Xpos_A0} {{-150 150 301}}
```

Here, you're making a new spectrum named `xpos_a0_gate1` from parameter `Xpos_A0` with a range of -150 to +150 cm and a resolution of 301 bins.<sup>2</sup> Repeat this for `gate2` using the name `xpos_a15_gate2` and for the middle 14 spectra (`Xpos_A1` to `Xpos_A15`) with `_andgate` in the name because we will apply the new `andgate` to them all. Next you need to bind them using the `sbind -all` command (as noted above).

### B.3.7 Displaying New Spectra

In the Xamine window, use the *Display+* button to view all the new spectra you've just bound. At this point, it's a good idea to save your configuration, name it something unique, and save it. You've just saved the setup that's currently in Xamine; you have not saved the spectra names or the gates, so if you've done a lot of work or feel like you might want to revisit these settings for this experiment, now might be a

---

<sup>2</sup>It is nice to select a bin number that is a multiple of the range you've selected plus one so the bin edges line up with the values.

good time to go to the TkCon shell, press h, and copy/paste the result to a text file (See Section 5).

### B.3.8 Applying Gates

Go the TkCon shell and type:

```
% apply gate1 xpos_a0_gate1
```

to tell SpecTcl that you're applying `gate1` to the spectrum called `xpos_a0_gate1`. Now repeat to apply `gate2` to the `xpos_a15_gate2` spectrum. The `apply` command can have a whole list of arguments so, to apply the `andgate` to all the middle 14 Xpos spectra you just made, you only need one line:

```
% apply andgate xpos\_a1\_andgate xpos\_a2\_andgate ...
```

## B.4 Analyzing Data

Go to the SpecTcl Control window, click on the red *Clear Spectra* button.<sup>3</sup> Now re-attach your data file. SpecTcl will start analyzing the data. Now's a good time for a coffee break; a typical run can have over 1,000,000 buffers to analyze. When it's done, the Spectra will look something like Figure B.5.

Notice the peaks seem to move from one side to the other as you look at successive bars. Most of these event are muons that pass through the left side of bar A15 through the right side of bar A0. So the overall pattern will look like a diagonal path through layer A.

---

<sup>3</sup>Note that it's very important to clear spectra whenever you make a change to the spectra or the gates.

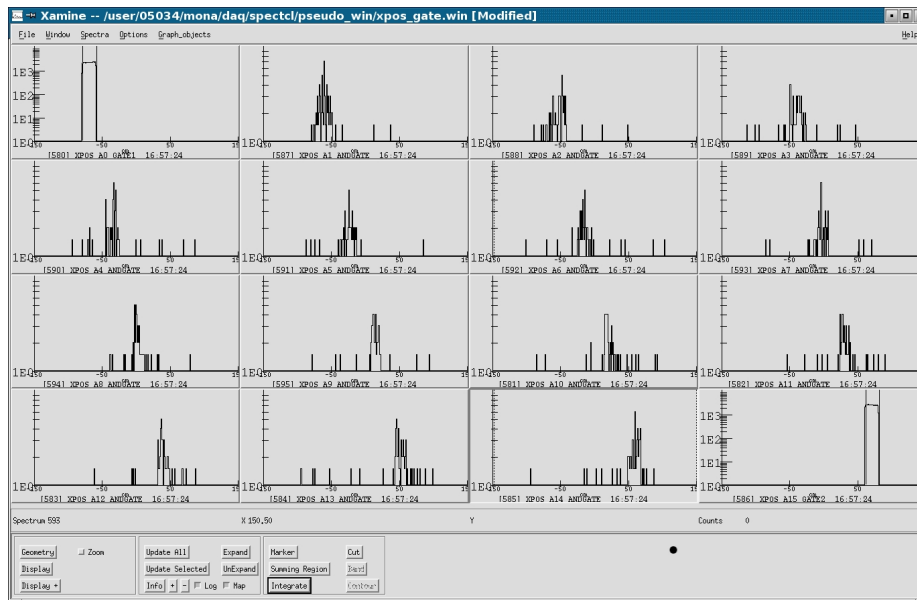


Figure B.5: Gated  $x$  position Xamine window.

## B.4.1 Exporting Data

When SpecTcl has finished analyzing the data, you might want to export it for later use. Go to the SpecTcl Control Window and click the *Write Any Spectra* button on the left. Select the spectra you would like to export, and don't forget to give it a unique name. The default format is `ascii` which works well with Excel. You may select any format you want to use. This will then save the `write` file in the `spectra` directory.

## B.4.2 Importing into Excel

Open *Excel*, click on *Data*, go to *Get External Data*, and select *Import Text File*. Change the file-type option to `all files (*.*)`, and select your `ascii` file. In the first page select *delimited* then *next*. In the following box, check both the `space` and `other` delimiter boxes. In the `other` box type a closed parentheses `)`. This will turn every space and closed-parentheses read in by Excel into a new column space, which makes life much easier for you. Now click *finish* and select the first cell to start the

import.

Next, if you've only imported one spectrum per Excel sheet and you want to automatically turn these columns into calibrated and compressed columns, you must first set your macros security to medium. Do this by selecting the `tools -> options -> security -> macro security` menus and then setting the macro security to medium. Now open the Excel file:

`/projects/proj1/mona/docs/spectcl-read-macro_calibrate.xls` that has the correct macros in it, and select the *Enable Macros* option. Once this file is opened in Excel go back to your data sheet and you can run the macro `test2` on your imported data. This will create many new columns and fill any missing zero's from the original histogram. One column fills with the calibrated values and then the following ones are the same data re-histogramed with `x2` and higher compression factors.

## B.5 Simplifying

### B.5.1 Settings Files

Now you can repeat the same gates and commands you just did for layer B. However, you're not going to do all that tedious typing again. Instead, you're going to put the bulk of your commands in a text file, and source the file from the TkCon shell. This will save you time if we ever want to revisit the analysis.

Open a text editor (use Kwrite or emacs). Emacs is preferred by people with a strong Unix background. If you are not entirely comfortable with it, use Kwrite; Kwrite's a lot like notepad, so you shouldn't have any problems.

When your text editor opens, go to the TkCon window, type `h` and then highlight the commands you used to create and apply the gates for layer A. Now select *Copy* from the TkCon *Edit* menu. In the editor select *Paste*, then edit the commands for layer B instead of layer A. You must delete the line numbers that the `h` command

inserts in front of the lines. Don't forget to type `sbind -all` at the end of the file if you create any spectra within. This is also a good place to save the in-line commands to create the gates you use (they must be created before they can be applied). Save the file in the `settings` directory as a `.tcl` file. To source the file and run the commands go back in the TkCon window, type:

```
% source settings\filename.tcl
```

This will read the file and run the commands between each `<return>` as if typed one at a time as an in-line command into the TkCon Window. If there is a syntax error in the file, the process breaks and all the commands after the error are not read in. In that case, just re-edit the file, comment out any commands before the error, and source it again.

## B.5.2 Creating Custom Pseudos

In the course of your analysis, you may find that you need to create a spectrum that's a calculation of two or more calibrated parameters (or any calculation not done within SpecTcl already). This technique will work for any reasonable arithmetic operation. A `pseudo` parameter is really just a procedure implemented while filling the SpecTcl parameters. Now you can finally tell SpecTcl to do whatever it was you wanted it to do. It can output any value you choose into a new parameter that can be put into a spectrum like the regular parameters. Three commands are involved:

### Parameter

First, you need to define a new parameter. It's a good idea to pick a high number for the id (higher than 5000), as this command won't work properly and will cause problems down the road if you assign an id that is already in use. Do not choose a number that is too high. Every parameter id is created up to the highest number, so extra large values will slow the analysis.

## Pseudo

Now you need to define the pseudo. The syntax here is a bit more complex:

```
% pseudo name {parameter1 parameter2 ...}
  {if {$parameter1isValid && $parameter2isValid ...}
    {return [expr($parameter1 * $parameter2)/$parameter2] }
    else {return -1}}
```

Note that the name of the pseudo should match the name of the parameter associated with it that you just made.

The syntax here is not intuitive if you're not experienced in TclTk, so let's take a minute to discuss it. First, note the `parameter1 parameter2 ...` part of the command. Remember when we made copies of existing spectra (section 3.6), we had to tell SpecTcl what we were copying? As you might suspect, this is the same idea. Be warned, though, any parameter you want to use in the pseudo calculation must be declared here.

The next part of the pseudo command is an `if` statement, followed by the expression to return if `true` and the expression to return if `false`.

The

```
{if {$parameter1isValid && $parameter2isValid ...}}
```

is a logical `and`; all parts must be true in order for the conditional to be true. This particular statement wants valid parameters; the `$` sign indicates that we're looking at the value of the parameter, and `isValid` demands that there be something assigned to it (note that this is case sensitive, so pay close attention to your declarations).

If the terms of the conditional are met, then the

```
{return [expr ($parameter1 * $parameter2)/$parameter2] }
```



expression will be evaluated. Note that we're telling SpecTcl to return the value of an expression [`expr ...`]. Again we insert a `$` in front of the parameter name to use it's value.

Notice that if the conditions of the if statement are not satisfied, some other number is returned. You should make this value marginally outside the spectrum you're defining, so you don't see bad data in your spectrum.

## Spectrum

Finally, you need to make a new spectrum to display the pseudo parameter you've just defined. The syntax is identical to creating a spectrum for a gated spectrum, as above, just use the pseudo parameter's name. The command is:

Some very useful pseudo scripts have been written by A. Ratkiewicz [91]. One sorts all the MoNA hits by time, within a set neutron-time gate. Another calculates the angles and velocities between internal MoNA hits (like between the first and second hit) to help with multiple neutron analysis. These `tcl` scripts are located in the `/user/mona/tools/` directory.

### B.5.3 Filtered Data

SpecTcl allows one to filter out only selected parameters that can then be read in to a different SpecTcl quicker than re-reading all the raw parameters and processing them. This is useful if you have a large set of data runs that take a long time to read, and if you've calibrated all your parameters and are only concerned with a small subset of the total parameters made. Since MoNA has over 1500 standard parameters (not including the hit parameters), it may be wise to crate a filtered file for the data. This process requires a special SpecTcl code that uses the filtered file as an input, and has the filtered parameters defined. For more information about this see Ref [90].

## B.5.4 Useful Tips

- In a unix shell, or the TkCon window, the `up arrow` key will display the last command. pressing the up arrow twice will display the command before the last, etc.
- In a unix shell, or the TkCon window, typing `h` will give you a history of past commands.
- Typing the command with no arguments will display an error message illustrating the expected syntax, for example: `% gate`.

# Appendix C

## MoNA Calibration Guide

### C.1 Introduction

The follow chapters describe how to prepare the MoNA detector for an experiment using a suite of fitting programs and procedures <sup>1</sup>.

The MoNA setup file called `MoNA_setup_run.tcl` in the `~/mona/config` directory contains the important flags to set to "true" after each successive calibration or fitting procedure is finished. They are:

`QDC_thres_flag`

`QDCfitted`

`TDCfitted`

`Xposfitted`

`Tmean_indie_offset`

Start by opening `MoNA_setup_run.tcl` and editing these flags to "false", then saving.

---

<sup>1</sup>Portions of this guide were originally written by MoNA Collaboration undergraduate students, including: J. Miller, M. Strongman, L. Elliott, D.B. Hecksel, M.M. Kleber, P.J. Voss, T. Pike, R. Pepin, and A. Ratkiewicz.

### C.1.1 Proper Links

Since the fitting codes run in a different directory from the configuration files, some linked files and directories are installed. In general the whole  $\tilde{\text{mona}}$  directory tree is copied from the preceding experiment and includes the wrong directory links and old calibration values. They must be checked to ensure they link to the proper destination. The command `>ls -la` can be used to double check if the links are set properly. The following commands should be done when first setting up a new experimental account, and to correct any old or mislabelled links.

#### TDC Calibration Links

In the  $\tilde{\text{mona}}/\text{contrib}/\text{tcal}$  directory the TDC calibration code looks for the TDC spectra written after reading a time calibration run. A link to the `/spectcl/spectra` directory is used:

```
> rm monatcaldata
> ln -fs ~/mona/daq/spectcl/spectra monatcaldata
```

The code then saves the TDC slope values to the MoNA configuration directory, so a link needs to be made to it:

```
> rm spectclconfig
> ln -fs ~/mona/config spectclconfig
```

#### HV, and QDC Calibration Links

In the  $\tilde{\text{mona}}/\text{contrib}/\text{hvfit}$  directory the high voltage gain matching code needs to input the `MoNARawQDCcosmics.asc` file created in SpecTcl from a cosmic background run. A link needs to be set:

```
> rm monacosdata
> ln -fs ~/mona/daq/spectcl/cosmics monacosdata
```

The gain matching code also needs to output the new voltage file to right directory:

```
> rm hvfiles
> ln -fs ~/mona/hv_control/hv_files hvfiles
```

The QDC calibration code runs from the `~/mona/contrib/hvfit` directory also and outputs the QDC slope and offset values to the MoNA configuration directory. So a third link is needed here:

```
> rm spectclconfig
> ln -fs ~/mona/config spectclconfig
```

## C.2 High Voltage Gain Matching

The phototubes (PMT's) of each MoNA detector bar may vary in their sensitivity for a given voltage setting. If one tube is more sensitive than another, a standard flash of light emitted from varying places along the bar will not be detected with uniform efficiency. If a weak light flash occurs nearer the more sensitive tube, that tube has a good chance of detecting it. However, the other, less sensitive tube may not detect it due to the fact that the light signal attenuates on its journey across the bar, and therefore becomes even weaker. This will cause low energy hits to be detected with non-uniform efficiency across the length of the bar because both tubes must fire for an event to be considered good. Therefore, data taken in that particular detector bar will be skewed. To solve this problem, the voltage levels of the two PMT's of each MoNA bar must be gain matched. Each tube must have its voltage level matched with the other in such a way as to ensure uniform detection efficiency across the bar. Gain matching is done using a routine that finds the position of the cosmic peak from a particular run and determines and executes the best adjustment in the voltages of the tubes to properly gain match the detector. Because these adjustments are

the program's best guesses, multiple iterations of the gain matching process must be completed before the PMT voltages are accurately matched.

### C.2.1 Getting Started

1. Open up two terminal windows, one to a *spice* machine, and another connected to *spdaq16*.
2. In the *spdaq16* terminal go to the `~/mona/hv_control` directory.
3. To make sure all of MoNA is turned type:

```
> ./Vallon.scr
```

### C.2.2 Take Cosmic Data

1. Let the voltages settle for a few minutes.
2. Be sure you are in the `hv_control` directory of the *spdaq16* terminal by using the command `> pwd`.
3. Now you must read out the current voltages into `hv_files/Vout_current.tcl` and copy them into `hv_files/Cosmic_volts.tcl` file by the commands:

```
> ./Vout.scr
```

```
> ./Vcopy.scr
```

4. Record a two-hour or longer run<sup>2</sup> of cosmic ray data with all detector bars. Use MoNA multiplicity set to `1-fold` and select self-trigger and self-stop on the XLM control.
5. Open MoNA SpecTcl [92] in the *spice* terminal window or from a Data U. machine.

---

<sup>2</sup>This must be a new recorded run for each iteration

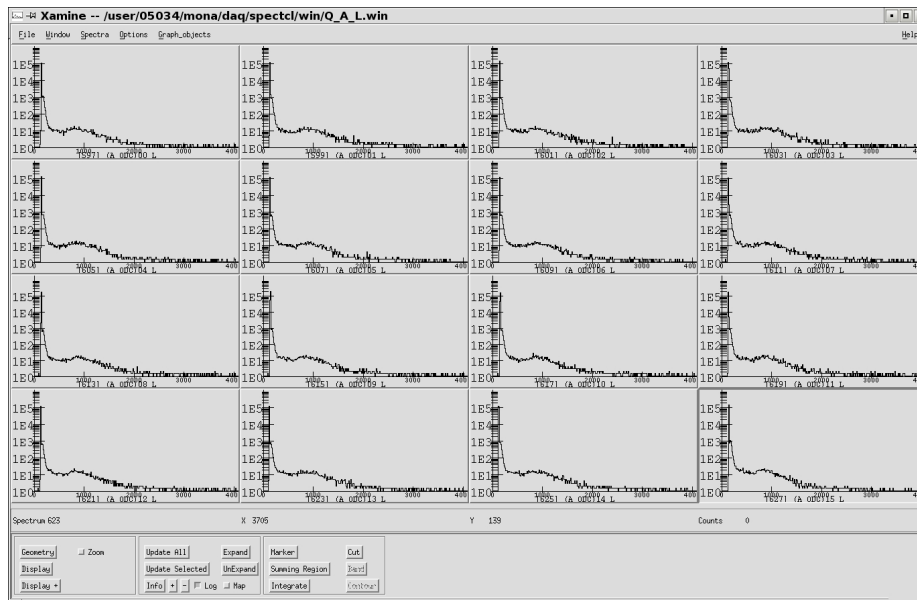


Figure C.1: Raw QDC Xamine spectra.

6. In the SpecTcl Control window, click *Create Raw Spectra*.
7. Then choose *Attach to File*, and select the run file recorded in step 1.
8. In Xamine go select **Window** -> **Read Configuration**, and pick one of the `/win/Q_x_x.win` window settings.
9. Allow SpecTcl to analyze all the buffers to ensure sufficient statistics for the cosmic peak fitting program. When the data is read in, click *Update All* in Xamine.
10. Look through the spectra in Xamine to make sure the data is usable (i.e. that there is a cosmic peak in each of the spectra). Select all the `/win/QDC.win` files to view all the QDC raw spectra. The spectra should look like Figure C.1.

with a pedestal peak near channel 100 and a cosmic muon bump (three orders of magnitude smaller) near channel 900. If there is a problem with one of the bars, double check that the voltage is on and that the inverter box is getting a good dinode signal from the PMT then inverting it for the QDC.

11. In the SpecTcl window, choose *Write Cosmic Spectra* to perform an `swrite` command on all raw QDC spectra. This also reads in the last `Cosmic_Volts.tcl` file and labels each spectra with the proper high voltage channel.
12. In the *spdaq16* terminal window, change directories:

```
> cd ~/mona/contrib/hvfit
```

### C.2.3 Voltage Matching Code

1. Now you run the high voltage fitting code [93] by typing the `> ./hv.sh` command. This runs a shell script that executes the program `fit_mona_spectra.f`.
2. When the process completes, there will be a listing of information about each channel and the changes that have been made. The six numbers are (left to right):

```
1.HV channel    2.Muon Peak bin    3.Pedestal bin
4.Difference(#2 - #3) 5.Current HV setting 6.New HV setting
```

The process also saves the new high voltage settings and links them to `/hv_files/QDCfittedHV.tcl`.

3. By just carefully viewing the listed numbers from the output of the `fit_mona_spectra` code we can determine if everything went smoothly without *Top-Drawer*.
4. Make sure that the numbers in column 4 are all about 800 and match column 2 minus column 3.
5. Check that the new voltages settings in column 6 are not too different from those in column 5.



6. If you are familiar with the program *TopDrawer*, try the next four listed items; otherwise, you're done with this part.

7. Try to open *TopDrawer* by typing:

```
> td spectratest.tdr
```

in the spice terminal window.

8. Press **Enter** each time you wish to change to the next set of 8 plots displayed. Each time you do this, the word *pause* will appear in the spice window. (Note: There are 288 spectra, so there will be over 30 *TopDrawer* screens to look through).

9. Look for a peak that appears around bin 800 and 2 white fit lines; one a gaussian fit to the peak and the other an exponential fit to the background (it appears as a straight line in the logarithmic scale).

10. When the last set has been viewed, pressing **Enter** will close *TopDrawer*.

## C.2.4 Setting New Voltages

1. Now you must apply the new high voltage settings by first going back to the *spdaq16* terminal window and changing directories to `~/mona/hv_control`.

2. Now source the new voltage values into the HV channels by typing:

```
> ./Vfitted.scr
```

Repeat Sections 2.2, 2.3, and 2.4 until performing another iteration would not significantly change the voltages, then move on to the QDC calibration procedure. Usually, twice is good enough if starting from voltages previously fitted for another experiment.

## C.3 QDC Calibration

QDC calibration should only be completed after the high voltage channels are fitted following the *High Voltage Gain Matching* directions from section 2. It is important to know the light-energy deposited by a scattered neutron event, and also important to suppress the null-result QDC pedestal events from swapping the Readout. Since every QDC has 32 channels and each pedestal is a positive bin value, all channels will readout if just one creates a valid trigger for that layer.

### C.3.1 Calibration Steps

1. Edit and save `MoNA_setup_run.tcl` with the QDC flag:

```
QDCfitted
```

2. Repeat the *Take Cosmic Data* section from Chapter 2.2, and make sure the recorded run in step 4 is brand new and was not used for voltage gain matching.
3. You need to execute the `calib.sh` shell script to perform the calibration. To do this, make sure you are in the `~mona/contrib/hvfit` directory.
4. Run the `calib.sh` program by typing the `> ./calib.sh` command.
5. When the code is finished, information about each channel will displayed. As on the screen, from left to right, the seven numbers correspond to the following:

```
1.HV Channel 2.Muon Peak bin 3.Pedestal bin 4.Diff(#2-#3)
5.QDC Threshold 6.QDC Slope 7.QDC Offset
```

6. Note that the QDC calibration code is:

```
QDC_Cal = (QDC_raw + QDC_offset) * QDC_slope
```

so the QDC offset is in units of raw bins and the QDC slope is in units of MeVee/bin. This is fitted to set the muon peak at 20.5 MeVee and the pedestal to zero.

7. Make sure that the numbers in column 4 are all about 800 and match column 2 minus column 3.
8. Check that the QDC threshold values are about:

$$\text{QDC Threshold} = ( (\text{Pedestal bin} + 3) / 16 ) + 1$$

9. Check that the QDC offset values are the same as the Pedestal Peak values.
10. Check that the QDC slope values are all about 0.028.
11. If the preceding checks are not confirmed then the *High Voltage Gain Matching* directions must be re-done.
12. This program also saves the new slope/offset data in: `~mona/config` and links to `QDCfittedTHRE.tcl` and `QDCfittedSLOOFF.tcl`.
13. Enter the `~mona/config` directory and check to see that there are current threshold and slope/offset files, based on the date and time of completion by using the command:

```
> ls -la
```

14. Edit and save `MoNA_setup_run.tcl` with the QDC flags:

```
QDC_thres_flag
```

You are now ready to run an experiment with voltage-matched PMT's and calibrated QDC parameters. The next time you take data, the QDC's will ignore values less than the threshold, so no pedestals are read. The energy of lost events due to the

pedestal suppression will be between 4 to 19 channels, which is less than 0.5 MeVee. Also, the QDC calibrated spectra will be fitted for 20.5 MeVee at the muon peak, and zero for the where the pedestal was.

## C.4 TDC Calibration

MoNA uses time-to-digital converters (TDC's) to set timing coincidences for events that occur in the array. In a sense, they are “fancy stop watches” for the detector. When a TDC channel receives a pulse from the anode of a PMT of a particular detector bar, it begins charging a capacitor. When the delayed logic stop occurs, the capacitor stops charging, and the amount of charge on the capacitor corresponds to the time the TDC was charging. However, each TDC does not charge at exactly the same rate as another, so the rate at which two different TDC channels charge will give different times for identical time events. This presents a problem that must be overcome with a calibration. The time calibrator (NIM box), which is physically daisy-chained to each of the TDC channels at the beginning of the process, gives precise signal spikes at equal and adjustable intervals over a predetermined and adjustable range. These signals give a standard by which to calibrate the TDC's to ensure proper timing for events that occur in MoNA. Since the same TDC channels are used from one experiment to the next this calibration is not needed for every experiment.

### C.4.1 Record Time Calibration Run

Before any fitting code can find the right TDC slope, a run must be recorded using the *Ortec* NIM Time Calibrator module connected through a NIM threshold discriminator and then to the test inputs of the MoNA CFD's. This setup has been connected, and only needs the time calibrator module installed to run again.

1. In the directory `mona/config`, open the file `MoNA_setup_run.tcl` and edit and

save the desired range for the width of the TDC window (in nanoseconds) under **Global Settings** where you find the command `set range`. The range is the total time that spans all 4095 channels; it can be set between 140 and 1200 ns.<sup>3</sup> Also, make sure the `TDCfitted` flag is set to "false".

2. Set both the range and the increment in the time calibration module (model 462, in the NIM crate) to the correct settings, and turn it on. The increment, period, or `delta t` is how often the TDC records a spike. The range should be set equal to or close than the range set in step 1.

3. Give a meaningful name to TDC calibration the run in the Readout window. For example:

```
TDC cal, Trange 350ns, Tdelta 40ns
```

4. Plug the *start* output of the time calibrator into the *CFD test input* discriminator channel on the left of the NIM crate, and double check that this signal is routed to all *CFD test* inputs.
5. Plug the *stop* output of the time calibrator into the *TDC test input* discriminator channel on the left of the NIM crate, and double check that this signal is routed to all *TDC common* inputs.
6. Make sure all the CFD's are running by checking their output (*OR*) lights to see them blinking fast.
7. Record a short 10 minute run with all detector bars. Use MoNA multiplicity set to `1-fold` and select self-trigger on the XLM control. Do not select self-stop, the time calibrator must send the both the start and the stop signals.
8. Open MoNA `SpecTcl` [92] in the *spice* terminal window or from a Data U. machine.

---

<sup>3</sup>Traditionally, we have used 350 ns for the TDC full scale.

9. In the SpecTcl Control window, click *Create Raw Spectra*.
10. Then choose *Attach to File*, and select the run file recorded in step 1.
11. In Xamine go select Window -> Read Configuration, and pick one of the `/win/TDC.win` window settings.
12. Allow SpecTcl to analyze all the buffers to ensure sufficient statistics for the TDC fitting program. When the data is read in, click *Update All* in Xamine.
13. Look through the spectra in Xamine to make sure the data is usable (i.e. that there are evenly spaced spikes in each of the spectra). Each spike must have more than 300 counts to get recognized by the calibration code. Select all the `/win/TDC.win` files to view all the raw TDC spectra. Pay special attention to some of the inner most MoNA bars like D7 to G9 and see if any are double-peaked. A suitable threshold value must be less than any double-peaked count. The fitting code will take any channel above threshold preceded by a channel below threshold and fit it to the next incremental period. Running the code with a threshold that runs through a double-peaked spike will cause the fitted slope to be very wrong.

Figure C.2 is a sample spectrum with the delta time set to 40 ns and a range of 350 ns.

14. Select *Write Any Spectra* in the SpecTcl Control window.
15. From the pop-up window, open *Spectrum List* and select all the TDC data spectra (there should be 320 total). Click *Accept and Close*.
16. Name the spectra file including the range and period you've chosen. Make sure that the ASCII is selected.
17. Click *Write Spectra*.

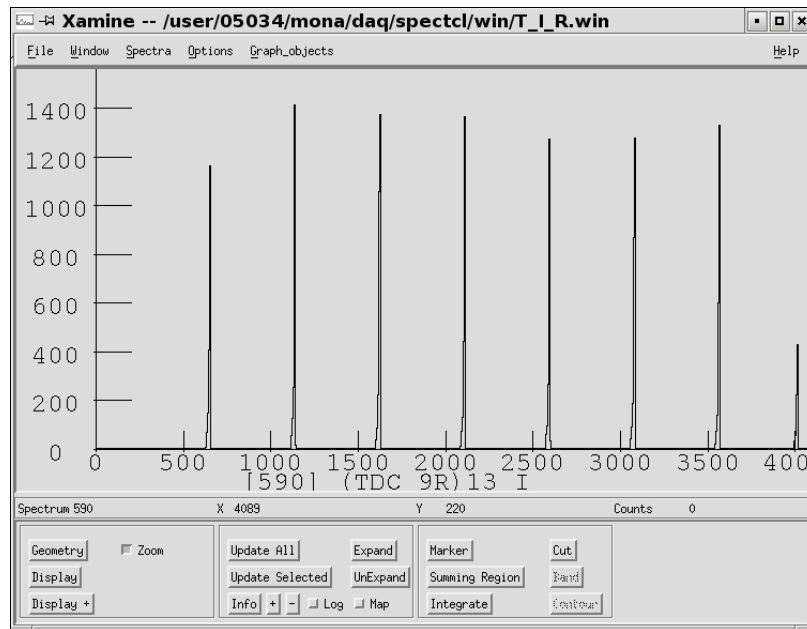


Figure C.2: Calibrated TDC Xamine spectra.

## C.4.2 Running Calibration Code

Running the `tdc_calib.f` code by sourcing the `test.sh` script will save a `slope_offset_datetime.tcl` file in the `contrib` and `mona/config` directories. It will also automatically link the latest one to `MoNA_TCAL_dynamic_var.tcl` to get used when running `SpecTcl`. The offset values for the TDC parameters are not very meaningful and set to 100 channels.

1. Log onto a *spice* machine as the experimental account with SSH Secure Shell and type
 

```
> cd ~/mona/contrib/tcal/monatcaldata
```
2. Use the `ls -la` command to reveal your spectra file, most likely among several others.
3. Type `cd ..` to back up a directory.

4. Now open to edit the `test.sh` script. It should look similar to this: <sup>4</sup>

```
#!/bin/sh
./tdc_calib <<EOF
monatcaldata/Tcal_run1002_350_40.asc
n
test.tdr
40.
1. 3840.
300.
EOF
ln -sf slope_offset_`cat datetmp.txt`.tcl slope_offset_latest.tcl
# exit
cp slope_offset_`cat datetmp.txt`.tcl spectclconfig/.
ln -sf slope_offset_`cat datetmp.txt`.tcl \
    spectclconfig/MoNA_TCAL_dynamic_var.tcl
exit
#
```

5. On line 3 of the script, change the filename after the `monatcaldata` directory to the one you desire to calibrate (the filename should correspond to the name of the file you just checked in step 2).
6. The first number under `test.tdr` should be changed to the calibration period (or  $\Delta t$ ) that the run was taken with in nanoseconds. On the next line, the 1. stands for the first channel and 3840. refers to the number of usable bins (255 less than the total 4095).<sup>5</sup>

---

<sup>4</sup>The `'cat datetmp.txt'` is a date-time stamp created by the code as a series of numbers MMD-DYYHHMMSS to include in these file names.

<sup>5</sup>More details about the script can be found in Ref [93].



7. The 300. stands for the threshold. If a channel contains more than 300 counts the program recognizes it as a peak. Edit this value to one that is suitable for your run.
8. Make sure the `exit` command underneath the count threshold is commented out of the executable program file by placing the pound symbol, `#`, in front of it.
9. Save your changes and exit the editor.
10. Run the `tdc_calib.f` code by typing:

```
> ./test.sh
```

in the *spice* window.

11. A long list of values and calibrating points will be printed to the screen, you can scroll up through some of the bars, but most shells don't scroll back far enough to see the fitting points for all 320 TDC channels.
12. If you are familiar with the viewer program *TopDrawer*, try running it by using the `td test.tdr` command. Then don't touch anything. To cycle through the graphs, press enter. Don't click on any of the windows. You must be in the shell window to cycle through but can't overlap the black graphs because each graph needs to be viewed. Verify that the points are evenly spaced by the specified increment and linear along the regression line. The vertical axis is the channel number and the horizontal axis spans the range setting in nanoseconds.
13. If a linear fit line seems to deviate from the line of points, you may need to start over with recording a new time calibration run.

14. You can check the slopes by opening the `slope_offset_latest.tcl` file and seeing if the slope values are close to  $(\text{range in ns})/4096$ . A range of 350 ns should have a slope near 0.08-9 ns/channel.
15. If the fitted slope are not near the range divided by 4095, you may need to start over with recording a new time calibration run, or re-running the fitting code with a different threshold value.

### C.4.3 File Names

As you can see the calibration file is saved in `~/mona/config` with no easy name to describe what it contains and the `MoNA_TCAL_dynamic_var.tcl` link always points to the latest calibration created. You may want to reset this link to a file run earlier and/or rename calibration files to ones with meaningful labels using the `ln -sf` or `cp` commands. Make sure the `MoNA_TCAL_dynamic_var.tcl` link points to the correct file for your experimental runs.

Now you can reopen `MoNA_setup_run.tcl` and edit the `TDCfitted` flag to `"true"`.

## C.5 X Position Calibration

The X position calibration may be done after an experiment is finished as long as a sufficiently long recorded run is taken at the end of the experiment, but some position and energy spectra during the experiment may look strange if this is not done beforehand. MoNA must be gain matched and the QDC and TDC slope/offset values must be fitted.

MoNA is a high efficiency neutron detector. Through measuring the position of the particle (neutron or other particle) it becomes possible to know the particle's path and thus extrapolate its energy. In order to do this properly the X-position parameter must be properly calibrated. By noting the difference in time signals from

the photomultiplier tubes at each end of a certain MoNA bar, we can produce a spectrum that displays the difference in the time signals (in nanoseconds) between the right and left sides of that bar. By performing this calibration, the user transforms the time difference spectrum in nanoseconds into a position spectrum in centimeters. This is very useful in reconstructing events when analyzing data. Another important reason for this is that the kinetic energy of the neutrons are calculated from  $KE = 1/2 * (m_n) * (d/t)^2$ . An accurate determination of the energy requires one to know the full 3d position of a hit in any given bar.

### C.5.1 Record Cosmic Run

Before any fitting code can find the correct X position slope and offset values, a long cosmic-ray run must be taken. This new run requires the previous calibrations to be performed first.

1. Record an overnight (12 hours) run of cosmic ray data with all detector bars. Use MoNA multiplicity set to 1-fold and select self-trigger and self-stop on the XLM control. Also be sure that you are using calibrated slope/offset values for both the QDC and TDC parameters and check that the calibration flags in `MoNA_setup_run.tcl`:
 

```

QDC_thres_flag
QDCfitted
TDCfitted
      
```
2. Open MoNA SpecTcl [92] in the *spice* terminal window or from a Data U. machine.
3. In the SpecTcl Control window, click *Create Pseudo Spec*.
4. In order to avoid any time walk that may occur with near-CFD-threshold events, you must apply a high-Qmean gate (from 8 to 120 MeVee) to each Xpos spectra.

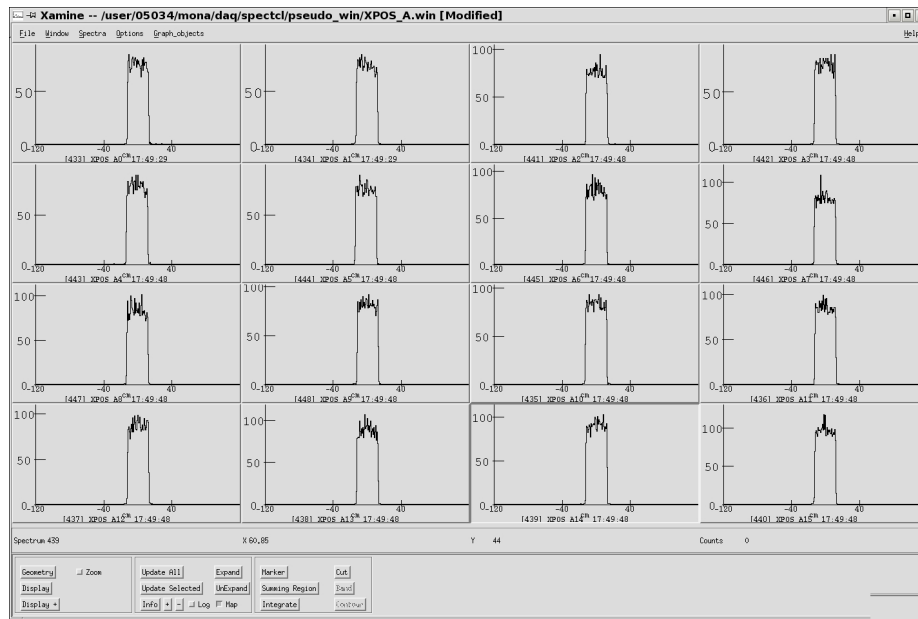


Figure C.3: X position Xamine spectra.

Do this by clicking *Apply Qgate to Xpos*. See Ref [94] for a detailed discussion on the CFD walk issue.

5. Then choose *Attach to File*, and select the run file recorded in step 1.
6. In Xamine go select **Window** -> **Read Configuration**, and pick one of the `/pseudowin/Xpos.win` window settings.
7. Allow SpecTcl to analyze all the buffers to ensure sufficient statistics for the Xpos fitting program. This may take over a half hour since the run was so long. When the data is read in, click *Update All* in Xamine.
8. Look through the spectra in Xamine to make sure the data is usable (i.e. that the edges of the Xpos spectra look sharp). Since the `Xposfitted` flag was set to "false", all the Xpos spectra will display the time difference (a width of about 25 ns), even though the spectra are still labelled with cm. Select all the `/pseudowin/Xpos.win` files to view all the Xpos spectra. The spectra should look like Figure C.3.

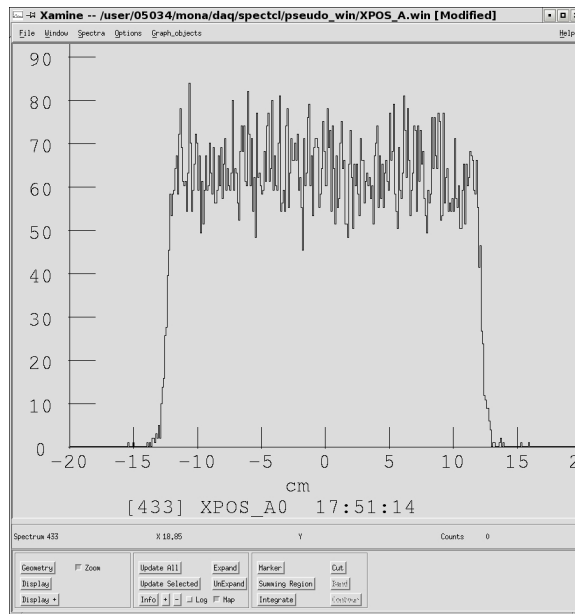


Figure C.4: X position A0 spectrum.

9. Figure C.4 is an expanded view for module A0.
10. Once the file is done loading, and the spectra look okay, push the *Write Xpos Spectra* button in the SpecTcl Control window.
11. When the TkCon confirms the `MoNAXposCosmics.asc` file is written, press the *Calibrate Xpos* button.
12. The TkCon window will scroll through a list of the values fitted for each bar. Scan the output and check that all the parameters have a reasonable slope value (near 8.0).
13. Reopen `MoNA_setup_run.tcl` and change the `Xposfitted` flag to `"true"`, and save.
14. Close SpecTcl and reopen it. The proper calibration will now be sourced to the program. If done properly, the width of an Xpos spectra of cosmic ray data from step 1 should be 200 cm and it should be centered about zero.

## C.6 Independent Tmean Offsets

Setting the independent Tmean offsets may be done after an experiment is finished as long as a sufficiently long recorded run is taken at the end of the experiment, but some timing and energy spectra during the experiment may look strange if this is not done before hand. MoNA must be gain matched and the QDC, TDC and Xpos slope/offset values must be fitted.

Since the various triggering signals to the TDC's are not individually wired but instead chained, the time for each TDC is slightly different. Even though all the PMT's have been gain matched, they still experience slightly different amplifying times. These inconsistencies lead to small, but significant, shifts in the average time calculated from the two TDC parameters (Tmean). In this process we will record cosmic rays passing through MoNA and gate on events that pass nearly straight down. The speed of cosmic ray muons are very nearly 29.98 cm/ns (speed of light,  $c$ ; the value of 29.8 cm/ns is used as the speed of the muons in calculations). So, if we look at the Tmean values for these events between two bars, we can calculate the proper time offset of these two bars relative to each other. If we gate on only muons travelling nearly straight down, the time difference is 0.344 ns for a 10 cm bar (10.26 cm is used as the dimensions of the bar because of tape and gaps between bars). If we use bar A8 as our reference (A8 offset is set to 0), the whole MoNA array, each bar, can then be set to have the proper time offsets. The Tmean differences between bars are calculated through pseudo parameters and the values read by a code from their spectra.

### C.6.1 Finding Independent Offsets

Before any offset values can be calculated, a long cosmic-ray run must be taken. This new run requires the all previous calibrations to be preformed first.

1. Record an overnight (12 hours) run of cosmic ray data with all detector bars.

Use MoNA multiplicity set to 3-fold, `cosmics` and select self-trigger and self-stop on the XLM control. Also be sure that you are using calibrated slope/offset values for both the QDC and TDC parameters and check that the calibration flags in `MoNA_setup_run.tcl`:

```
QDC_thres_flag
QDCfitted
TDCfitted
Xposfitted
```

2. Open MoNA SpecTcl [92] in the *spice* terminal window or from a Data U. machine.
3. From the TkCon window type:

```
source ~/mona/contrib/tmean_offset_cal/source.tcl
```

This will execute all the necessary `tcl` code to create the proper pseudos, make the straight-down gates, and apply them to the new parameters.

4. Then choose *Attach Multiple*, and select all of the run files recorded in step 1. Or using the `attach -pipe cat` command in the TkCon window, manually type in all of the run files recorded in step 1 then select *Start Analysis*.
5. In Xamine select **Window -> Read Configuration**, and pick one of the three `/win/tmean_cal_x-x.win` window settings to view the spectra.
6. Allow SpecTcl to analyze all the buffers to ensure sufficient statistics. This may take overnight since the run was so long. When the data is read in, click *Update All* in Xamine.

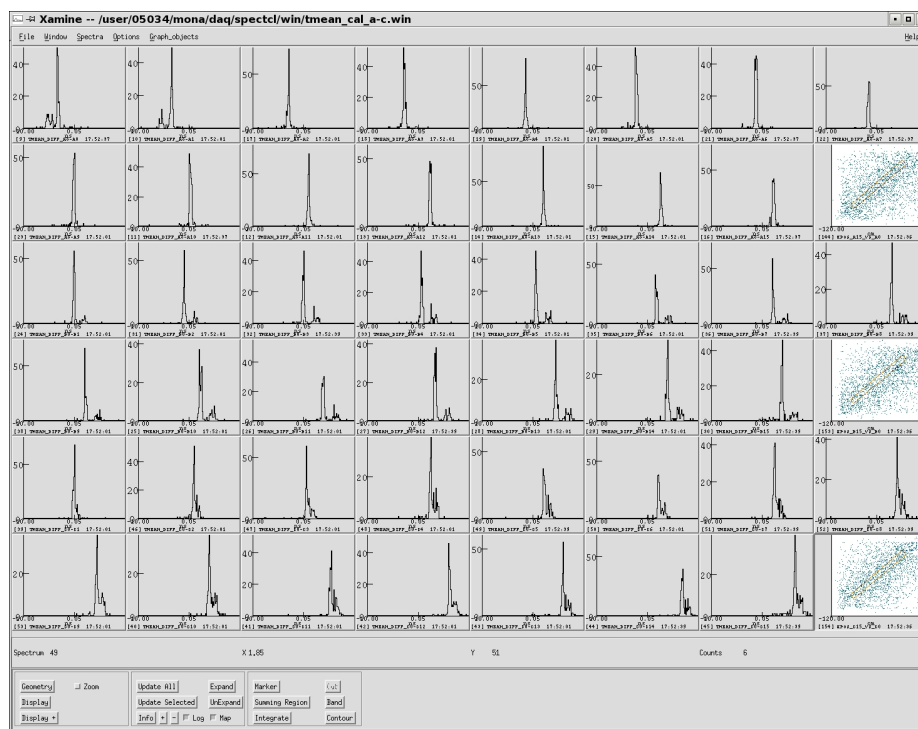


Figure C.5: Tmean difference spectra.

7. Look through the spectra in Xamine to make sure the data is usable ,i.e. that there is a distinct peak in each Tmean-difference spectrum as shown in Figure C.5.
8. Write all tmean\_diff spectra using the *Write Tmean\_offsets Spec* button on the MoNA SpecTcl window.
9. Open a *spice* terminal window in directory  $\tilde{m}$ ona/contrib/tmean\_offset\_cal and then open MoNA\_Tmean\_indie\_offsets. Note that before you run this executable you must delete or rename the file  $\tilde{m}$ ona/config/MoNA\_Tmean\_indie\_offsets.tcl; otherwise running the code will return an error. This will open the executable that will calculate the Tmean independent offsets. It calculates these by finding a gravity fit (weighted average) 0.3 ns to either side of the peak bin (measured). The program assumes the x axis (in ns) is symmetric about 0 (i.e. -10 to + 10 ns).



For layer A the offsets for bar, N, are:

$$\text{Offset} = -[\text{Theory}(\text{A8-AN}) - \text{Measured}(\text{A8-AN})]$$

For the cross terms (e.g. A15-B0) the offsets for layer, X, are:

$$\text{Offset} = [\text{Theory}(\text{A15-X0}) - \text{Measured}(\text{A15-X0})] - \text{Offset}(\text{A15-A8})$$

For all other layers the offsets for layer, X, and bar, N, are:

$$\text{Offset} = \text{Offset}(\text{A15-X0}) - [\text{Theory}(\text{X0-XN}) - \text{Measured}(\text{X0-XN})]$$

10. Edit `MoNA_setup_run.tcl` and save with `Tmean_indie_offset` set to "true" to read the `MoNA_Tmean_indie_offsets.tcl` file during next start up.
11. If you now restart `SpecTcl` and repeat steps 3-7, the peaks in each spectra should show up right at the `theoretical` values listed in the file `Tmean_offsets_theoretical`. In between steps 3 and 4 you must reread the independent offset file you just made (since the first line of `source.tcl` reads in a blank set of offsets).

```
source $env(MONA_CONFIGDIR)/MoNA_Tmean_indie_offsets.tcl
```

12. If you would like to redo the Tmean independent offsets, you must delete or rename the file

`/config/MoNA_Tmean_indie_offsets.tcl` before executing the code again.

Double check that all the calibration flags in `MoNA_setup_run.tcl` (mentioned in Chapter 1) are set to "true". For future runs, MoNA is now calibrated with data specific for the experiment.

# Appendix D

## Tandem SpecTcl Guide

### D.1 Getting Started

The tandem version of SpecTcl for the Sweeper-MoNA setup is a complex and large set of files compiled to form a complex and powerful analysis tool. It unpacks all the raw channels and converts many of them to calibrated parameters and even some to very useful physics parameters. Please familiarize yourself with the *Mona SpecTcl Guide* [92] and the online *SpecTcl User's Guide* [90] before proceeding. Concepts in those documents will not be reviewed.

One of the most noticeable differences is that an extra control window is used with the tandem SpecTcl. This **Tree Parameter GUI** has four tabbed pages (**Spectra**, **Parameters**, **Variables**, **Gates**). These will be discussed in detail in section 2.3. The other main visual difference is that the SpecTcl Control Window has two graphics in the center and a few extra buttons to track forward and do inverse tracking to the target. These extra features will be discussed in section 4.

#### D.1.1 Standard Variables

In the Tandem version, the `Tandem_spectcl.tcl` file replaces the `MoNA_spectcl_run.tcl` file and also creates a couple tandem parameters and sets the tandem

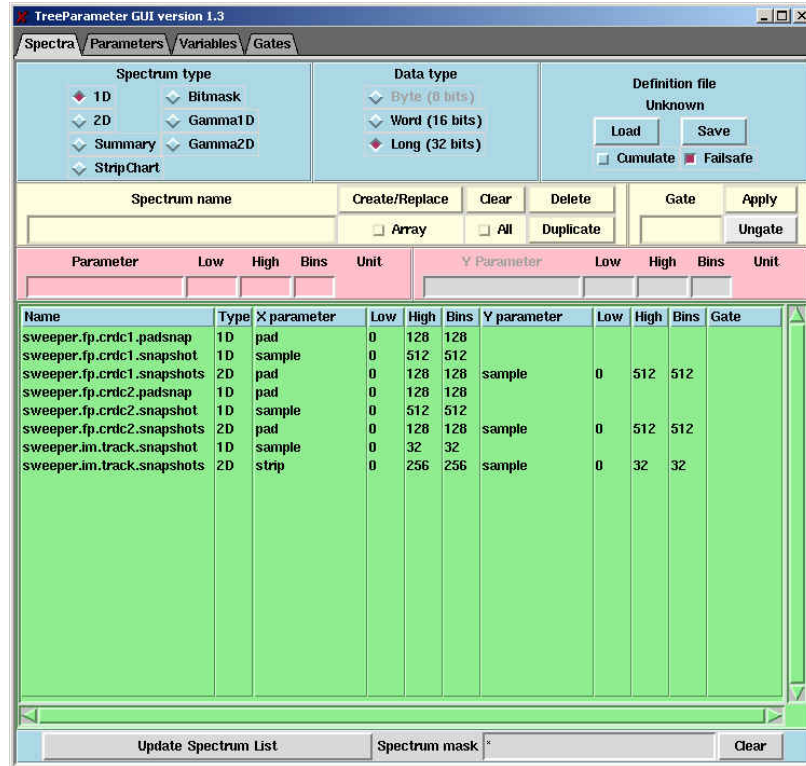


Figure D.1: Tree parameters user window.

variable `target.eloss`. This is the extra energy to add to the fragment energy for e-loss through half of the reaction target in units of MeV/u. As covered in the *Mona SpecTcl Guide* [92], the `MoNA_Z_pos` variable is set in the `MoNA_setup_run.tcl` file within the `mona/config` directory. This sets the distance, in centimeters, from the target to the center of bar MoNA bar A8. The `tmean_offset` variable is also set in the `MoNA_setup_run.tcl` file.

### D.1.2 Loading a Settings File

The front page of the *Tree Parameter GUI* is shown in Figure D.1.

The button *Load* in the upper left corner can be used to load a file a definition file containing all the spectra, gates, and variable settings and values. Using the *Cumulate* option will overwrite only the values set in the new configuration file. So if you set a variable and then load a new configuration file that also sets a value for that

variable, the value will be overwritten. It is wise to have a standard configuration file that only has variables set, so others can make their own spectra and then set the variables using that standard file with the *Cumulate* option. The current settings for all spectra, parameters, variables, and gates (that can be edited using the directions in the next section) can be saved by using the *Save* button. These files should be stored in the `/settings` directory.

This first page of the *Tree Parameter GUI* also is where the spectra can be created (for `sweeper` and `user` tree parameters only).

## D.2 Tree Structure

The Sweeper, and some MoNA, variables and parameters are defined in a tree structure. The two base tree labels are `sweeper` and `user`.

### D.2.1 Sweeper Tree

This tree contains all the sweeper parameters and variables written by D. Bazin, including:

```
fp (CRDC's, thin and thick scintillators, IC)
im (beam-line tracking)
tof (rf, xfp, potscint timing)
trigger (tigger channels)
```

These branches hold parameters like CRDC/beam-line tracking positions and angles, Ion Chamber energies, thin and thick scintillator energies and various timing channels.

## D.2.2 User Tree

This tree contains calibrated parameters created by W.A. Peters. Many of the Sweeper parameters cannot be calibrated without major changes to the code, so this tree was made to input many raw Sweeper parameters and then calibrate them with user defined variables. Branches of this tree include:

```
tof (rf, xfp, potscint, and thin timing, also fragment velocity)
e (thin and thick e-loss)
```

These branches hold parameters that can be calibrated and manipulated within the `CUser` tree code.

## D.2.3 Using the Tree Parameter GUI

### Making Spectra

The following directions apply only to `sweeper` and `user` tree branches. For MoNA spectra, use the TkCon window or the pre-set buttons on the SpecTel Control window [92]. MoNA spectra will indeed be displayed in the spectra tab of this GUI and can be edited once created. D. Bazin has written some excellent documentation about using the Tree Parameters [95].

1. In the upper left hand corner of the window, select the type of spectrum you wish to create. For information about the different types see Ref [90].
2. Next, select the *X Parameter* label to use the drag-down menu and move cursor to find the tree parameter you want.
3. The default parameter limits will be displayed to the right of the name.
4. Edit the parameter limits `Low`, `High`, `Bins` as desired.

5. Select *Create/Replace* and your spectrum will be displayed in the columns below.
6. Double-click any spectrum to edit any of the limit values and then repeat previous step.
7. Apply any gate that is made by selecting the Gate drag-down menu and then *Apply*.
8. Save time by saving definition file using *Save* button.

### Changing Parameters

On the second page you can change the default settings for any parameter. These are the same limit values that are displayed when a parameter is selected for a spectrum, as described above.

1. First click the designation button for an empty row. It will turn red.
2. Select a parameter using the *Parameter* label drag-down menu.
3. The default values will be displayed.
4. Edit the values for **High**, **Low**, **Bins**, **Unit**.
5. Select *Set* to make the changes or *Load* to revert back to previously set values.
6. Select *Change Spectra* to apply changes to all spectra containing that parameter.

### Changing Variables

Changing tree variables on the third page of the Tree Parameter control window is done analogous to changing parameter values as in the previous section.

1. First click the designation button for an empty row. It will turn red.

2. Select a variable from the *Variable* drag-down menu.
3. The default values will be displayed.
4. Edit the values for **Value**, **Unit**.
5. Select *Set* to make the changes or *Load* to revert back to previously set values.

## Changing Gates

The forth page in the Tree Parameter GUI deals with gates. Gates can be made by using in-line commands in the TkCon window [92] or by using *Contour* or *Cut* buttons in Xamine. If any gates have been made you can double-click the name of any gate and view its dependencies and type. You can then edit the values or delete the gate. Compound gates can be made by using the in-line command, or selecting the **And** type.

## D.3 SpecTcl Code Procedures

### D.3.1 Raw Sweeper Parameters

The Sweeper code does not calibrate any timing parameters but does indeed have many other parameters that are very useful. The most important code for the Sweeper parameters deals with the four tracking detectors. The two beam-line trackers (PPAC's or CRDC's) and the focal plane CRDC's are read in through an XLM module and a large chunk of data is taken for each valid hit. Gas tracking detectors have many parallel wires that collect the ionizing charge from the gas as a particle passes through. There is also a time channel to determine the drift time (usually the y direction) of the ionized electrons.

Another gas detector the Sweeper code reads is the Ion Chamber. This works in a similar fashion as the CRDC's but is not used to determine the position. It has

16 charge collecting pads that are used to get a precise measurement of energy-loss through the gas.

The thin and thick plastic scintillators at the end of the focal plane are used for timing and e-loss measurements. These two each have four PMT's and are recorded by eight QDC and TDC channels. The cyclotron RF and the A1900 extended focal plane timing detector (xfp), along with the pot scintillator (potscint) finish off the sweeper timing channels.

Each time is common started by the Sweeper trigger, which is a logic-delayed signal from the upper left PMT on the thin scintillator. So, the `thin_ul_time` raw parameter has the same spectra as the raw `sweeper.trigger` parameter. Every timing channel immediately subtracts this `sweeper.trigger` raw tdc value from itself in the code, to get ride of the logic unit's time jitter when it delays the PMT signal.<sup>1</sup> The subtraction looks like this in the code:

```
thin.tul = thin.time_ul - sweeper.trigger (similar for all four PMT's)
pot = pot - sweeper.trigger
rf = rf - sweeper.trigger
xfp = xfp - sweeper.trigger
```

The actual raw tdc values for RF, xfp, and potscint times are lost, while for those for the eight thin/thick times are not because a new raw parameter is used for the subtracted values.

These raw parameters can not be adjusted by any slopes or offsets. For this reason gates applied to these parameters are rather robust. If you can separate the desired events from these spectra then using a gate with these will make sure you don't need to reset the gates once the all the calibrations are made (within the `user` tree).

---

<sup>1</sup>Subtracting un-calibrated raw time parameters is not wise, but these timing channels are all on the same TDC and have very nearly the same slope to nanoseconds.



### D.3.2 Tree Calibrations

The Sweeper code does not calibrate the timing channels, but it does have a calibrated energy-loss parameter for the Ion Chamber (IC) and calibrated position and tracking parameters. The User code calibrates the timing channels and also the thin/thick e-loss (done within the `CUser.cpp` file).

#### User Potscint, RF, XFP

These are calibrated timing parameters that use their respective slope/offset values to calibrate the corresponding raw Sweeper timing parameter. Potscint, for example:

```
user.tof.potscint.cal = sweeper.tof.pot * user.tof.potscint.slope +  
potscint.offset
```

Note, that the slope for each raw Sweeper timing channel might not be the same and should be negative since the trigger (`thin_ul`) is used in common-start mode. Set the offset for the potscint from a known beam through the Sweeper magnet to the thin plastic. Be sure to calibrate and save the definition file before trying to use the third-level parameters described below.

#### User Thin Time

The timing channels for the four PMT's of the thin scintillator are calibrated and then averaged:

```
user.tof.thin_ul.cal = sweeper.tof.thin.tul * user.tof.thin_ul.slope +  
user.tof.thin_ul.offset (similar for all four PMT's)
```

```
user.tof.thin_time.cal = (ul.cal + ur.cal + dl.cal + dr.cal / 4) *  
thin_time.slope + thin_time.offset
```

The offset for `thin_ul` should be set to place the spectrum peak at zero, and the other three thin times at, or near, 1 ns. The offset for the average, `thin_time`, should be set to place the peak at about 0.5 ns. The slope for the four individual thin PMT times should be positive and then set the average slope to negative 1 (so it can be subtracted properly from the potscint time).

### **User Thin/Thick e-loss**

These parameters are analogous to the timing channels. Here each thin/thick Sweeper raw ADC channel is calibrated and then the four are averaged. In addition, the two averaged energy-loss parameters are added together to form `user.e.total.cal`.

### **Sweeper Positions and Angles**

Variables can be set to calibrate the gain and pedestal values for each CRDC pad. The x position is calibrated by taking the weighted average of all the pads above threshold and then, using the slope (2.54 mm per pad), is converted to millimeters. Using a mask to calibrate the y direction (from the drift time), these positions can have a precision of better than one millimeter.

The angles are then calculated from these positions and the distance between them (`sweeper.fp.gap`). Furthermore, you can set the `track.zfp` variable and get the calculated x,y positions at this z point in front or behind CRDC1. These two extra x,y parameters are called `track.xfp` and `track.yfp`. These two tracking parameters will become important later.

### **Sweeper Ion Chamber**

Each pad for the IC has it's own slope and offset variables and then the overall e-loss (`fp.ic.de`) parameter has a slope and offset.

### D.3.3 Third-Level Parameters

Many of the calibrated parameters are still not at the level of being useful for a true physical analysis of the reaction of interest. The third-level parameters are used to calculate some useful ones.

All the other `user.tof` parameters are differences of two calibrated times. For example:

```
user.tof.rf_pot.cal = user.tof.rf.cal - user.tof.potscint.cal *  
rf_pot.slope + rf_pot.offset
```

The respective slope/offsets should not need to be other than 1 and 0 since the components are already calibrated.

#### User Pot\_Thin Time

Having the `potscint` and `thin_time` calibrated parameters don't tell you the time-of-flight of the fragments until you subtract the two. The parameter for `potscint - thin_time`, as described above for the difference, is constructed similarly here, but with the added feature to adjust the time based on the tracking angle and position:

```
user.tof.pot_thin.cal = user.tof.potscint.cal - user.tof.thin_time.cal +  
sweeper.fp.track.xfp * sweeper.tof.potthinxfp +  
sweeper.fp.track.afp * sweeper.tof.potthinafp
```

To get the unadjusted tof, just set these adjustment variables to 0. The first line of this calibration is saved as the `frag_time` in the code and used for the fragment's velocity. This adjustment is useful for separating isotopes of the same element by rotating the time about the tracked dispersive position and angle to account for differing charge-to-mass ratios through the dipole.

## User Fragment Velocity

Here the `user.tof.pot.thin.cal` parameter is used without the adjustments described above as `frag_time`, along with `user.tof.vfrag.offset` in centimeters, to get the fragment velocity in cm/ns.<sup>2</sup> The `user.tof.vdiff.cal` parameter is the difference (in cm/ns) between the neutron velocity (calculated from hit 1) and the fragment velocity (it's slope and offset should be 1 and zero, respectively).

### D.3.4 MoNA Hits

The code to fill the hit parameters is processed as each bar is calibrated, and so `hit_1` is the first valid one the code calibrates as it parses through all 144 bars making the `Bar` parameters [92]; starting at A0 and ending at I15. These hit parameters are not ordered by time and should only be used as approximate checks during run time. See Ref [91] for ways to time-order all the hits. The `Multi_hit` parameter is the number of valid hits for that MoNA event, defined as two valid raw TDC channels for one bar. The hit parameters include:

```
X_hit, Y_hit, Z_hit
TOF_hit, KE_hit, Q_hit
Theta_hit, Phi_hit
Multi_hit
```

### D.3.5 Valid Tandem Hit

In the `CHitParam.cpp` code I have written a process to find the first MoNA hit based on time-of-flight. I first exclude events that are too fast to be neutrons by taking asking if the time is greater than 50 ns for all hits. This is required to avoid calculations using hits from a gamma-ray created at the target. 50 nanoseconds is

---

<sup>2</sup>You should follow the directions from section 2.3 and change the units for `vfrag.offset` to cm, and the units for the `vfrag.cal` and `vdiff.cal` to cm/ns.

the time a gamma-ray takes to travel 15 meters. If MoNA is placed further than 14.5 meters away from the target `CHitParam.cpp` should be edited and this value should be increased accordingly. After I am assured of at least one good hit, the code then scans the hits for the lowest time value and saves it's index. The rest of the Tandem parameters continue to use only that hit index, including the `KE_neutron` and `Tandem_e_decay` parameters. The code to find the first hit greater than 50 ns is here:

```
// First check that the MoNA array counter had at least one hit
if (Counter >= 1) {

    // initialize temp variable.
    double temp = 0.0;
    // array place of ToF first hit, initial value for hit 1 (count 0).
    int first_count = 0;
    // MoNA hit ToFarray[first_count], initial value to hit 1.
    double ToF_first = ToFarray[0];
    // condition set true when ToF has hit greater than 50 ns.
    bool good_hit = false;

    // loop through the ToF to find earliest and
    // set first_count to index of earliest
    for (int j = 0; j < Counter; j++) {

        // Check if MoNA ToF array has a hit with time great than 50 ns.
        if (ToFarray[j] >= 50.0) {
            // set good_hit true is there is one
            good_hit = true;
        }
    }
}
```

```

// continue to look for earliest ToF that is greater than 50 ns.
temp = ToFarray[j];
if (temp < ToF_first) {
    ToF_first = temp;
    // Set first_count to array index of earliest hit.
    first_count = j;
}
}
}

```

### D.3.6 Tracked Parameters

By using an inverse map, the SpecTcl code calculates not only the position and angle of the fragment at the target, but also the relative energy to the magnet's center track. An inverse map is just a transformation matrix from the focal plane coordinates to target coordinates (the newest inverse maps also inputs the forward-tracked target position). Directions to utilize this feature are described in section 4. The most important parameters calculated by this method are:

```

sweeper.fp.track.ata,bta,yta,
sweeper.im.track.xta,yta,ata,bta, sweeper.fp.track.dta

```

These are used to further calculate the energy of the fragment at the midpoint of the target (parameter `target.e`). After I've found a `good_hit` in the `CHitParams.cpp` these calculations are performed:

```

// m_fFragmass is the mass of the fragment in units amu.
double Famu = m_fFragmass;
double amu = 931.494013; // MeV/amu

```

```

// Calculating energy from Brho, mass, charge values.
double Frag_betagamma_o = (m_fFragBrho / 3.107 * m_fFragQ / Famu);
double Frag_gamma_o = sqrt(Frag_betagamma_o * \
    Frag_betagamma_o + 1.0);
// Frag_KE_o is the central track energy in MeV/u
double Frag_KE_o = amu * (Frag_gamma_o - 1.0);

// set energy from delta (ParamDT) and central_energy
// in MeV/u then add m_fTargeteloss (target.eloss) to target.e

double Frag_KE = ( ((double)rEvent[m_nParamDT] + 1.0) * \
    Frag_KE_o) + m_fTargeteloss ;

rEvent[m_nResultTE] = Frag_KE; //set target.e in MeV/u

```

The `target.eloss` variable (`m_fTargeteloss`) is the estimated energy the fragment loses half way through the target (in MeV/u) and it is added to the tracked energy to get the energy at the midpoint. This is a decent estimate for the fragment's energy assuming the reaction occurs at the target's midpoint.

### D.3.7 MoNA Tandem Parameters

The Tandem MoNA code calculates some useful parameters as well. The `Tandem_vdiff` hit parameters are miss-named and are actually just the velocity for that MoNA hit (in cm/ns) and not a difference at all. It is calculated from the `ToF_hit` parameters and the `MoNA_Z_pos` variable. The `KE_hit` parameters are calculated from the velocity and the mass of a neutron. A good practice is to gate this parameter on the neutron peak from the `ToF_hit` parameter. The following calculations are also done within

the CHitParam.cpp code.

### **KE\_neutron**

This is actually the first tandem parameter to be set after verifying that MoNA recorded a hit with a valid neutron time greater than 50 ns.

```
//Check if good_hit set to "true".
if (good_hit) {
    // if so, set result KE_neutron to MoNA KE hit of first_count
    rEvent[m_nResultKE_n] = KEarray[first_count];
```

The index [first\_count] refers to the first neutron event greater than 50 ns in time-of-flight.

### **Theta**

The angle between the fragment and the neutron is calculated from the fragment tracked angles and the neutron angle using vector analysis. This value goes into the Theta parameter.

```
// First add both vectors
double Both_Sum = Frag_x * Xarray[first_count] + \
    Frag_y * Yarray[first_count] + \
    Frag_z * Zarray[first_count];

double Frag_R2 = (pow (Frag_z,2.0) + pow (Frag_y,2.0) + \
    pow (Frag_x,2.0)); //r-vector squared

double Frag_distance = (pow (Frag_R2,0.5)); // in cm
double Both_Product = Distance[first_count] * Frag_distance ;
```



```
// solve for cos(theta) = AxBx + AyBy + AzBz / A*B
double cos_theta = (Both_Sum / Both_Product);

rEvent[m_nResultThe] =( acos(cos_theta) * 180.0/PI);
```

Here again [first\_count] refers to the first neutron event greater than 50 ns in time-of-flight.

### Decay Energy

The energy of the fragment at the target (calculated using an inverse map) along with the Theta parameter and the neutron energy is used to calculate the invariant mass of the decay state. The velocity difference parameter KE\_vdiff is also calculated from their respective kinetic energies.

```
// from KE(MeV/u) to gamma, with c=1, Vc=29.9792458 cm/ns
double Namu = Nmass/amu; //Neutron mass in amu = 1.008665.
double N_beta = pow(( Nvel[first_count]/Vc),2.0); //squared
double N_gamma = sqrt(1.0/(1.0 - N_beta));
double Frag_gamma = 1.00 + (Frag_KE / amu);
double Frag_beta = (1.0 - (1.0/(Frag_gamma * Frag_gamma)));

// setting KE_vdiff parameter to velocity difference.
rEvent[m_nResultKV] = (sqrt(N_beta) - sqrt(Frag_beta)) * Vc;

double Pneutron = Namu * sqrt(N_beta) * N_gamma;
double Pfrag = Famu * sqrt(Frag_beta) * Frag_gamma;

// Calculate M0^2 + PMo^2 = m1^2 + m2^2 +
```

```

// 2(En*Ef - Pn*Pf*cos(theta))
// first convert KE into total E for N and Frag

double Eneutron = N_gamma * Namu; // Total N E
double Efrag = Frag_gamma * Famu ; // Total frag E
double Etotal = Namu*Namu + Famu*Famu + \
    2.0000*(Efrag*Eneutron - (Pneutron*Pfrag*cos_theta));

double Qamu = sqrt(Etotal) - Namu - Famu; // in amu/c^2

rEvent[m_nResultEdecay] = Qamu*amu; //Tandem_e_decay in MeV/c^2

```

Here `Nvel` is the neutron velocity for `first_count`. Note that `N_beta` is  $(v_n/c)^2$ , and similarly for `Frag_beta`, that's why it is square-rooted for many of the calculations.

## D.4 Analysis Suggestions

The following sections are written to help with some of the standard analysis procedures. The Control window for Tandem SpecTcl is a little different than for the MoNA version as shown by Figure D.2.

### D.4.1 Tandem Control Buttons

For the most part, the buttons on the Tandem SpecTcl Control window are the same as for the MoNA SpecTcl [92] but for a few exceptions.

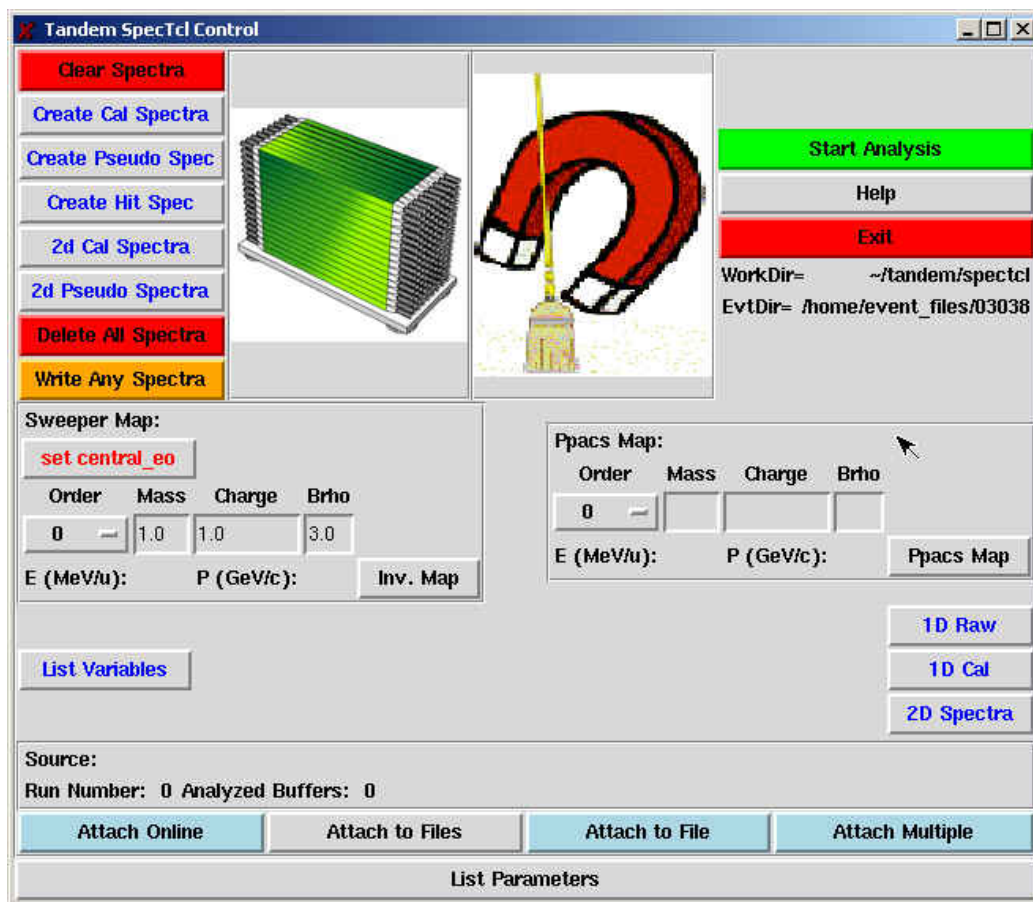


Figure D.2: Tandem SpecTcl control window.

## Customized Buttons

The `tandem/spectcl/tcl` directory contains a few files that are sourced by the gray buttons with the blue lettering. The *1D Raw* button sources the `tcl/SpecGen.tcl` file. The *1D Cal* button sources the `tcl/CalcParameter1DSpectra.tcl` file. The *2D Spectra* button sources the `tcl/CalcParameter2DSpectra.tcl` file. These three files can be edited to include any custom commands or spectra you choose.

## D.4.2 Beamline Forward Tracking

Forward tracking can only be completed after the beam-line tracking detectors have been calibrated for from mask runs, and the `sweeper.im.gap` variable is set to the

distance between them. The *Ppacs map*<sup>3</sup> button is used in conjunction with the **Order**, **Mass**, **Charge**, **Brho** input frames to forward track the position and angle of the fragment at target from the information from the beam-line tracking detectors. These inputs should correspond to the mass and charge of the fragment you wish to track through the triplet magnet. The **Order** should be set to 3 (or higher if the forward map was made to a higher order). The **Brho** input should correspond to the **Brho** value setting of the triplet. Check the experiment's logbook for this number. When a forward map file is made this **Brho** value is needed.

Once the input frames are filled with the appropriate values, make sure the `sweeper.im.track.map.maxparameters` variable is set to 5. Now an appropriate forward map must be made (.map extension) and sourced with the *Ppacs map* button. A good check to see if it is working is to source a collimator run with a known beam and known energy. The positions at the target should be centered near zero.

### D.4.3 Sweeper Inverse Tracking

Inverse tracking can only be completed after the CRDC's have been calibrated for position from mask runs. The *Inv. map* button is used in conjunction with the **Order**, **Mass**, **Charge**, **Brho** input frames to calculate the energy of the fragment at target from information from the focal plane CRDC detectors. These inputs should correspond to the mass and charge of the fragment you wish to track through the Sweeper magnet. The **Order** should be set to 3 (or higher if the inverse map was made to a higher order). The **Brho** input should correspond to the **Brho** value setting of the Sweeper magnet before the run. Check the experiment's logbook for this number. This number is also needed to make the inverse map, so you can check with the person who calculates the inverse maps as well.

Once the input frames are filled with the appropriate values the `sweeper.fp.track`

---

<sup>3</sup>This button is used with both beam line tracking PPAC's or CRDC's.

`.map.maxparameters` variable should be set to 4 if you wish to use the old inverse maps that do not require the beam-line detectors, or to 5 for the new inverse maps that take into account the x position at the target from the forward tracking map described above that require the beam-line detectors.<sup>4</sup> Now an appropriate inverse map must be made (`.inv` extension) and sourced with the *Inv. map* button. A good check to see if it is working is to source a collimator run with a known beam and known energy. The positions at the target should be centered near zero, and the energy should match.

#### D.4.4 MoNA Timing

For proper MoNA timing, the potscint signal should be routed as the common stop for all TDC's. During the experiment be sure to take a few `self triggered` runs with some thick stopping material in place of the target. This will create a lot gamma rays streaming toward MoNA. Applying a gate to the front of MoNA or to bar A8 will fix the distance they travel to be equal to the variable `MoNA_Z_pos` in centimeters. The `tmean_offset` variable should then be set to move gamma peak to the time light takes to travel to the front of MoNA (`MoNA_Z_pos` divided by 29.98). Click the *List Variables* button to display current values in the TkCon window.

#### D.4.5 Isotopic Separation

The best technique for separating isotopes is to gate a particular proton number using the calibrated Ion Chamber `fp.ic.de` parameter and apply this gate to a 2d de-tof spectrum. Use the adjustable `user.tof.pot_thin.cal` parameter for the x axis and set the `sweeper.tof.potthinAFP`, `potthinAFP` variables to shift the time based of the tracked positions and angles. These are not the forward tracked or the inverse tracked parameters. These parameters have not been transformed from the focal plane

---

<sup>4</sup>The new `.inv` maps use as an input the x position at the target (`sweeper.im.track.xta`) calculated from the forward mapping.

coordinate system. They are just tracked to a z position in front (negative) or behind (positive) CRDC1, using the `sweeper.fp.track.zfp` variable. It is also good practice to display the tracked `sweeper.fp.track.afp` or `sweeper.fp.track.xfp` parameters versus the adjustable time to help you choose the best values. With some luck you'll find some settings for the three variables that really separate the isotopes. For detailed directions on this subject see Ref [96].

#### **D.4.6 Decay Energy**

The `Tandem_E_decay` parameter incorporates the angle between the neutron and the fragment, and when the all the tracking and calibrations are completed, it is the best calculation we have to get the decay energy of neutron-unbound states.

#### **D.4.7 Multiple Neutrons**

Since MoNA is so large and it's depth is considerable (90 cm), often a single neutron will react more than once inside it's volume and be recorded as more than one hit in the hit parameters. The most likely case is where the neutron strikes a proton in one bar the proton travels out the side of the bar into a neighboring bar, thereby causing two hits from one neutron. The most interesting case is where there are indeed two neutrons entering MoNA and each reacts with a different bar to cause two hits. These different scenarios are difficult to distinguish. Using the time-ordered pseudo parameters [91] we can make a good attempt to separate these events.

When the hits are sorted by time-of-flight we can look at the distance between two hits to see if they are neighboring bars. The velocity of the second hit should be less than the first if the same neutron reacts twice. There are also other, more advanced, calculations and parameters that can be made to determine the number of incoming neutrons, including the energy deposited by the first hit versus the scattered angle between two hits.

## D.4.8 Limitations

The `Tandem_E_decay` code does not require any signal in the respective QDC parameters, so a careful simulation code must accompany any final analysis to account for some ‘soft’ neutron events near the edges of MoNA that don’t deposit enough light to be seen by both CFD’s at each end of the bar. This will induce a slight undercounting of events at ends of the MoNA bars and should be mimicked in a simulation like `GEANT`.

The threshold for the QDC’s are set about 10 channels above the pedestal by the QDC fitting program to ensure the pedestals are not read out for all MoNA events and thereby swamping the data acquisition with 288 meaningless values. In practice this corresponds to an energy of about 0.5 MeVee, and is a bit higher than the -10 mV setting for each CFD that triggers the TDC channels. Therefore, we get plenty of MoNA events with a valid pair of TDC channels that do not have valid QDC data. The `CHitParam` code could be edited to require a QDC signal at each end of the MoNA bar, but this will cut a non-negligible fraction of events from the data, and we use the ToF parameter to calculate neutron energy anyway.

## BIBLIOGRAPHY

- [1] K. S. Krane. *Introductory Nuclear Physics*. (John Wiley and Sons), 1988.
- [2] A. Bohr and B. R. Mottelson. *Nuclear Structure*, volume 1. World Scientific, New Jersey, 1998.
- [3] M. Goeppert-Mayer. The Shell Model, 1963. Nobel Lecture.
- [4] M. Goeppert-Mayer and J. H. D. Jensen. *Elementary Theory of Nuclear Shell Structure*. Wiley, New York, 1955.
- [5] J. K. Tuli. Nuclear Wallet Cards. *National Nuclear Data Center*, 7th Edition, April 2005.
- [6] E. K. Warburton and B. A. Brown. *Phys. Rev. C*, 46(3):923, 1992.
- [7] M. Thoennessen, S. Yokoyama, A. Azhari, T. Baumann, J. A. Brown, A. Galonsky, P. G. Hansen, J. H. Kelley, R. A. Kryger, E. Ramakrishnan, and P. Thirolf. *Phys. Rev. C*, 59(1):111, 1999.
- [8] I. Tilquin, Y. El Masri, M. Parlog, Ph. Collon, M. Hadri, Th. Keutgen, J. Lehmann, P. Leleux, P. Lipnik, A. Ninane, F. Hanappe, G. Bizard, D. Durand, P. Mosrin, J. Peter, R. Regimbart, and B. Tamain. *Nucl. Instr. and Meth. A*, 365:446, 1995.
- [9] Nuclear Enterprises Ltd., Edinburgh, Scotland, UK.
- [10] P. D. Zecher, A. Galonsky, J. J. Kruse, S. J. Gaff, J. Ottarson, J. Wang, F. Deak, A Horvath, A. Kiss, Z. Seres, K. Ieki, Y. Iwata, and H. Schelin. *Nucl. Instr. and Meth. A*, 401:329, 1997.
- [11] Saint-Gobain Crystals & Detectors, Scintillation Products, 12345 Kinsman Rd., Newbury, OH 44065, USA, <http://www.detectors.saint-gobain.com/home.asp> .
- [12] Th. Blaich, Th. W. Elze, H. Emling, H. Freiesleben, K. Grimm, W. Henning, R. Holzmann, G. Ickert, J. G. Keller, H. Klingler, W. Kneissl, R. Konig, R. Kulesa, J. V. Kratz, D. Lambrecht, J. S. Lange, Y. Leifels, E. Lubkiewicz, M. Proft, W. Prokopowicz, C. Schutter, R. Schmidt, H. Spies, K. Stelzer, J. Stroth, W. Walus, E. Wajda, H. J. Wollersheim, M. Zinser, and E. Zude. *Nucl. Instr. and Meth. A*, 314:136, 1992.
- [13] N. Fukuda, T. Nakamura, N. Aoi, N. Imai, M. Ishihara, T. Kobayashi, H. Iwasaki, T. Kubo, A. Mengoni, M. Notani, H. Otsu, H. Sakurai, S. Shimoura, T. Teranishi, Y. X. Watanabe, and K. Yoneda. *Phys. Rev. C*, 70(5):054606, 2004.



- [14] B. Luther, T. Baumann, M. Thoennessen, J. Brown, P. DeYoung, J. Finck, J. Hinnefeld, R. Howes, K. Kemper, P. Pancella, G. Peaslee, W. Rogers, and S. Tabor. *Nucl. Instr. and Meth. A*, 505:33, 2003.
- [15] T. Baumann, J. Boike, J. Brown, M. Bullinger, J. P. Bychoswki, S. Clark, K. Daum, P. A. DeYoung, J. V. Evans, J. Finck, N. Frank, A. Grant, J. Hinnefeld, G. W. Hitt, R. H. Howes, B. Isselhardt, K. W. Kemper, J. Longacre, Y. Lu, B. Luther, S. T. Marley, D. McCollum, E. McDonald, U. Onwuemene, P. V. Pancella, G. F. Peaslee, W. A. Peters, M. Rajabali, J. Robertson, W. F. Rogers, S. L. Tabor, M. Thoennessen, E. Tryggestad, R. E. Turner, P. J. VanWylen, and N. Walker. *Nucl. Instr. and Meth. A*, 543:517, 2005.
- [16] A. F. Zeller et al. *Adv. in Cyro. Eng. A*, 45:643, 2000.
- [17] M. D. Bird et al. *IEEE Trans. Applied Superconductivity*, 15:1252, 2005.
- [18] T. Baumann, H. Ikeda, M. Kurokawa, T. Nakamura M. Miura, Y. Nishi, S. Nishimura, A. Ozawa, I. Tanihata T. Sugimoto, and M. Thoennessen. *Nucl. Instr. and Meth. A*, 505:25, 2003.
- [19] F. Ajzenberg-Selove. *Nucl. Phys. A*, 490:1, 1998.
- [20] M. Meister, K. Markenroth, D. Aleksandrov, T. Aumann, L. Axelsson, T. Baumann, M. J. G. Borge, L. V. Chulkov, W. Dostal, B. Eberlein, Th. W. Elze, H. Emling, C. Forssen, H. Geissel, M. Hellstrom, R. Holzmann, B. Jonson, J. V. Kratz, R. Kulesa, Y. Leifels, A. Leistenschneider, I. Mukha, G. Munzenberg, F. Nickel, T. Nilsson, G. Nyman, A. Richter, K. Riisager, C. Scheidenberger, G. Schrieder, H. Simon, O. Tengblad, and M. V. Zhukov. *Phys. Rev. Lett.*, 88(10):102501, 2002.
- [21] K. Alder and A. Winther. *Electromagnetic Excitation*. North-Holland, Amsterdam/Oxford, 1975.
- [22] A. Winther and K. Alder. *Nucl. Phys. A*, 319:518, 1979.
- [23] C. A. Bertulani and G. Baur. *Phys. Rep.*, 163:299, 1988.
- [24] J. A. Tostevin. *Nucl. Phys. A*, 682:320c, 2001.
- [25] N. Austern, Y. Iseri, M. Kamimura, M. Kawai, G. Rawitscher, and M. Yahiro. *Phys. Rep.*, 154:125, 1987.
- [26] T. Kobayashi, O. Yamakawa, K. Omata, K. Sugimoto, T. Shimoda, N. Takahashi, and I. Tanihata. *Phys. Rev. Lett.*, 60:2599, 1988.
- [27] B. A. Brown, 2007. Private communication.
- [28] P. G. Hansen and J. A. Tostevin. *Annu. Rev. Nucl. Part. Sci.*, 53:219, 2003.

- [29] A. Navin, D. W. Anthony, T. Aumann, T. Baumann, D. Bazin, Y. Blumenfeld, B. A. Brown, T. Glasmacher, P. G. Hansen, R. W. Ibbotson, P. A. Lofy, V. Madalena, K. Miller, T. Nakamura, B. V. Pritychenko, B. M. Sherrill, E. Spears, M. Steiner, J. A. Tostevin, J. Yurkon, and A. Wagner. *Phys. Rev. Lett.*, 85(2):266, 2000.
- [30] S. D. Pain, W. N. Catford, N. A. Orr, J. C. Angelique, N. I. Ashwood, V. Bouchat, N. M. Clarke, N. Curtis, M. Freer, B. R. Fulton, F. Hanappe, M. Labiche, J. L. Lecouey, R. C. Lemmon, D. Mahboub, A. Ninane, G. Normand, N. Soic, L. Stuttge, C. N. Timis, J. A. Tostevin, J. S. Winfield, and V. Ziman. *Phys. Rev. Lett.*, 96(3):032502, 2006.
- [31] R. C. York et al. Proposed Upgrade of the NSCL. *IEEE Part. Accel. Conf.*, page 345, 1998.
- [32] A. Del Guerra. *Nucl. Instr. and Meth.*, 135:337, 1976.
- [33] D. A. Kellogg. *Phys. Rev.*, 90(2):224, 1953.
- [34] L. Celano, G. Tagliente, G. D’Erasmus, A. Pantaleo, and N. Colonna. *Nucl. Instr. and Meth. A*, 392:304, 1997.
- [35] CAEN S.p.A. Via Vetraia, 11 55049 - Viareggio (LU), Italy, <http://www.caen.it/nuclear/>.
- [36] Photonis dept. Burle Industries Inc. P.O. Box 60, 9300 AB Roden, Netherlands. <http://www.photonis.com/products/photomultiplier-tubes>.
- [37] Magnetic Shield Corporation, 740 North Thomas Drive, Bensenville, IL 60106, USA, <http://www.magnetic-shield.com/> .
- [38] IL. Karsh, A. Bohm, K-Th. Brinkmann, L. Demirors, and M. Pfuff. *Nucl. Instr. and Meth. A*, 460:362, 2001.
- [39] Jan Toke. *User’s Manual, Systems*. JTEC Instruments, 32 Thompson Rd., Rochester, NY, USA, December 2002. Revision B.
- [40] W. Rogers et al., 2007. Westmont College, CA, USA. Private communication.
- [41] R. Madey, J. W. Watson, M. Ahmad, B. D. Anderson, A. R. Baldwin, A. L. Casson, W. Casson, R. A. Cecil, A. Fazely, J. M. Knudson, C. Lebo, W. Pairsuwan, P. J. Pella, J. C. Varga, and T. R. Witten. *Nucl. Instr. and Meth.*, 214:401, 1983.
- [42] J. M. Paul. *Nucl. Instr. and Meth.*, 96:51, 1971.
- [43] GEANT. CERN library long writeup. Technical Report W5013, CERN, 1994.
- [44] T. Baumann, 2007. NSCL design drawings. Private communication.
- [45] D. J. Morrissey, B. M. Sherrill, M. Steiner, A. Stolz, and I. Wiedenhoever. *Nucl. Instr. and Meth. B*, 204:90, 2003.

- [46] A. Schiller, T. Baumann, D. Bazin, J. Brown, P. DeYoung, N. Frank, A. Gade, J. Hinnefeld, R. Howes, R. A. Kryger, J.-L. Lecouey, B. Luther, W. A. Peters, J. R. Terry, M. Thoennessen, and K. Yoneda. volume 831, page 92. AIP, 2006.
- [47] N. Frank. *Spectroscopy of Neutron Unbound States in Neutron Rich Oxygen Isotopes*. PhD thesis, Michigan State University, 2006.
- [48] Wave Metrics. IGOR PRO 5.0.1.0. 10200 SW Nimbus, G-7, Portland, OR, USA.
- [49] M. Berz and J. Hoefkens. COSY INFINITY version 8.1. Technical Report MSUCL-1196, MSU/NSCL, 2001. <http://cosy.nsl.msu.edu>.
- [50] N. Frank, A. Schiller, D. Bazin, W. A. Peters, and M. Thoennessen. *Nucl. Instr. and Meth. A*, submitted May 2007.
- [51] H. Scheit. Simple Track for MoNA, 2006. NSCL.
- [52] M. B. Chadwick et al. *Nucl. Data Sheets*, 107:2931, 2006.
- [53] A. Fassò, A. Ferrari, J. Ranft, P. R. Sala, G. R. Stevenson, and J. M. Zazula. Fluka92. In *Proceedings of the Workshop on Simulating Accelerator Radiation Environments*, 1993.
- [54] P. A. Aarnio et al. Fluka user's guide. Technical Report TIS-RP-190, CERN, 1987, 1990.
- [55] R. Madey, F. M. Waterman, A. R. Baldwin, J. Knudson, J. D. Carlson, and J. Rapaport. *Nucl. Instr. and Meth.*, 151:445, 1978.
- [56] R. J. Glauber. *Phys. Rev.*, 99(5):1515, 1955.
- [57] R. H. Stokes and P. G. Young. *Phys. Rev.*, 178:2024, 1969.
- [58] P. G. Hansen and B. Jonson. *Europhys. Lett.*, 4:409, 1987.
- [59] T. Otsuka, M. Ishihara, N. Fukunishi, T. Nakamura, and M. Yokoyama. *Phys. Rev. C*, 49(5):R2289–R2292, 1994.
- [60] T. Nakamura, S. Shimoura, T. Kobayashi, T. Teranishi, K. Abe, N. Aoi, Y. Doki, M. Fujimaki, N. Inabe, N. Iwasa, K. Katori, T. Kubo, H. Okuno, T. Suzuki, I. Tanihata, Y. Watanabe, A. Yoshida, and M. Ishihara. *Phys. Lett. B*, 331(3-4):296–301, July 1994.
- [61] N. C. Summers, 2007. Private communication.
- [62] K. L. Yurkewicz, D. Bazin, B. A. Brown, J. Enders, A. Gade, T. Glasmacher, P. G. Hansen, V. Maddalena, A. Navin, B. M. Sherrill, and J. A. Tostevin. *Phys. Rev. C*, 74(2):024304, 2006.
- [63] V. R. Pandharipande, I. Sick, and P. K. A. deWitt Huberts. *Rev. Mod. Phys.*, 69:981, 1997.

- [64] J. R. Terry, D. Bazin, B. A. Brown, J. Enders, T. Glasmacher, P. G. Hansen, B. M. Sherrill, and J. A. Tostevin. *Phys. Rev. C*, 69(5):054306, 2004.
- [65] A. Gade, D. Bazin, B. A. Brown, C. M. Campbell, J. A. Church, D. C. Dinca, J. Enders, T. Glasmacher, P. G. Hansen, Z. Hu, K. W. Kemper, W. F. Mueller, H. Olliver, B. C. Perry, L. A. Riley, B. T. Roeder, B. M. Sherrill, J. R. Terry, J. A. Tostevin, and K. L. Yurkewicz. *Phys. Rev. Lett.*, 93(4):042501, 2004.
- [66] A. Gade, D. Bazin, B. A. Brown, C. M. Campbell, J. A. Church, D. C. Dinca, J. Enders, T. Glasmacher, P. G. Hansen, Z. Hu, K. W. Kemper, W. F. Mueller, H. Olliver, B. C. Perry, L. A. Riley, B. T. Roeder, B. M. Sherrill, J. R. Terry, J. A. Tostevin, and K. L. Yurkewicz. *Phys. Rev. C*, 69(3):034311, 2004.
- [67] A. Gade, D. Bazin, C. A. Bertulani, B. A. Brown, C. M. Campbell, J. A. Church, D. C. Dinca, J. Enders, T. Glasmacher, P. G. Hansen, Z. Hu, K. W. Kemper, W. F. Mueller, H. Olliver, B. C. Perry, L. A. Riley, B. T. Roeder, B. M. Sherrill, J. R. Terry, J. A. Tostevin, and K. L. Yurkewicz. *Phys. Rev. C*, 71(5):051301, 2005.
- [68] J. Enders, T. Baumann, B. A. Brown, N. H. Frank, P. G. Hansen, P. R. Heckman, B. M. Sherrill, A. Stolz, M. Thoennessen, J. A. Tostevin, E. J. Tryggestad, S. Typel, and M. S. Wallace. *Phys. Rev. C*, 67(6):064301, 2003.
- [69] H. P. Blok G. J. Kramer and L. Lapikas. *Nucl. Phys. A*, 679:267, 2001.
- [70] M. B. Tsang, Jenny Lee, and W. G. Lynch. *Phys. Rev. Lett.*, 95(22):222501, 2005.
- [71] Jenny Lee, J. A. Tostevin, B. A. Brown, F. Delaunay, W. G. Lynch, M. J. Saelim, and M. B. Tsang. *Phys. Rev. C*, 73(4):044608, 2006.
- [72] C. K. Gelbke et al. Isotope Science Facility at Michigan State University. Technical Report MSUCL-1345, NSCL/MSU, 2006.
- [73] J. A. Tostevin. *J. Phys. G*, 25:735, 1999.
- [74] J. A. Tostevin, 2007. Private communication.
- [75] U. C. Bergmann, M. J. G. Borge, R. Boutami, L. M. Fraile, H. O. U. Fynbo, P. Hornshoj, B. Jonson, K. Markenroth, I. Martel, I. Mukha, T. Nilsson, G. Nyman, A. Oberstedt, Y. Prezado Alonso, K. Riisager, H. Simon, O. Tengblad, F. Wenander, and K. Wilhelmsen Rolander. *Nucl. Phys. A*, 692:427, 2001.
- [76] M. Huhta, P. F. Mantica, D. W. Anthony, B. A. Brown, B. S. Davids, R. W. Ibbotson, D. J. Morrissey, C. F. Powell, and M. Steiner. *Phys. Rev. C*, 57(6):R2790, 1998.
- [77] G. Gori, F. Barranco, E. Vigezzi, and R. A. Broglia. *Phys. Rev. C*, 69(4):041302, 2004.

- [78] F. M. Nunes, I. J. Thompson, and J. A. Tostevin. *Nucl. Phys. A*, 703:593, 2002.
- [79] P. G. Hansen and B. M. Sherrill. *Nucl. Phys. A*, 693:133, 2001.
- [80] H. G. Bohlen, R. Kalpakchieva, W. von Oertzen, T. N. Massey, B. Gebauer, S. M. Grimes, T. Kokalova, A. Lenz, M. Milin, Ch. Schulz, S. Thummerer, S. Torilov, and A. Tumino. *Nucl. Phys. A*, 734:345, 2004.
- [81] S. D. Pain. *Experimental Measurements of the  $N = 8$  Shell Breaking in the  $^{12}\text{Be}$  Ground State*. PhD thesis, University of Surrey, 2004.
- [82] D. J. Millener. *Nucl. Phys. A*, 693:394, 2001.
- [83] A. Schiller, N. Frank, T. Baumann, D. Bazin, B. A. Brown, J. Brown, P. A. DeYoung, J. E. Finck, A. Gade, J. Hinnefeld, R. Howes, J.-L. Lecouey, B. Luther, W. A. Peters, H. Scheit, M. Thoennessen, and J. A. Tostevin. *Submitted to Phys. Rev. Lett.*, 2007.
- [84] C. Hoffman et al. *to be submitted*, 2007.
- [85] A. Horvath, K. Ieki, A. Kiss, A. Galonsky, M. Thoennessen, T. Baumann, D. Bazin, C. Bordeanu, N. Carlin, M. Csanad, F. Deak, P. DeYoung, N. Frank, T. Fukuchi, Zs. Flp, A. Gade, D. R. Galaviy, A. Galonskz, C. Hoffman, R. Iysak, W. A. Peters. H. Schelin, A. Schiller, R. Sugo, Y. Seres, and G. Veres. *Eur. Phys. J. A*, 27:217, 2005.
- [86] G. A. Christian et al. *to be submitted*.
- [87] W. Rogers et al. <http://physics.westmont.edu/research/cmda>.
- [88] J. Miller, M. Strongman, L. Elliott, D. B. Hecksel, M. M. Kleber, P. J. Voss, T. Pike, R. Pepin, A. Ratkiewicz, and W. A. Peters. MoNA Calibration Guide. Technical report, MSU/NSCL, 2005. <http://www.cord.edu/dept/physics/mona/analysis.html>.
- [89] W. A. Peters. Tandem SpecTcl Guide. Technical report, MSU/NSCL, 2006. <http://www.cord.edu/dept/physics/mona/analysis.html>.
- [90] R. Fox. SpecTcl User's Guide. Technical report, MSU/NSCL, 2003. <http://docs.nscl.msu.edu/daq/spectcl>.
- [91] A. Ratkiewicz and W. A. Peters. Time Sorting Pseudo Codes. Technical report, MSU/NSCL, 2005. <http://www.cord.edu/dept/physics/mona/analysis.html>.
- [92] A. Ratkiewicz and W. A. Peters. MoNA SpecTcl Guide. Technical report, MSU/NSCL, 2006. <http://www.cord.edu/dept/physics/mona/analysis.html>.

- [93] K. Yoneda and W. A. Peters. MoNA Fitting Codes. Technical report, MSU/NSCL, 2004.  
<http://www.cord.edu/dept/physics/mona/analysis.html>.
- [94] G. A. Christian and W. A. Peters. MoNA Position Calibration. Technical report, MSU/NSCL, 2005.  
<http://www.cord.edu/dept/physics/mona/analysis.html>.
- [95] D. Bazin. Tree Parameters. Technical report, MSU/NSCL, 2005.  
<http://docs.nscl.msu.edu/daq/appnotes/TreeParameter.html>.
- [96] N. Frank. Sweeper Isotope Separation. Technical report, MSU/NSCL, 2005.  
<http://www.cord.edu/dept/physics/mona/analysis.html>.